Dry Aerosol Direct Writing for Selective Nanoparticle Deposition

Aghajani, S.

DOI
10.4233/uuid:cc6cd71d-d46c-4db6-8f55-38ca841391f9

Publication date
2023

Document Version
Final published version

Citation (APA)
Aghajani, S. (2023). *Dry Aerosol Direct Writing for Selective Nanoparticle Deposition*. [Dissertation (TU Delft), Delft University of Technology]. https://doi.org/10.4233/uuid:cc6cd71d-d46c-4db6-8f55-38ca841391f9

Dry Aerosol Direct Writing

for selective **nanoparticle** deposition

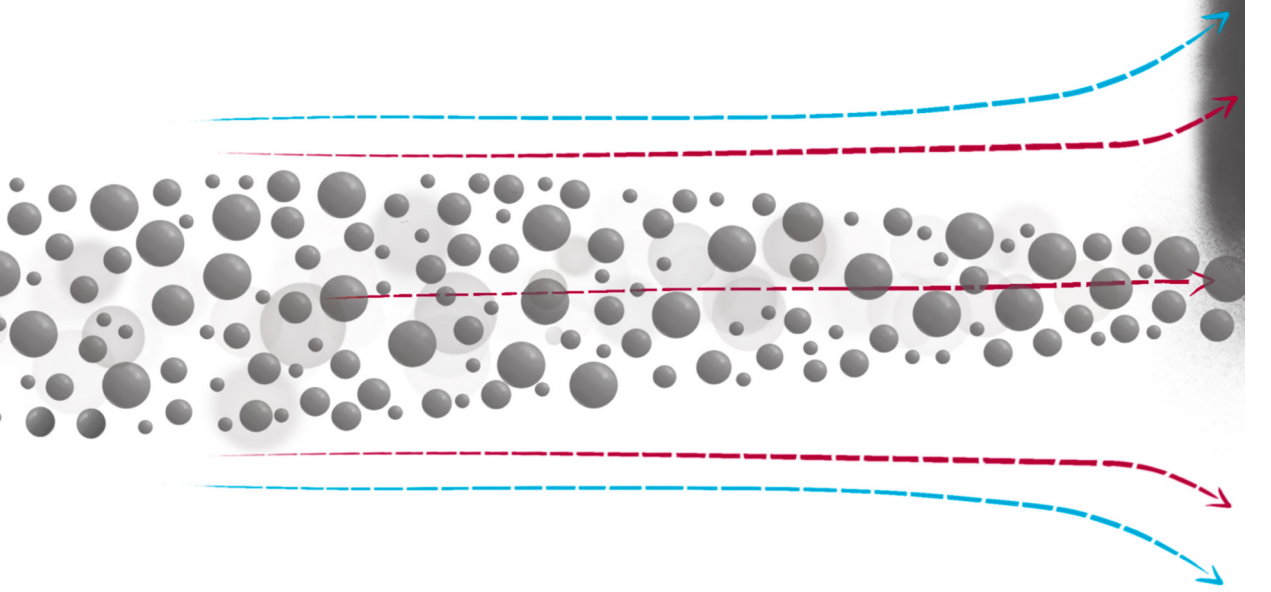

Saleh **AGHAJANI**

Dry Aerosol Direct Writing for Selective Nanoparticle Deposition

Dry Aerosol Direct Writing for Selective Nanoparticle Deposition

Dissertation

for the purpose of obtaining the degree of doctor
at Delft University of Technology,
by the authority of the Rector Magnificus Prof.dr.ir. T.H.J.J. van der Hagen,
chair of the Board for Doctorates,
to be defended publicly on,
Wednesday 08 February 2023 at 15:00 o'clock.

by

Saleh AGHAJANI

Master of Science in Materials Engineering & Nanotechnology,
Politecnico di Milano, Italy,
born in Tehran, Iran.

This dissertation has been approved by the promotors:

Promotor: Dr. ir. M. Tichem
Copromotor: Dr. A. Accardo

Composition of the doctoral commitee:

Rector Magnificus,	Chairman
Dr. ir. M. Tichem,	Delft University of Technology
Dr. A. Accardo,	Delft University of Technology
Independant members:	
Prof. dr. U. Staufer,	Delft University of Technology
Prof. dr. S. Conoci,	University of Messina, Italy
Prof. dr. J.G.E. Gardeniers,	University of Twente, Netherlands
Prof. dr. ir. J. Westerweel,	Delft University of Technology
Prof. dr. G.Q. Zhang,	Delft University of Technology, Reserve member

Keywords	Nanoparticle, Dry Aerosol Direct-Writing, Aerodynamic focusing, Surface-Enhanced Raman Scattering (SERS), Thermal-treatment
Printed by:	ProefschriftMaken, The Netherlands
Front & Back:	Artistic visualization of nanoparticle focusing by a sheath gas nozzle
Cover design:	Mahdis Jahangiri

ISBN 978-94-6384-408-6

An electronic version of this dissertation is available at
http://repository.tudelft.nl

TU Delft Delft University of Technology

Summary

Microprocessors, long-lasting batteries, and sensors are a number of examples of nanotechnology revolutionising our daily lives. Nanotechnology is the study, development, and manufacturing of structures and devices which derive unique and novel properties from nanoscale phenomena. To realise such structures and devices, a set of processes summarised under the term 'nanomanufacturing' (NM) is required to fabricate at the nanoscale. NM includes a wide range of strategies and methods where nanoparticles (NPs) serve as one of the building blocks. Therefore, NP manipulation is essential to addressing the desired applications. Because of their flexibility and efficiency, direct writing (DW) methods have received considerable attention in many studies. With nanoparticle direct writing, patterns and features can be created locally on a surface without the need for lithography processes. Inkjet printing (IJP) and aerosol jet printing (AJP) are widely used DW NP deposition methods for creating patterns with a resolution of less than 100 μm. Both these methods deposit NP from the liquid phase and employ a variety of chemical agents, which can lead to contamination, affecting the properties of the film. Additionally, due to liquid-substrate interaction, high-resolution NP deposition using wet techniques necessitates proper surface modification. Compared to NP liquid-phase-based approaches, dry methods do not involve any chemical agent, thus reducing the possibility of contamination. To use dry-synthesised NPs in a direct-writing method, particles in a gas flow should be focused and deposited on a substrate. The main challenge in fabricating high-resolution patterns employing dry-synthesised NPs is the deposition of fine NPs (<100 nm) from the gas flow onto a defined location or region on the substrate due to their extremely small size and lower relaxation time (time required for a particle to adjust its velocity to a new condition).

This dissertation presents a novel, simple, and solvent-free method for selective NP deposition on various substrates, enabling the DW of NPs. The particle generator is based on the spark ablation method (SAM), which generates metal NPs featuring sizes <20 nm. **Chapter 2** discusses aerosol physics as the foundation of the proposed NP deposition process by examining the forces acting on a particle suspended in a gaseous flow. It is demonstrated that the most important force acting on a particle in a flow is the Stokes drag force, while other forces are negligible. On this basis, particle trajectory calculation is performed (**Chapter 3**) for nozzle optimisation at low computational cost.

After introducing the overall context of this work in **Chapter 1** and aerosol physics in **Chapter 2**, the performance of two aerodynamic focusing strategies, based on a converging nozzle (CN) and a sheath-gas nozzle (SGN) design, for writing high-resolution and sharp patterns is investigated numerically and experimentally in **Chapter 3**. In an SGN, a secondary flow acts as a moving wall and confines the aerosol flow to the flow's centric region, resulting in an additional aerodynamic focusing compared to a CN. Numerical analysis revealed that, unlike the CN, the SGN can better collimate particles within the nozzle while being less sensitive to design parameters. Moreover, it is found that the collection efficiency (CE) and focusing ratio (FR) both improved using the SGN, and smaller particles were collected on the substrate. The experimental results showed that the SGN can write narrower lines than the CN, down to 27% of

the nozzle diameter due to the confinement of the main flow in the centric region. Insensitivity to design parameters simplifies the manufacturing of nozzles capable of printing patterns with feature sizes smaller than 100 μm. In addition, this dissertation assesses the morphological and optical properties of patterns deposited via dry aerosol direct-writing (dADW) and the level of control that can be exerted over these properties through post-deposition thermal treatment. The morphology, microstructure, and nanostructure of as-deposited Cu and Au NPs are investigated in **Chapters 4** and **5** respectively, and it is discovered that both have a similar morphology with dense and randomly shaped microstructures formed by primary NPs and agglomerates of various sizes, resulting in a high-porosity three-dimensional (3D) structure with nanometric features. It is shown that different morphologies and nanostructures can be formed depending on the material, time, and temperature of the thermal treatment process. This is significant because the nanostructure and morphology influence the optical properties of the NP film as well as the local enhancement of the electromagnetic field. Finally, an investigation is carried out on how the suggested additive nanomanufacturing method performs in the context of the fabrication of surface-enhanced Raman scattering (SERS) devices. This investigation is reported in **Chapters 4** and **5** for copper and gold NP films, respectively, by assessing the detection of a low concentration reference dye (Rhodamine B (RhB)). On the as-deposited patterns, the detection limit for Au and Cu NP patterns is as low as 1 nM and 1 μM, respectively. Furthermore, it is discovered that post-deposition thermal treatment is highly effective for increasing the SERS signal of CuNPs films by a factor of ten. On the other hand, heat treatment is less effective for AuNPs in terms of SERS signal enhancement, but it is effective in terms of tuning of optical properties, which enable resonance Raman scattering, as reported in **Chapter 5**.

In conclusion, this work proves the capability of dry aerosol direct writing for the selective deposition of very fine nanoparticles in high-resolution patterns with widths smaller than 100 μm. Furthermore, because the morphology and optical properties can be easily controlled and tuned using simple and low-temperature thermal treatment, the dADW method can fabricate a wide range of functionalities, including patterns for surface-enhanced Raman scattering applications.

Samenvatting

Microprocessors, batterijen die lang meegaan en biosensoren zijn een aantal voorbeelden waar nanotechnologie een revolutie teweegbrengt in ons dagelijks leven. Nanotechnologie is de studie, ontwikkeling en productie van nanostructuren en componenten die unieke en nieuwe eigenschappen ontlenen aan nanoschaal-gerelateerde eigenschappen. Om dergelijke structuren en componenten te realiseren zijn nanomanufacturing (NM) processen vereist. NM omvat een breed scala aan strategieën en methoden, en nanoparticles (NPs) dienen als bouwstenen in veel van deze methoden, en als gevolgis het kunnen maniupleren van NPs van essentieel belang. Vanwege hun flexibiliteit en efficiëntie hebben met name direct-write (DW)-methoden veel aandacht gekregen in onderzoek. Met direct schrijven van nanodeeltjes kunnen patronen en structuren lokaal op het oppervlak worden gecreëerd zonder dat lithografische processen nodig zijn. Inkjet printen (IJP) en aerosol jet printen (AJP) zijn veelgebruikte DW depositiemethoden voor NPs, waarmee patronen gemaakt kunnen met een resolutie van minder dan 100 μm. Beide methoden zijn gebaseerd op natte technieken voor NP-synthese waarbij gebruik gemaakt wordt van een verscheidenheid aan chemische middelen, die tot verontreiniging kunnen leiden en de eigenschappen van de film kunnen veranderen. Bovendien, als gevolg van vloeistof-substraat interactie, is vaak oppervlaktemodificatie nodig om NP depositie te kunnen doen met hoge resolutie. In tegenstelling tot natte NP synthese zijn er bij droge synthesemethoden geen chemische middelen aanwezig, waardoor de kans op contaminatie wordt verkleind. Om NPs die in een droge methodiek gesynthetiseerd zijn in een DW depositiemethode te gebruiken, moeten de NPs in een gasstroom worden gefocust en op een substraat worden gedeponeerd. De belangrijkste uitdaging bij het fabriceren van patronen met hoge resolutie met behulp van de droog gesynthetiseerde NPs de afzetting van fijne NPs (<100 nm) op een gedefinieerde locatie of regio op het substraat vanwege hun kleine afmetingen en lagere relaxatietijd.

Dit proefschrift presenteert een nieuwe, eenvoudige, en oplosmiddelvrije methode voor selectieve depositie van NPs op verschillende type substraten, waardoor de DW van nanodeeltje mogelijk wordt. De deeltjesgenerator is gebaseerd op de vonkablatiemethode (Spark Ablation Method, SAM), die verschillende metalen nanodeeltjes kan genereren, afhankelijk van het materiaal van de electroden. **Hoofdstuk 2** bespreekt aërosol-fysica, die de basis vormt van het voorgestelde nanodeeltje-depositiesysteem, en introduceert de krachten die werken op een deeltje dat in een gasstroom is gesuspendeerd. De belangrijkste kracht die werkt op een deeltje in een stroming is de Stokes-wrijvingskracht, terwijl de andere krachten verwaarloosbaar klein zijn in vergelijking daarmee. Dit inzicht wordt gebruikt voor het efficient bereknen van de baan van de deeltjes in **Hoofdstuk 3** ter optimalisatie van het nozzleontwerp.

De prestaties van twee aerodynamische focuseringsstrategieën, een convergerende nozzle (CN) en een sheath-gas nozzle (SGN), voor het schrijven van scherpe patronen met een hoge resolutie, worden onderzocht in **Hoofdstuk 3**. Numerieke analyse toont aan dat, in tegenstelling tot CN, SGN deeltjes beter kan collimeren terwijl de prestaties minder gevoelig is voor de ontwerpparameters. Bovendien verbeteren zowel de verzamelefficiëntie (Collection Efficiency, CE) als de focusverhouding (Focusing Ratio, FR) met behulp van SGN en kunnen ook kleinere deel-

tjes op het substraat worden verzameld. De experimentele resultaten tonen aan dat met SGN smallere lijnen, tot 27% van de nozzle diameter, geschreven kunnen worden dan met CN, dankzij het vernauwen van de hoofdstroom in het centrale gebied van de nozzle veroorzaakt door een secundaire (sheath gas) stroom. Het combineren van deze parameters vereenvoudigt de productie van de spuitmonden die patronen kunnen printen met kenmerkgroottes kleiner dan 100 μm. Daarnaast evalueert dit proefschrift de morfologische en optische eigenschappen van patronen die via dADW zijn gedeponeerd en de mate van controle die over deze eigenschappen kan worden uitgeoefend door thermische behandeling na de depositie. De morfologie, microstructuur en nanostructuur van gedeponeerde Cu en Au NP's worden respectievelijk onderzocht in de **Hoofdstukken 4** en **5**. Beide NP films hebben een vergelijkbare morfologie met dichte en willekeurig gevormde microstructuren, gevormd door primaire NP's en agglomeraten van verschillende groottes, resulterend in een driedimensionale (3D) structuur met hoge porositeit met nanometrische kenmerken. Er wordt aangetoond dat verschillende morfologieën en nanostructuren kunnen worden gevormd afhankelijk van het materiaal, de tijd, en de temperatuur van het thermische behandelingsproces. Dit is belangrijk omdat de nanostructuur en morfologie de optische eigenschappen van de NP-film beïnvloeden, evenals de lokale versterking van het elektromagnetische veld. Ten slotte wordt onderzocht hoe de voorgestelde ANM-methode presteert in de context van de fabricage van structuren voor surface-enhanced Raman scattering (SERS). Deze doelstelling wordt geëvalueerd in **Hoofdstukken 4** en **5** respectievelijk voor koper- en gouden NP-films door de detectie van een lage concentratie referentiekleurstof (Rhodamine B (RhB)) te beoordelen. De detectie limiet van de gedeponeerde Au- en Cu NP-patronen is 1 nM en 1 μM, respectievelijk. Verder is aangetoond dat thermische behandeling na de depositie zeer effectief is in het verhogen van het SERS-signaal van CuNPs-films, tot een factor tien. Aan de andere kant is warmtebehandeling minder effectief voor SERS-signaalversterking in geval van de AuNP's, maar het is wel effectief voor het modificeren van de optische eigenschappen, die de resonantie Raman-verstrooiing mogelijk maken, zoals aangetoond in **Hoofdstuk 5**.

Dit werk bewijst de potentie van droog aërosol direct write voor de selectieve afzetting van zeer fijne nanodeeltjes voor het maken van patronen met hoge resolutie met breedtes kleiner dan 100 μm. Bovendien, omdat de morfologie en optische eigenschappen gemakkelijk kunnen worden gemodificeerd met behulp van een eenvoudige thermische behandeling op een lage temperatuur, kan de dADW-methode een breed scala aan functionaliteiten integreren, waaronder oppervlakteversterkte Raman-verstrooiing.

Contents

1

Introduction

1.1 Nanoscience & Nanotechnology: There is plenty of room at the bottom

Since its inception by Richard Feynman in 1959, nanoscience and nanotechnology have grown in importance as a field of research and development, revolutionising materials and products and their manufacturing [1]. Nanoscience is the study and development of materials with dimensions ranging from 0.1 to 100 nm to provide a fundamental understanding of phenomena and materials at the nanoscale [2]. At the same time, nanotechnology is the study and development of nanostructures, devices, and systems which derive unique and novel properties from nanoscale phenomena [2]. The 0.1 to 100 nm range originates from the fact that at this scale, surface effects become dominant over bulk effects [1]. Chemical properties, catalysis and interfacial interactions, for example, enhance due to the high surface-to-volume ratio [3–5]. In addition to surface-to-volume ratio, quantum mechanics becomes the primary approach for describing the many phenomena at the nanoscale, such as absorption and fluorescence [6], photonic [7] and electronic bandgap [8], thermoelectric effect [9], and magnetic property [10].

In this thesis, I aim to contribute to the field of nanotechnology by focusing on nanomanufacturing and functionality development, with a particular emphasis on metal nanoparticles and their optical properties. The aimed optical phenomenon in metals originates from localised surface plasmon resonance (LSPR) present at the surface of nanoscale features caused by collective oscillations of the electron cloud at the metal-dielectric interface in the presence of incident light [11–14]. Amplification of the electromagnetic (EM) field and selective photon absorption originates from light-matter interaction in this confined region. Surface-enhanced infrared absorption [15], surface-enhanced Raman scattering (SERS) [16–18], surface-enhanced fluorescence [6, 19], refractive index change-based sensing [20], and many more functionalities and applications have been developed based on this EM enhancement.

1.2 Nanomanufacturing (NM)

In order to exploit the unique physical, mechanical, optical, electronic, and magnetic properties at the nanoscale, a process called nanomanufacturing (NM) is required to fabricate nanoscale structures and devices [21, 22]. Nanomanufacturing techniques are commonly classified as either top-down, which means starting from larger structures and etching down to reach the desired size, or bottom-up, involving the construction of structures atom by atom (Figure 1.1) [1, 2]. Bottom-up approaches are best suited for short-range order structuring (few nm up to several μm), whereas top-down approaches are best suited for producing structures with long-range order [21]. Lithographic patterning with UV and EUV sources is the most common top-down fabrication approach. In today's microelectronic chip manufacturing, optical lithography has become a mature field, with current techniques achieving dimensions of less than 10 nanometres [23].

By using lithography methods, it is possible to fabricate high precision 2D and 3D nanostructures with precise control over shape, interspacing, and location. A pattern size of about <5 nm can be achieved using scanning beam techniques like electron-beam lithography. In this case, an electron beam is used to create a pattern on the surface. Although these methods are enormously precise, they rely on complex and expensive equipment. It is now possible to print in extremely small dimensions using mechanical printing techniques such as nanoimprinting

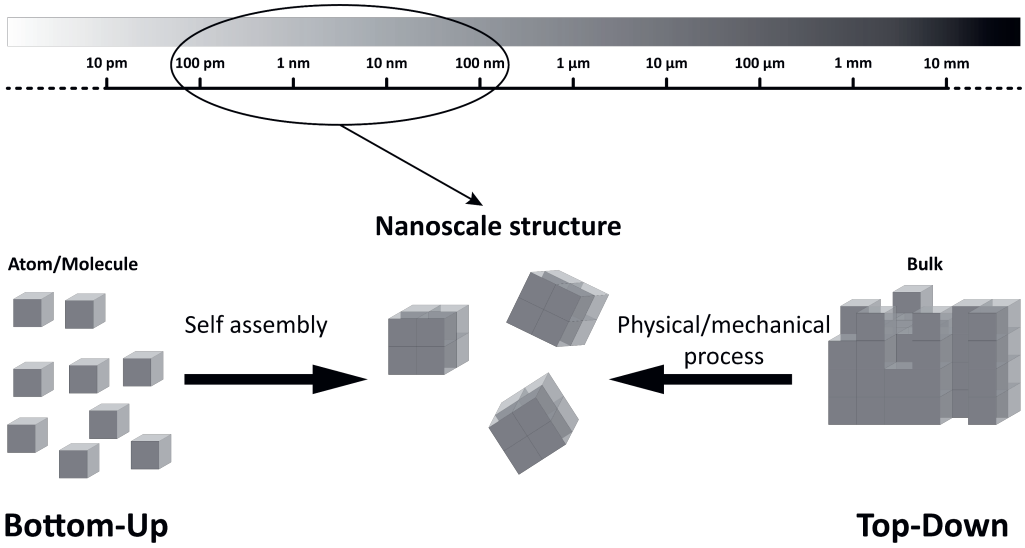

Figure 1.1: Schematic view of top-down and bottom-up nanomanufacturing

lithography, stamping, and molding to reach 20-50 nm feature size. To create a pattern, a "stamp" is first made using a high-resolution technique such as electron-beam lithography, which is subsequently applied to create patterns on a surface. Aside from using a broader range of materials, it is possible to perform these techniques in a laboratory with far less expensive equipment than is required for conventional lithography. However, they need lithography methods for stamp production, which are costly and have a limited lifetime. Furthermore, imprint techniques are multistep and rely on wet processing methods, raising the risk of chemical contamination and handling many toxic substances.

The bottom-up approach entails building nanostructures and devices starting with a single atom or molecule. The bottom-up methods are based on self-assembly, which is inspired by nature and employs nanoscale chemical or physical forces to assemble basic units into larger structures. The processes of self-assembly range from the condensation of atomic vapours on surfaces to the coalescence of atoms in liquids to produce size-selective nanoparticles or structures of semiconductors, magnetic, and other materials. Self-assembly can be used for on-surface nanostructure fabrication, such as fabrication of quantum dots by epitaxial-strain-induced method [24]. But, self-assembly methods commonly create nanoparticles in gas or liquid phases. When using liquid-mediated growth, the level of control over the nanoparticles' size and shape is higher compared to gas-phase mediated methods. Controlling the surfactants and other chemical agents allows for a wide range of sizes and shapes, including spheres, rods, cubes, pyramids, and star-shaped particles of diverse materials [25]. However, due to the presence of various chemical agents, liquid-mediated methods may introduce impurity into the process.

In contrast to the liquid synthesis method, the gas-mediated process does not require chemical agents. During the gas-mediated synthesis process, the bulk material is heated to vaporise or atomise, following which the atoms are carried away by an inert carrier gas such as helium nitrogen or argon [26]. Coalescence and condensation of the vaporised material cause the tem-

perature of the evaporated material to drop, resulting in extremely small particle generation. Several methods for heating the substrate include Joule heating, which uses a high amount of energy due to the uniform temperature increase, plasma discharge, and laser vaporisation.

Due to the nature of self-assembly methods, particles are in a gas or liquid medium and must immobilise on the substrate for use in various applications, which can be accomplished in multiple ways. For liquid-mediated particles, again self-assembly is the primary cause of the deposition process in which particles acquire a particular spatial distribution with respect to one other and the boundaries of the medium, resulting in thermodynamic equilibrium and a decrease in the system's free energy. Drop-casting and the Langmuir-Blodgett technique are typical self-assembly-based processes used for deposition over a wide area. In self-assembly methods, achieving optimal surface coverage is also dependent on surface modification, which can be related to the surface's wettability or a functional layer in the Langmuir-Blodgett approach. In the case of particles formed using gas-mediated methods, alternative approaches are established for particle immobilisation on the surface generally by providing an external force to guide them to deposit on the surface. External forces include electrostatic, diffusive, optical, thermophoresis, electrophoresis and aerodynamic forces. The deposition processes which rely on the majority of previous forces are either material or substrate-dependent, or they lead to wide-area deposition, whereas for many applications, localised deposition is required.

1.3 Additive nanomanufacturing (ANM)

Additive manufacturing (AM) is the process of fabricating a part by depositing material point-by-point or layer-by-layer from a computer-aided design file. AM is widely used at a macroscopic scale for prototyping and low-volume production in dentistry and medical care, automotive, aerospace, fashion, high-tech precision industry, and entertainment. These industries have harvested the benefits of AM's design freedom and faster time-to-market manufacturing and have expanded it to include polymer, metal, and ceramic materials. Several studies have been performed over many years to extend AM into the nanoscale domain or to use nanoscale building blocks to include AM benefits in nanotechnology. Additive nanomanufacturing (ANM) approaches are AM methods that have a resolution of less than 100 μm or use <100 nm particles as building blocks [27, 28]. Generally, ANM methods require less expensive equipment than lithographic methods, making them suitable for rapid prototyping in nanotechnology [27]. The objective of ANM is to construct patterns or structures with high accuracy, high resolution, and at low cost, using materials ranging from biomaterials to ceramics and metals [28]. There are various methods categorised in ANM with diverse resolutions, such as dip-pen lithography [29, 30], inkjet printing [31–34], laser writing [35, 36], optical tweezer [37, 38], scanning tunnel microscopy [39, 40], AerosolJet printing [41–45], and capillary assisted particle assembly [46, 47].

Direct writing (DW) methods are an important category in ANM that allow the deposition of functional or structural patterns from various materials without the use of masks or subsequent etching processes in a data-driven manner. DW methods are capable of achieving 100 μm resolution down to the molecular level in metals, insulators, and organic materials [30–32, 34, 48–54]. DW methods can be broadly classified into four types: flow-based, energy beam-based, tip-based, and droplet-based [48]. Flow-based DW employs a microdispensing system equipped with a needle or orifice to deposit features as small as 25 μm at speeds of up to 300

mm/s [49, 50]. These methods use liquid resin or solution-based inks and are less sensitive to ink viscosity. The second type of DW is energy beam-based, in which a laser is used to transform and/or propel material onto a substrate [35], or a laser is used to induce polymerisation and build 3D micro and nanostructures [51, 52]. Matrix-assisted pulsed laser evaporation DW (MAPLE-DW) [55] and laser-guided DW (LG-DW) [35, 56] and are examples of energy-based DW which use a laser to radiate a transparent substrate to induce material transfer.

In MAPLE-DW, the desired material is dissolved in a matrix solvent and pre-coated on support, forming a ribbon, and a laser causes rapid evaporation of the surrounding matrix and ejection of the portion, which is then transported to the desired location with a resolution of 30 μm [55]. Inks with the proper viscosity and UV absorption are needed for this process. LG-DW uses a weekly focused continuous laser to target an object in a suspension and propel it to a growth surface using optical forces instead of a print ribbon and pulsed laser [56]. Although a wide range of techniques and resolutions can be achieved using transfer/propel energy-based methods, 3D printing is complex with these techniques. On the other hand, laser-based polymerisation methods are capable of easily building 3D structures from the ground up. For 2.5D and 3D nano and microstructures, two-photon polymerisation (2PP) is the most commonly used direct laser writing technique, which uses femtosecond pulses of laser light to control the photopolymerisation of a photoresist resin in a controlled region called a voxel [51, 52]. Ceramic and metallic material fabrication via 2PP has yet to be fully realised, despite advances in resin technology that allow 3D polymeric features to be written at typically 10 to 500 nm/s with nanoscale resolution.

Tip-based DWs include dip-pen lithography (DPN) [30] and its variant, the nano fountain pen (NFP) [53], and capillary-based liquid micro droplet deposition [47]. The DPN is a nanofabrication process based on scanning probe microscopy that combines direct-write compatibility with high-resolution atomic force microscopy (AFM) [30]. This technique allows the manipulation of individual nanoparticles, all the way down to molecules and atoms to achieve patterns and structures on a substrate with the highest possible resolution. NFP uses a hollow tip in contact with the substrate to dispense liquid or ink, transporting molecules to the surface via mass diffusion [53]. In the capillary-based liquid microdroplet deposition, a meniscus forms due to the application of pressure into a capillary, which causes deposition of particles on the substrate in the region as small as 10% of capillary's inner diameter and has dimensions as small as 32 nm for a 300 nm diameter capillary if the liquid meniscus touches the substrate. Tip-based DWs are inherently slow processes although they maintain accuracy and resolution.

The fourth category is droplet-based DW, which includes Inkjet printing (IJP) [31, 32, 34, 54] and aerosol-jet printing (AJP) [41, 42, 45], with IJP being the most commonly used direct writing method. In these methods, a droplet containing resin or nanoparticles deposit on the substrate, forming patterns on the substrate [32, 33]. Droplets in IJP have a typical size of 50-100 μm and are formed due to thermal, piezoelectric, hydrodynamic, electrostatic, or acoustic actuation. The formed droplets are ejected from the nozzle, and move towards the substrate with a 5-10 m/s velocity. The final resolution is defined by the size of the droplets and the droplet-substrate interaction, which is determined by the droplet's surface tension and the wettability of the substrate [33, 34]. Furthermore, when patterns are created using nanoparticles as building blocks, the droplet-substrate interaction becomes more critical as particles move to the droplet's periphery, causing the coffee-stain effect. Common piezoelectric actuation drop-on-demand (DOD) IJPs can achieve a minimum resolution of 20 μm, and electrohydrodynamic printing (E-jet) can

achieve a resolution of less than 10 μm. Significantly, since IJP depends on the printing ink's viscosity, only a narrow range of viscosities can be used, and a degree of volatility is necessary for the ink to dry properly after it is deposited [33]. However, too much volatility can easily clog nozzles. AJP, on the other hand, can handle a broader range of viscosity due to the difference in the droplet generation mechanism it employs compared to IJP. Droplets with sizes less than 5 μm are formed in AJP using an ultrasonic or pneumatic atomiser from a precursor liquid ink. A carrier gas (an inert gas such as argon or nitrogen) transports droplets to an aerodynamic focusing nozzle, where droplets gain kinetic energy through aerodynamic forces and are focused to form localised patterns on the substrate [41], [45]. AJP can achieve 10 μm resolution by controlling the size of droplets going to the nozzle in the range of 1-3 μm and removing smaller droplets via a virtual impactor. The liquid-substrate interaction, similar to IJP, is essential for high-resolution patterning; additionally, AJP suffers from overspray (deposition of droplets in a sparse form around the pattern), which cause reducing the sharpness of the patterns [41]. Furthermore, both IJP and AJP rely on liquid-mediated particle production processes, with particles generated employing a variety of chemical agents ranging from reducing agents to ligands.

1.4 dry Aerosol Direct Writing (dADW) for ANM

In this dissertation, I present a dry direct writing nanoparticle deposition method using a gas-mediated particle generator. The nanoparticle generator is based on the spark ablation method (SAM), which allows for the low-cost synthesis of very fine nanoparticles as an alternative to conventional liquid-mediated methods [57–59]. In SAM, a high voltage is applied between two (semi)conducting electrodes, resulting in a spark and raising the local temperature to a level high enough to cause the electrode to evaporate [57]. At atmospheric pressure, a non-reactive carrier gas transports the atomic cloud from the generation site (Figure 1.2). The atoms condensate rapidly and consolidate into primary particles of 0-20 nm, which later may agglomerate to generate larger particles [57, 59]. The benefit of SAM is that it generates a wide range of metallic nanoparticles such as Au, Cu, Ag, Pt, Al, and Ni and allows the synthesis of alloys NPs by either employing different materials as electrodes or alloyed electrodes [58, 59]. By injecting the appropriate additional gas into the carrier gas, ceramics (metal oxide, nitride, or sulphide) can also be formed. As a result, SAM has been a valuable and cost-effective method for producing ultrapure and very small particles of various materials without using solvents or other potentially harmful substances.

To fully realise the benefits of SAM as a dry particle generator in nanotechnology, particles must immobilise on the surface, and in many cases, on specific regions of the substrate. As a result, the primary goal of this dissertation is to employ the advantages of the SAM particle generator in a system allowing direct writing of nanoparticles to fabricate patterns. The main challenge for fabricating high-resolution patterns is the size of the SAM generated particles. At this size regime (< 100 nm), particles behave like flow and tend to follow the streamline instead of leaving the streamline to deposit on a substrate [41, 60–63]. Additionally, direct writing necessitates that NPs deposit in a focused regime on the substrate, allowing sharp pattern fabrication. Various strategies for achieving focused deposition are surveyed in **Chapter 3**, including aerodynamic [63–67], electrostatic [36], and electro/thermos phoresis [68, 69] focusing, with aerodynamic focusing outperforming others.

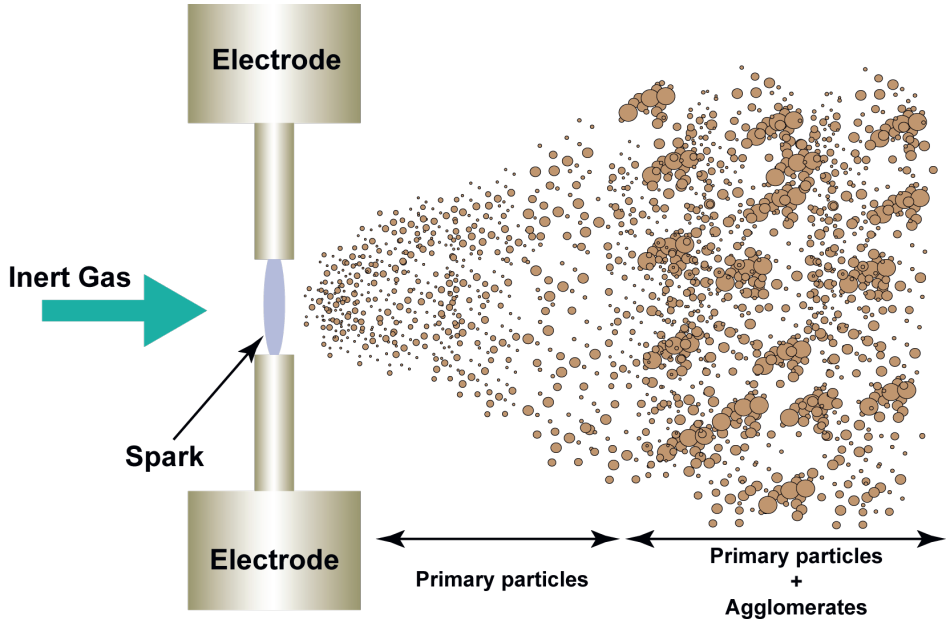

Figure 1.2: Schematic of spark ablation method (SAM)

Given the fact that SAM-generated particles are polydispersed, aerodynamic focusing methods such as aerodynamic lenses or varying section nozzles [70, 71] are less efficient than sheath gas nozzles (SGN) that rely on a secondary flow to focus the nanoparticles. SGN has been used and studied for AJP and proven to be an efficient nozzle system for high-resolution printing while working in a subsonic flow regime and focuses droplets above 1 µm [41, 45, 72]. To extend the implementation of SGN in the proposed dry aerosol direct writing (dADW) method, the effect of various parameters such as SGN design parameters and process parameters on the resolution and sharpness of patterns are investigated considering the size of particles and flow regime of dADW. Furthermore, to assess the performance of dADW as an alternative ANM method in printing patterns for specific applications, I focused on the optical properties of metal nanoparticles that enable the fabrication of surface-enhanced Raman scattering sensors.

1.5 Case study: Surface-Enhanced Raman Scattering (SERS)

Raman Spectroscopy is a non-destructive, label-free, and ultrasensitive vibrational spectroscopic technique that provides a wide range of information regarding the chemical structure of various species and their phase [73–76]. In Raman Spectroscopy, a monochromatic high-intensity laser light interacts with the substance under investigation; the majority of light scatters with the same wavelength due to Rayleigh scattering (elastic scattering), providing no information; however, a minority of the light scatters with different wavelengths depending on the chemical structure of the analytes and due to photon-phonon interaction, which is known as Raman scattering (inelastic scattering) (Figure 1.3) [73, 76, 77]. Although Raman scattering provides valuable information, the process has very low efficiency, and Raman scattering is a rare event,

i.e. approximately one photon out of 10^7 photons leads to scattering. When dealing with low-concentration analytes, the low efficiency of Raman spectroscopy becomes considerably more critical because the number of molecules available to interact with light is likewise drastically reduced when compared to bulk substances [77–79].

Various strategies can be used to compensate for this signal inefficiency, such as increasing the intensity of incident light, using optical lenses to focus the light and increase photon density, or using surface enhancement strategies. The first two strategies have limits due to the physical restrictions of lasers and lenses, whereas the surface-enhancement approach can even reach a single molecule detection level. In surface-enhancement strategies, the Raman signal of the analytes is enhanced due to the presence of metallic nanometric structures on the surface. There are two mechanisms involved in this signal amplification: long-range electromagnetic (EM) enhancement and short-range chemical enhancement (CE) [80, 81]. The CE mechanism can increase the signal up to one or two orders of magnitude, which is a minor effect compared to the EM mechanism. CE is defined as the interaction of chemisorbed molecules with a metallic nanostructured surface and is attributed to two effects: 1) charge-transfer between the surface and molecule causes the formation of an intermediate with a higher Raman scattering cross-section compared to an unabsorbed molecule, 2) charge transfer mechanisms between molecules and metal surfaces can yield Raman excitation photons when the lowest unoccupied molecular orbital (LUMO) and the highest-occupied molecular orbital (HOMO) of the molecules fall symmetrically around the Fermi level of the metal [82].

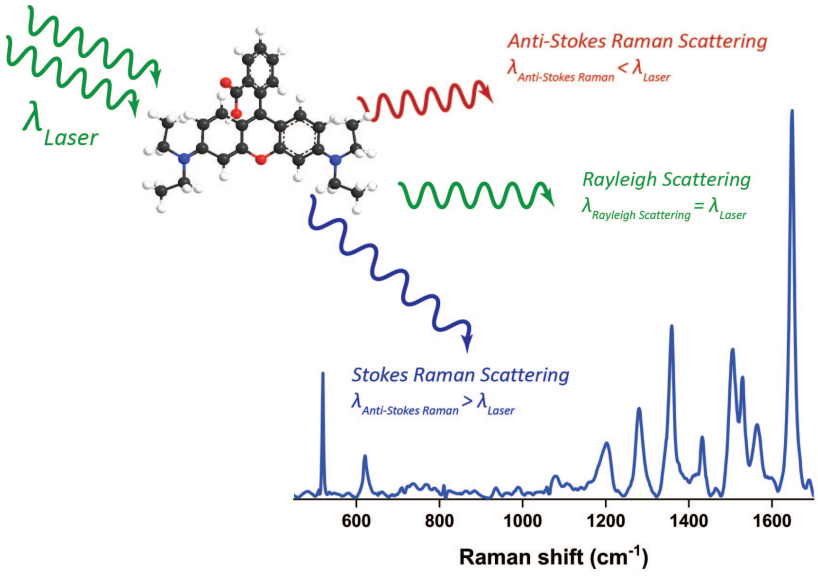

Figure 1.3: Schematic of Raman spectroscopy

The primary mechanism involved in surface enhancement is electromagnetic amplification due to metallic nanostructures, which can reach enhancement up to 6-8 orders of magnitude [83]. The presence of this mechanism is due to the formation of localised surface plasmon resonances (LSPR), which is the result of the collective oscillation of electrons on the surface

of a metallic nanostructures feature when illuminated by an electromagnetic wave [83–86]. As a result of the electromagnetic amplification surrounding metallic nanostructures (called hot spots), a molecule will be subjected to a significantly higher incidence intensity. The same magnification process is repeated for scattered Raman, resulting in a significant improvement in the Raman signal. The surface-enhanced Raman scattering (SERS) signal is highest when both the incident light and the scattered signal of molecules resonate with the plasmon frequency, resulting in a very high enhancement [76, 87]. Therefore, the EM enhancement depends on LSPRs efficiency, which can be tailored by material type, size, shape, distribution, and spacing of nanostructures.

1.6 Aim of this research

This thesis aims to develop a unique approach based on the spark ablation method (SAM) for selective direct writing of metallic nanoparticles on a substrate and investigate the level of control over the morphology, optical characteristics, and performance of the deposited pattern as a SERS substrate. Several research objectives are established to achieve this overall objective:

1. Evaluating the effect of process and nozzle design parameters on the resolution of patterns consisting of <100nm diameter nanoparticles.

2. Investigating the effect and level of control over the morphology and optical properties of nanoparticle film using post-deposition thermal treatment.

3. Exploring the performance of nanoparticle patterns as SERS-active substrates

1.7 Thesis outline

The research questions summarised above are addressed in the following chapters of this dissertation. Except for **Chapter 6** each chapter is based on a published journal paper. The physics of a particle carried in a gas flow, and theoretical and experimental specifications of dry aerosol direct writing (dADW) are discussed in **Chapter 2**. **Chapter 3** focuses on dADW and optimisation of the deposition performance using aerodynamic focusing through numerical and experimental investigation. Two aerodynamic nozzle concepts, a converging nozzle (CN) and a sheath gas nozzle (SGN), are numerically investigated to evaluate the effect of design and operating parameters on printed pattern resolution compared to experimental results.

Chapters 4 and **5** are devoted to the investigation of patterns for their optical and morphological properties, as well as their performance as a surface-enhanced Raman scattering spectroscopy (SERS) for copper (Cu) and gold (Au) nanoparticles, respectively. The effect of post-deposition thermal treatment on the micro-and nanostructure of patterns, and as a result, on the optical property and performance of both Cu and Au as SERS substrates are also explored in these chapters. In addition, the effect of post-deposition thermal treatment on the photoluminescence response of the pattern of gold nanoparticles under various time and temperature conditions is investigated in **Chapter 5** of this thesis. Finally, in **Chapter 6**, the thesis's conclusions are summarised, and an outlook on future research is provided.

References

[1] M. Bououdina and J. P. Davim, "Handbook of research on nanoscience, nanotechnology, and advanced materials," *Handbook of Research on Nanoscience, Nanotechnology, and Advanced Materials*, pp. 1–617, 3 2014.

[2] G. L. Hornyak, H. Tibbals, J. Dutta, and J. J. Moore, "Introduction to nanoscience and nanotechnology," 12 2008.

[3] C. Xie, Z. Niu, D. Kim, M. Li, and P. Yang, "Surface and interface control in nanoparticle catalysis," 1 2020.

[4] J. B. Sambur and P. Chen, "Approaches to single-nanoparticle catalysis," *http://dx.doi.org/10.1146/annurev-physchem-040513-103729*, vol. 65, pp. 395–422, 4 2014.

[5] N. Yan, C. Xiao, and Y. Kou, "Transition metal nanoparticle catalysis in green solvents," *Coordination Chemistry Reviews*, vol. 254, pp. 1179–1218, 5 2010.

[6] A. B. Chinen, C. M. Guan, J. R. Ferrer, S. N. Barnaby, T. J. Merkel, and C. A. Mirkin, "Nanoparticle probes for the detection of cancer biomarkers, cells, and tissues by fluorescence," 10 2015.

[7] S. Park, X. Xiao, J. Min, C. Mun, H. S. Jung, V. Giannini, R. Weissleder, S. A. Maier, H. Im, and D. Kim, "3d plasmonic nanostructures: Self-assembly of nanoparticle-spiked pillar arrays for plasmonic biosensing (adv. funct. mater. 43/2019)," *Advanced Functional Materials*.

[8] M. M. Karkare, "Estimation of band gap and particle size of tio2 nanoparticle synthesized using sol gel technique," *Proceedings - 2014 IEEE International Conference on Advances in Communication and Computing Technologies, ICACACT 2014*, 2015.

[9] S. Ortega, M. Ibáñez, Y. Liu, Y. Zhang, M. V. Kovalenko, D. Cadavid, and A. Cabot, "Bottom-up engineering of thermoelectric nanomaterials and devices from solution-processed nanoparticle building blocks," *Chemical Society Reviews*, vol. 46, pp. 3510–3528, 6 2017.

[10] D. Peddis, C. Cannas, A. Musinu, A. Ardu, F. Orruì, D. Fiorani, S. Laureti, D. Rinaldi, G. Muscas, G. Concas, and G. Piccaluga, "Beyond the effect of particle size: Influence of cofe2o4 nanoparticle arrangements on magnetic properties," *Chemistry of Materials*, vol. 25, pp. 2005–2013, 5 2013.

[11] H. Chen, L. Shao, Q. Li, and J. Wang, "Gold nanorods and their plasmonic properties," *Chemical Society Reviews*, vol. 42, pp. 2679–2724, 2013.

[12] J. Zheng, X. Cheng, H. Zhang, X. Bai, R. Ai, L. Shao, and J. Wang, "Gold nanorods: The most versatile plasmonic nanoparticles," *Chemical Reviews*, vol. 121, pp. 13342–13453, 2021.

[13] A. Comin and L. Manna, "New materials for tunable plasmonic colloidal nanocrystals," *Chemical Society Reviews*, vol. 43, pp. 3957–3975, 2014.

[14] X. Zhang, C. R. Yonzon, and R. P. V. Duyne, "Nanosphere lithography fabricated plasmonic materials and their applications," 2006.

[15] N. S. Mueller, E. Pfitzner, Y. Okamura, G. Gordeev, P. Kusch, H. Lange, J. Heberle, F. Schulz, and S. Reich, "Surface-enhanced raman scattering and surface-enhanced infrared absorption by plasmon polaritons in three-dimensional nanoparticle supercrystals," *ACS Nano*, vol. 15, pp. 5523–5533, 3 2021.

[16] Z. Wang, S. Zong, L. Wu, D. Zhu, and Y. Cui, "Sers-activated platforms for immunoassay: Probes, encoding methods, and applications," *Chemical Reviews*, vol. 117, pp. 7910–7963, 2017.

[17] R. Haldavnekar, K. Venkatakrishnan, and B. Tan, "Next generation sers- atomic scale platform for molecular level detection," *Applied Materials Today*, vol. 18, 2020.

[18] H. Dizajghorbani-Aghdam, T. S. Miller, R. Malekfar, and P. F. McMillan, "Sers-active cu nanoparticles on carbon nitride support fabricated using pulsed laser ablation," *Nanomaterials*, vol. 9, pp. 22–25, 2019.

[19] B. Y. Hsieh, Y. F. Chang, M. Y. Ng, W. C. Liu, C. H. Lin, H. T. Wu, and C. Chou, "Localized surface plasmon coupled fluorescence fiber-optic biosensor with gold nanoparticles," *Analytical Chemistry*, vol. 79, pp. 3487–3493, 2007.

[20] J. S. Sekhon, "Facile tuning and refractive index sensitivity of localized surface plasmon resonance inflection points in hollow silver nanoshells," *Plasmonics*, vol. 16, pp. 283–292, 2 2021.

[21] J. A. Liddle and G. M. Gallatin, "Nanomanufacturing: A perspective," 3 2016.

[22] S. Dimov, E. Brousseau, R. Minev, and S. Bigot, "Micro- and nano-manufacturing: Challenges and opportunities," *Proceedings of the Institution of Mechanical Engineers, Part C: Journal of Mechanical Engineering Science*, vol. 226, pp. 3–15, 1 2012.

[23] M. Imboden and D. Bishop, "Top-down nanomanufacturing," *Physics Today*, vol. 67, p. 45, 11 2014.

[24] R. E. Caflisch, M. F. Gyure, B. Merriman, S. J. Osher, C. Ratsch, D. D. Vvedensky, and J. J. Zinck, "Island dynamics and the level set method for epitaxial growth," *Applied Mathematics Letters*, vol. 12, pp. 13–22, 5 1999.

[25] C. J. Murphy, T. K. Sau, A. M. Gole, C. J. Orendorff, J. Gao, L. Gou, S. E. Hunyadi, and T. Li, "Anisotropic metal nanoparticles: Synthesis, assembly, and optical applications," *J. Phys. Chem. B*, vol. 109, pp. 13857–13870, 2005.

[26] S. Yatsuya, S. Kasukabe, and R. Uyeda, "Formation of ultrafine metal particles by gas evaporation technique. i. aluminium in helium," *Japanese Journal of Applied Physics*, 1973.

[27] D. S. Engstrom, B. Porter, M. Pacios, and H. Bhaskaran, "Additive nanomanufacturing – a review," *Journal of Materials Research*, vol. 29, pp. 1792–1816, 6 2014.

[28] Z. Ahmadi, S. Lee, N. Shamsaei, and M. Mahjouri-Samani, "Additive nanomanufacturing of functional materials and devices," *https://doi.org/10.1117/12.2578381*, vol. 11677, p. 116770U, 3 2021.

[29] J. Hyun, S. J. Ahn, W. K. Lee, A. Chilkoti, and S. Zauscher, "Molecular recognition-mediated fabrication of protein nanostructures by dip-pen lithography," *Nano Letters*, vol. 2, pp. 1203–1207, 11 2002.

[30] G. Liu, M. Hirtz, H. Fuchs, Z. Zheng, G. Liu, Z. Zheng, M. Hirtz, and H. Fuchs, "Development of dip-pen nanolithography (dpn) and its derivatives," *Small*, vol. 15, p. 1900564, 5 2019.

[31] J. G. Korvink, P. J. Smith, and D. Y. Shin, *Inkjet-based micromanufacturing*. 2012.

[32] L. Mu, Z. Hu, Z. Zhong, C. Jiang, J. Wang, J. Peng, and Y. Cao, "Inkjet-printing line film with varied droplet-spacing," *Organic Electronics*, vol. 51, pp. 308–313, 12 2017.

[33] A. Kamyshny and S. Magdassi, "Inkjet ink formulations," *Inkjet-based Micromanufacturing*, pp. 173–189, 2012.

[34] J. Stringer and B. Derby, "Formation and stability of lines produced by inkjet printing," *Langmuir*, vol. 26, pp. 10365–10372, 6 2010.

[35] D. J. Odde and M. J. Renn, "Laser-guided direct writing for applications in biotechnology," 1999.

[36] R. Streubel, M. B. Wilms, C. Doñate-Buendía, A. Weisheit, S. Barcikowski, J. H. Schleifenbaum, and B. Gökce, "Depositing laser-generated nanoparticles on powders for additive manufacturing of oxide dispersed strengthened alloy parts via laser metal deposition," *Japanese Journal of Applied Physics*, vol. 57, p. 040310, 3 2018.

[37] J. R. Moffitt, Y. R. Chemla, S. B. Smith, and C. Bustamante, "Recent advances in optical tweezers," *https://doi.org/10.1146/annurev.biochem.77.043007.090225*, vol. 77, pp. 205–228, 6 2008.

[38] E. R. Dufresne and D. G. Grier, "Optical tweezer arrays and optical substrates created with diffractive optics," *Review of Scientific Instruments*, vol. 69, p. 1974, 5 1998.

[39] E. E. Ehrichs, S. Yoon, and A. L. D. Lozanne, "Direct writing of 10 nm features with the scanning tunneling microscope," *Applied Physics Letters*, vol. 53, p. 2287, 12 1998.

[40] Y. Z. Li, L. Vazquez, R. Piner, R. P. Andres, and R. Reifenberger, "Writing nanometer-scale symbols in gold using the scanning tunneling microscope," *Applied Physics Letters*, vol. 54, p. 1424, 8 1998.

[41] Y. Chen, J. Dong, W. Gao, J. Qi, X. Yan, and X. Kong, "Enhanced fluorescence effect from complex nanostructure decorated with the native oxide layer," *Journal of Optics (India)*, vol. 47, pp. 283–287, 2018.

[42] D. Hines, Y. Gu, A. Martin, P. Li, J. Fleischer, A. Clough-Paez, G. Stackhouse, A. Dasgupta, and S. Das, "Considerations of aerosol-jet printing for the fabrication of printed hybrid electronic circuits," *Additive Manufacturing*, vol. 47, p. 102325, 11 2021.

[43] E. B. Secor, "Principles of aerosol jet printing," *Flexible and Printed Electronics*, vol. 3, p. 035002, 9 2018.

[44] R. Salary, J. P. Lombardi, M. S. Tootooni, R. Donovan, P. K. Rao, P. Borgesen, and M. D. Poliks, "Computational fluid dynamics modeling and online monitoring of aerosol jet printing process," *Journal of Manufacturing Science and Engineering, Transactions of the ASME*, vol. 139, 2017.

[45] A. Mahajan, C. D. Frisbie, L. F. Francis, C. D. Frisbie, L. F. Francis, C. D. Frisbie, and L. F. Francis, "Optimization of aerosol jet printing for high-resolution, high-aspect ratio silver lines," *ACS Applied Materials and Interfaces*, vol. 5, pp. 4856–4864, 2013.

[46] S. Ni, J. Leemann, I. Buttinoni, L. Isa, and H. Wolf, "Programmable colloidal molecules from sequential capillarity-assisted particle assembly," *Science Advances*, vol. 2, 4 2016.

[47] V. Flauraud, M. Mastrangeli, G. D. Bernasconi, J. Butet, D. T. L. Alexander, E. Shahrabi, O. J. F. Martin, and J. Brugger, "Nanoscale topographical control of capillary assembly of nanoparticles," *Nature Nanotechnology*, pp. 1–24, 2016.

[48] J. M. Hoey, A. Lutfurakhmanov, D. L. Schulz, and I. S. Akhatov, "A review on aerosol-based direct-write and its applications for microelectronics," *Journal of Nanotechnology*, vol. 2012, pp. 1–22, 2012.

[49] S. Mypati, A. Docoslis, and D. P. Barz, "Direct writing of liquids by micro dispensing: Stability and shape of laminar jets with high froude numbers," *Chemical Engineering Journal*, vol. 381, p. 122645, 2 2020.

[50] L. J. Wei and C. H. Oxley, "Carbon based resistive strain gauge sensor fabricated on titanium using micro-dispensing direct write technology," *Sensors and Actuators A: Physical*, vol. 247, pp. 389–392, 8 2016.

[51] C. Maibohm, O. F. Silvestre, J. Borme, M. Sinou, K. Heggarty, and J. B. Nieder, "Multi-beam two-photon polymerization for fast large area 3d periodic structure fabrication for bioapplications," *Scientific Reports 2020 10:1*, vol. 10, pp. 1–10, 5 2020.

[52] A. Accardo, R. Courson, R. Riesco, V. Raimbault, and L. Malaquin, "Direct laser fabrication of meso-scale 2d and 3d architectures with micrometric feature resolution," *Additive Manufacturing*, vol. 22, pp. 440–446, 8 2018.

[53] K. Hwang, C. Y. Shin, R. Mingwu, S. H. Lee, and H. mo Kim, "Design of a nano-printer based on afpn (active fountain pen nano-lithography) using switch control," *Journal of Mechanical Science and Technology 2011 25:4*, vol. 25, pp. 977–985, 6 2011.

[54] C. Novara, F. Petracca, A. Virga, P. Rivolo, S. Ferrero, A. Chiolerio, F. Geobaldo, S. Porro, and F. Giorgis, "Sers active silver nanoparticles synthesized by inkjet printing on mesoporous silicon," *Nanoscale Research Letters*, vol. 9, pp. 1–7, 2014.

[55] P. K. Wu, B. R. Ringeisen, J. Callahan, M. Brooks, D. M. Bubb, H. D. Wu, A. Piqué, B. Spargo, R. A. McGill, and D. B. Chrisey, "The deposition, structure, pattern deposition, and activity of biomaterial thin-films by matrix-assisted pulsed-laser evaporation (maple) and maple direct write," *Thin Solid Films*, vol. 398-399, pp. 607–614, 11 2001.

[56] Y. Nahmias, R. E. Schwartz, C. M. Verfaillie, and D. J. Odde, "Laser-guided direct writing for three-dimensional tissue engineering," *Biotechnology and Bioengineering*, vol. 92, pp. 129–136, 10 2005.

[57] N. S. Tabrizi, M. Ullmann, V. A. Vons, U. Lafont, and A. Schmidt-Ott, "Generation of nanoparticles by spark discharge," *Journal of Nanoparticle Research*, vol. 11, pp. 315–332, 2 2009.

[58] N. S. Tabrizi, Q. Xu, N. M. van der Pers, and A. Schmidt-Ott, "Generation of mixed metallic nanoparticles from immiscible metals by spark discharge," *Journal of Nanoparticle Research*, vol. 12, pp. 247–259, 1 2010.

[59] N. S. Tabrizi, Q. Xu, N. M. van der Pers, U. Lafont, and A. Schmidt-Ott, "Synthesis of mixed metallic nanoparticles by spark discharge," *Journal of Nanoparticle Research*, vol. 11, pp. 1209–1218, 7 2009.

[60] I. S. Akhatov, J. M. Hoey, O. F. Swenson, and D. L. Schulz, "Aerosol focusing in micro-capillaries: Theory and experiment," *Journal of Aerosol Science*, vol. 39, pp. 691–709, 2008.

[61] S. Fuerstenau, A. Gomez, and J. F. de la Mora, "Visualization of aerodynamically focused subsonic aerosol jets," *Journal of Aerosol Science*, 1994.

[62] D. L. Johnson, D. Leith, and P. C. Reist, "Drag on non-spherical, orthotropic aerosol particles," *Journal of Aerosol Science*, vol. 18, pp. 87–97, 2 1987.

[63] I. S. Akhatov, J. M. Hoey, O. F. Swenson, and D. L. Schulz, "Aerosol flow through a long micro-capillary: collimated aerosol beam," *Microfluidics and Nanofluidics*, vol. 5, pp. 215–224, 8 2008.

[64] G.-Y. Lee, J.-I. Park, C.-S. Kim, H.-S. Yoon, J. Yang, S.-H. Ahn, and W. E. Boeing, "Aerodynamically focused nanoparticle (afn) printing: Novel direct printing technique of solvent-free and inorganic nanoparticles," *ACS Appl. Mater. Interfaces*, vol. 6, p. 13, 2014.

[65] D. L. Schulz, J. M. Hoey, D. Thompson, O. F. Swenson, S. Han, J. Lovaasen, X. Dai, C. Braun, K. Keller, and I. S. Akhatov, "Collimated aerosol beam deposition: Sub 5-μm resolution of printed actives and passives," 2008.

[66] D. L. Roberts and J. P. Mitchell, "The effect of nonideal cascade impactor stage collection efficiency curves on the interpretation of the size of inhaler-generated aerosols," *AAPS PharmSciTech*, 2013.

[67] F. D. Fonzo, A. Gidwani, M. H. Fan, D. Neumann, D. I. Iordanoglou, J. V. Heberlein, P. H. McMurry, S. L. Girshick, N. Tymiak, W. W. Gerberich, and N. P. Rao, "Focused nanoparticle-beam deposition of patterned microstructures," *Applied Physics Letters*, 2000.

[68] S. Opiolka, F. Schmidt, and H. Fissan, "Combined effects of electrophoresis and thermophoresis on particle deposition onto flat surfaces," *Journal of Aerosol Science*, vol. 25, pp. 665–671, 6 1994.

[69] E. Tabesh, H. R. Salimijazi, M. Kharaziha, M. Mahmoudi, and M. Hejazi, "Development of an in-situ chitosan-copper nanoparticle coating by electrophoretic deposition," *Surface and Coatings Technology*, vol. 364, pp. 239–247, 4 2019.

[70] R. Mei, "An approximate expression for the shear lift force on a spherical particle at finite reynolds number," *International Journal of Multiphase Flow*, 1992.

[71] X. Wang, F. E. Kruis, and P. H. McMurry, "Aerodynamic focusing of nanoparticles: I. guidelines for designing aerodynamic lenses for nanoparticles," *Aerosol Science and Technology*, vol. 39, pp. 611–623, 7 2005.

[72] J. Q. Feng, "Available online at www.jafmonline.net," *Journal of Applied Fluid Mechanics*, vol. 10, pp. 1735–3645, 2017.

[73] D. K. Lim, K. S. Jeon, H. M. Kim, J. M. Nam, and Y. D. Suh, "Nanogap-engineerable raman-active nanodumbbells for single-molecule detection," *Nature Materials*, vol. 9, pp. 60–67, 2010.

[74] M. Liebel, N. Pazos-Perez, N. F. van Hulst, and R. A. Alvarez-Puebla, "Surface-enhanced raman scattering holography," *Nature Nanotechnology*, vol. 15, pp. 1005–1011, 12 2020.

[75] G. McNay, D. Eustace, W. E. Smith, K. Faulds, and D. Graham, "Surface-enhanced raman scattering (sers) and surface-enhanced resonance raman scattering (serrs): A review of applications," *Applied Spectroscopy*, vol. 65, pp. 825–837, 2011.

[76] S. Y. Ding, E. M. You, Z. Q. Tian, and M. Moskovits, "Electromagnetic theories of surface-enhanced raman spectroscopy," *Chemical Society Reviews*, vol. 46, pp. 4042–4076, 2017.

[77] N. Kim, M. R. Thomas, M. S. Bergholt, I. J. Pence, H. Seong, P. Charchar, N. Todorova, A. Nagelkerke, A. Belessiotis-Richards, D. J. Payne, A. Gelmi, I. Yarovsky, and M. M. Stevens, "Surface enhanced raman scattering artificial nose for high dimensionality fingerprinting," *NanoScience and Technology*.

[78] S. Sebastian, *Surface Enhanced Raman Spectroscopy: Analytical, Biophysical and Life Science Applications*. 2011.

[79] K. Kneipp, Y. Wang, H. Kneipp, L. T. Perelman, I. Itzkan, R. R. Dasari, and M. S. Feld, "Single molecule detection using surface-enhanced raman scattering (sers)," *Physical Review Letters*, vol. 78, pp. 1667–1670, 1997.

[80] E. C. L. Ru, E. Blackie, M. Meyer, and P. G. Etchegoint, "Surface enhanced raman scattering enhancement factors: A comprehensive study," *Journal of Physical Chemistry C*, 2007.

[81] C. Zong, M. Xu, L. J. Xu, T. Wei, X. Ma, X. S. Zheng, R. Hu, and B. Ren, "Surface-enhanced raman spectroscopy for bioanalysis: Reliability and challenges," *Chemical Reviews*, vol. 118, pp. 4946–4980, 2018.

[82] L. Jensen, C. M. Aikens, and G. C. Schatz, "Electronic structure methods for studying surface-enhanced raman scattering," *Chemical Society Reviews*, vol. 37, p. 1061, 2008.

[83] K. A. Willets and R. P. V. Duyne, "Localized surface plasmon resonance spectroscopy and sensing," *Annual Review of Physical Chemistry*, vol. 58, pp. 267–297, 5 2007.

[84] X. Zhang, W. Y. Cui, Y. Lei, X. Zheng, J. Zhang, and T. J. Cui, "Spoof localized surface plasmons for sensing applications," *Advanced Materials Technologies*, p. 2000863, 2 2021.

[85] J. S. Duque, J. S. Blandón, and H. Riascos, "Localized plasmon resonance in metal nanoparticles using mie theory," vol. 850, p. 012017, 6 2017.

[86] D. M. Kim, J. S. Park, S.-W. Jung, J. Yeom, and S. M. Yoo, "Biosensing applications using nanostructure-based localized surface plasmon resonance sensors," *Sensors*, vol. 21, p. 3191, 5 2021.

[87] B. Sharma, R. R. Frontiera, A. I. Henry, E. Ringe, and R. P. V. Duyne, "Sers: Materials, applications, and the future," *Materials Today*, vol. 15, pp. 16–25, 2012.

2

Aerosol Science and Technology

This chapter discusses the physics of a particle in a flow while taking into account all forces acting on it, as well as the method and system that is used throughout the experimental work.

The contents of this chapter is based on published journal papers:

- **Section 2.1** in: Aghajani, S., Accardo, A., & Tichem, M. (2020). Aerosol Direct Writing and Thermal Tuning of Copper Nanoparticle Patterns as Surface-Enhanced Raman Scattering Sensors. ACS Applied Nano Materials, 3(6), 5665–5675. DOI:10.1021/acsanm.0c00887
- **Section 2.2** in: Aghajani, S., Accardo, A., & Tichem, M. (2022). Process and nozzle design for high-resolution dry aerosol direct writing (dADW) of sub-100 nm nanoparticles. Additive Manufacturing, 54, 102729. DOI:10.1016/J.ADDMA.2022.102729

2.1 Aerosol physics

The behaviour of particles in a gas flow is extensively studied in aerosol physics [1–6]. These studies primarily focus on uncharged spherical particles suspended in a medium serving as a carrier fluid with various force fields acting on them (Figure 2.1). Newton's Second Law can be used to calculate the trajectory of a particle in a shear flow as follows:

$$\left(\frac{4}{3}\right)\pi r_p^3 \rho_p \left(\frac{\hat{d}\vec{v}_p}{\hat{d}t}\right) = \sum \vec{F} \tag{2.1}$$

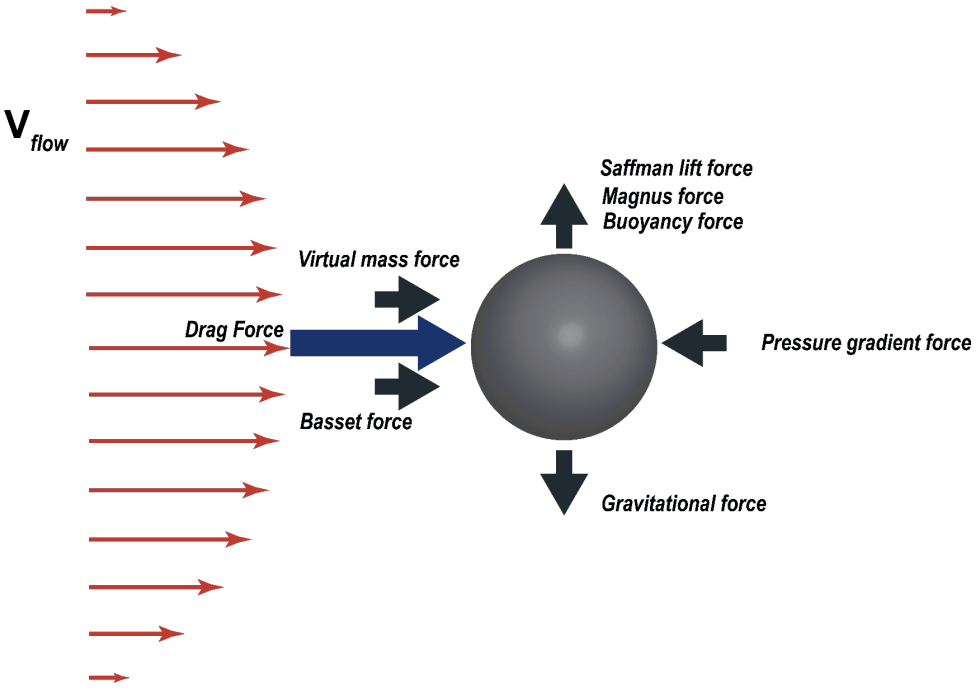

Figure 2.1: Particle in the flow and forces acting on it

Where r_p, and ρ_p are the particle radius and density, respectively, $\vec{v}_p$ is the particle's velocity and $\sum \vec{F}$ represents all the forces acting on a particle. Depending on the conditions, $\sum \vec{F}$ contains a number of force components:

$$\sum \vec{F} = \vec{F}_D + \vec{F}_G + \vec{F}_{Ba} + \vec{F}_{V\,m} + \vec{F}_{\mathrm{Pr}} + \vec{F}_B + \vec{F}_{Ma} + \vec{F}_{Sa} \tag{2.2}$$

Where $\vec{F}_D$ is the steady flow viscous Stokes drag force, $\vec{F}_G$ is gravitational force, $\vec{F}_{Ba}$ is the non-steady viscous drag (Basset force), $\vec{F}_{V\,m}$ is the virtual mass force originating from the inertia of media surrounding the moving particle, $\vec{F}_{\mathrm{Pr}}$ is the pressure gradient force evolving from a gradient of media pressure across the particle's surface, $\vec{F}_B$ is the buoyancy force, $\vec{F}_{Ma}$ is the Magnus force originating from a rotating particle in a gas flow, and $\vec{F}_{Sa}$ is the Saffman lift force

originating from a gradient in the velocity field to which the particle is exposed [1–4]. In addition, there is randomness in the particle motion due to the Brownian motion force [5]. The Stokes drag force is the primary force acting on a particle in a flow, and it is determined by the particle radius (r_p), the relative velocity of the fluid to the particle velocity ($\vec{v}_f - \vec{v}_p$), and the medium dynamic viscosity (μ_f) [6, 7],

$$\vec{F}_D = 6\pi r_p \mu_f \left(\vec{v}_f - \vec{v}_p\right) \tag{2.3}$$

The Stokes drag force is often the dominant force; all other forces are only considered in the study if their ratio to the Stokes force is significant. The assumption for calculating the Stokes drag force $\vec{F}_D$ (equation 2.3) is a zero velocity of the flow at the particle's surface. However, this assumption does not hold for small particle r_p < 250 nm and rarefied flows, since in this condition, the mean free path of molecules becomes comparable to the size of particles due to the low density of the flow [5, 8–10]. To include these effects in the Stokes drag force, the Cunningham slip correction factor (C_s) must be applied as follows [9, 11, 12]:

$$\begin{aligned} \vec{F}_{D,c} &= \frac{\vec{F}_D}{C_s} \\ C_s &= 1 + Kn(C_1 + C_2 e^{-\frac{C_3}{Kn}}) \\ Kn &= \frac{\lambda}{2r_p} \\ \lambda &= (\frac{\mu_f}{P})\sqrt{\frac{\pi RT}{2M}} \end{aligned} \tag{2.4}$$

Where $\vec{F}_{D,c}$ is the modified drag force due to Cunningham slip correction factor, Kn is Knudsen number which is depend on r_p and mean free path (λ) of the molecules. The mean free path is depend on temperature (T), pressure (p), and dynamic viscosity (μ_f) of the gas. Based on equation 2.4, increasing the temperature or decreasing the pressure increases the mean free path of the molecules and thus the Cunningham slip correction factor. Inserting equation 2.4 into equations 2.1 and 2.2 and considering the effect of all forces negligible except Stokes drag force, this yields to:

$$\begin{aligned} \tau_{s,c}\left(\frac{\hat{d}\vec{v}_p}{\hat{d}t}\right) + \vec{v}_p &= \vec{v}_f \\ \tau_{s,c} &= \frac{2r_p^2 \rho_p C_s}{9\mu_f} \end{aligned} \tag{2.5}$$

In this equation, a quantity is known as relaxation time τ [s] appears, which is affected by particle size ($\propto r_p^2$) and density as well as gas properties such as dynamic viscosity, pressure, and temperature (due to Cunningham slip correction factor). The relaxation time is the time it takes for a particle to adjust its velocity to a new condition or set of forces. This value is very small for nanoparticles (about 2 µs for a gold nanoparticle with a radius of 100 nm at room pressure), indicating that particles in this size range adapt quickly to new situations and that a particle can be expected to maintain its trajectory for this period of time. The ratio of this value to the flow's characteristic time (V_f/L), where L represents the length that a particle is expected to preserve its trajectory, yields a dimensionless number known as the Stokes number (St).

Low Stokes numbers (St<1) indicate that particles adapt sooner to new flow conditions than expected length; therefore, particle follows the streamlines , whereas, if a particle's behaviour

is described by a large Stokes number (St>1), its inertia is dominant, and the particle will leave the streamline and keep its initial trajectory (Figure 2.2). Furthermore, when a particle flow is directed towards a substrate that is perpendicular to the gas flow for deposition, the Stokes number governs the behaviour. The gas flow will be deflected, and 90 ° bends in the streamlines will form; depending on the particle's inertia, the particle will either follow the streamline and leave the system undeposited, or they will leave the streamline and impact on the surface (Figure 2.2). This is the main principle behind developing impactors, which provide binary particle size selection based on inertia. High Stokes number means high inertia, which can be obtained through either high velocity or high mass (density or size); clearly, reducing particle size makes it increasingly difficult to make particles leave the streamlines. Due to the effect of the Cunningham slip factor on the relaxation time, the strategy for depositing very small particles onto substrates via impaction is to increase their velocity while decreasing the downstream pressure. This explains why aerosol jet printing in an ambient environment is limited to, relatively speaking, larger particles (1-2 µm droplets) [13–15].

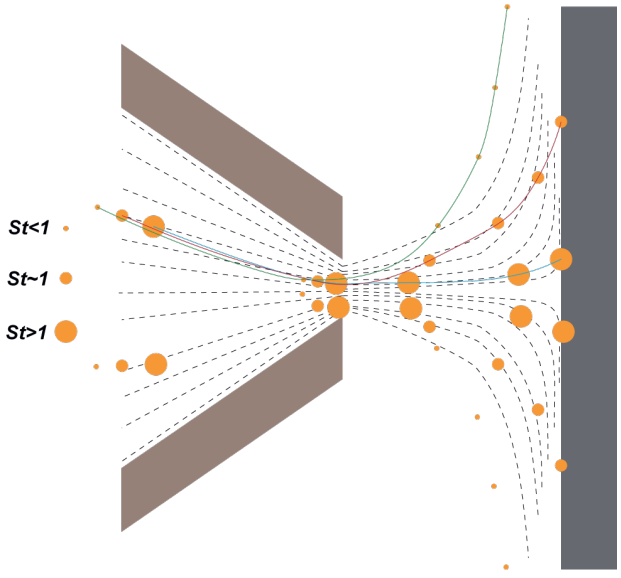

Figure 2.2: Effect of Stokes number on the trajectory of particles

Table 2.1 shows the forces mentioned in equation 2.2, their influencing parameters, and their ratio to the drag force. The gravitational force $\vec{F}_G$ depends on the size of particles to the power of three, which is negligible for nanoparticles. For the ratio of Bassett force $\vec{F}_{Ba}$ to Stokes force, it can be seen that it depends on τ_s / t and ρ_f / ρ_p, which is only relevant in case of high accelerations in the flow (swift change in the flow situation compared to the relaxation time) or a high ratio of medium to particle density. For metallic nanoparticles in a carrier gas of argon, which is the configuration present in the proposed dADW method in this thesis, the ratio of densities is very small (about ~0.0004 for gold and argon), and due to the small-sized nanoparticles, the relaxation time is also very small; hence we are focusing on the steady-state situation which leads

to negligible Bassett force $\left(\vec{F}_{Ba} \approx 0\right)$. For the virtual mass force $\vec{F}_{Vm}$, the body and the medium cannot occupy the same space simultaneously, and hence in the case of extremely high accelerations, the inertia of the medium to be pushed away needs to be considered. Our study focused on the steady-state flow, which means flow velocity is not time-dependant $\left(dv_f/dt = 0\right)$, and the ratio of densities is very small; therefore, neglecting virtual mass has not much loss over the accuracy of our study.

Table 2.1: The forces acting on a particle in the flow and their relation to the Stokes drag force, [references mentioned in the table]

Name of the Force	The ratio to the Stokes drag force
$\vec{F}_G = \frac{4}{3}\pi r_p^3 \rho_p \vec{g}$	$\frac{\left\|\vec{F}_G\right\|}{\left\|\vec{F}_D\right\|} \cong \tau_s \frac{g}{\left\|\vec{v}_f - \vec{v}_p\right\|}$ $\tau_s = \frac{2r_p^2 \rho_p}{9\mu_f}$
$\vec{F}_{Ba} = 6r_p^2 \sqrt{\pi \mu_f \rho_f} \int_{-\infty}^{t} \left(\frac{\frac{d\vec{v}_p}{dt} - \frac{d\vec{v}_f}{dt} - \vec{v}_p.\nabla\vec{v}_f}{\sqrt{t-\tau}} \right) d\tau$ [16]	$\frac{\left\|\vec{F}_{Ba}\right\|}{\left\|\vec{F}_D\right\|} \cong \sqrt{\frac{18\rho_f \tau_s}{\pi \rho_p t}}$ $\tau_s = \frac{2r_p^2 \rho_p}{9\mu_f}$
$\vec{F}_{Vm} = -C_M \left(\frac{4}{3}\pi r_p^3 \rho_f\right)\left(\frac{d\vec{v}_f}{dt} - \frac{d\vec{v}_p}{dt}\right)$ [2, 17]	$\frac{\left\|\vec{F}_{Vm}\right\|}{\left\|\vec{F}_D\right\|} = -C_M \left(\tau_s \frac{\rho_f}{\rho_p}\right)\left(\frac{\left(\frac{d\vec{v}_f}{dt} - \frac{d\vec{v}_p}{dt}\right)}{\left(\vec{v}_f - \vec{v}_p\right)}\right)$
$\vec{F}_{\mathrm{Pr}} = \left(\frac{4}{3}\pi r_p^3 \rho_f\right)\left(\frac{Dv_f}{Dt}\right)$ $\frac{Dv_f}{Dt} = \frac{dv_f}{dt} - \left[\left(\left(\vec{v}_p - \vec{v}_f\right)\right).\vec{\nabla}\right] v_f$ [18]	$\frac{\left\|\vec{F}_{\mathrm{Pr}}\right\|}{\left\|\vec{F}_D\right\|} = \left(\tau_s \frac{\rho_f}{\rho_p}\right)\left(\frac{\left(\frac{Dv_f}{dt}\right)}{\left(\vec{v}_f - \vec{v}_p\right)}\right)$
$\vec{F}_B = \left(V_p\right)\left(\rho_f - \rho_p\right)\vec{g}$ [19]	$\frac{\left\|\vec{F}_B\right\|}{\left\|\vec{F}_D\right\|} \cong \frac{2\pi r_p^2 (\rho_f - \rho_p)}{9\left(\vec{v}_f - \vec{v}_p\right)}\vec{g}$
$\vec{F}_{Ma} = -\pi r_p^3 \rho_f \left(\frac{1}{2}\vec{\omega} - \vec{\Omega}\right) \times \left(\vec{v}_f - \vec{v}_p\right)$ [18]	$\frac{\left\|\vec{F}_{Ma}\right\|}{\left\|\vec{F}_D\right\|} = \frac{r_p^2 \rho_f}{6\mu_f}\left\|\frac{1}{2}\vec{\omega} - \vec{\Omega}\right\|$
$\vec{F}_{Sa} = 1.615 r_p^2 \left\|\vec{v}_f - \vec{v}_p\right\| \sqrt{\mu_f \rho_f \frac{\partial\left(\vec{v}_f - \vec{v}_p\right)}{\partial r}}.sgn\left(\frac{\partial\left(\vec{v}_f - \vec{v}_p\right)}{\partial r}\right)$ [1, 3, 20]	$\frac{\left\|\vec{F}_{Sa}\right\|}{\left\|\vec{F}_D\right\|} \cong \frac{1.615}{6\pi} r_p \sqrt{\frac{\rho_f}{\mu_f}} \sqrt{\frac{\partial\left(\vec{v}_f - \vec{v}_p\right)}{\partial r}}$

The pressure gradient force $\vec{F}_{\mathrm{Pr}}$ is related to the gradient of the pressure around a particle which is very small for submicron particles; moreover, its ratio to the Stokes force depends on the relaxation time and ratio of densities; for submicron particles, the force can be neglected. The buoyancy force $\vec{F}_B$ originates from a solid object which is (partially) immersed in a liquid or gaseous medium and is equal to the weight of the amount of medium displaced, *i.e.* is directly related to the volume of the (immersed part of the) object and the density of the medium. The Buoyancy force is only significant for the particle's trajectory if the particle is large; therefore, this force can be neglected in our study. The Magnus force $\vec{F}_{Ma}$ is only significant for larger particles and only when they rotate (spin) with high angular velocity, and its ratio to the Stokes force depends on the particle size, which makes it a negligible force compared to the $\vec{F}_D$ fine nanoparticles. Finally, the Saffman force depends on the shear rate and magnitude of the rela-

tive velocity of the particle to the flow velocity, and comparative to the stokes force is essential that either the size of particles is large or the shear rate is high. However, in this study, as the maximum size of particles considered in our study is 100 nm, the Saffman force is negligible compared to the Stokes force. Brownian motion, resulting from the random impact of medium molecules on the particle, is significant if the thermal energy is high compared to other effects. In the high-velocity fields, we focus on, this is not the case. Hence, we conclude that the behaviour of particles in a flow, and ignoring particle-particle interactions, can sufficiently be described by considering the Stokes force only.

2.2 dry Aerosol Direct Writing (dADW) setup

For experimental verification of the dry Aerosol Direct Writing (dADW) process, throughout the entire thesis a setup has been used for the spatially-selective deposition of metal nanoparticles (MNPs), consisting of a commercial particle generator (VSParticle G1) and a deposition unit as illustrated schematically in Figure 2.3.a. The particle generator exploits the Spark Ablation Method (SAM) (Figure 2.3.b). In SAM, the discharge of electrons (sparks) between two electrodes generates a locally high temperature (typically 20,000 K [21]) at the spark location [22, 23]. The introduced energy leads to local evaporation of the electrode material.

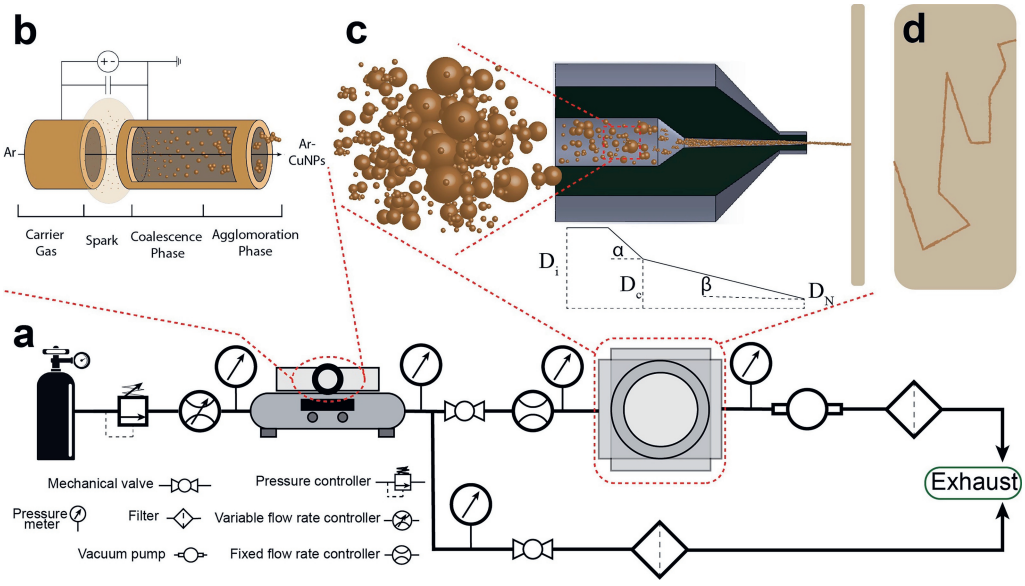

Figure 2.3: Schematic representation of a) the aerosol direct writing system and its components: b) Spark ablation method working principle; c) NPs and agglomerates of NPs focusing in a long converging nozzle, and axisymmetric view of the nozzle and its configuration; d) example of deposited NP pattern.

The vapor is carried away by an inert gas (Argon), controlled by a Bronkhorst HighTech El-Flow Prestige (inlet volumetric flow rate between 150 to 20,000 sccm), and is quenched very

shortly after its evaporation by passing through an orifice in the system, which causes the metal vapor to cool down and coalesce into primary spherical NPs [24] (10^9 to 10^{12} cm^{-3} particles, a polydispersed mixture with particle sizes between 1 and 20 nm [22]). After that, the NPs start to form agglomerates of diverse shape and size (tens to hundreds of nanometers), by particle-particle interaction and impaction. The parameters to control particle size and amount are the frequency of the electrical field, the current, and the Argon gas flow.

The deposition unit consists of a vacuum chamber, a dry pump, a focusing nozzle, and a stage. The stage controller consists of two SmarAct SLC-1750-M-E-HV positioners for patterning of a substrate with in-plane motions (X, Y) of the stage and one SmarAct SLC-1750-O20-D-HV positioner for out-of-plane motion (Z) of the stage to precisely control the distance of the nozzle to the substrate. The experimental setup including Argon flask, SAM particle generator, pressure sensors, and vacuum chamber is shown in Figure 2.4.

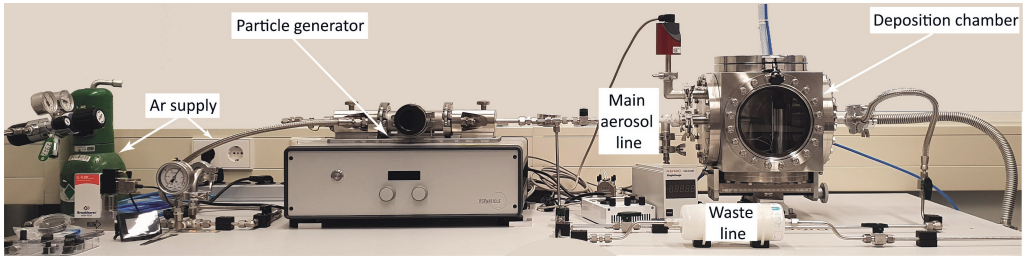

Figure 2.4: The experimental setup for dry aerosol direct writing (dADW)

References

[1] I. S. Akhatov, J. M. Hoey, O. F. Swenson, and D. L. Schulz, "Aerosol focusing in micro-capillaries: Theory and experiment," *Journal of Aerosol Science*, vol. 39, pp. 691–709, 2008.

[2] I. S. Akhatov, J. M. Hoey, O. F. Swenson, and D. L. Schulz, "Aerosol flow through a long micro-capillary: collimated aerosol beam," *Microfluidics and Nanofluidics*, vol. 5, pp. 215–224, 8 2008.

[3] R. Mei, "An approximate expression for the shear lift force on a spherical particle at finite reynolds number," *International Journal of Multiphase Flow*, 1992.

[4] J. Ran, L. Zhang, Q. Tang, and M. Xin, "Numerical simulation of the particle motion characteristics in boundary layer of gas-solid rotary flow," *Journal of Fluids Engineering, Transactions of the ASME*, vol. 128, pp. 596–601, 5 2006.

[5] O. Abouali and G. Ahmadi, "A model for supersonic and hypersonic impactors for nanoparticles," *Journal of Nanoparticle Research*, vol. 7, pp. 75–88, 2 2005.

[6] R. A. Millikan, "Coefficients of slip in gases and the law of reflection of molecules from the surfaces of solids and liquids," *Physical Review*, 1923.

[7] J. F. D. L. Mora and P. Riesco-Chueca, "Aerodynamic focusing of particles in a carrier gas," *Journal of Fluid Mechanics*, 1988.

[8] W. C. Hinds, "Aerosol technology," *Journal of Chemical Information and Modeling*, vol. 53, pp. 1689–1699, 2019.

[9] E. Cu, "On the velocity of steady fall of spherical particles through fluid medium," *Proceedings of the Royal Society of London. Series A, Containing Papers of a Mathematical and Physical Character*, vol. 83, pp. 357–365, 3 1910.

[10] D. J. Carlson and R. F. Hoglund, "Particle drag and heat transfer in rocket nozzles," *AIAA Journal*, vol. 2, pp. 1980–1984, 5 1964.

[11] C. N. Davies, "Definitive equations for the fluid resistance of spheres," *Proceedings of the Physical Society*, vol. 57, pp. 259–270, 1945.

[12] J. Q. Feng, "Available online at www.jafmonline.net," *Journal of Applied Fluid Mechanics*, vol. 10, pp. 1735–3645, 2017.

[13] R. Salary, J. P. Lombardi, M. S. Tootooni, R. Donovan, P. K. Rao, P. Borgesen, and M. D. Poliks, "Computational fluid dynamics modeling and online monitoring of aerosol jet printing process," *Journal of Manufacturing Science and Engineering, Transactions of the ASME*, vol. 139, 2017.

[14] E. B. Secor, "Principles of aerosol jet printing," *Flexible and Printed Electronics*, vol. 3, p. 035002, 9 2018.

[15] A. Mahajan, C. D. Frisbie, L. F. Francis, C. D. Frisbie, L. F. Francis, C. D. Frisbie, and L. F. Francis, "Optimization of aerosol jet printing for high-resolution, high-aspect ratio silver lines," *ACS Applied Materials and Interfaces*, vol. 5, pp. 4856–4864, 2013.

[16] B. V. Ramarao and C. Tien, "Role of basset force on particle deposition in stagnation flow," *Journal of Aerosol Science*, vol. 21, pp. 597–611, 1 1990.

[17] K. Inthavong, J. Wen, Z. Tian, and J. Tu, "Numerical study of fibre deposition in a human nasal cavity," *Journal of Aerosol Science*, vol. 39, pp. 253–265, 3 2008.

[18] J. S. Marshall, "Discrete-element modeling of particulate aerosol flows," *Journal of Computational Physics*, vol. 228, pp. 1541–1561, 3 2009.

[19] Z. Wang, P. K. Hopke, P. A. Baron, G. Ahmadi, Y. S. Cheng, G. Deye, and W. C. Su, "Fiber classification and the influence of average air humidity," *http://dx.doi.org/10.1080/02786820500380198*, vol. 39, pp. 1056–1063, 11 2007.

[20] J. M. Hoey, A. Lutfurakhmanov, D. L. Schulz, and I. S. Akhatov, "A review on aerosol-based direct-write and its applications for microelectronics," *Journal of Nanotechnology*, vol. 2012, pp. 1–22, 2012.

[21] R. Reinmann and M. Akram, "Temporal investigation of a fast spark discharge in chemically inert gases," *Journal of Physics D: Applied Physics*, vol. 30, pp. 1125–1134, 4 1997.

[22] N. S. Tabrizi, M. Ullmann, V. A. Vons, U. Lafont, and A. Schmidt-Ott, "Generation of nanoparticles by spark discharge," *Journal of Nanoparticle Research*, vol. 11, pp. 315–332, 2 2009.

[23] S. Schwyn, E. Garwin, and A. Schmidt-Ott, "Aerosol generation by spark discharge," *Journal of Aerosol Science*, vol. 19, pp. 639–642, 10 1988.

[24] T. Pfeiffer, J. Feng, and A. Schmidt-Ott, "New developments in spark production of nanoparticles," *Advanced Powder Technology*, vol. 25, pp. 56–70, 1 2014.

3

Process and nozzle design for high-resolution dADW

One of the essential requirements to create nanoparticle (NP)-based applications and functions is the ability to control their deposition in specific locations. Many methods have been proposed, with wet direct writing (DW) techniques such as inkjet printing being the most employed. These methods generally depend on off-line and solvent-based NP synthesis leading to contamination and impurity in the final NP film as well as inhomogeneity in the deposition caused by solution-substrate interactions. This dissertation introduces a dry aerosol direct writing (dADW) method, which combines spark ablation-based and solvent-free NP synthesis with spatially selective deposition using aerodynamic focusing in a vacuum chamber. The challenge is to print high-resolution lines and spots of nanoparticles with a diameter < 100 nm. We study two aerodynamic nozzle concepts, a converging nozzle (CN) and a sheath gas nozzle (SGN), and investigate numerically how their design, as well as operating parameters, relate to the deposition process performance. This is quantified by three criteria: contraction factor, focusing ratio, and collection efficiency. We also compared our numerical results to experimental assays by manufacturing two SGNs and three CNs and evaluating the performance of each nozzle in terms of resolution, sharpness and thickness of the line. Using one of the SGN designs with an outlet diameter of 248 μm and an aerosol to total flow rate ratio of 0.17, we achieved a high-resolution line with a width of 67 μm, *i.e.*, equal to 27% of the nozzle diameter, when printing <100 nm Au NPs. The presented additive manufacturing method enables, therefore, the creation of high-resolution and sharp patterns of metallic nanoparticles, which can be employed in a wide range of applications, ranging from interconnects to optical and gas sensors.

The contents of this chapter have been published in:

- Aghajani, S., Accardo, A., & Tichem, M. (2022). Process and nozzle design for high-resolution dry aerosol direct writing (dADW) of sub-100 nm nanoparticles. Additive Manufacturing, 54, 102729. DOI:10.1016/J.ADDMA.2022.102729

Section 3.4 contains unpublished material.

3.1 Introduction

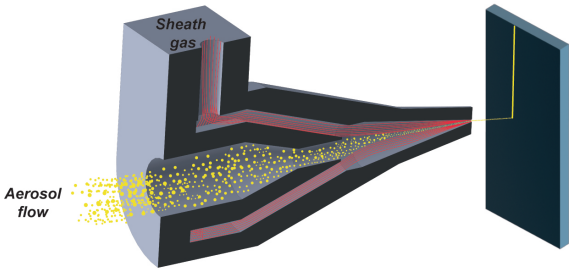

Nanoparticles (NPs) are the foundation of many devices and applications with complex properties and functionalities [1–6]. This includes optical coatings [7], catalysis [6], biosensors [8, 9], electrical interconnects [10] and many more. As a result, NP manipulation is required for a wide range of scientific and industrial applications. Localised NP patterning, in particular, has received considerable attention in many studies due to its flexibility and compatibility, including microelectronics [11, 12], optics [13–15] and sensing [16, 17]. Several techniques have been proposed to enable localised NP deposition, with direct writing (DW) methods being one of the most prominent. Nanoparticle direct writing is a class of additive manufacturing techniques that uses a controlled deposition of nanoparticles to produce patterns and features on the surface without the need for lithography processes. Techniques such as inkjet printing (IJP) [18–21] and aerosol-jet printing (AJP) [3, 22–25] are widely-used examples of nanoparticle DW deposition techniques. In both methods, droplets of liquid containing nanoparticles stabilised by surfactants [25–27] are deposited on the substrate [19, 23] to create desired patterns. However, the use of chemical agents in the synthesis of NPs and for stabilisation of the suspension during printing may lead to contamination and affect the properties of the NP film.

In contrast to solvent-based NP deposition methods, in dry techniques, no chemical agents are present during particle synthesis and deposition, which reduces the possibility of particle contamination and impurity. Methods such as cold spray [28, 29], Aerosol deposition [30], and Aerodynamically Focused Nanoparticle (AFN) [16, 31] have been used for dry particle deposition. Methods such as cold spray and aerosol deposition, on the other hand, are used primarily for microparticles and do not take into account the focusing of particles on the substrate, while other approaches, such as AFN, rely on off-line particle synthesis.

In our previous work [8, 32], we used a dry Aerosol Direct Writing (dADW) technique to selectively generate patterns of NPs on substrates. In our method, particles are generated in-line using a spark ablation process [33]. They are subsequently transported using an inert gas (Ar) to a vacuum chamber for deposition immediately after formation as primary particles and agglomerates of primary particles. Spark ablation can produce extremely small primary particles with a size distribution in the 20 nm range and smaller [34, 35]. The focused deposition of these nanoparticles, *i.e.*, those with an aerodynamic diameter of less than 100 nm, is challenging due to their low inertia and tendency to follow streamlines through which they leave the deposition chamber without being deposited. There are several strategies for focusing particles, including aerodynamic [16, 36–40], electrostatic [41], and electro/thermo-phoretic [42, 43] focusing. Given the working principle of dADW, and due to the charge neutrality of NPs, the electrostatic and electro/thermophoresis focusing methods are not optimal for particle focusing in dADW. On the other hand, because of the presence of carrier gas and the simple operating concept of aerodynamic focusing nozzles, this method surpasses others. Various aerodynamic focusing nozzles have been proposed as aerosol collimation strategies. The simplest aerody-

namic focusing nozzle is converging nozzle (CN) (Figure 3.1.a), which has a single converging section, forcing the aerosol flow to be focused as well as accelerated. The CN requires a pressure difference: the upstream (P_u) and downstream pressure of the nozzle (P_d), and the ratio of these two pressures (P_u/P_d) defines the flow regime downstream of the nozzle, which is subsonic ($Ma < 1$), sonic ($Ma = 1$) or supersonic ($Ma > 1$). If the pressure ratio of P_u/P_d reaches a critical point equal to $\left(\gamma + 1/\gamma\right)^{\gamma/\gamma-1}$ (where γ stands for the heat capacity ratio, which is 1.66 for argon gas [44]), a so-called choked flow is achieved, and the flow velocity at the throat becomes sonic ($Ma = 1$). Until this point, increasing the pressure ratio (P_u/P_d) leads to an increase in the flow rate, but the flow rate reaches its maximum at the critical point and stays constant for higher pressure ratios. Further increase in the pressure ratio (P_u/P_d) causes a supersonic regime downstream of the nozzle, characterised by a robust expansion zone after the nozzle outlet causing the gas to gain higher velocities ($Ma > 1$). Placing an impaction plate in front of this expansion zone causes the formation of a bow shock, which is a stagnation plane close to the plate with a sudden difference in gas pressure and velocity. The expansion zone propels particles to achieve higher velocities and, as a result, a higher Stokes number; however, the stagnation plane and sharp deflection in the streamline in front of the impaction plate cause defocusing or even prevent deposition of smaller particles. The micro-capillary design is a variation on the simple converging nozzle. In this design, the Saffman force is significant and helpful in bringing particles of sufficient size 0.5-5 μm closer to the central axis [45].

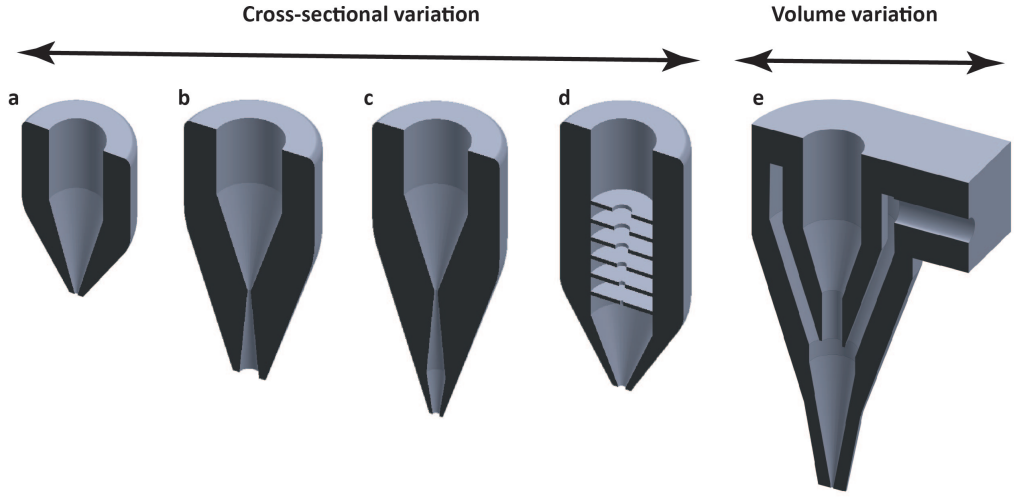

Figure 3.1: Aerodynamic focusing nozzles: a) converging nozzle, b) converging-diverging nozzle, c) converging-diverging-converging nozzle, d) aerodynamic lenses, and e) sheath-gas nozzle

Adding a diverging section after a converging nozzle leads to a Converging-Diverging Nozzle (CDN), also known as a De Laval nozzle (Figure 3.1.b). This design is used in a variety of applications, including thrusters and cold spray printing [8]. In the ideal design, which resembles an asymmetric hourglass shape, the flow enters the nozzle in the subsonic regime. The converging section causes choked flow at the throat (Ma=1), and as the flow expands after the

throat, supersonic velocities (Ma > 1) are attained. It is common to see this type of nozzle used in cold spray deposition, which is primarily effective for particles larger than 1 μm in size, and where collimation is less of a concern and the main purpose is to create a dense layer [28]. A further extension of the concept results in a Converging-Diverging-Converging Nozzle (CDCN), a two-throat system (Figure 3.1.c). This concept, which operates in a subsonic regime, has resulted in well-collimated aerosols with micron-size droplets [32] or particles.

Aerodynamic Lenses (AL) (Figure 3.1.d) have a single diameter tube with one or more abrupt restrictions, known as orifices, followed by a converging section in the outlet. Because of the particles' inertia, such restrictions cause the particles to concentrate in the central region, *i.e.* the flow's central axis. As a result, one or more ALs in a tube will cause the particles to exit the nozzle in a more confined region around the nozzle axis [8, 22, 46]. The flow regime in this method is generally laminar, and the level of particle focusing depends on particle size [46]. The design of the restrictions depends on the particle size, flow rate and upstream-pressure, which makes this focusing method very particle-size dependant [46, 47]. Sheath-gas nozzles (SGN) focus the particles in the central region of the flow by introduction a secondary gas flow (Figure 3.1.e) [22]. The second flow acts as a virtual tube and confines the main flow in the centric region; moreover, the sheath gas flow acts as a moving virtual wall, particularly after the nozzle throat, preventing defocusing of the main flow after the nozzle.

Based on the aerosol physics of a particle travelling through a gas medium (See Section 2.1) and the working principles of various aerodynamic focusing nozzles, sheath gas nozzles outperform the other aerodynamic nozzle systems. They are less sensitive to the size of particles in contrast to CDCN and AL, the confinement of the aerosol flow in the centric region of the nozzle leads to a more uniform and higher velocity for NPs, and the sheath-gas flow, acting as a moving wall surrounding the aerosol flow, reduces defocusing of the aerosol flow also after leaving the nozzle. Aerosol-jet printing (AJP) employs a similar approach for focusing droplets; however, SGN in AJPs operates at ambient pressure and in a subsonic flow regime, and droplets have sizes >1 μm [3, 22, 48]. The purpose of this chapter is to deepen the knowledge, evaluate and validate the performance of the sheath-gas nozzle (SGN) for the additive manufacturing of fine nanoparticles of below 100 nm and compare it to the conventional converging nozzle (CN) through numerical and empirical approaches. We identified the critical nozzle design parameters and the operating process parameters resulting in narrow lines for both types of nozzles, including half-angle of converging section, nozzle outlet radius, inner aerosol radius for SGN, downstream pressure, working distance and aerosol to total flow rate ratio for SGN. In order to support this analysis, we created finite element models in COMSOL Multiphysics [49] and related the design and process parameters to three figures of merit: the contraction factor, the focusing ratio, and the collection efficiency. Finally, we 3D printed two SGNs and three CNs and carried out experiments to evaluate the performance of each nozzle in terms of sharpness, resolution, and thickness. The morphology of lines in different parts of lines printed with both SGN and CN were investigated.

3.2 Materials and methods

3.2.1 Finite element modelling

We used COMSOL Multiphysics 5.5 to create finite element models that relate nozzle design and operating parameters to the deposition line width. This is accomplished in two steps. First, the

gas flow profile throughout the system is determined, which includes the inlet(s), nozzle, and impaction plate placed in a vacuum chamber. Secondly, particles are introduced into the inlet at discrete radial entrance positions, and particle trajectories are computed. The stationary Reynolds-averaged Navier–Stokes (RANS) equations are used to determine the flow field in combination with a k–ε model to describe the turbulence. Sutherland's law is used to determine the dynamic viscosity and gas conductivity (See Section A.1).

Because of the symmetry of the system around the axial line of the nozzle, an axisymmetric 2D simulation, as shown in Figure 3.2.a is used to reduce the computational cost of the simulation. A general design of a sheath gas and deposition systems system is depicted in Figure 3.2.a. The two up-stream boundaries are defined in COMSOL as an aerosol and sheath gas inlet with: a characteristic-based flow condition, a defined averaged gas flow velocity in the form of Mach number, a pressure (P_u) of 1 bar and a temperature of 293 K. The outlet pressure is defined as downstream pressure (P_d) with hybrid flow conditions. The boundary conditions that are applied to other walls are regarded as non-slip. The variable design parameters are the nozzle throat (exit diameter), the half-angle of the converging section, and the diameter of the aerosol nozzle when it meets the sheath gas. The variable process parameters are the working distance (distance between the nozzle throat and the impaction plate), the ratio of aerosol gas flow to total flow, and the downstream pressure. Table 3.1 summarises the parameter value ranges that were tested for both CNs and SGNs. As for the particles, a number of discrete diameter values of 5, 10, 20, 50, and 100 nm are tested. The trajectory of particles is calculated for gold with a density of 19300 kg/m^3. The boundary condition in the FE model for the axial symmetry line is pass-through, allowing particles to cross the boundary unrestrained. The model assumes that after a particle reaches the impaction plate, it 'freezes' and sticks to the surface at that position.

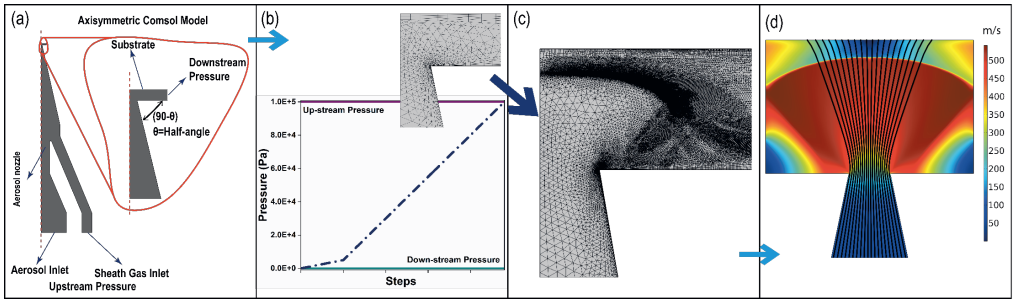

Figure 3.2: Steps of COMSOL simulation, a) axisymmetric geometry considering inlet of aerosol and sheath gas, and impaction plate, b) course mesh for initial rough flow calculation with stepwise increase of inlet pressure, c) accurate simulation of the flow using adaptive mesh refinement and d) calculation of particle trajectory using the accurate flow simulation results.

To overcome the convergence problem in the flow profile calculation caused by the high-pressure ratio between the upstream and downstream position in the nozzle, the calculation is run for a coarse mesh and with a stepwise increase of upstream pressure, as shown in Figure 3.2.b until it reaches 1 bar. The second step improves the modelling using this flow field as an initial value for the second calculation with two levels of adaptive mesh refinement. The adaptive mesh refinement takes the previous mesh and refines it in areas where it is needed,

such as around the bow shock, to achieve a highly accurate flow regime in that position (Figure 3.2.c).

These flow fields are then used to calculate particle trajectories by assuming a one-way interaction of particles in the flow, as the particle concentration is low and has no effect on the flow field (Figure 3.2.d). The particles enter the aerosol inlet at the same velocity as the flow and are distributed uniformly along the radius. The Stokes drag force is the primary force acting on a particle in this system (as explained in Section 2.1), with extra time steps for wall interactions and rarefaction effects for the Cunningham slip correction factor explained in the Section 2.1. The modelling results of the trajectory include the particle position on the impaction plate (if deposited), and the radial and axial velocity of a particle along its path is then used in MATLAB for data process and visualisation.

Table 3.1: Parameters and value ranges considered in the modelling

	Design parameters		Operating parameters	
Converging nozzle	Half-angle (θ°)	1, 2.5, 5, 10, 15, 30	Working distance (μm)	200, 300, 400, 600, 800, 1000, 1200
	Nozzle throat diameter (μm)	400, 600, 800	Downstream pressure P_d (Pa)	10, 100, 500, 1000, 2000, 5000
Sheath gas nozzle	Half-angle (θ°)	1, 2.5, 5, 10, 15, 30	Working distance (μm)	200, 300, 400, 600, 800, 1000, 1200
	Radius of aerosol nozzle (mm)	1, 1.5, 2, 3	Downstream pressure P_d (Pa)	10, 100, 500, 1000, 2000, 5000
			The ratio of aerosol flow rate to the total flow rate	2/8, 3/8, 4/8, 5/8, 6/8, 7/8

3.2.2 dADW and nozzle manufacturing

The experimental setup which is used for nozzle performance studies (Figure 2.4) is explained in Section 2.2. The electrodes are used in this study are made of a 99.99% pure gold. In this study, the SAM voltage and current are set to V = 1.1 kV and I = 8 mA, respectively, resulting in a stable particle generation process. Both converging and sheath gas nozzles are designed in SolidWorks Figure 3.3 and 3D printed using "3DM Tough" and a digital light projection Envisiontec Micro Plus Hires setup. After printing and chemical removing the unexposed regions via sonication for 5 minutes in an IPA bath, the nozzles were UV cured for 6 minutes to improve the mechanical properties. To ensure a leak-free connection of the nozzles to the aerosol stream, the aerosol inlet of the nozzles is printed with a smaller diameter and mechanically drilled to 10 mm diameter for precise fitting. The nozzle's sheath gas inlet is drilled to an M5 hole and threaded to connect to a stainless-steel joint and clean argon gas (Figure 3.3.b). Two nozzles with converging half-angles of 10 ° and actual outlet diameters of 484 and 248 μm are manufactured for the experimental investigation of the sheath gas nozzle. Three nozzles with manufactured outlet diameters of 166.5, 238.0, and 339.0 μm were used for the converging nozzle. Silicon substrates were used for deposition, which were first cleaned with acetone and isopropanol and then placed in an oxygen plasma chamber for 30 minutes before printing to remove any impurities from the substrate. The clean substrate is mounted on a holder perpendicular to the nozzle's central axis in the vacuum chamber. A SmarAct SLC-1750-O20-D-HV precision positioner controls the distance between the nozzle and the substrate. Using the in-plane SLC-1750-M-E-HV positioner, patterns were created by moving the stage relative to the nozzle. The nozzle's upstream pressure (Pu) is always set to 1 bar at room temperature, and the vacuum pressure (P_d) varies for each nozzle.

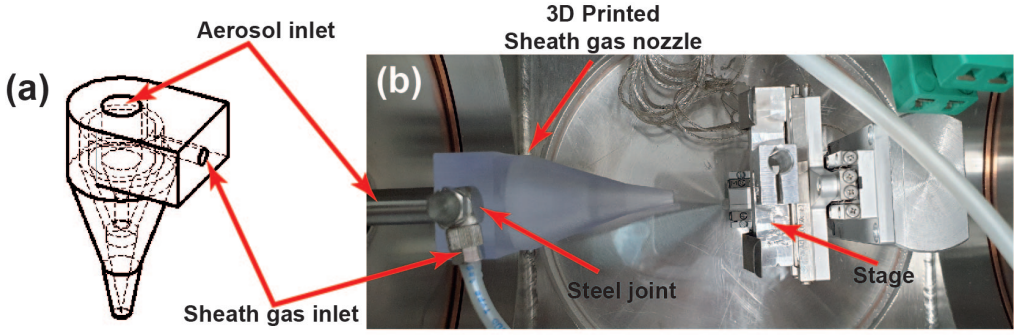

Figure 3.3: a) The sheath gas nozzle designed in SolidWorks, b) connection of the 3D printed nozzle with the aerosol and sheath gas inlets in the setup (Figure 2.4).

3.2.3 White-light interferometry

White-light interferometry with a Contour GT-K 3D optical profilometer (Bruker Corporation, Billerica, MA, USA) and integration of three measurements for each line were used to determine line width and thickness. The white-light interferometry data were post-processed in MATLAB to remove the background and calculate the thickness and width of the line at 640 cross-sections for the entire length of the line. Because of the Gaussian profile in the cross-section [19], the reported thickness is defined as the average thickness along the cross-section, as shown in the Figure A.1.

3.2.4 Morphology characterization

SEM measurements were carried out with a field-emission high-resolution Helios G4 setup detecting secondary electrons through-the-lens detector (TLD). Optical images were captured using a Keyence digital microscope (VHX-6000) with a magnification range of 20× to 2000×. The HDR (high dynamic range) function improved the resolution and contrast between substrate regions with and without deposited AuNPs by allowing the capture of multiple images at varying shutter speeds. The boundary of the line was chosen as the region where there was a clear difference in the contrast.

3.3 Results and discussion

3.3.1 Numerical results

The simulation results for both converging and sheath gas nozzles are presented in this section. To express the performance of the deposition processes, we use three main figures of merit: the contraction factor (CF), the focusing ratio (FR), and the collection efficiency (CE). The contraction factor (CF) indicates particle collimation within the nozzle system and is defined based on the particle's radial position relative to the local nozzle radius at the entrance and exit of the nozzle, respectively:

$$CF = \frac{R_{i-Inltet}/Radius_{Inlet}}{R_{i-Throat}/Radius_{Throat}} \tag{3.1}$$

$R_{i-Inlet}$ and $R_{i-Throat}$ are the radial position of the i-th particle in the inlet and nozzle throat, respectively, while $Radius_{Inlet}$ and $Radius_{Throat}$ are inlet radius and nozzle throat radius, respectively. A CF>1 indicates that particles are effectively pushed towards the central axis, beyond the effect expected from a decrease in nozzle diameter. The focusing ratio (FR) is defined as the line width (or deposition spot size diameter) divided by the nozzle throat diameter. FR<1 indicates that the deposit's lateral width or spot radius is smaller than the nozzle throat diameter, and FR>1 means a divergence in the deposition width. The collection efficiency (CE) indicates how many particles have been deposited on the substrate. This is calculated by dividing the number of particles that ended up on the substrate by the total number of particles introduced into the flow. A higher CE with lower FR indicates better performance of the nozzle.

3.3.1.1 Flow simulation

In the first set of results, the flow field after the nozzle and in front of the impaction plate is discussed, and a comparison is made between the accuracy of different meshes in the calculation of the flow profile when using adaptive mesh refinement. The flow field, including the axial flow velocity, the radial flow velocity, the pressure gradient in the nozzle throat and in the area between nozzle throat and impaction plate, is shown in Figure 3.4 for an outlet pressure (P_d) of 100 Pa and pressure ratio P_u/P_d=1000. An imaginary plane, known as a Mach-disk or bow-shock, is formed when high-pressure ratio flows impinge on impaction plates necessitates mesh refinement [50–52]. A coarse mesh was used in the first set of results, and the Mach-disk is not visible. Refining the mesh in the area around the Mach disc results in a clear presentation of the disc, with a very sharp change in axial velocity, radial velocity and pressure. The effect of this plane is more evident for the axial velocity and the pressure; the axial velocity decreases from ~450 to ~100 m/s, and the pressure increases from ~150 to ~600 mbar. This abrupt change in velocity and pressure affect the relaxation time and the Stokes number, particularly for smaller particles, lowering their deposition probability. As a result, there are two regions after the nozzle: the first starts at the nozzle throat and continues until the Mach-disk, which is an expansion zone that causes particles to accelerate to higher velocities; the second one starts at the Mach-disk and continues until the impaction plate, which is a stagnation zone that causes particles to decelerate.

3.3.1.2 Converging nozzle (CN)

We first review the simulation results for the converging nozzle (CN). Table A.1 summarises the modelled configurations and the value range for each design and operational parameter. The contraction factor (CF) for the CN is ≈ 1 for each modelled situation, *i.e.*, the focusing of particles in the nozzle is due to the decrease in radius only, which is understandable given the considered dominant force (Stokes drag force only). The operational parameters (working distance and downstream pressure) have hardly any effect on the CF; as for the design parameters, the half-angle of the converging section has a more noticeable effect than the nozzle throat diameter but is still negligible. Details of the effects of design and operating parameters on the CF are discussed in the Section A.3.1.1, Figure A.2-A.4.

The effects of design and operating parameters on the focusing ratio (FR) and collection efficiency (CE) of gold nanoparticles for the converging nozzle are shown in Figure 3.5. The CE for all parameters (Figure 3.5. b, d, f and h) shows that nanoparticles of 5 nm are either not deposited or partially deposited depending on the design and operational parameters; particles of all other sizes are deposited.

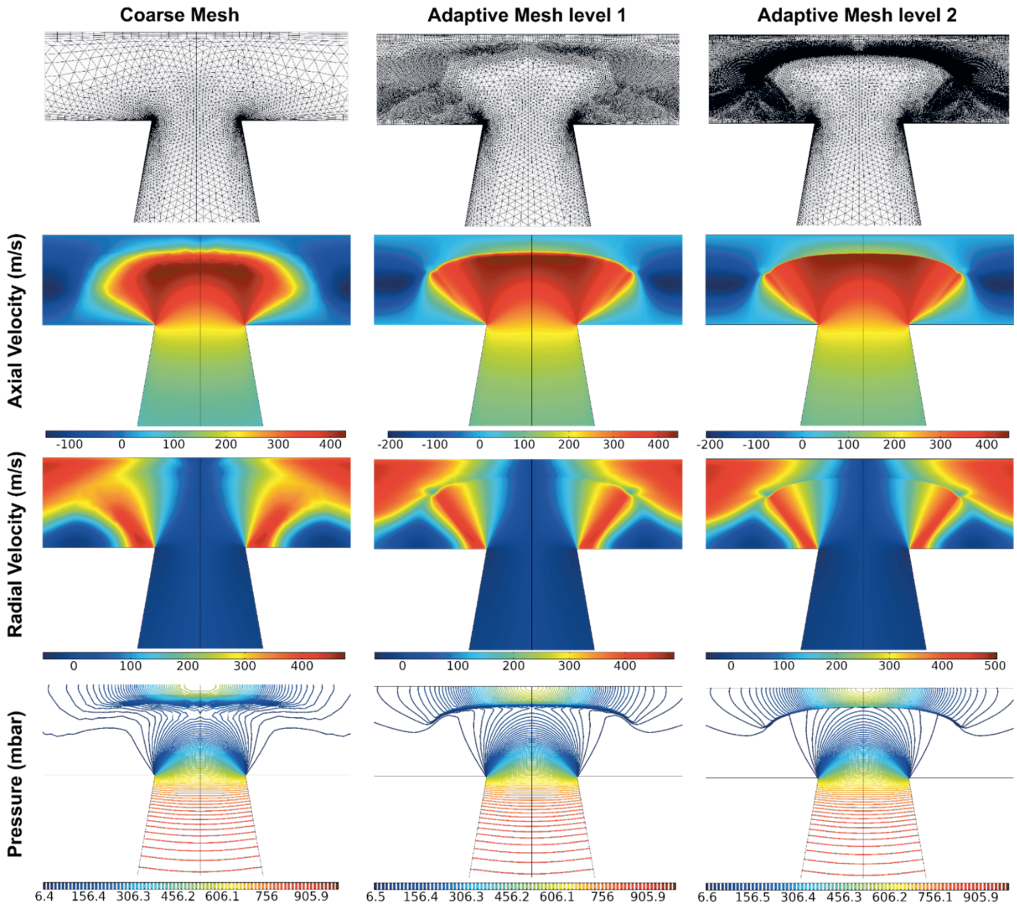

Figure 3.4: Effect of meshing on the final result of axial flow velocity, radial velocity, and pressure for coarse, first-level, and second-level mesh refinement. The outlet pressure is set to 100 Pa, the nozzle diameter is 400 µm, and the working distance is 400 µm.

Figure 3.5. a, c, e, and g show that FR is highly dependent on particle size, with larger particles having a lower FR than smaller ones, implying that higher inertia leads to better particle focusing on the substrate. As the inertia of the particles increases, the Stokes number of the particles increases as well, resulting in the particles' trajectory from the nozzle to the impaction plate being preserved. Increasing the nozzle half-angle results in a smaller value for FR, and the best FR is achieved with larger particles (Figure 3.5.a). For the smallest particles considered (5 nm diameter), the simulation suggests a threshold value for the half-angle to have 100% CE (Figure 3.5.b). For the nozzle throat diameter, there is again a threshold value that determines the deposition for the smallest particles (Figure 3.5.c), and the effect on FR depends on the particle size (Figure 3.5.d), implying that the deposition width is determined by the nozzle throat diameter and has a constant relationship. The downstream pressure has little effect on FR within the chosen value range (Figure 3.5.e) and particularly affects the CE for the smallest particles

(Figure 3.5.f). Increasing the downstream pressure affects the relaxation number of particles through the gas mean free path and the Cunningham slip correction factor equations 2.4 and 2.5), which mainly affects smaller-sized particles (5 nm). Also, an increase in downstream pressure results in a weaker expansion zone with lower flow velocity, and hence particle velocity, after the nozzle exit, see also Figure A.5. e. When the axial and radial velocity of particles hitting the substrate are considered (Figure A.5), it is clear that smaller particles hit the substrate with a relatively low axial velocity and a high radial velocity, reducing perhaps their deposition probability in reality. The effect of the nozzle to substrate distance (working distance, WD) on both

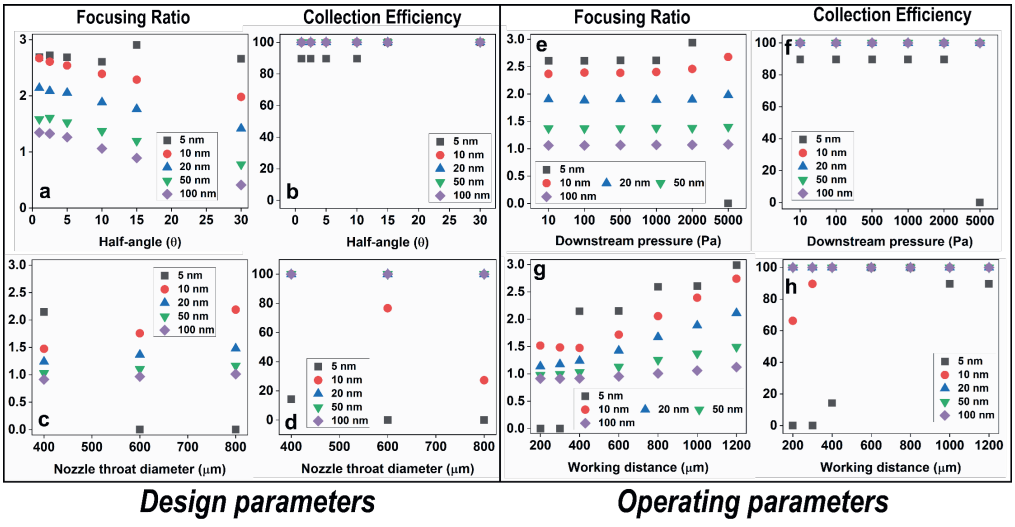

Figure 3.5: The focusing ratio and collection efficiency for gold nanoparticles of different sizes in the presence of a CN, varying a, b) the half-angle of the converging nozzle, c, d) the nozzle throat diameter, e, f) the downstream pressure, and g, h) the working distance.

CE and FR is more complex; see Figure 3.5.g and 3.5.h. There is a threshold value for the WD to guarantee particle deposition, in line with impactor theories (Figure 3.5.h) [53]. For larger particle sizes, the FR stays constant with increasing WD, but for smaller particles, FR increases with increasing WD (Figure 3.5. g). This can be understood by analysing the flow field after the nozzle exit (Figure A.6). For small WD (WD/D=0.5, WD =200 μm), the gas cannot fully expand, causing the gas energy to primarily lead to high radial flow velocity rather than axial velocity, which leads to rejection of particle deposition, particularly for <10 nm particles. Figure A.5. g shows that for low WD, 10 nm nanoparticles impinge on the substrate at such low velocity that their chance of deposition is perhaps negligible. Increasing the WD above 300 μm leads to complete gas expansion, and a further increase of WD leads to a larger high-velocity zone before the bow-shock. This increased expansion zone allows particles to accelerate to high velocities and, as a result, high Stokes numbers, enabling them to overcome the deceleration in the stagnation zone so that even very small particles will deposit on the substrate, but on broader regions.

3.3.1.3 Sheath gas nozzle (SGN)

Table A.2 contains the configuration and specific geometrical and operational details for each study and the range of each parameter to investigate SGN nozzles. Two additional parameters are investigated for this nozzle system: the aerosol nozzle radius and the aerosol flow rate to total flow rate ratio. The computational results for the sheath gas nozzle are depicted and discussed in Section A.3.1.2, considering the effect of design and operating parameters on the CF (Figure A.7). Unlike the converging nozzle, the CF reaches values above 1, demonstrating the effectiveness of this nozzle in forcing particles towards the centric regions beyond what can be expected from the geometrical convergence. The results show that design parameters of convergence half-angle and inlet nozzle radius or process parameters of downstream pressure and working distance do not affect CF. The most significant insight from Figure A.7 is the effect of aerosol to total flow rate ratio on CF, which shows that the CF is roughly equal to the square root of total flow rate to aerosol flow rate ratio ($\sqrt{\dot{Q}_{Total}/\dot{Q}_{Aerosol}}$).

Figure 3.6 depicts the effects of design and operation parameters on the FR and CE of (gold) nanoparticles. The inner nozzle radius has a minor effect on the FR and CE (Figure 3.6. a and b) and the particles' axial and radial velocities during deposition (Figure A.11. a and b). Increasing the half-angle of the converging section reduces the width of the deposition spot and leads to better focusing (Figure 3.6.c) but has no effect on the axial and radial velocities of nanoparticles during deposition (Figure A.11. c and d). It is also clear that the collection efficiency is independent of the half-angle (Figure 3.6.d) and is primarily determined by the inertia of the nanoparticles; thus, low inertia particles have a low deposition probability (5 nm nanoparticles). The FR and the CE are independent of downstream pressure in the chosen range (Figure 3.6. e and f); moreover, this parameter has a negligible effect on the axial and radial velocity of the particles during deposition (Figure A.11. e and f). The distance of the nozzle to the substrate (WD) has a significant impact on the FR of nanoparticles (Figure 3.6.g). Increasing the WD improves the probability of smaller nanoparticles to be collected (Figure 3.6.h) and increases their axial velocity without affecting their radial velocity (Figure A.11. g and h). The ratio of aerosol flow to total flow is the most critical parameter affecting the focusing ratio—the confinement of aerosol flow by sheath gas results in a decrease in nanoparticle deposition width. The further reduction of aerosol flow causes FR<1 (Figures 3.6.i), especially for smaller inertia nanoparticles, which was impossible to achieve with a converging nozzle. Figures 3.6.j indicates that the flow rate ratio does not affect the CE of particles of different sizes.

In conclusion, sheath gas nozzles are preferable to converging nozzles for the effective trapping of small particles due to: 1) the ability to achieve a narrower line width with a larger nozzle diameter, which is advantageous for both nozzle manufacturing and printed line resolution; 2) better performance in trapping of smaller size nanoparticles; 3) a lower sensitivity to downstream pressure, which allows the system to operate with a less demanding vacuum environment; and 4) a lower sensitivity to design parameters. Higher sheath gas flow rates in an SGN result in better CF for all particle diameter ranges and better FR, resulting in smaller line width. The nozzle throat diameter is the second most important parameter, as the final deposition feature resolution for both converging and sheath gas nozzles depends on the outer diameter of the nozzle. In order to examine the effect of material density on CF, FR, and CE, the same study was repeated for copper NPs and results are presented in section A.3.2.1 and A.3.2.2 in Figures A.12 – A.19. These results show that the density of particles has only a minimal effect on CF for both converging and sheath gas nozzles, but it has a significant effect on both CE and

FR. Lower material density results in lower inertia, which has the same effect as smaller size in terms of the overall effect. The model confirms that the line width will be higher, and CE will be lower for lower density nanoparticles compared to similar-sized particles with higher densities.

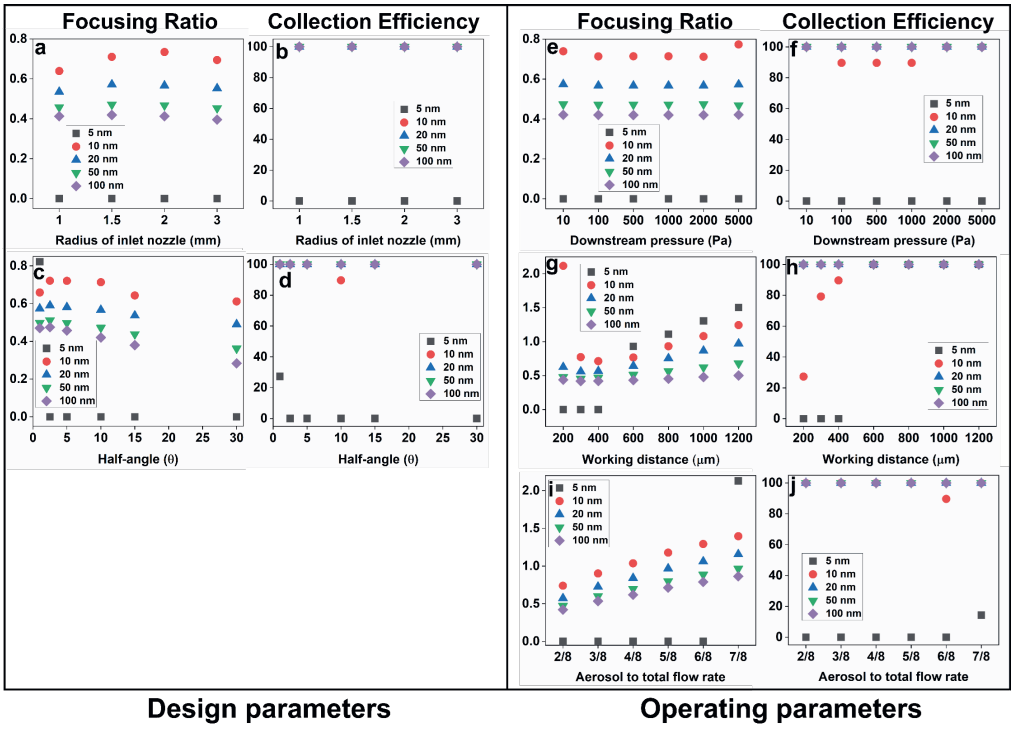

Figure 3.6: Focusing ratio and collection efficiency for gold nanoparticles of different sizes for SGN a, b) for Aerosol throat diameter, c, d) for the half-angle of the converging section, e, f) for downstream pressure, g, h) for the distance between nozzle and the impaction plate (working distance), and i, j) for the ratio of aerosol flow rate to the total flow rate.

3.3.2 Experimental results

This section presents the experimental results for both converging and sheath gas nozzles. We first assess each nozzle's performance in terms of line morphology and dimensions, and then we investigate the effect of operating parameters such as working distance and aerosol flow to total flow rate ratio on the width and thickness of the line printed with each nozzle. Moreover, we investigate the overspray problem in the line, which is caused by the deposition of particles on a broader region with lower density, which decreases the line's resolution and sharpness.

3.3.2.1 Characterization of the line printed with converging nozzle

Figure 3.7.a-f depicts SEM images of a line of gold nanoparticles (AuNPs) deposited on a silicon substrate with a converging nozzle (throat diameter of 339 μm) and the typical morphology and density of the AuNPs. Figure 3.7.b,c show the morphology of the line in the centric region,

which is characterised by the presence of high porosity randomly formed 3D microstructures with nanometric features. A closer examination of the microstructures in Figure 3.7.d reveals that they are 3D porous structures formed by a nanometric network of AuNPs. When moving towards the line's outer region, first, we observe a region of lower density of particles, followed by a splash area with random and low-density deposition of nanoparticles and agglomerates of nanoparticles. Figure 3.7.e shows that larger particles are deposited closer to the centre of the line (left side of the image), while further away from the line, smaller particles are deposited, which is consistent with simulation results showing that particles of smaller size deposit over a broader region.

Figure 3.7.g shows an optical microscopy image of three regions of the deposited line: 1- the centric region, which features a clear texture and colour and contains dense packing of nanoparticles; 2- the boundary region, which has a different texture but high surface coverage and less dense packing, and 3- the splash zone, which has sparse deposition, and characterised by a low density of particles spread within a broader region, which decreases the resolution. As shown in the image, the width of the centric region is 283 μm, and the width of the line, including the boundary region, is 394 μm. Line width measurements from the optical microscope and white light interferometry (WLI) are in good agreement (see Figure 3.7.h. The splash zone is not evident in the WLI data but is visible in the SEM and optical images (Figure 3.7.g,i). This is due to lower coverage in this zone, and the thickness is in the order of noise of the WLI measurement. The greyscale intensity graph for the SEM image of the line in Figure 3.7.i was created by integrating the entire image, so the splash zone has a low intensity. When the greyscale data is compared to the WLI results, it is clear that the width estimated using the WLI findings considers the line's boundary but not the splash area.

Figure A.20. a1-d1 illustrates SEM images of the border between the boundary and splash zones of a line printed by a nozzle with a diameter of 339.0 μm and four WDs of L/D equal to 1.18, 1.33, 1.62, and 2.95. The border is clearly visible for larger WDs (Figure A.20. b1-d1) due to differences in the contrast of the two zones caused by differences in either surface coverage or thickness of the deposited layer, and slightly visible for L/D=1.18 due to a decrease in surface coverage (Figure A.20. a1). Furthermore, the images in Figure A.20.a1-d1 reveal that for lower WDs (1.18 and 1.33) in both the boundary and splash zones, the smaller particles are not deposited because there is a clear contrast between the deposited AuNPs and the black background as the substrate. However, increasing the WD (1.62 and 2.95) results in the deposition of finer nanoparticles, resulting in the formation of a grey background in Figure A.20. c1 and d1. Higher magnification SEM images of Figure A.20. a2-d2 in the splash zone clearly show the presence of finer AuNPs for higher WDs. The same trends were observed in numerical results in Figure 3.5.h, indicating that increasing the distance between the substrate and the nozzle increases the probability of depositing finer nanoparticles. The splash zone far from the line's edge shown in Figure A.20. a3-d3, indicating that increasing the WD causes a higher likeliness of trapping finer nanoparticles, in line with modelling results.

3.3.2.2 Characterization of the line printed with sheath gas nozzle

Figure 3.8 shows high-magnification SEM images of lines printed with an SGN. The AuNPs were deposited on a silicon substrate employing a sheath gas nozzle with an outlet diameter of 248 μm, an aerosol to the total flow rate of 0.31, and a working distance of 250 μm. In Figures 3.8.a–c, high magnification SEM images of typical morphology and density of AuNPs in the centric

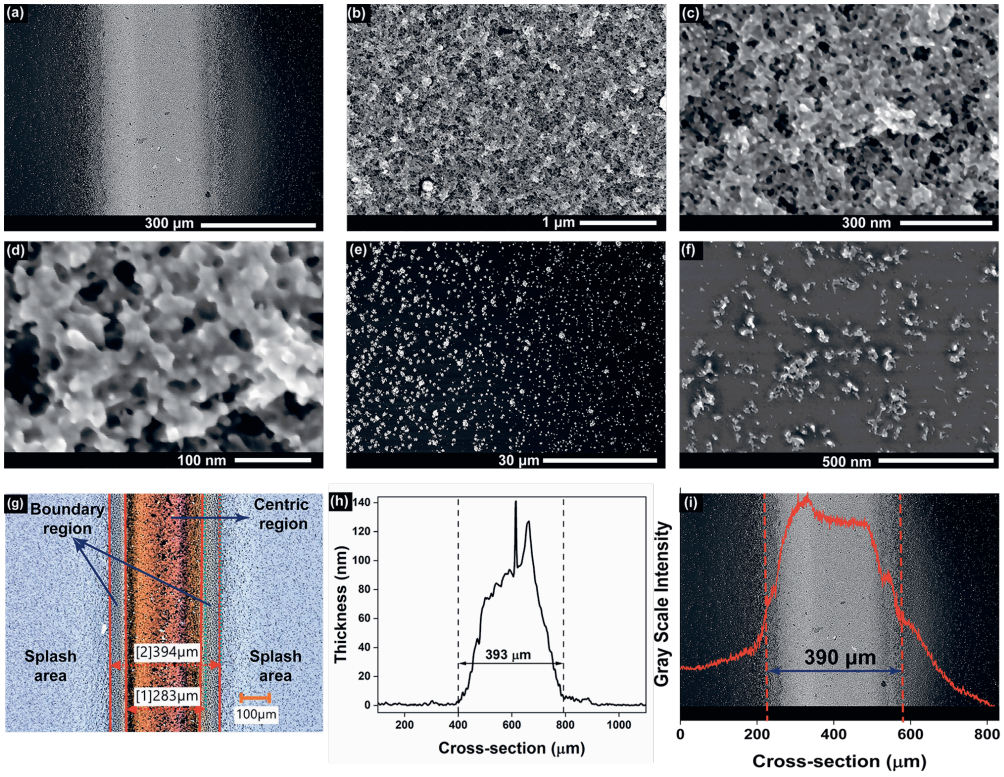

Figure 3.7: a) SEM image of a line printed with a CN of 339 µm and WD of 450 µm, b-d) high magnification images of the morphology of the printed line in the centric region, e) SEM image of the boundary and splash area, f) HR-SEM of particles deposited in the splash area, g) optical microscopy image of the line, h) profile of the line measured with white light interferometry, i) SEM image of the line and greyscale intensity diagram of the line.

region are shown. The morphology of the lines printed with the SGN is comparable to lines written with the CN.

However, it becomes apparent when comparing the SGN printed lines in Figures 3.8.d-f with the CN printed lines in Figures 3.7.a and Figure A.20. a1-d1 that the main effect of the SGN is on the line's boundary and splash zone. By comparing the SGN lines' boundary in Figure 3.8.g-i with the CN lines in Figure A.20. a1-d1, the splash area is barely visible, and the lines have a distinct edge. When the splash area in Figures 3.8.j-l is examined in greater detail, only a very small splash area appears to exist next to the edge of the line, indicating that the particles barely deposit in this area. The splash zone in the SEM images of the CN printed lines (Figure A.20. a1-d1) has a length of more than 40 µm after the boundary region and extends to a larger area, whereas the splash zone in the SGN printed lines has a length of only a few micrometres after the boundary region. This demonstrates that utilising SGN improves the sharpness of the printed line, which is significantly essential when printing lines with a small spacing between them.

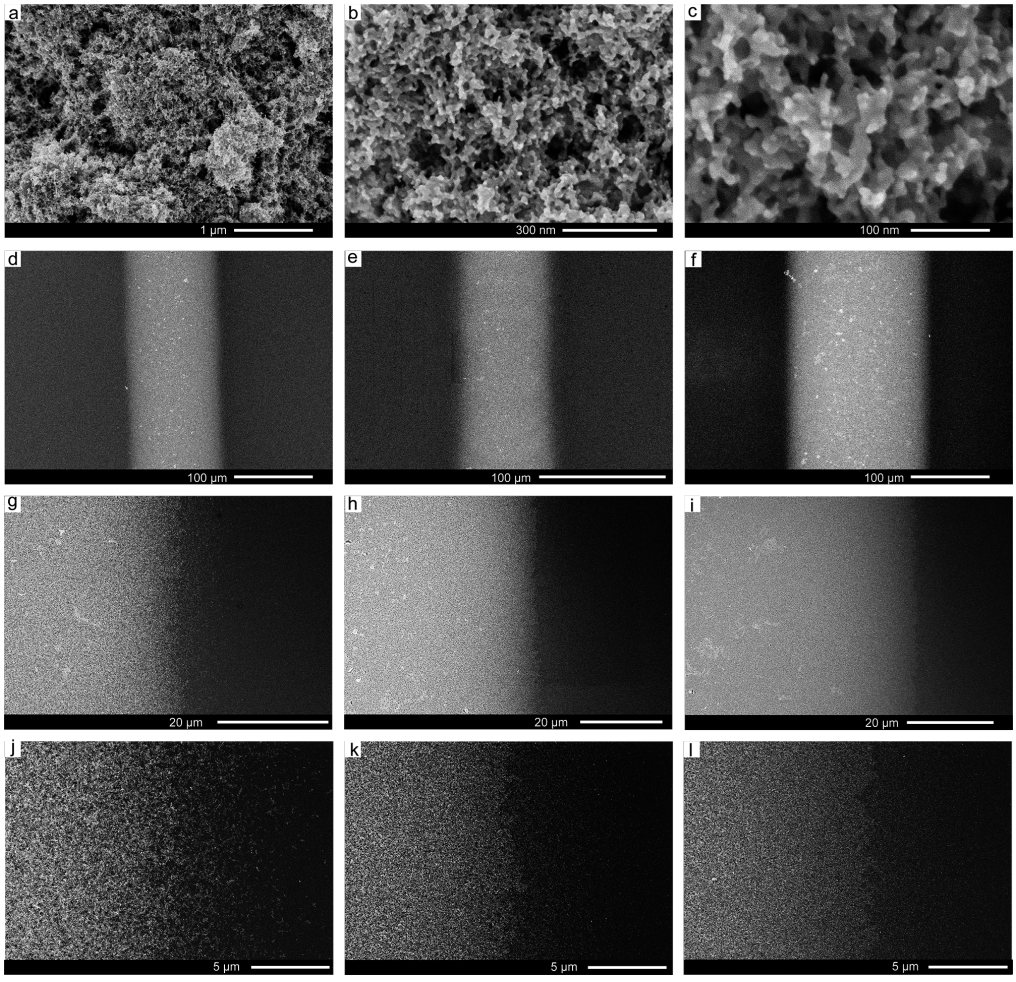

Figure 3.8: a-c) high magnification SEM images of the morphology of the centric region of the printed line with an SGN of 248 µm outlet diameter and aerosol to total flow rate (a/T) = 0.31 and WD = 250 µm. The lines and boundaries of the line printed with 248 µm SGN nozzle and process parameters of d) a/T = 0.17 and WD = 700 µm, and boundary and splash area in g) and j), e) a/T = 0.1 and WD = 400 µm, and boundary and splash area in h) and k), f) a/T = 0.31 and WD = 400 µm, and boundary and splash area in i) and l).

3.3.2.3 Effect of working distance on the CN printed line dimensions

Figure 3.9. a,b shows how the working distance (WD) affects the thickness and width of the lines printed with three converging nozzles with diameters of 166.5, 238.0, and 339.0 µm respectively and a stage speed of 0.44 m/s. By increasing the WD, the thickness of the lines decreases while the width of the lines increases. This is in agreement with the modelling results (Figure 3.5 and Figure A.6). The variation in width increases as the WD increases, as shown in Figure 3.9.b; however, these variations are not visible in the optical microscopy images, as shown in Figure

A.21. Nonetheless, as the WD increases, the thickness decreases and its amplitude approaches that of noise in the white light interferometry results. As a result, the edge in the boundary is not a defined region, as it appears as a hue in Figure A.21.

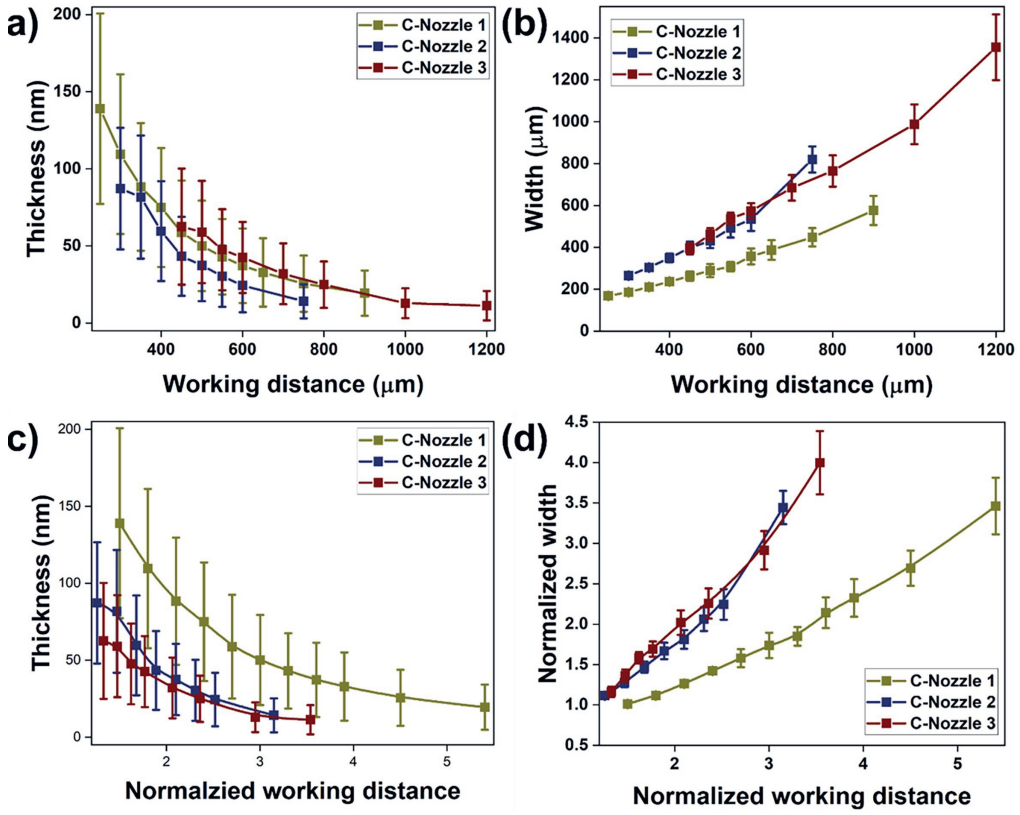

Figure 3.9: Effect of working distance on a) thickness and b) width of the AuNPs line printed with three converging nozzles of C-Nozzle 1-3 with a diameter of 166.5, 238 and 339 μm. c) Thickness and d) normalised width to normalised working distance with corresponding nozzle diameter. The stage speed is set to 0.44 mm/s.

Figure 3.9.c depicts the thickness as it relates to the normalised working distance to the corresponding nozzle diameters (WD/D). As shown in the graph, for the same WD/D, the thickest line is deposited by the smallest nozzle, and this may be due to variations in the concentration of nanoparticles in the carrier gas. The power of the SAM set up (current=8mA and voltage=1.1kV) is constant for all measurements; thus, the amount of material atomised and ablated from the electrodes is constant; however, the argon gas flow rate varies for different nozzles due to stagnation upstream of the nozzle and changes with respect to the nozzle diameters. For nozzles with diameters of 166.5, 238.0, and 339.0 μm, the flow rate of argon is 0.59, 0.99, and 1.39 lpm, respectively. As a result, lower flow rates result in higher particle concentration and number deposited in the narrower region, resulting in higher thicknesses for smaller diameter nozzles.

When comparing the normalised width and normalised working distance to the corresponding nozzle diameters in Figure 3.9, it is possible to see that the smallest nozzle has a lower normalised width, but the other two nozzles follow the same trends. One explanation for a narrower line using a smaller nozzle is that the smallest nozzle has a higher degree of agglomeration. The nucleation and growth of primary nanoparticles in the SAM particle generator are symmetrical at an early stage after atomisation and formation of the elemental cloud, which is caused by the high energy of the atoms and results in the formation of spherical polydispersed primary nanoparticles with size distributions less than 20 nm [34, 35]. Following this stage and energy reduction by both the nucleation-growth mechanisms and the reduction of temperature in the gas flow, the growth mechanism shifts to the agglomeration mechanism. In this mechanism, particles begin to form arbitrary shapes as a result of impaction with one another. In addition, as previously stated, the concentration of nanoparticles is higher due to the lower flow rate of argon, which primarily increases the probability of particle interaction and, consequently, the likelihood of agglomeration.

Furthermore, a lower flow rate results in a lower average flow velocity in the connection tube and a long time for particles to travel from the generation site to the deposition chamber compared to higher flow rates. As a result, even with a constant agglomeration rate for all nozzles, longer transportation times result in a different agglomeration size distribution. The minimum width of the lines obtained for a converging nozzle is 168 μm and generated using the nozzle with the smallest diameter (166.5 μm), with an FR of approximately 1. Considering the numerical results, it is expected that this FR occurred for larger particles distribution of 50 to 100 nm.

3.3.2.4 Effect of flow ratio and working distance on the SGN printed line dimensions

The aerosol to total flow ratio results for two sheath gas nozzles with exit diameters of 248 and 484 μm, respectively, are summarised in Figure 3.10. Using the WLI technique, we measured the width and thickness of lines for 648 cross-sections and three different working distances. The stage speed for deposition of AuNPs with a 248 μm nozzle is 0.11 mm/s, and 0.22 mm/s with a 484 μm nozzle. The dADW flow rate is a function of the nozzle diameter, which influences the concentration of nanoparticles in the stream and, most likely, the particle size distribution due to agglomeration during transportation, as previously stated. Although the outlet diameter of each sheath gas nozzle remains constant throughout the experiment, the aerosol flow rate will change due to changes in the aerosol to total flow ratio, resulting in changes in nanoparticle concentration. A waste channel between the spark discharge generator and the nozzle is employed to maintain a constant nanoparticle concentration. As a result, the total flow rate is 0.42 lpm for a 248 μm nozzle and 1.7 lpm for a 484 μm nozzle. However, it should be noted that the particle generator's power is fixed; as a result, the particle concentration differs between the two nozzle experiments.

As shown in Figures 3.10.a-d, the average thickness and width of the deposited line increase with decreasing sheath gas for all working distances. On the other hand, the relationship between the width and thickness and the flow rate ratio is unique for each nozzle, rather than following any general pattern. This could be due to a difference in nanoparticle concentration between the nozzles, with a smaller diameter nozzle having a higher concentration and, therefore, larger particles sizes due to agglomeration. Figure 10 shows that lines up to ~300 and ~600

μm in width were printed using nozzles of 248 and 484 μm in diameter and an aerosol to flow rate of 0.5. With a low aerosol to total flow ratio of 0.17, lines can be produced as narrow as 67 μm. This means that by using an SGN, it is possible to deposit AuNPs in lines with widths equal to approximately 27% of the nozzle throat diameter and at a distance equal to 1.2 times the nozzle throat diameter. Further, the width and thickness of the line are strongly related to the working distance (WD) as they all increase simultaneously due to higher collection efficiency at higher WDs. As shown in Figure 3.10, a width of 170 μm, as the narrowest line achieved with a CN, was deposited using a 248 μm SGN and at working distances of 400 and 500 μm while similar line width was printed with a CN of 166.5 μm diameter and a working distance of 200 μm.

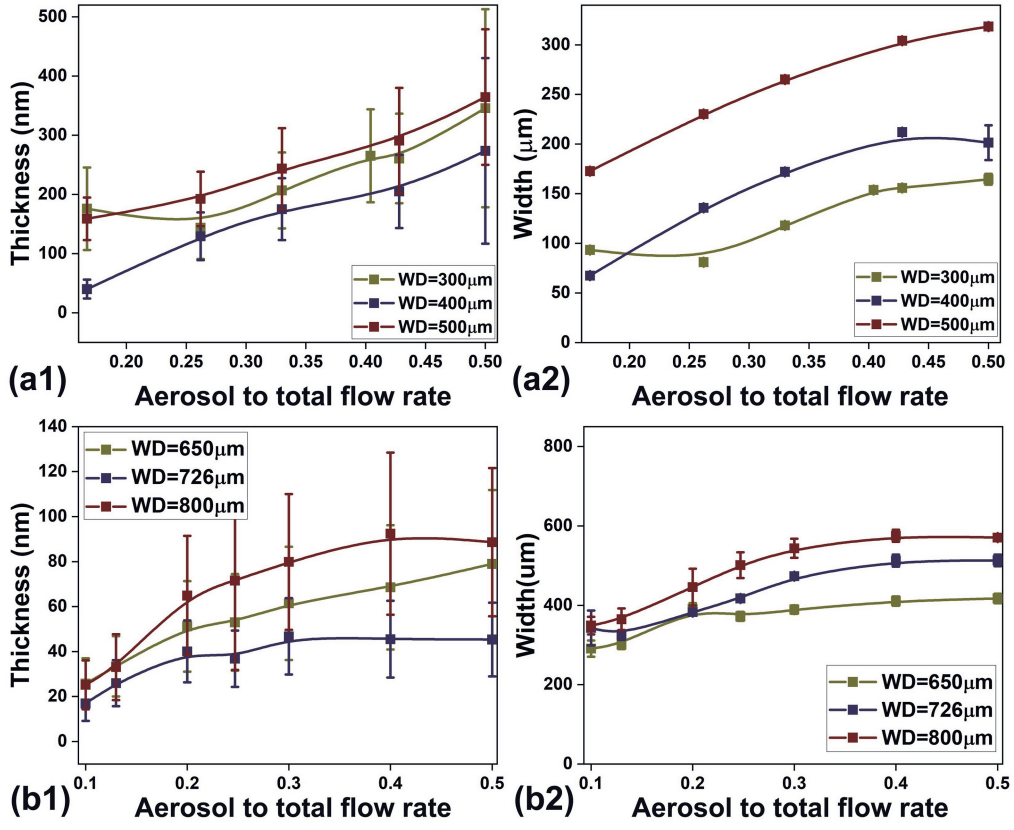

Figure 3.10: Effect of aerosol to total flow rate ratio on a, c) thickness, b, d) width for lines printed with nozzles of a, b) 248 μm and c, d) 484 μm diameter.

3.4 Sheath gas nozzle (SGN) modular design [1]

The results of this chapter demonstrated that SGNs are efficient in terms of resolution and line sharpness. Furthermore, it demonstrated that the resolution of the line is affected by the nozzle's outlet diameter and the aerosol-to-total-flow ratio. As a result, two strategies can be used to reduce the width of the printed line: 1- Reduce the aerosol to total flow ratio, i.e. increase the sheath flow; 2- Reduce the outlet diameter. The first has a limited range, which means that with a fixed nozzle diameter, the minimum resolution is a percentage of the nozzle diameter; for example, with a nozzle diameter of 248 μm and an aerosol to a total flow rate ratio of 0.16, the width of 61 μm is equal to 27% of the nozzle diameter achieved. To achieve a lower line width, effectively <50 μm, a SGN with a smaller nozzle diameter is required.

The nozzles used in this study were all manufactured using 3D printing, which has a finite resolution, especially when printing long channels. As a result, manufacturing a SGN nozzle with a diameter < 100 μm is challenging and can be accomplished using a high-resolution 3D printing technique like the 2-photon polymerization (2PP) method or using commercial nozzles like dispensing tips. 2PP is able to manufacture channels as small as 1 μm, but the overall size of the SGN cannot be printed due to 2PP limitations, necessitating the printing of a larger structure with another 3D printer that requires a lower resolution. However, using two methods for printing different parts of SGN requires material matching in each printing to ensure sealed and leakage-free printing, which necessitates a thorough investigation.

To avoid the complexities of multiple 3D printing, we used commercial dispensing tips tips of various diameters for the high-resolution section (converging section with nozzle outlet), and 3D printing for the other parts. As shown in Figure 3.11. a and cross-sectional view of assembled nozzle in Figure 3.11. b, this nozzle has a modular design and comprises four 3D printed sections, two O-rings for sealing. The main body (1) (Figure 3.11.a) has a primary inlet of 10 mm for aerosol flow and a 6 mm inlet for sheath gas. The second component, the aerosol converging nozzle (3), is used to collimate aerosol flow from a 10 mm inlet to a 2 mm outlet. The third component, the Luer-lock connection (4), is the essential part of the design. Firstly because the aerosol flow and sheath gas meet in this part and collimate in a converging nozzle to a 1 mm diameter outlet. Secondly, this part has the Luer-lock connection for the commercial dispensing nozzle. The final component is a cap (6), which connects to the main body. Two O-rings are used to prevent aerosol or sheath gas leakage, one in the main body (1) and one in the luer-lock connection (4). The commercial dispensing tip with a luer-lock connection connects to the (4), and enable this modular nozzle to collimate the aerosol flow in various diameters.

Figures 3.11.c and d show the same modular SGN with two different dispensing nozzles, 434 μm and 227 μm in inner diameter. Figure 3.11.e demonstrates the preliminary result of the modular SGN with dispensing nozzle of 78 μm inner diameter. The width of the line deposited with the 78 μm nozzle and an aerosol to total flow ratio of 0.18 is 21.3 μm, which is approximately 27% of the outlet diameter of the dispensing nozzle. Although this modular design is in the first stage and requires extensive testing with various dispensing nozzle sizes and aerosol to total flow ratios, the ease of changing the dispensing nozzle and printing with a wide range of widths, 20-1000 μm, make it a practical design for dADW.

[1] The content of this section is unpublished.

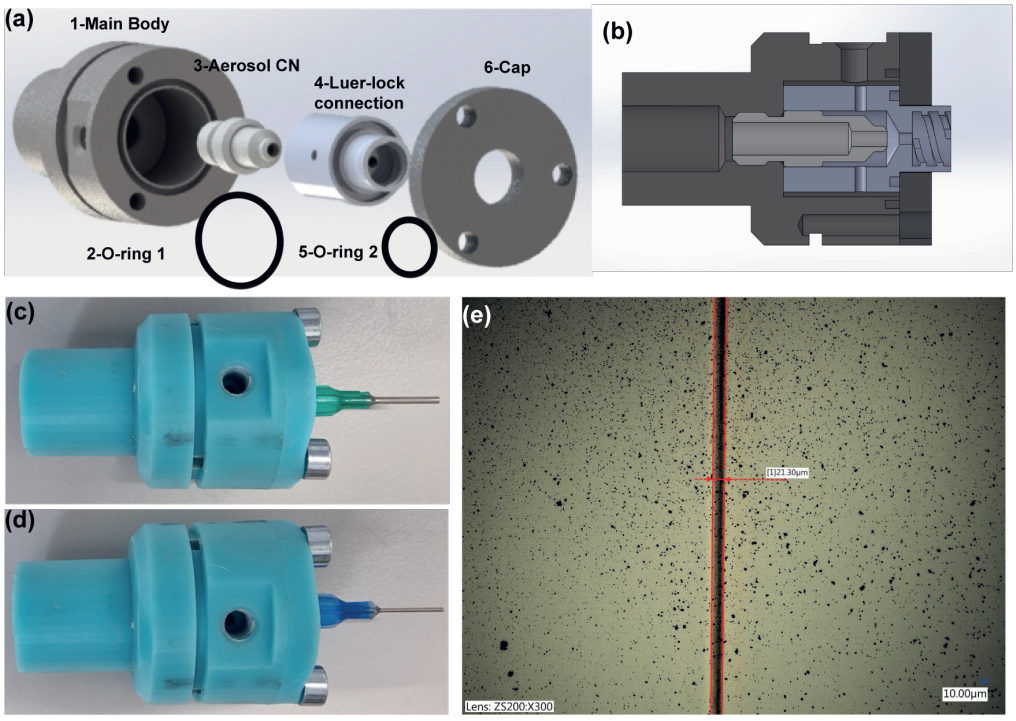

Figure 3.11: a) Schematic view of components of modular SGN, b) modular SGN with syringe of 434 µm diameter, c) modular SGN with syringe of 227 µm diameter, d) width of the line printed with modular SGN with 78 µm diameter and a/T=0.18 (the substrate contains contaminations).

3.5 Conclusions

In this study, we evaluate the performance of dry aerosol direct-writing (dADW) as a simple and solvent-free method for additive manufacturing high-resolution micrometric patterns of <100 nm-sized nanoparticles through aerodynamic focusing. We investigate, via numerical and experimental approaches, the effect of design and operating parameters on the resulting resolution of sub-100 nm gold nanoparticles lines deposited via a converging nozzle (CN) and sheath gas nozzle (SGN). We assessed three main parameters: the contraction factor (CF), the focusing ratio (FR), and the collection efficiency (CE) to analyse the numerical data. As a result, we discovered that, firstly, CNs are unable to deposit very fine nanoparticles (less than 10 nm) or are only partially capable of depositing in a very wide region. Secondly, they are unable to efficiently collimate the particles in the flow and achieve high CF; thirdly, the width of the line is related to both the nozzle diameter and the working distance (WD), and finally are sensitive to the design parameters. This means that when using a WD equal to the diameter of the nozzle, the narrowest line one can expect to print with a CN is in the order of the diameter size of the nozzle throat. Therefore, printing patterns with widths less than 100 µm would necessitates precise nozzle manufacturing and precise nozzle positioning with respect to the substrate. SGNs, on the other hand, firstly are extremely efficient in collimating a beam of particles and achiev-

ing high CF due to the presence of a secondary flow, which acts as a virtual tube surrounding the aerosol flow. Secondly, they show very low sensitivity to design parameters for CF and FR, resulting in simplifying the nozzle's design and manufacturing. Thirdly, SGN enables particle deposition in a region smaller than the diameter of the nozzle throat when using a WD equal to the diameter of the nozzle. The combination of low sensitivity to design parameters and the ability to achieve a narrower line while using larger nozzle sizes and greater WDs simplify the design and manufacturing of SGNs.

Although modelling was carried out in order to understand the effect of parameters that we were able to control in the dADW machine or manufacturing of the nozzle, there are a number of variables that were not taken into consideration in the numerical study, which resulted in a difference between the simulation and experimental results. A freeze boundary condition is assumed for the impaction plate in our models, which may differ from reality. In this assumption, particles are considered deposited as soon as they come into contact with the substrate at any impaction velocity, with no consideration given to bouncing of particles from the surface or detachment of particles from the substrate as a result of low interaction between particles and the substrate. Therefore, the particle collection efficiency estimated in simulation is expected to be higher than in experiments. Furthermore, as particles hit the substrate with a lower axial velocity in the outer region of the line, it is reasonable to expect that the line width will be larger in the numerical results. In our modelling, another simplifying assumption is related to the neglection of surface roughness and surface energy and their possible effect on the deposition width and the collection efficiency, which may need to be considered in future studies.

Another source of discrepancy between simulation and experimental data is the assumption of spherical particles in the simulations. While this assumption holds true for primary nanoparticles because their growth is symmetrical, it does not hold true for agglomerated particles, which are formed by the aggregation of several primary nanoparticles resulting in arbitrary shapes and sizes. It is important to note that, as previously stated in the text, the size distribution of particles in the aerosol flow varies for different nozzles due to agglomeration, the effect of variation in the concentration of nanoparticles, and longer transportation time. Finally, manufacturing the nozzle using a stereolithography 3D printer produces a final part composed of layers of 25 μm thickness that are adhered to one another and generate an interior micrometric roughness, which is not considered in the simulation, which may affect the results.

According to the experimental results, lines printed with both CNs and SGNs have a Gaussian cross-section with a varying thickness from 10s of nanometres to 100s of nanometres depending on process parameters such as stage velocity and contain randomly formed 3D microstructures with high porosity and nanometric features. The splash area, defined as an outer area with sparse deposition of finer nanoparticles, is the main difference between CN and SGN lines, and its presence reduces the achievable resolution of the line, moreover, reduce the sharpness of the line. CNs have a very large splash area that extends to the width of the line, reducing the CN's performance in both resolutions and collecting NPs in desired regions. The splash area in a line generated using SGNs, on the other hand, is limited to a few micrometres after the boundary, which increases the sharpness of the line. Notably, the experimental results confirm that increasing WD increases line width, as shown in both SGN and CN modelling.

Furthermore, we test the effect of the aerosol to total flow ratio on the width of the SGN-printed line. The results show that decreasing the aerosol flow rate reduces the width of the line and concentrates the nanoparticles in a region smaller than the nozzle's diameter. The

smallest line printed with CNs has a minimum size equal to the nozzle size. Alternatively, the same line width was printed using an SGN with a greater outlet diameter and greater WDs. The narrowest line generated by a single part 3D print SGN was 67 μm, with a nozzle diameter of 248 μm and a WD of 400 μm, *i.e.*, width is about 27% of the nozzle diameter. This demonstrates that dADW can print high-resolution patterns of nanoparticles with width ranging from 67 μm to 600 μm and thickness ranging from 20 nm up to 400 nm. Due to the solvent-free, room temperature and atmospheric pressure, and in-line particle generation, dADW can be utilised to fabricate nanostructured patterns for optical sensors, gas sensors, and interconnects. Moreover, this method enables the generation and deposition of various metal NPs in the form of patterns on a variety of substrates such as paper, silicon and polymer [8, 32].

References

[1] S. Xu, W. Tang, D. B. Chase, D. L. Sparks, and J. F. Rabolt, "A highly sensitive, selective, and reproducible sers sensor for detection of trace metalloids in the environment," *ACS Applied Nano Materials*, vol. 1, pp. 1257–1264, 3 2018.

[2] Y. Y. Cai, J. G. Liu, L. J. Tauzin, D. Huang, E. Sung, H. Zhang, A. Joplin, W. S. Chang, P. Nordlander, and S. Link, "Photoluminescence of gold nanorods: Purcell effect enhanced emission from hot carriers," *ACS Nano*, vol. 12, pp. 976–985, 2018.

[3] Y. Chen, J. Dong, W. Gao, J. Qi, X. Yan, and X. Kong, "Enhanced fluorescence effect from complex nanostructure decorated with the native oxide layer," *Journal of Optics (India)*, vol. 47, pp. 283–287, 2018.

[4] N. Kim, M. R. Thomas, M. S. Bergholt, I. J. Pence, H. Seong, P. Charchar, N. Todorova, A. Nagelkerke, A. Belessiotis-Richards, D. J. Payne, A. Gelmi, I. Yarovsky, and M. M. Stevens, "Surface enhanced raman scattering artificial nose for high dimensionality fingerprinting," *NanoScience and Technology*.

[5] J. Xu, Z. Lian, B. Wei, Y. Li, O. Bondarchuk, N. Zhang, Z. Yu, A. Araujo, I. Amorim, Z. Wang, B. Li, and L. Liu, "Strong electronic coupling between ultrafine iridium–ruthenium nanoclusters and conductive, acid-stable tellurium nanoparticle support for efficient and durable oxygen evolution in acidic and neutral media," *ACS Catalysis*, vol. 10, pp. 3571–3579, 3 2020.

[6] Y. Kotolevich, O. Martynyuk, J. C. Ramos, J. E. Ortega, R. Vélez, V. M. Rojas, A. A. Tapia, S. Martinez-Gonzalez, H. J. Vazquez, M. Farías, R. Zanella, A. Pestryakov, N. Bogdanchikova, and V. C. Corberán, "Nanostructured silica-supported gold: Effect of nanoparticle size distribution and electronic state on its catalytic properties in oxidation reactions," *Catalysis Today*, vol. 366, pp. 77–86, 4 2021.

[7] R. Kumar, A. Kumar, N. Verma, V. Khopkar, R. Philip, and B. Sahoo, "Ni nanoparticles coated with nitrogen-doped carbon for optical limiting applications," *ACS Applied Nano Materials*, vol. 3, pp. 8618–8631, 9 2020.

[8] S. Aghajani, A. Accardo, and M. Tichem, "Aerosol direct writing and thermal tuning of copper nanoparticle patterns as surface-enhanced raman scattering sensors," *ACS Applied Nano Materials*, vol. 3, pp. 5665–5675, 6 2020.

[9] Y.-C. Kao, X. Han, Y. H. Lee, H. K. Lee, G. C. Phan-Quang, C. L. Lay, H. Y. F. Sim, V. J. X. Phua, L. S. Ng, C. W. Ku, T. C. Tan, I. Y. Phang, N. S. Tan, and X. Y. Ling, "Multiplex surface-enhanced raman scattering identification and quantification of urine metabolites in patient samples within 30 min," *ACS Nano*, vol. 14, pp. 2542–2552, 2 2020.

[10] M. Haghgoo, R. Ansari, and M. K. Hassanzadeh-Aghdam, "The effect of nanoparticle conglomeration on the overall conductivity of nanocomposites," *International Journal of Engineering Science*, vol. 157, p. 103392, 12 2020.

[11] W. Cui, W. Lu, Y. Zhang, G. Lin, T. Wei, and L. Jiang, "Gold nanoparticle ink suitable for electric-conductive pattern fabrication using in ink-jet printing technology," *Colloids and Surfaces A: Physicochemical and Engineering Aspects*, vol. 358, pp. 35–41, 4 2010.

[12] J. Li, L. Liu, D. Zhang, D. Yang, J. Guo, and J. Wei, "Fabrication of polyaniline/silver nanoparticles/multi-walled carbon nanotubes composites for flexible microelectronic circuits," *Synthetic Metals*, vol. 192, pp. 15–22, 6 2014.

[13] D. Lau and S. Furman, "Fabrication of nanoparticle micro-arrays patterned using direct write laser photoreduction," *Applied Surface Science*, vol. 255, pp. 2159–2161, 12 2008.

[14] M.-H. Chien, M. M. Shawrav, K. Hingerl, P. Taus, M. Schinnerl, H. D. Wanzenboeck, and S. Schmid, "Analysis of carbon content in direct-write plasmonic au structures by nanomechanical scanning absorption microscopy," *Journal of Applied Physics*, vol. 129, p. 063105, 2 2021.

[15] M. R. Lee, H. K. Lee, Y. Yang, C. S. L. Koh, C. L. Lay, Y. H. Lee, I. Y. Phang, and X. Y. Ling, "Direct metal writing and precise positioning of gold nanoparticles within microfluidic channels for sers sensing of gaseous analytes," *ACS Applied Materials and Interfaces*, vol. 9, pp. 39584–39593, 11 2017.

[16] G. Y. Lee, M. S. Kim, H. S. Yoon, J. Yang, J. B. Ihn, and S. H. Ahn, "Direct printing of strain sensors via nanoparticle printer for the applications to composite structural health monitoring," *Procedia CIRP*, vol. 66, pp. 238–242, 1 2017.

[17] G.-Y. Lee, M.-S. Kim, S.-H. Min, H.-S. Kim, H.-J. Kim, R. Keller, J.-B. Ihn, and S.-H. Ahn, "Highly sensitive solvent-free silver nanoparticle strain sensors with tunable sensitivity created using an aerodynamically focused nanoparticle printer," *ACS Applied Materials & Interfaces*, vol. 11, pp. 26421–26432, 7 2019.

[18] C. Novara, F. Petracca, A. Virga, P. Rivolo, S. Ferrero, A. Chiolerio, F. Geobaldo, S. Porro, and F. Giorgis, "Sers active silver nanoparticles synthesized by inkjet printing on mesoporous silicon," *Nanoscale Research Letters*, vol. 9, pp. 1–7, 2014.

[19] J. G. Korvink, P. J. Smith, and D. Y. Shin, *Inkjet-based micromanufacturing*. 2012.

[20] Z. P. Yin, Y. A. Huang, N. B. Bu, X. M. Wang, and Y. L. Xiong, "Inkjet printing for flexible electronics: Materials, processes and equipments," 2010.

[21] D. Deng, Y. Jin, Y. Cheng, T. Qi, and F. Xiao, "Copper nanoparticles: Aqueous phase synthesis and conductive films fabrication at low sintering temperature," *ACS Applied Materials and Interfaces*, vol. 5, pp. 3839–3846, 2013.

[22] A. Mahajan, C. D. Frisbie, L. F. Francis, C. D. Frisbie, L. F. Francis, C. D. Frisbie, and L. F. Francis, "Optimization of aerosol jet printing for high-resolution, high-aspect ratio silver lines," *ACS Applied Materials and Interfaces*, vol. 5, pp. 4856–4864, 2013.

[23] E. B. Secor, "Principles of aerosol jet printing," *Flexible and Printed Electronics*, vol. 3, p. 035002, 9 2018.

[24] R. Salary, J. P. Lombardi, M. S. Tootooni, R. Donovan, P. K. Rao, P. Borgesen, and M. D. Poliks, "Computational fluid dynamics modeling and online monitoring of aerosol jet printing process," *Journal of Manufacturing Science and Engineering, Transactions of the ASME*, vol. 139, 2017.

[25] D. Hines, Y. Gu, A. Martin, P. Li, J. Fleischer, A. Clough-Paez, G. Stackhouse, A. Dasgupta, and S. Das, "Considerations of aerosol-jet printing for the fabrication of printed hybrid electronic circuits," *Additive Manufacturing*, vol. 47, p. 102325, 11 2021.

[26] G. Chen, Y. Gu, H. Tsang, D. R. Hines, and S. Das, "The effect of droplet sizes on overspray in aerosol-jet printing," *Advanced Engineering Materials*, vol. 20, 8 2018.

[27] A. Kamyshny and S. Magdassi, "Inkjet ink formulations," *Inkjet-based Micromanufacturing*, pp. 173–189, 2012.

[28] S. V. Klinkov, V. F. Kosarev, and M. Rein, "Cold spray deposition: Significance of particle impact phenomena," *Aerospace Science and Technology*, vol. 9, pp. 582–591, 10 2005.

[29] S. Bagherifard, A. H. Astaraee, M. Locati, A. Nawaz, S. Monti, J. Kondás, R. Singh, and M. Guagliano, "Design and analysis of additive manufactured bimodal structures obtained by cold spray deposition," *Additive Manufacturing*, vol. 33, p. 101131, 5 2020.

[30] J. Akedo, "Room temperature impact consolidation (rtic) of fine ceramic powder by aerosol deposition method and applications to microdevices," *Journal of Thermal Spray Technology 2008 17:2*, vol. 17, pp. 181–198, 3 2008.

[31] G.-Y. Lee, J.-I. Park, C.-S. Kim, H.-S. Yoon, J. Yang, S.-H. Ahn, and W. E. Boeing, "Aerodynamically focused nanoparticle (afn) printing: Novel direct printing technique of solvent-free and inorganic nanoparticles," *ACS Appl. Mater. Interfaces*, vol. 6, p. 13, 2014.

[32] S. Aghajani, A. Accardo, and M. Tichem, "Tunable photoluminescence and sers behaviour of additively manufactured au nanoparticle patterns," *RSC Advances*, vol. 11, pp. 16849–16859, 2021.

[33] N. S. Tabrizi, M. Ullmann, V. A. Vons, U. Lafont, and A. Schmidt-Ott, "Generation of nanoparticles by spark discharge," *Journal of Nanoparticle Research*, vol. 11, pp. 315–332, 2 2009.

[34] N. S. Tabrizi, Q. Xu, N. M. van der Pers, U. Lafont, and A. Schmidt-Ott, "Synthesis of mixed metallic nanoparticles by spark discharge," *Journal of Nanoparticle Research*, vol. 11, pp. 1209–1218, 7 2009.

[35] N. S. Tabrizi, Q. Xu, N. M. van der Pers, and A. Schmidt-Ott, "Generation of mixed metallic nanoparticles from immiscible metals by spark discharge," *Journal of Nanoparticle Research*, vol. 12, pp. 247–259, 1 2010.

[36] D. L. Schulz, J. M. Hoey, D. Thompson, O. F. Swenson, S. Han, J. Lovaasen, X. Dai, C. Braun, K. Keller, and I. S. Akhatov, "Collimated aerosol beam deposition: Sub 5-μm resolution of printed actives and passives," 2008.

[37] D. L. Roberts and J. P. Mitchell, "The effect of nonideal cascade impactor stage collection efficiency curves on the interpretation of the size of inhaler-generated aerosols," *AAPS PharmSciTech*, 2013.

[38] F. D. Fonzo, A. Gidwani, M. H. Fan, D. Neumann, D. I. Iordanoglou, J. V. Heberlein, P. H. McMurry, S. L. Girshick, N. Tymiak, W. W. Gerberich, and N. P. Rao, "Focused nanoparticle-beam deposition of patterned microstructures," *Applied Physics Letters*, 2000.

[39] I. S. Akhatov, J. M. Hoey, O. F. Swenson, and D. L. Schulz, "Aerosol focusing in micro-capillaries: Theory and experiment," *Journal of Aerosol Science*, vol. 39, pp. 691–709, 2008.

[40] X. Wang, F. E. Kruis, and P. H. McMurry, "Aerodynamic focusing of nanoparticles: I. guidelines for designing aerodynamic lenses for nanoparticles," *Aerosol Science and Technology*, vol. 39, pp. 611–623, 7 2005.

[41] R. Streubel, M. B. Wilms, C. Doñate-Buendía, A. Weisheit, S. Barcikowski, J. H. Schleifenbaum, and B. Gökce, "Depositing laser-generated nanoparticles on powders for additive manufacturing of oxide dispersed strengthened alloy parts via laser metal deposition," *Japanese Journal of Applied Physics*, vol. 57, p. 040310, 3 2018.

[42] S. Opiolka, F. Schmidt, and H. Fissan, "Combined effects of electrophoresis and thermophoresis on particle deposition onto flat surfaces," *Journal of Aerosol Science*, vol. 25, pp. 665–671, 6 1994.

[43] E. Tabesh, H. R. Salimijazi, M. Kharaziha, M. Mahmoudi, and M. Hejazi, "Development of an in-situ chitosan-copper nanoparticle coating by electrophoretic deposition," *Surface and Coatings Technology*, vol. 364, pp. 239–247, 4 2019.

[44] F. M. White, *Fluid Mechanichs, 7th Edition.* 2011.

[45] R. Mei, "An approximate expression for the shear lift force on a spherical particle at finite reynolds number," *International Journal of Multiphase Flow*, 1992.

[46] X. Wang, A. Gidwani, S. L. Girshick, and P. H. McMurry, "Aerodynamic focusing of nanoparticles: Ii. numerical simulation of particle motion through aerodynamic lenses," 2005.

[47] B. Wang, Y. Xiong, and A. N. Osiptsov, "Two-way coupling model for shock-induced laminar boundary-layer flows of a dusty gas," *Acta Mechanica Sinica/Lixue Xuebao*, vol. 21, pp. 557–563, 2005.

[48] J. Q. Feng, "Available online at www.jafmonline.net," *Journal of Applied Fluid Mechanics*, vol. 10, pp. 1735–3645, 2017.

[49] COMSOL, "Comsol multiphysics® v. 5.5. www.comsol.com. comsol ab, stockholm, sweden," 2018.

[50] Q. LI, Y. LYU, T. PAN, D. LI, H. LU, and Y. GONG, "Development of a coupled supersonic inlet-fan navier–stokes simulation method," *Chinese Journal of Aeronautics*, vol. 31, pp. 237–246, 2018.

[51] P. Biswas, C. Plagan, and C. Plagan, "High-velocity inertial impactors," *Environmental Science and Technology*, 1984.

[52] O. Abouali and G. Ahmadi, "A model for supersonic and hypersonic impactors for nanoparticles," *Journal of Nanoparticle Research*, vol. 7, pp. 75–88, 2 2005.

[53] W. C. Hinds, "Aerosol technology," *Journal of Chemical Information and Modeling*, vol. 53, pp. 1689–1699, 2019.

4

dADW and thermal tuning of Cu nanoparticle patterns as SERS sensors

Surface-Enhanced Raman Scattering (SERS) substrates are of great interest for detecting low-concentrated analytes. However, issues such as multi-step processing, cost, and possible presence of hazardous substances in the fabrication still represent a significant drawback. In this work, an innovative direct writing method is introduced for solvent-free and spatially-selective deposition of fine metal copper nanoparticles (CuNPs), with size distribution below 20 nm, generated in-line through a Spark Ablation Method (SAM). The deposited CuNPs' morphology and composition were characterized by scanning electron microscopy (SEM), atomic force microscopy (AFM), and energy-dispersive X-ray spectroscopy (EDS). The resulting CuNP patterns feature porous 3D micro-domains with nanometric structures serving as hot-spots for Raman signal enhancement. Low-temperature post-treatment (below 200 ℃) of the deposited CuNPs significantly evolves its morphology and leads to sintering of NPs into a semi-crystalline structure with sharp geometric features, which resulted in a more than tenfold increase of the enhancement factor (up to 2.1×10^5) compared to non-heat-treated samples. The proposed method allows creating SERS substrates constituted by sharp 3D metallic nanopatterns selectively deposited onto specific regions-, which paves the way for new printed, highly sensitive SERS-based sensors.

The contents of this chapter have been published in:

- Aghajani, S., Accardo, A., & Tichem, M. (2020). Aerosol Direct Writing and Thermal Tuning of Copper Nanoparticle Patterns as Surface-Enhanced Raman Scattering Sensors. ACS Applied Nano Materials, 3(6), 5665–5675. DOI:10.1021/acsanm.0c00887

4.1 Introduction

Surface-Enhanced Raman Scattering (SERS) spectroscopy is a rapid, label-free, and straightforward technique employed in many applications ranging from low concentration and even single-molecule detection [1, 2] to DNA studies [3], due to its ability to provide a variety of information on chemical and structural features of different species. SERS is widely used in many fields such as biology [4], material science [5], food analysis [6], and medicine [7] and is based on the amplification of the Raman signal by several orders of magnitudes taking place on metallic nanostructured surfaces and enabling ultrasensitive fingerprinting of molecules.

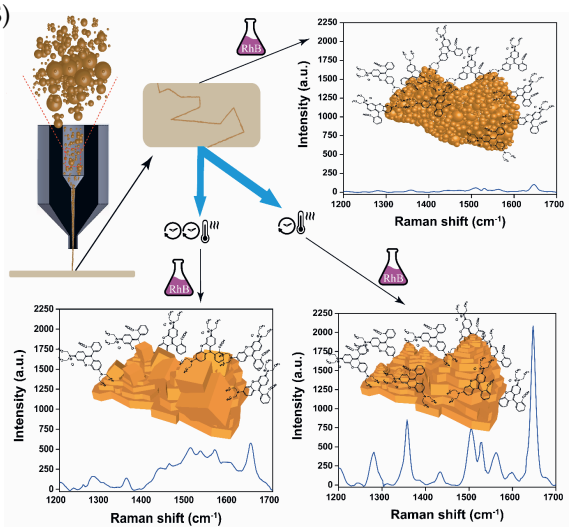

In the amplification of the Raman signal, two primary mechanisms must be taken into account: chemical enhancement and electromagnetic enhancement [8]. The chemical enhancement is highly molecule-specific [9] and is primarily related to charge transfer mechanisms between the molecule and the metal. The other enhancement mechanism, which has the highest impact on the total enhancement, is the electromagnetic (EM) one [10]. The EM enhancement of the Raman signal is due to Localized Surface Plasmon Resonance (LSPR) taking place at the surface of metal particles featuring nanometric roughness [5]. These excitations are due to collective oscillations of the electron cloud in the presence of incident light at the interface between a metal and a dielectric. Surface plasmons are localized because of their confinements within the surface of a nanoparticle (NP) or on edges and corners of a metallic nanostructure. The results of this confinement are 1) selective photon absorption depending on the size and shape of the nanostructure; 2) amplification of the EM field [11]. The regions of a surface with the ability to enhance the Raman signal are referred to as hot-spots [12].

Noble metals, such as silver [13, 14] and gold [15, 16], structured with feature sizes of few nanometers to hundreds of nanometers, and having LSPR in the visible regions of the spectrum, are widely employed as SERS-active substrates. Alternatively, copper, a less expensive material, is another metal employed in SERS-active substrates; it generally leads to lower Raman enhancement compared to substrates made of gold or silver. The low SERS effect of a Cu SERS substrate can be compensated by using a 3D structure instead of a 2D configuration to increase the number of hot-spots. The presence of a 3D structure also increases the number of adsorbed probe molecules around the hot-spots due to the higher surface area. Different strategies have been developed for manufacturing SERS-active substrates such as chemical reduction [17, 18], self-assembly [19, 20], screen printing [21] electrochemical deposition [22, 23], dealloying or decomposition [24], thermal decomposition [25], and nanosphere lithography (NSL) [26]. All these methods are characterized by either multi-step processes, high temperature, high level of vacuum, presence of hazardous chemicals, or expensive instruments. Furthermore, these meth-

ods create SERS-active regions all over the surface; however, for the integration of SERS into a sensor or a microfluidic device, it would be desirable to have SERS-active patterns in a specific location. To fabricate local SERS-active patterns, methods such as electron beam lithography (EBL) [27] and photolithography [28] can be employed to create nanopatterns in the desired location with high control over the shape, size, and spacing of hot-spots; however they are expensive, time-consuming and limited to typical semiconductor material systems. In this work, we report an innovative approach allowing selective direct writing of copper nanoparticle patterns via dry Aerosol Direct Writing (dADW), and heat treatment of the deposited film to tune and significantly improve the SERS signal enhancement.

In dADW, an in-line Spark Ablation Method (SAM) is used to generate metal or alloy NPs [29, 30], which are deposited in well-defined regions of the substrate using an aerodynamically focusing system. The deposited pattern is composed of 3D nanoparticles' microstructures featuring a height of hundreds of nanometers with high porosity and nanometric roughness. We also report how the tuning of process parameters, such as the deposition speed and nozzle to substrate distance, has a direct influence on the width of the pattern and the density of the nanoparticles. Furthermore, we show that the morphology of the deposited film is significantly affected by a low-temperature thermal post-treatment (below 200 ℃), converting the porous structure into multi-faceted micro-domains with sharp corners and edges. A low concentration analyte, Rhodamine (RhB), is used to study the tunability of the SERS signal enhancement in relation to the evolution of the CuNP film morphology. Compared to untreated samples, a SERS signal enhancement of more than one order of magnitude was achieved.

4.2 Materials and Methods

4.2.1 Sample preparation

The dADW setup (explained in Section 2.2) was used for the deposition of copper nanoparticles (CuNPs) for fabrication of SERS-active substrates using copper electrodes (99.99% purity). The focusing nozzle consists of a converging section with a 10 mm diameter inlet (D_i) and half angle of 45° (α) followed by a 20 mm converging capillary nozzle (L_c) with a 2 mm diameter inlet (D_c) and half angle of 2° (β) ending in a 400 μm diameter throat (D_N) representing the outlet of the focusing nozzle (Figure 3.1.c). The nozzle is designed in SOLIDWORKS and manufactured using an Envisiontech Micro plus high resolution stereolithographic 3D printer with 25 μm resolution, and post-processed by UV-curing for 3 minutes.

Concerning the fabrication of patterned active-SERS substrates, 1-inch sized silicon substrates, cleaned with acetone and isopropanol, are mounted on the stage in the vacuum chamber. For each nozzle-to-substrate distance, three samples were prepared by printing CuNP on a clean silicon substrate with a flux of 930 sccm, 1 Bar upstream pressure, vacuum pressure of 270±1% Pa, deposition writing speed of 50 μm s^{-1} and SAM voltage and current setting of V=1.2 kV, I=8 mA respectively. Concerning the thermal post-treatment, the silicon substrates with CuNPs patterns were placed in a Binder VD23 vacuum oven with a vacuum pressure of 0.01 mbar.

4.2.2 Morphology characterization

The morphology of the patterned area was characterized by scanning electron microscopy (SEM), atomic force microscopy (AFM) and optical microscopy (OM). The SEM measurements were per-

formed with the following SEM microscopes: Jeol JSM-6010LA, field-emission high-resolution Jeol JSM-6500F, and FEI NovaNano, all with a secondary electron detector. The elemental analysis of deposited patterns was performed through an energy-dispersive X-ray spectrometer integrated into the SEM Jeol JSM-6010LA setup at a magnification of 2500 and acceleration voltage of 15 kV. For each configuration of heat treatment (no heat-treatment, 1 hour @100 ℃, 1 hour @200 ℃, 2 hours @200 ℃), four EDS analyses were performed randomly in the centric regions and two in the boundary zones. The optical pictures were recorded with a Keyence digital Microscope VHX-6000 able to magnify from 20X to 2000X. The HDR (High Dynamic Range) function, allowing to capture multiple images at varying shutter speeds, improved the resolution and the contrast between substrate regions with and without deposited CuNPs. The boundary of the line was therefore chosen as the region where there was a clear difference in the contrast. For each distance between the nozzle and the substrate, the width of three lines printed on three silicon substrates was measured.

The AFM measurements were performed by a JPK Nanowizard 4 coupled to a Zeiss microscope in QI^{TM} mode. Silicon tips TESPA-HAR with the resonant frequency of 320 kHz, force constant of 42 N m^{-1}, a high aspect ratio of at least 5:1, and a curvature radius of 10 nm were used. The high aspect ratio of the tip enables the imaging of surfaces with high differences in height, reducing possible tip-sample convolution artifacts. Three scan areas of 3.0×3.0 (μm^2), 1.5×1.5 (μm^2) and 0.5×0.5 (μm^2) were used to study the morphology of the samples. All AFM measurements were performed in air at room temperature and were leveled with linear subtraction of background data for both horizontal and vertical lines by using GWYDDION 2.55 software.

4.2.3 SERS measurements

Concerning SERS studies, a Rhodamine B (RhB) solution with a concentration of 1.0×10^{-6} M was prepared out of RhB powder, purchased from Sigma Aldrich, and deionized water. To ensure a homogeneous distribution of the probe molecule on the nanostructured surface, an immersion method was used. The samples were immersed in the RhB solution for 12 hours to ensure sufficient molecule adsorption on the samples. After that, the samples were removed from the solution, washed thoroughly with deionized water to remove the excess of RhB and dried with a Nitrogen stream. Compared to droplet-on-substrate deposition protocols, our approach prevented "coffee-stain effects" that could lead to the accumulation of the probe-molecules at the edge of a drying droplet deposited on the substrate [31]. Concerning Raman spectroscopy measurements, a Horiba LabRAM HR setup, equipped with an Argon ion laser operating at 488 nm, 514 nm and 633 nm, a CCD camera, and a 50X (NA=0.5) objective was used. All SERS spectra were acquired with the laser operating at 514 nm at a power of 20 μW, with an acquisition time of 30 seconds and an average laser beam spot size of about 2 μm measured on bare silicon, unless mentioned otherwise. The spectra were collected over the range of 500 cm^{-1} to 1700 cm^{-1} with a spectral resolution of ~0.3 cm^{-1}. The spectral data were recorded using LabSpec6 software, and baseline correction was performed to remove the fluorescent background. To assess the level of reproducibility of SERS signal on the fabricated patterns, the Raman signal of RhB on CuNPs deposited patterns with and without heat-treatment was measured at 18 different locations within the patterns.

4.3 Results and discussion

4.3.1 Effect of process parameters on dADW printed lines

Figure 2.3.c shows the schematic of a designed focusing nozzle, which enables the experimental setup to deposit CuNPs selectively on the substrate. The focusing nozzle accelerates the carrier gas and propels the particles due to the pressure difference between the upstream (P_u) and downstream (P_d) of the nozzle. The ratio of the upstream to downstream pressure (vacuum pressure) of the nozzle defines the mode of flow at the outlet of the nozzle: subsonic, sonic, or hypersonic.

A pressure ratio (P_d/P_u) lower than 0.49 ($P_d/P_u=\left(2/\gamma+1\right)^{\gamma/\gamma-1}$, with γ= 1.66 for argon, [32]) causes a sonic flow mode. Further decrease in the pressure ratio leads to a strong expansion of the gas outside of the nozzle and enables the gas to reach higher velocities. When this expansion of gas impinges onto a plate, a stagnation plane is created in front of the plate by the so-called bow-shock. Across the bow shock, a sharp difference in pressure and velocity of gas appears with a zero velocity on the plate. The nanoparticles' velocity is affected significantly by any change in the flow because of their low inertia; therefore, they can reach higher velocity outside the nozzle in the expansion zone of the gas. This allows them to leave the streamline and deposit on the target substrate. The highest pressure ratio between upstream and downstream of the nozzle takes place when a stagnation point at atmospheric pressure (10^5 Pa) and clean room temperature (293 K) is reached, and the vacuum pump works at its highest power. In this configuration, the flow rate controller is set at 930 sccm, the vacuum pressure is equal to 270 Pa±2%, and the pressure ratio is $\left(377^{-1}\right) < P_d/P_u < \left(363^{-1}\right)$.

The other parameter affecting the expansion of the gas after the nozzle and further deposition of the NPs on the substrate is the distance between the nozzle and the substrate. A small distance causes a weaker gas expansion and lower gas and particle velocity. On the other hand, a high distance leads to a fully expanded gas and high particle velocity, but also a higher distance of bow shock to the substrate. This further increases the traveling path of particles to reach the substrate and, consequently, reduces the chance of deposition. Figure 4.1.a1-a8 shows the optical microscopy images of the variation in the width of the deposited line according to different distances between the nozzle and the substrate.

Figure 4.1.b shows that the width of the lines depends on two factors: the distance between the nozzle and the substrate and the diameter of the nozzle. Increasing the distance of the nozzle to the substrate from 200 μm ($0.5\times D_N$) to 1600 μm ($4.0\times D_N$) leads to an increase in the width of the line from 265 μm ± 2% (~$0.65\times D_N$) to 505 μm ± 2% (~$1.25\times D_N$). Increasing the width of the line also leads to a decreasing density of the particles and less uniform deposition; however, this can be compensated by increasing deposition time. The results show that, by controlling the distance of the nozzle to substrate and the time of deposition, it is possible to create patterns with various widths in the range of the diameter of the nozzle. In further studies, we will consider the fabrication of nozzles with smaller diameters. Although all the SERS experiments in this work were performed on Si surfaces, the direct writing methodology has also been validated on other kinds of substrates (Figure B.1).

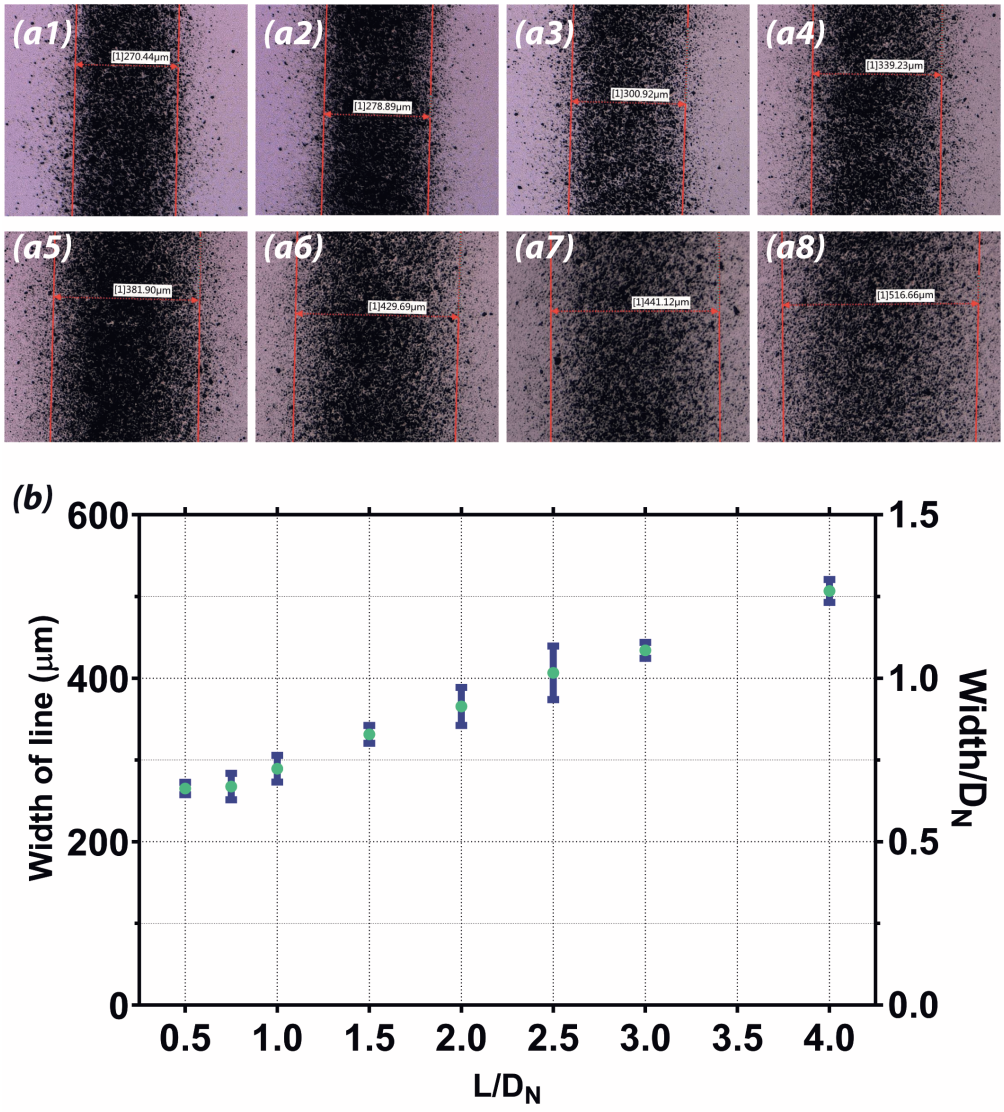

Figure 4.1: Optical microscopy of the variation of the width lines at a nozzle-to-substrate distance of a1) 200 µm, a2) 300 µm, a3) 400 µm, a4) 600 µm, a5) 800 µm, a6) 1000 µm, a7) 1200 µm, a8) 1600 µm. b) Relationship between the width of the deposited line and the ratio between the nozzle-to-substrate distance and the nozzle diameter (L/D_N). For each distance between the nozzle and the substrate, the width of 3 lines printed on three silicon substrates was measured by using HDR images. All lines were printed on silicon substrates with a flux of 930 sccm, 1 Bar upstream pressure, the vacuum pressure of 270±1% Pa, deposition writing speed =50 µm s^{-1}, nozzle throat of 400 µm, and SAM voltage/current setting of V=1.2 kV, I=8 mA.

4.3.2 Effect of Thermal treatment on the Morphology of printed lines

Figure B.2.a and Figure 4.2.a show a film of copper nanoparticles (CuNPs) deposited on a silicon substrate and the typical morphology of the film in low-magnification SEM images. The agglomerates of NPs with different shapes and sizes, together with primary NPs in various sizes, formed a dense layer on the substrate that contains valleys and hills in a three-dimensional (3D) configuration (Figure 4.2.b). A closer look at the structure of the film is provided in Figure B.2.d,e with a high-resolution SEM and by AFM images depicted in Figure 4.3.a,b. We observe that the 3D structure is composed of a random network of very fine NPs featuring a sponge-like morphology characterized by high porosity and surface area. Apart from NPs and agglomerates of NPs deposited on the substrate, Figure 4.2.a indicates the presence of microparticles with size ranging from hundreds of nanometers to few micrometers. Microparticles result from the solidification of larger units of molten metal occasionally ejected from the surface of the electrode into spherical particles[32], such as the microparticle shown in Figure B.2.f. The number of these microparticles in regions close to the center of the line (Figure B.2.a) is higher than in regions closer to the boundary of the line (Figure B.2.b) since microparticles have higher mass and consequently higher inertia compared to NPs.

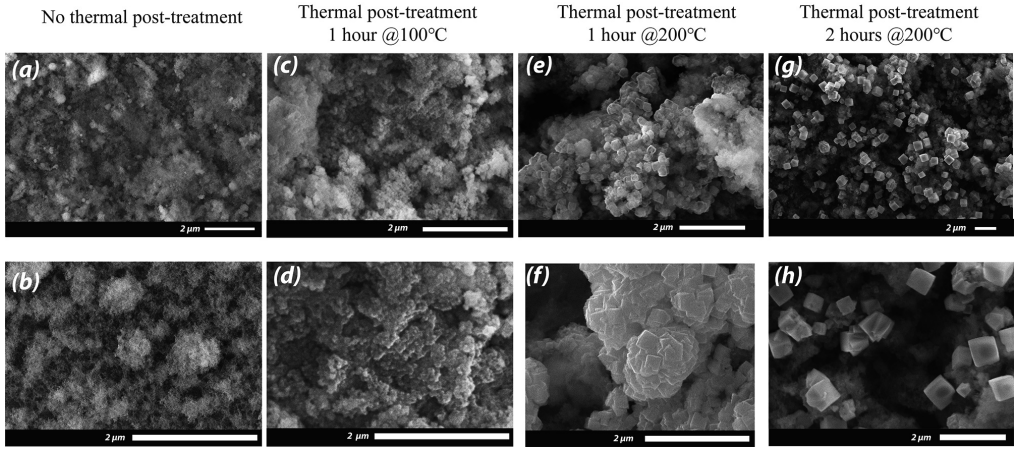

Figure 4.2: a, b) SEM images of the morphology of CuNPs, agglomerates, and Cu microparticles deposited on the silicon substrate. c, d): Transformation of the CuNPs deposited on a silicon substrate to crystalline form after thermal treatment in the vacuum oven for 1 hour at 100 ℃. e, f): After thermal treatment in the vacuum oven for 1 hour at 200 ℃. g, h) Crystal growth after thermal treatment in the vacuum oven for 2 hours at 200 ℃. All CuNPs deposited with SAM voltage/current setting of V=1.2 kV, I=8 mA.

The evolution of the surface morphology by different thermal post-treatments is shown in Figure 4.2.c–h and Figure 4.3.c–h. The melting temperature of nanoparticles (T_{NP}) and their sintering temperature are a function of the nanoparticle's size (D_{NP}) and decrease drastically from the bulk melting temperature (T_{Bulk}) following the law $(T_{NP}-T_{Bulk})/T_{Bulk}=f(-1/D_{NP})$ [33–35]. The dependence of the melting temperature of nanoparticles on their size is particularly important for particles with a size below 20 nm [35]. The SEM images (Figure 4.2.c,d) and

AFM images (Figure 4.3.c,d) show that the 3D sponge-like structure, composed by individual CuNPs, start to sinter at a temperature of 100 ℃ and transform into a compacted structure with micrometric 3D domains containing particulate shapes of tens of nanometers and lower porosity compared to non-heat treated samples.

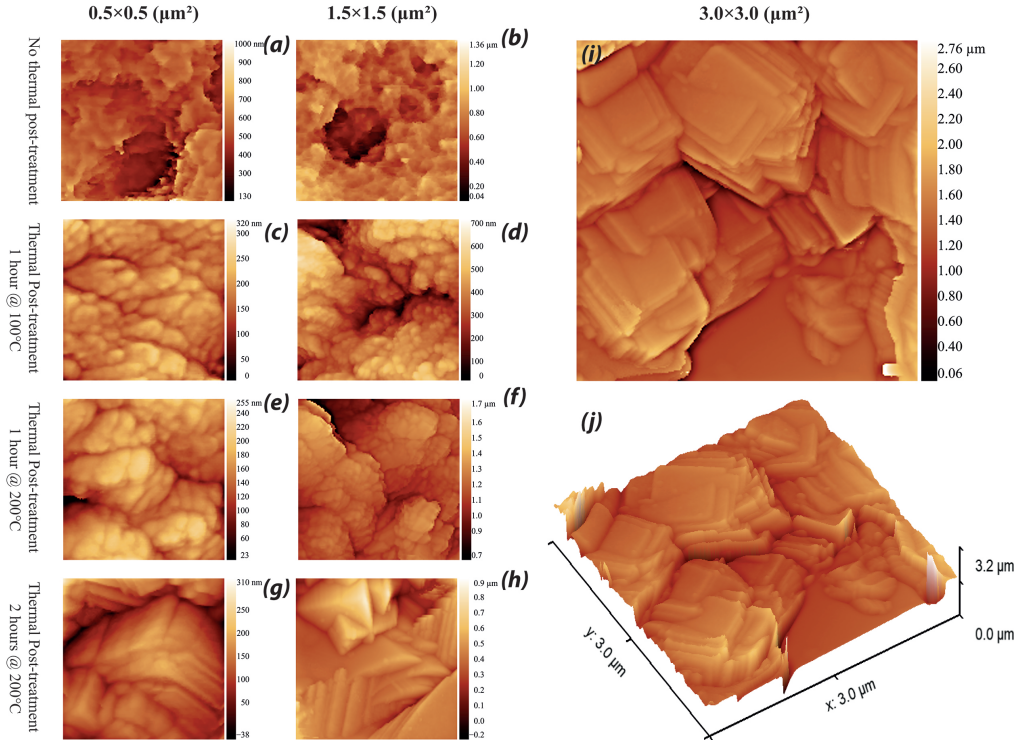

Figure 4.3: AFM morphology of 0.5×0.5 (μm^2) and 1.5×1.5 (μm^2) areas of a, b) samples without heat-treatment, c, d) samples heat-treated at 100 ℃ and 1 hour, e, f) samples heat-treated at 200 ℃ and 1 hour, g, h) Samples heat-treated at 200 ℃ and 2 hours. AFM morphology of i) 3.0×3.0 (μm^2) area of the thermal post-treated sample at 200 ℃ and 2 hours in the vacuum oven and j) its 3D view. All CuNPs deposited with SAM voltage/current setting of V=1.2 kV, I=8 mA

The surface morphology of deposited CuNPs and heat-treated in a vacuum oven for 1 hour at 200 ℃ is depicted in Figure 4.2.e,f. The AFM images of Figure 4.3.e,f show that the thermally treated sample at 200 ℃ features a morphology similar to the ones treated at 100 ℃ but with larger particulate sizes. Figure B.3.d and Figure 4.2.f show that the 3D micrometric domains contain corners and edges with a size ranging from tens of nanometers to a maximum of two hundred nanometers.

Increasing the sintering time to 2 hours provokes further fusing of CuNPs into larger shapes and ordered structures, as shown in Figure 4.2.g,h and Figure 4.3.g,h. The previously formed compacted 3D structures, after 1 hour treatment at 200 ℃ undergo further re-ordering, leading to multi-facet 3D aggregates with size between hundreds of nanometers until a maximum of

2 micrometers, as shown in Figure 4.3.i,j. The frequency of the presence of these cubic copper aggregates decreases by moving from the center of the line towards the boundaries, as shown in Figure B.4.a (the right side of both pictures are closer to the center of the line). In the boundary regions, CuNPs turned into aggregates with micrometric size; however, they have a less ordered shape compared to cubic aggregates present in the centric regions (Figure B.4.b-d). This difference in the microstructure of the thermal treated CuNPs at different positions of the line may be related to the differences in the amount of material present in the centric regions compared to the boundary of the line. This lack of material in the boundary region limits the formation of larger and more-ordered aggregates. The other possible explanation might be related to the presence of copper with different oxidation states at the surface in different regions of the line.

To quantify the presence of oxidations states, we performed an elemental analysis of the fabricated samples by using energy-dispersive X-ray spectrometry (EDS, Table B.1, Figure B.5), on two regions: in the centric regions of the line with higher CuNPs coverage over the deposited area and in the boundary regions featuring lower CuNPs coverage. The EDS results reported in Table B.1 show the presence of copper, oxygen, silicon, and carbon. The presence of silicon in the elemental analysis is due to the penetration of the X-ray into the film until the silicon substrate. Its presence is, therefore, lower in the inner regions compared to the boundary ones due to the higher coverage of CuNPs and higher thickness of the film. The EDS analysis of a silicon substrate without CuNPs is shown in Figure B.5.a and highlights the only presence of silicon without any trace of carbon. Therefore, we attribute the presence of carbon in the CuNPs deposited substrates to the reaction of copper nanoparticles with CO_2 in the air. It should be noted that oxidation of copper occurs very shortly after it is exposed to air because of the chemical reactivity of CuNPs [36] and the relatively low thickness of CuNPs film. Figure 4.4 shows the ratio of copper to oxygen in the CuNPs deposition at the boundary of the deposition area and within inner regions of the line [37]. The sample without heat-treatment shows that the centric regions oxidized uniformly, leading to the formation of copper(II) oxide (CuO); however, the boundary has a higher oxygen ratio compare to inner regions.

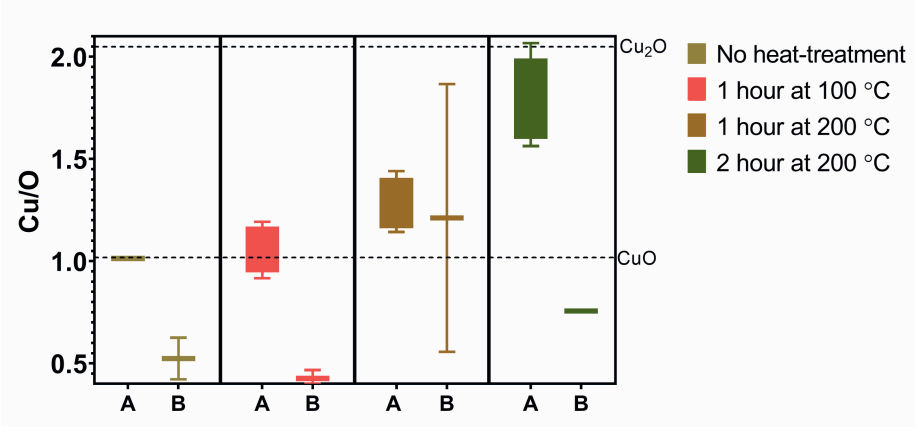

Figure 4.4: The elemental ratio of copper to oxygen in different samples, A: inside the line, B: boundary of the line

To evaluate the effect of heat-treatment on the elemental compositions of the samples, the EDS characterization was also performed on heat-treated samples. As shown in Figure 4.4, the centric regions for almost all samples have a higher ratio of copper to oxygen compared to boundary regions. This ratio starts to increase in the centric regions with an increase of time or temperature of the thermal treatment, which is an indication of the transformation of the CuO to Cu_2O. Unlike bulk copper oxide (CuO), which reduces directly to copper, the CuO nanoparticles firstly completely reduce to Cu_2O by ($4CuO(s) \longrightarrow 2Cu_2O(s)+O_2(g)$) and then to Cu ($2Cu_2O(s) \longrightarrow 4Cu(s)+O_2(g)$) [38, 39], which is a reaction that requires a temperature higher than 200 ℃. [40] The Cu_2O is a stable compound of copper with cubic crystalline structure [41]; therefore, the gradual increase in the ratio of copper to oxygen in the centric regions from 1 to 2 leads to a transformation of the nanostructure from spherical shape to larger cubical shape. The higher ratio of oxygen to copper in the boundary regions might relate to the presence of finer nanoparticles with a higher surface area.

4.3.3 Performance of dADW printed lines as SERS substrate

According to the morphology characterization results mentioned above, the film of CuNPs features high-roughness and a sponge-like 3D morphology containing nanostructures with a size distribution between 0 and 20 nm. To evaluate the SERS performance, a series of Raman experiments were performed by using low concentration Rhodamine B (RhB) as a probe molecule. The schematic of a typical deposited CuNPs line on a silicon substrate is shown in Figure 4.5.a. For each experiment, the width of a line is divided into six regions, and in each region, three Raman acquisitions on three different points are performed. The Raman points are specific regions in the cross-section of the deposited line, which are chosen because of their clearly distinct morphology. In this configuration, the Raman signal of RhB was measured at 18 different points to assess the level of reproducibility of the SERS signal on the fabricated patterns. Rhodamine B (RhB) with a concentration of 1.0×10^{-6} M was adsorbed on the CuNPs deposition and showed a distinguishable Raman signal under laser excitation at 514 nm. The SERS effect is higher when the laser excitation promotes the LSPR on the metal nanostructure. However, the laser excitation options of Raman equipment have limited options, and, for complex nanostructures, LSPR occurs at multiple wavelengths due to the presence of higher-order multipole plasmonic modes [42]. In this study, a combination of theoretical calculation based on Mie Theorem for very fine spherical copper nanoparticles [43] and a series of experiments on complex nanostructures were employed to find the best laser excitation, which is 514 nm. The procedure is explained in detail in the Section B.4.

The characteristic Raman spectrum of RhB is shown in Figure 4.5.b with its most important peaks: 621 cm^{-1} (for xanthene ring puckering), 1199 cm^{-1} and 1279 cm^{-1} (for C-C bridge band stretching and aromatic C-H bending), 1358 cm^{-1} (for aromatic C-C bending), 1505 cm^{-1} and 1528 cm^{-1} (for aromatic C-H bending), and 1648 cm^{-1} (for aromatic C-C bending and C=C stretching). In Figure 4.5.b, at 520.7 cm^{-1}, the silicon peak is also shown, and it is present in the SERS spectrum of RhB if the CuNPs deposited line is not thick enough to cover the silicon substrate completely. For SERS characterization, the five peaks of RhB (1279 cm^{-1}, 1358 cm^{-1}, 1505 cm^{-1}, 1528 cm^{-1} and 1648 cm^{-1}) were considered.

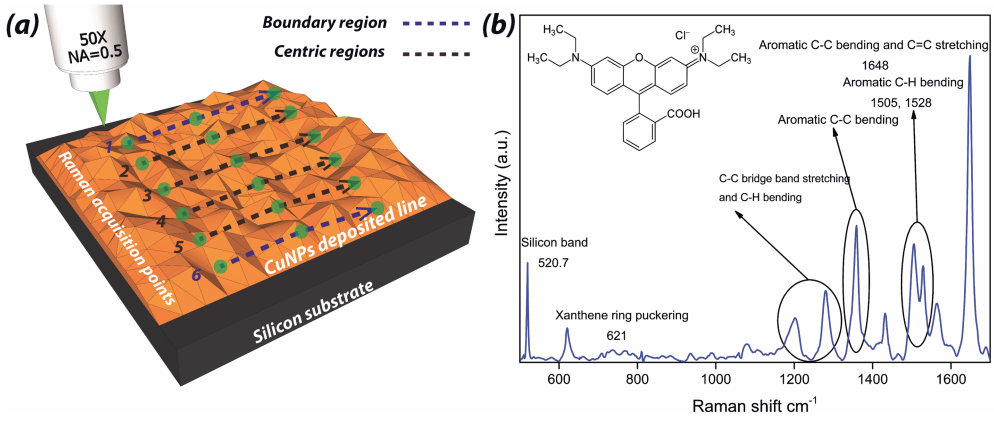

Figure 4.5: a) Schematic view of the typical Raman acquisition map over a deposited line (the green circles are the acquisition points). b) Raman spectrum Rhodamine B. Raman measurement conditions: Argon ion laser operating at 514 nm and power of 20 μW; acquisition time = 30 s; objective lens = 50X (NA=0.5).

The first set of experiments are related to the adsorption of RhB on the patterns of CuNPs deposited on a silicon substrate with SAM setting of 1.2kV and 8.0mA and fixed nozzle-to-substrate distance of 400 μm (L/D_N = 1). Figure 4.6.a, c report 18 Raman spectra of RhB on CuNPs deposited on the silicon substrate with two writing speeds of 10 μm s^{-1} and 2 μm s^{-1} in the spectral range of 1200 to 1700 cm^{-1}.

The values on the oblique axes in Figure 4.6.a,c relates to regions shown in Figure 4.5.a and contains three Raman acquisitions for each region. The distribution of the five main characteristic peaks of RhB for the 6 Raman points is shown in Figure 4.6.b and d. The spectra acquired on NPs patterns fabricated at both writing speed show that 1.0×10^{-6} M RhB is detectable, and all characteristic peaks of RhB are observable with the highest peaks at 1648 cm^{-1}. Furthermore, Figure 4.6.b and d showed that the highest intensities for each peak of RhB occur in the region far from the center and closer to the boundary. We tentatively attribute this to the lower surface area and lower LSPR in the centric regions, which contain a higher number of microparticles.

The effect of thermal post-treatment with different time and temperatures on the enhancement of the Raman signal of 1.0×10^{-6} M RhB is shown in Figure 4.7. Comparing the Raman spectrum of 1.0×10^{-6} M RhB adsorbed on non-heat-treated CuNPs to the heat-treated ones for 1 hour at 100 ℃ (respectively, Figure 4.6.a and Figure 4.7.a), it is clear how the SERS intensity is amplified on average by a factor 4. Thermal treatment of CuNPs at 100 ℃ triggers the sintering of the fine nanoparticles into larger structures, although the temperature or the heating time are not sufficient for inducing a significant coalescence of the NPs.

The SERS intensity is further improved by increasing the temperature of the vacuum oven from 100 ℃ to 200 ℃ (Figure 4.7.b), which averagely enhanced the signal intensity by a factor 10 compared to the non-heat-treated CuNPs. Thermal treatment of CuNPs at 200 ℃ for 1 hour leads to the formation of aggregates with larger nano-feature size, as shown in Figure 4.2.e,f, and this induces a red-shift in the LSPR [44–46] of copper structures, therefore, a better amplification of electromagnetic wave and consequently Raman signal.

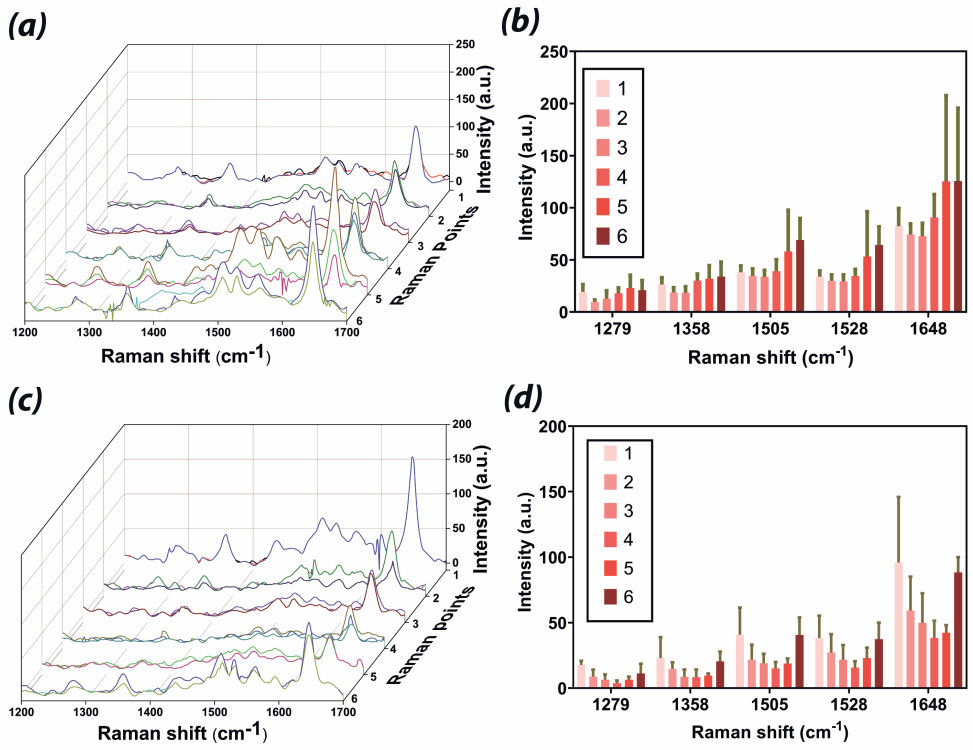

Figure 4.6: a, c) Raman spectra of 1.0×10^{-6} M RhB on CuNPs patterns obtained at writing speed of 10 μm s^{-1} and 2 μm s^{-1} respectively for 18 points in 6 regions. b, d) Averaged intensities of main peaks of RhB for each of the 6 Raman regions corresponding to Raman spectra of a) and c), respectively. Raman measurement conditions: Argon ion laser operating at 514 nm and power of 20 μW; acquisition time = 30 s; objective lens = 50X (NA=0.5).

The prolongation of the heat-treatment at 200 ℃ from 1 hour to 2 hours, leads to a significant decrease of the SERS intensity in the centric region of the line and an increase in the boundary regions (Figure 4.7.c). As mentioned above, the morphology of the thermal-treated CuNPs in the centric regions treated at 200 ℃ for 2 hours, is characterized by the presence of large cubic aggregates with a feature size of several hundreds of nanometers and less effectiveness as a hot-spot for the enhancement of the SERS signal.

The other hindering point of over-sintered CuNPs relates to a decrease in the surface area of the microstructure due to fusing NPs hence lower area for adsorption of RhB molecules. As shown for the SERS signal of RhB on CuNPs without heat-treatment, the highest intensities for heat-treated samples takes place as well at the boundary of the deposited line. This phenomenon can be explained by the presence of a higher number of edges and corners in the structures closer to the boundaries of the heat-treated CuNP films.

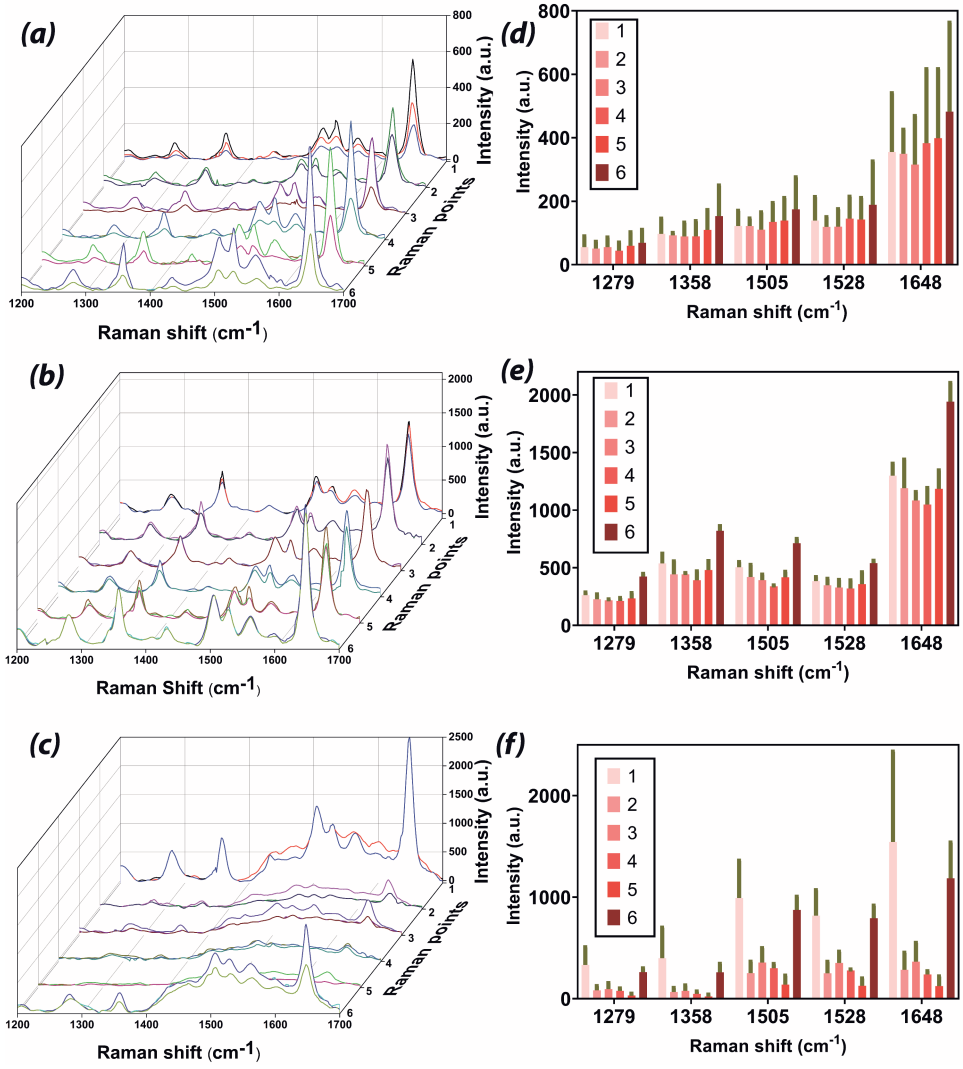

Figure 4.7: Raman spectra of 1.0×10-6 M RhB on CuNPs patterns obtained at writing speed of 2 μm s-1 and a) 1-hour thermal treatment of 100 ℃ b) 1-hour thermal treatment of 200℃ c) 2 hours thermal treatment of 200 ℃ in a vacuum oven (18 points in 6 regions). d), e) and f): Averaged intensities of main peaks of RhB for each of the 6 Raman regions corresponding to the Raman spectra of a), b), and c), respectively. Raman measurement conditions: Argon ion laser operating at 514 nm and power of 20 μW; acquisition time = 30 s; objective lens = 50X (NA=0.5).

The enhancement factor (EF), a quantitative parameter to compare the efficiency of active SERS substrates, was calculated based on the intensity of the 1648 cm^{-1} peak, which is the most

intense spectral feature of RhB, by using the following equation [47–50]:

$$EF = \frac{I_{SERS}}{I_0} \times \frac{C_0}{C_{SERS}} \tag{4.1}$$

Where I_{SERS} and I_0 are the intensities of the 1648 cm^{-1} peak for C_{SERS}=1.0×10^{-6} M and C_0=1.0×10^{-3} M of RhB, respectively. For calculating the EF, a reference sample was prepared by immersing a bare silicon substrate in a 1.0×10^{-3} M (1 mM [51]) RhB solution for 12 hours, and I_0 measured three times and averaged to a value of ~7.317 (a.u.) (Figure B.9). Figure 4.8 shows the evolution of the EF, taking into account 18 Raman points on different regions of the patterns for samples with and without thermal post-treatment. The highest EF is 2.1×$10^{5,}$ and the highest averaged EF is 1.6×10^5 for the heat-treated samples at 200 ℃ for 1 hour; moreover, these samples show the best reproducibility and lowest standard deviation compared to other samples. This value is comparable to other reported copper-based SERS-active substrates [18, 52, 53] and is close to the EF of gold SERS substrates [50, 54] and silver SERS substrates [55]. These results indicate that the SERS features of CuNPs, selectively deposited on a substrate by aerosol direct writing, can be significantly enhanced via thermal post-treatment up to a level comparable with one of other noble metals.

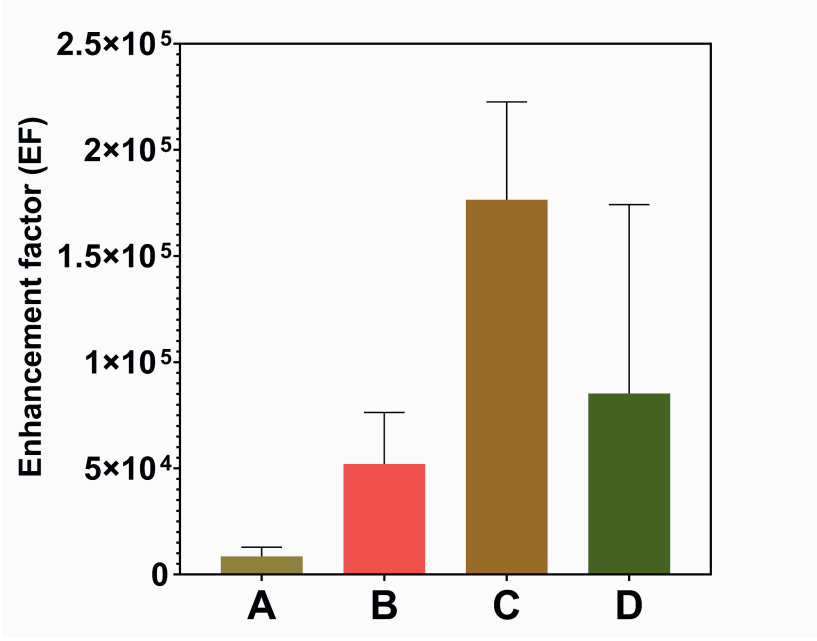

Figure 4.8: The average enhancement factor (EF) for A) non-heat-treated sample B) thermal post-treatment at 100 ℃ for 1 hour C) thermal post-treatment at 200 ℃ for 1 hour D) thermal post-treatment at 200 ℃ for 2 hours. All CuNPs were deposited with SAM voltage/current setting of V=1.2 kV, I=8 mA, and writing speed of 2 μm s^{-1}. Raman measurement conditions: Argon ion laser operating at 514 nm and power of 20 μW; acquisition time = 30 s; objective lens = 50X (NA=0.5).

4.4 Conclusions

In this work, we proposed a novel, simple, and solvent-free direct writing method for the selective deposition of micrometric metal (copper) nanoparticles' patterns, and we demonstrated their application as SERS sensors. By varying the parameters of the writing process and by introducing a thermal post-treatment, we were able to tune the morphology of the deposited patterns and significantly enhance the Raman signal of a reference dye (Rhodamine B). The selectively deposited films were composed by a collection of dense spherical primary particles with various sizes. The smallest line-width that we achieved was equal to 265 µm and largely depends on the size of the 3D printed nozzle. Narrower patterns can be achieved in future through high-resolution laser-assisted 3D printing (laser stereolithography [56] or two-photon polymerization [57]) of nozzles featuring smaller orifices. The deposited patterns of copper NPs with sponge-like structures allowed the detection of 1.0×10^{-6} M concentration of RhB. A low-temperature thermal post-treatment at 100 ℃ for 1 hour triggered a transformation of the microstructures by fusing nanoparticles into larger nanostructures. This transformation of the film morphology caused an enhancement of the Raman signal of RhB. The highest enhancement of the Raman signal of RhB was achieved with a thermal treatment at 200 ℃ for 1 hour (EF ≈ 2.1×10^{5}). Increasing the time of thermal treatment from 1 hour to 2 hours at 200 ℃, resulted in a decrease of the Raman signal intensity and a further change of the morphology into microparticulate structures induced by the fusion of the nanoparticles. A great advantage of this method is the ability to selectively deposit metal and alloy NPs patterns with a 3D microstructure on different kinds of substrates (Si, glass, paper). This feature could allow in the future to integrate metallic nanofeatures within specific regions of microfluidic devices. At the same time, the easy tunability of the nanometallic morphology through process parameters, the possibility to extend the method to other more performing materials (e.g., Au and Ag), and its integrability with other fabrication methods, paves the way for the realization of new SERS sensors.

References

[1] K. Kneipp, Y. Wang, H. Kneipp, L. T. Perelman, I. Itzkan, R. R. Dasari, and M. S. Feld, "Single molecule detection using surface-enhanced raman scattering (sers)," *Physical Review Letters*, vol. 78, pp. 1667–1670, 1997.

[2] D. K. Lim, K. S. Jeon, H. M. Kim, J. M. Nam, and Y. D. Suh, "Nanogap-engineerable raman-active nanodumbbells for single-molecule detection," *Nature Materials*, vol. 9, pp. 60–67, 2010.

[3] K. Kneipp, H. Kneipp, V. B. Kartha, R. Manoharan, G. Deinum, I. Itzkan, R. R. Dasari, and M. S. Feld, "Detection and identification of a single dna base molecule using surface-enhanced raman scattering (sers)," *Physical Review E*, vol. 57, pp. R6281–R6284, 6 1998.

[4] J. Kneipp, H. Kneipp, and K. Kneipp, "Sers-a single-molecule and nanoscale tool for bioanalytics," *Chemical Society Reviews*, vol. 37, pp. 1052–1060, 2008.

[5] S.-Y. Ding, J. Yi, J.-F. Li, B. Ren, D.-Y. Wu, R. Panneerselvam, and Z.-Q. Tian, "Nanostructure-based plasmon-enhanced raman spectroscopy for surface analysis of materials," *Nature Reviews Materials*, vol. 1, p. 16021, 6 2016.

[6] J. Zheng and L. He, "Surface-enhanced raman spectroscopy for the chemical analysis of food," *Comprehensive Reviews in Food Science and Food Safety*, vol. 13, pp. 317–328, 5 2014.

[7] L. A. Lane, X. Qian, and S. Nie, "Sers nanoparticles in medicine: From label-free detection to spectroscopic tagging," *Chemical Reviews*, vol. 115, pp. 10489–10529, 2015.

[8] B. Sharma, R. R. Frontiera, A. I. Henry, E. Ringe, and R. P. V. Duyne, "Sers: Materials, applications, and the future," *Materials Today*, vol. 15, pp. 16–25, 2012.

[9] L. Jensen, C. M. Aikens, and G. C. Schatz, "Electronic structure methods for studying surface-enhanced raman scattering," *Chemical Society Reviews*, vol. 37, p. 1061, 2008.

[10] K. A. Willets and R. P. V. Duyne, "Localized surface plasmon resonance spectroscopy and sensing," *Annual Review of Physical Chemistry*, vol. 58, pp. 267–297, 5 2007.

[11] S. E. J. Bell and M. R. McCourt, "Sers enhancement by aggregated au colloids: effect of particle size," *Physical Chemistry Chemical Physics*, vol. 11, pp. 7348–7349, 2009.

[12] S. L. Kleinman, R. R. Frontiera, A. I. Henry, J. A. Dieringer, and R. P. V. Duyne, "Creating, characterizing, and controlling chemistry with sers hot spots," *Physical Chemistry Chemical Physics*, vol. 15, pp. 21–36, 2013.

[13] M. K. Hossain, Y. Kitahama, G. G. Huang, X. Han, and Y. Ozaki, "Surface-enhanced raman scattering: Realization of localized surface plasmon resonance using unique substrates and methods," *Analytical and Bioanalytical Chemistry*, vol. 394, pp. 1747–1760, 2009.

[14] M. Liu, R. Xiang, Y. Lee, K. Otsuka, Y. L. Ho, T. Inoue, S. Chiashi, J. J. Delaunay, and S. Maruyama, "Fabrication, characterization, and high temperature surface enhanced raman spectroscopic performance of sio2 coated silver particles," *Nanoscale*, vol. 10, pp. 5449–5456, 2018.

[15] M. Qin, X. Zhou, J. Zhu, M. Ma, H. Wang, and L. Yang, "Synthesis of gold nanorods with varied length-diameter ratios-applications using sers for the detection of drugs," *Journal of Dispersion Science and Technology*, pp. 1–8, 12 2019.

[16] W. Yue, Z. Wang, Y. Yang, L. Chen, A. Syed, K. Wong, and X. Wang, "Electron-beam lithography of gold nanostructures for surface-enhanced raman scattering," *Journal of Micromechanics and Microengineering*, vol. 22, p. 125007, 12 2012.

[17] D. Li, J. Liu, H. Wang, C. J. Barrow, and W. Yang, "Electrochemical synthesis of fractal bimetallic cu/ag nanodendrites for efficient surface enhanced raman spectroscopy," *Chemical Communications*, vol. 52, pp. 10968–10971, 2016.

[18] A. Mao, M. Ding, X. Jin, X. Gu, C. Cai, C. Xin, and T. Zhang, "Direct, rapid synthesis of water-dispersed copper nanoparticles and their surface-enhanced raman scattering properties," *Journal of Molecular Structure*, vol. 1079, pp. 396–401, 2015.

[19] Y.-X. Yuan, L. Ling, X.-Y. Wang, M. Wang, R.-A. Gu, and J.-L. Yao, "Surface enhanced raman spectroscopic readout on heavy metal ions based on surface self assembly," *Journal of Raman Spectroscopy*, vol. 38, pp. 1280–1287, 10 2007.

[20] Y. He, R. Wang, T. Jiao, X. Yan, M. Wang, L. Zhang, Z. Bai, Q. Zhang, and Q. Peng, "Facile preparation of self-assembled layered double hydroxide-based composite dye films as new chemical gas sensors," *ACS Sustainable Chemistry & Engineering*, vol. 7, pp. 10888–10899, 6 2019.

[21] W. Wu, L. Liu, Z. Dai, J. Liu, S. Yang, L. Zhou, X. Xiao, C. Jiang, and V. A. Roy, "Low-cost, disposable, flexible and highly reproducible screen printed sers substrates for the detection of various chemicals," *Scientific Reports*, vol. 5, p. 10208, 9 2015.

[22] B. Bozzini, L. D'Urzo, and C. Mele, "A novel polymeric leveller for the electrodeposition of copper from acidic sulphate bath: A spectroelectrochemical investigation," *Electrochimica Acta*, vol. 52, pp. 4767–4777, 4 2007.

[23] R. Han, H. Wu, C. Wan, and W. Pan, "Templated nanoporous copper and nickel: Novel substrates for surface-enhanced raman scattering," *Scripta Materialia*, vol. 59, pp. 1047–1050, 11 2008.

[24] F. Diao, X. Xiao, B. Luo, H. Sun, F. Ding, L. Ci, and P. Si, "Two-step fabrication of nanoporous copper films with tunable morphology for sers application," *Applied Surface Science*, vol. 427, pp. 1271–1279, 2018.

[25] Z. Lu, H. Si, Z. Li, J. Yu, Y. Liu, D. Feng, C. Zhang, W. Yang, B. Man, and S. Jiang, "Sensitive, reproducible, and stable 3d plasmonic hybrids with bilayer ws 2 as nanospacer for sers analysis," *Optics Express*, vol. 26, p. 21626, 2018.

[26] G. H. Chan, J. Zhao, E. M. Hicks, G. C. Schatz, and R. P. V. Duyne, "Plasmonic properties of copper nanoparticles fabricated by nanosphere lithography," *Nano Letters*, vol. 7, pp. 1947–1952, 7 2007.

[27] L. Gunnarsson, E. J. Bjerneld, H. Xu, S. Petronis, B. Kasemo, and M. Käll, "Interparticle coupling effects in nanofabricated substrates for surface-enhanced raman scattering," *Applied Physics Letters*, vol. 78, pp. 802–804, 2001.

[28] H.-N. Wang, A. Dhawan, Y. Du, D. Batchelor, D. N. Leonard, V. Misra, and T. Vo-Dinh, "Molecular sentinel-on-chip for sers-based biosensing," *Physical Chemistry Chemical Physics*, vol. 15, p. 6008, 2013.

[29] N. S. Tabrizi, Q. Xu, N. M. van der Pers, and A. Schmidt-Ott, "Generation of mixed metallic nanoparticles from immiscible metals by spark discharge," *Journal of Nanoparticle Research*, vol. 12, pp. 247–259, 1 2010.

[30] N. S. Tabrizi, Q. Xu, N. M. van der Pers, U. Lafont, and A. Schmidt-Ott, "Synthesis of mixed metallic nanoparticles by spark discharge," *Journal of Nanoparticle Research*, vol. 11, pp. 1209–1218, 7 2009.

[31] A. Accardo, V. Shalabaeva, M. Cotte, M. Burghammer, R. Krahne, C. Riekel, and S. Dante, "Amyloid β peptide conformational changes in the presence of a lipid membrane system," *Langmuir*, vol. 30, pp. 3191–3198, 2014.

[32] F. M. White, *Fluid Mechanichs, 7th Edition.* 2011.

[33] P. Buffat and J.-P. P. Borel, "Size effect on the melting temperature of gold particles," *Physical Review A*, vol. 13, pp. 2287–2298, 6 1976.

[34] E. Roduner, "Size matters: why nanomaterials are different," *Chemical Society Reviews*, vol. 35, p. 583, 2006.

[35] O. A. Yeshchenko, I. M. Dmitruk, A. A. Alexeenko, and A. M. Dmytruk, "Size-dependent melting of spherical copper nanoparticles embedded in a silica matrix," *Physical Review B*, vol. 75, p. 085434, 2 2007.

[36] H. Meng, Z. Chen, G. Xing, H. Yuan, C. Chen, F. Zhao, C. Zhang, Y. Wang, and Y. Zhao, "Ultrahigh reactivity and grave nanotoxicity of copper nanoparticles," *Journal of Radioanalytical and Nuclear Chemistry*, vol. 272, pp. 595–598, 6 2007.

[37] N. R. Dhineshbabu and V. R. N. N. R. Vetumperumal, "Study of structural and optical properties of cupric oxide nanoparticles," *Applied Nanoscience*, vol. 6, pp. 933–939, 2016.

[38] A. Hornés, A. B. Hungría, P. Bera, A. L. Cámara, M. Fernández-García, A. Martínez-Arias, L. Barrio, M. Estrella, G. Zhou, J. J. Fonseca, J. C. Hanson, and J. A. Rodriguez, "Inverse ceo2/cuo catalyst as an alternative to classical direct configurations for preferential oxidation of co in hydrogen-rich stream," *Journal of the American Chemical Society*, vol. 132, pp. 34–35, 2010.

[39] C. D. O. Teixeira, S. D. S. Montani, L. A. Palacio, and F. M. Z. Zotin, "The effect of preparation methods on the thermal and chemical reducibility of cu in cu-al oxides," *Dalton Transactions*, vol. 47, pp. 10989–11001, 2018.

[40] P. D. Kirsch and J. G. Ekerdt, "Chemical and thermal reduction of thin films of copper (ii) oxide and copper (i) oxide," *Journal of Applied Physics*, vol. 90, pp. 4256–4264, 2001.

[41] J. Pike, S.-W. Chan, F. Zhang, X. Wang, and J. Hanson, "Formation of stable cu2o from reduction of cuo nanoparticles," *Applied Catalysis A: General*, vol. 303, pp. 273–277, 4 2006.

[42] H. Müller, "Optical properties of metal clusters," *Zeitschrift für Physikalische Chemie*, 1996.

[43] G. V. Hartland, "Optical studies of dynamics in noble metal nanostructures," *Chemical Reviews*, vol. 111, pp. 3858–3887, 2011.

[44] S. Link and M. A. El-Sayed, "Spectral properties and relaxation dynamics of surface plasmon electronic oscillations in gold and silver nanodots and nanorods," *Journal of Physical Chemistry B*, vol. 103, pp. 8410–8426, 1999.

[45] J. A. Scholl, A. L. Koh, and J. A. Dionne, "Quantum plasmon resonances of individual metallic nanoparticles," *Nature*, vol. 483, pp. 421–427, 2012.

[46] O. A. Yeshchenko, I. M. Dmitruk, A. M. Dmytruk, and A. A. Alexeenko, "Influence of annealing conditions on size and optical properties of copper nanoparticles embedded in silica matrix," *Materials Science and Engineering B: Solid-State Materials for Advanced Technology*, vol. 137, pp. 247–254, 2007.

[47] M.-L. Zhang, X. Fan, H.-W. Zhou, M.-W. Shao, J. A. Zapien, N.-B. Wong, and S.-T. Lee, "A high-efficiency surface-enhanced raman scattering substrate based on silicon nanowires array decorated with silver nanoparticles," *The Journal of Physical Chemistry C*, vol. 114, pp. 1969–1975, 2 2010.

[48] A. J. Pereira, J. P. Gomes, G. F. Lenz, R. Schneider, J. A. Chaker, P. E. N. D. Souza, and J. F. Felix, "Facile shape-controlled fabrication of copper nanostructures on borophosphate glasses: Synthesis, characterization, and their highly sensitive surface-enhanced raman scattering (sers) properties," *Journal of Physical Chemistry C*, vol. 120, pp. 12265–12272, 2016.

[49] Q. LI, Y. LYU, T. PAN, D. LI, H. LU, and Y. GONG, "Development of a coupled supersonic inlet-fan navier–stokes simulation method," *Chinese Journal of Aeronautics*, vol. 31, pp. 237–246, 2018.

[50] V. Suresh, L. Ding, A. B. Chew, and F. L. Yap, "Fabrication of large-area flexible sers substrates by nanoimprint lithography," *ACS Applied Nano Materials*, vol. 1, pp. 886–893, 2 2018.

[51] M. A. El-Aal, T. Seto, M. Kumita, A. A. Abdelaziz, and Y. Otani, "Synthesis of silver nanoparticles film by spark discharge deposition for surface-enhanced raman scattering," *Optical Materials*, vol. 83, pp. 263–271, 2018.

[52] P. Fu, X. Shi, F. Jiang, and X. Xu, "Superhydrophobic nanostructured copper substrate as sensitive sers platform prepared by femtosecond laser pulses," *Applied Surface Science*, vol. 501, p. 144269, 2020.

[53] L. Y. Chen, J. S. Yu, T. Fujita, and M. W. Chen, "Nanoporous copper with tunable nanoporosity for sers applications," *Advanced Functional Materials*, vol. 19, pp. 1221–1226, 2009.

[54] S. Xu, W. Tang, D. B. Chase, D. L. Sparks, and J. F. Rabolt, "A highly sensitive, selective, and reproducible sers sensor for detection of trace metalloids in the environment," *ACS Applied Nano Materials*, vol. 1, pp. 1257–1264, 3 2018.

[55] X. Zhang, Y. Mo, B. Liu, C. Hu, S. Chen, H. Shi, and J. Chen, "Fabrication of scale-like silver-nanosheets-grafted carbon-fenced conductive silver nanowires as effective 3d sers substrates," *ACS Applied Nano Materials*, vol. 1, pp. 4771–4780, 9 2018.

[56] A. Accardo, R. Courson, R. Riesco, V. Raimbault, and L. Malaquin, "Direct laser fabrication of meso-scale 2d and 3d architectures with micrometric feature resolution," *Additive Manufacturing*, vol. 22, pp. 440–446, 8 2018.

[57] R. C. L. N. Kramer, E. J. Verlinden, L. Angeloni, A. V. D. Heuvel, L. E. Fratila-Apachitei, S. M. V. D. Maarel, and M. K. Ghatkesar, "Multiscale 3d-printing of microfluidic afm cantilevers," *Lab on a Chip*, vol. 20, pp. 311–319, 2020.

5

Tunable photoluminescence and SERS behaviour of Au nanoparticle patterns

The ability to tune the localised surface plasmon resonance (LSPR) behaviour of metal nanostructures has great importance for many optical sensor applications such as metal (plasmon) enhanced fluorescence spectroscopy and surface-enhanced Raman scattering (SERS). In this study, we used dry Aerosol Direct Writing (dADW) to selectively deposit fine gold nanoparticles (AuNPs) patterns. A low-temperature thermal post-treatment (below 200 ℃) provides enough energy to merge and transform AuNPs into larger features significantly different from non-thermally treated samples. The optical behaviour of non-treated and thermally treated AuNP films was investigated by photoluminescence (PL) spectroscopy. The PL measurements showed a red-shift, compared to bulk gold, using 488 nm and 514 nm laser excitation, and a blue-shift using 633 nm laser excitation. The thermal post-treatment leads to a further blue-shift compared to non-treated samples in the presence of both 514 and 633 nm laser. Finally, the AuNPs patterns were employed as a SERS-active substrate to detect low-concentrated (10^{-8} M) Rhodamine B. This method's ability to selectively deposit 3D gold nanostructures and tune their optical behaviour through a low-temperature thermal treatment allows optimisation of the optical response and enhancement of the Raman signal for specific bio-analytes.

The contents of this chapter have been published in:

- Aghajani, S., Accardo, A., & Tichem, M. (2021). Tunable photoluminescence and SERS behaviour of additively manufactured Au nanoparticle patterns. RSC Advances, 11(28), 16849–16859. DOI:10.1039/D1RA02266K

5.1 Introduction

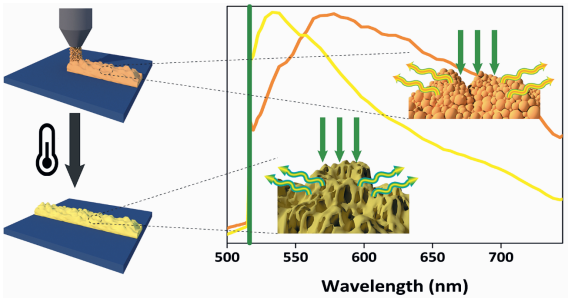

Metal nanoparticles (MNPs) and metal nanostructures (MNSs) are used for detection purposes in optical biosensors due to their unique optical behaviours [1–5]. Biosensors based on MNPs and MNSs allow simple, rapid, straightforward, and label-free detection of analytes and biomarkers in very low concentrations with high selectivity and sensitivity [6–9] due to the electromagnetic field enhancement of the structures [8, 10]. The electromagnetic enhancement comes from the coherent oscillation of electron clouds, excited by incident light at the metal/dielectric interface. These collective oscillations are either confined on the surface of the metallic structure and referred to as surface plasmon resonance (SPR) or confined in nanometric features and referred to as localised surface plasmon resonance (LSPR) [11, 12]. This effect has been used in detection methods such as surface-enhanced infrared absorption spectroscopy (SEIRAS) [13], metal (plasmon) enhanced fluorescence (MEF/PEF) [14–16], surface-enhanced Raman scattering (SERS) spectroscopy [17–20], and surface-enhanced resonance Raman scattering (SERRS) spectroscopy [21–23]. SERS and SERRS are used in many applications because they can provide unique Raman spectroscopy fingerprints of low concentrated analytes down to micro and nanomolar [7, 24].

For an ideal SERS-active substrate, a high enhancement of SERS signal, low limit-of-detection (LOD), high reproducibility of the SERS response, and low manufacturing cost are needed. This requires tailoring the size, shape, and density of nanostructures and selecting optimal material. The typical material for the fabrication of a SERS substrate is gold because of its visible range LSPRs and high chemical stability. Different methods are proposed for the fabrication of SERS-active substrates, such as electron beam lithography [25] and photolithography [3]. However, the complexity and multi-step processing nature of these methods increase the time and cost of fabrication of SERS-substrates. To overcome the complexity of the previous methods, different strategies have been developed to manufacture SERS substrates, such as nanosphere lithography (NSL)[26–28], Langmuir-Blodgett technique [29], chemical reduction [30], self-assembly [31], and electrochemical deposition [32]. However, all these methods use either wet processes, which involve the presence of different liquids and hazardous chemicals and high risk of contamination, or high temperature and expensive instruments. Moreover, for SERS bio-application, the active surface ideally needs to be integrated into a microfluidic device, which requires the ability to manufacture SERS-active regions on the substrate selectively. In this work, we used our recently reported dry aerosol direct writing method (dADW) [20] to create patterns of gold nanoparticles on a silicon substrate and study the effect of post-deposition thermal treatment on the morphology and photoluminescence of the deposited AuNPs patterns and the performance of these patterns as SERS-active substrates. The dADW method allows direct, spatially selective, one-step processing and robust deposition of metal or alloy NPs (with a particle size distribution of 0-20 nm) on a wide variety of substrates, including Si, polymers, paper, and glass. The technique allows fine control over the density of NPs and the resolution of the patterns through

process parameters, such as the deposition speed and nozzle to substrate distance. The absence of any chemical for particle generation or stabilisation of NPs and the presence of argon as carrier gas prevents the introduction of impurities. The deposited AuNPs patterns, typically characterised by hills and valleys with hundreds of nanometers differences in height, form a porous 3D microstructure with nanometric features. We report the effect of low-temperature (below 200℃) post-deposition thermal treatment resulting in a conversion of the nanoscale-roughness porous microstructure into larger nanostructure with smooth surfaces. Furthermore, we show that the evolution of morphology affects the AuNPs film's photoluminescence, especially when subjected to laser excitation of 514 nm and 632 nm, leading to a blue-shift in the peak compared to the non-treated deposited Au patterns. The deposited AuNPs demonstrated high SERS sensitivity in detecting Rhodamine B (RhB) as a probe molecule, with a 10^{-8} M and a 10^{-7} M detection limit under, respectively, laser excitation of 514 nm and 633 nm.

5.2 Materials and Methods

5.2.1 Sample preparation

To fabricate SERS-active substrates, dADW setup (explained in Section 2.2) was used to deposit AuNPs in the form of patterns on a silicon substrate. For electrodes pure gold (99.99% pure) were used to generate gold nanoparticles. A 3D printed converging nozzle with 400 μm outlet diameter aerodynamically focuses the AuNPs and deposits them on the substrate by impaction. All substrates were first cleaned with acetone and isopropanol and, immediately before the deposition, placed in an oxygen plasma chamber for 30 minutes to remove any impurity on the substrate and to increase the adhesion of AuNPs upon deposition. This cleaned substrate is then mounted on the stage in the vacuum chamber perpendicular to the nozzle. The substrate's distance to the nozzle is controlled with an out-of-plane precise SmarAct SLC-1750-O20-D-HV positioner, while the in-plane deposition pattern is controlled with two SmarAct SLC-1750-M-E-HV positioners. Following the same configuration of process parameters for earlier copper nanoparticle deposition [20], all samples were prepared with a fixed nozzle to substrate distance of 400 μm, a flux of 1050 sccm of argon gas, 1 bar upstream pressure, a vacuum pressure of 275 ± 2% Pa, deposition speed of 80 μm s^{-1}, SAM voltage and the current setting of V = 0.9 kV and I = 5 mA respectively. For thermal post-treatment, AuNPs patterned on silicon substrates were placed in a Binder VD23 Vacuum oven with a vacuum pressure of 0.01 mbar, with 8 different thermal treatment programs in terms of temperature and time, see Table 5.1. For each sample, two silicon substrates with two lines of AuNPs patterns were made.

5.2.2 Morphology Characterisation

To study the deposited patterns' morphology, white light interferometry, scanning electron microscopy (SEM), and atomic force microscopy (AFM) were used. The white-light interferometry was performed with a Contour GT-K 3D optical profilometer (Bruker Corporation, Billerica, MA, USA) with ~10-50 nm resolution and an objective of 20X. Line profiles were obtained by integrating three measurements at each location. The white-light interferometry data were post-processed with GWYDDION 2.55 software to remove the effect of the background. The SEM measurements were performed with a field-emission high-resolution Helios G4, all with a secondary electron through-the-lens (TLD) detector. A JPK Nanowizard 4 coupled to a Zeiss microscope in QI mode was used for AFM measurements. High-resolution silicon AFM tips

Table 5.1: Samples with different temperature and time for thermal post-treatment

Sample	Temperature(℃)	Time (min)
S 1	-	-
S 2	100	15
S 3	100	30
S 4	100	120
S 5	120	15
S 6	120	30
S 7	150	5
S 8	150	15
S 9	200	5

of SAA-SPI-SS were used from Bruker with the nominal resonant frequency of 55 kHz, force constant of 0.25 N m^{-1}, an aspect ratio of at least 5:1 in the last 100 nm, and a nominal curvature radius of 1 nm. The combination of the low radius probe and the tip's high aspect ratio enables high-resolution imaging of surfaces with substantial height differences, thus decreasing the possible convolution effect to the minimum. All AFM measurements were performed at room temperature with two scan areas of 1.0 × 1.0 and 0.25 × 0.25 μm^2. GWYDDION 2.55 software was used for the post-processing of AFM measurements data.

5.2.3 SERS and photoluminescence measurements

Photoluminescence and Raman spectroscopy measurements were performed on a Horiba LabRAM HR setup, equipped with an argon-ion laser operating at 488 and 514 nm, and a helium-neon laser operating at 633 nm, a liquid-nitrogen cooled CCD camera, and objectives of 50X (NA = 0.5) and 10X (NA = 0.25). The photoluminescence (PL) studies were performed using an objective of 10X and acquisition time of 20 s, with the previously mentioned lasers over 30 random locations within the AuNPs deposited patterns, including centric and boundary regions of the patterns. The two optical filters in the excitation laser path and the scattered response path from the sample remove any wavelength below the desired excitation lasers. The spectrums were collected over the range of 450-750 nm for the 488 nm excitation laser, 500-750 nm for the 514 nm excitation laser, and 600-1000 nm for the 633 nm excitation laser.

For SERS studies, different Rhodamine B (RhB) concentrations were prepared out of RhB powder, purchased from Sigma-Aldrich, diluted in deionised water. For a homogeneous and monolayer distribution of the probe molecule on the nanostructured surface, at first, the silicon substrate containing AuNPs patterns was immersed in the RhB solution for 12 hours to have sufficient molecules adsorbed the samples. Then, samples were removed from the solution and washed with deionised water to remove an excess of RhB and dried with nitrogen. Two laser excitations of 514 nm and 633 nm focused with an objective of 50X were used for the SERS study, and spectrums were acquired with an acquisition time of 10 s and integration of 2. Similar to PL studies, data were recorded using LabSpec6 software, and baseline subtraction was performed to remove the background. The SERS signal of RhB was recorded over the spectral range 500-1700 cm^{-1} with a spectral resolution of 0.6 cm^{-1}. The Raman signal of RhB on AuNPs deposited pat-

terns with and without heat treatment was measured at 160 different random locations within the patterns to assess the SERS signal's reproducibility.

5.3 Results and Discussion

5.3.1 Morphology of deposited film

Figure 5.1 shows a white light interferometry image of a line of deposited AuNPs on a silicon substrate. The colour indicates the height of the deposited features, and, at specific locations, sudden peaks can be observed. This can also be seen in the 3D image of the line in Figure 5.1.b and the cross-sectional profile in Figure 5.1.c1-c5. Peaks are related to agglomerates of primary nanoparticles or microparticles. Primary nanoparticles carried in argon gas from the generation site to the deposition site start to agglomerate by impaction or columbic forces, creating larger particles with random sizes and shapes. These agglomerates of AuNPs are characterised by higher mass and inertia; therefore, they will deposit mainly in the central region, as confirmed in Figure 5.1.a. Next to agglomerates of AuNPs, gold microparticles also exist in the flow related to molten gold ejection from electrodes [33, 34]. These microparticles are more than 500 nm diameter in size with a spherical shape, as shown in Figure C.1. a-c, they will deposit as well more often in the centric region due to their higher inertia [20].

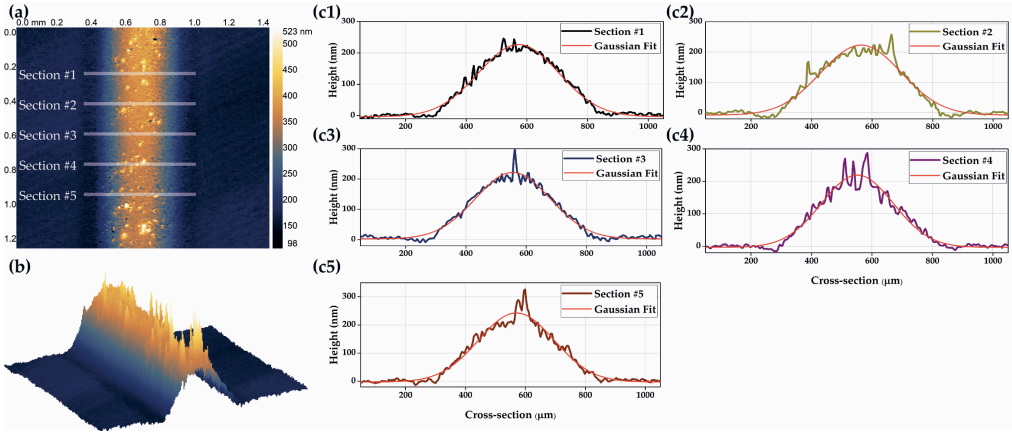

Figure 5.1: a) White-light interferometry image of a line of AuNPs deposited on a silicon substrate, b) 3D view of the line, c1-c5) profile of the line at five sections showed in a) with a Gaussian fit. The AuNPs were deposited with SAM voltage/current setting of V = 0.9 kV and I = 5 mA, the nozzle to substrate distance of 400 μm and deposition speed of 120 μm s^{-1}

In dADW, particles are carried to the deposition chamber via the argon gas, and their final localisation on the substrate depends on their mass and velocity when leaving the nozzle system. The velocity depends on the NP's position relative to the nozzle's centreline since the gas's velocity profile has a maximum at the centreline and has zero velocity on the nozzle's wall. Therefore, particles closer to the centreline have higher velocity and higher inertia; hence they will more likely deposit on the substrate. Likewise, particles further away from the centreline and closer to the nozzle wall reach lower velocity due to a lower flow velocity; they will less

likely deposit, particularly if their mass is small. Consequently, most particles in the centric region of the flow ended up on the substrate and formed the centric region of the patterned line (a yellowish region in Figure 5.1.a).

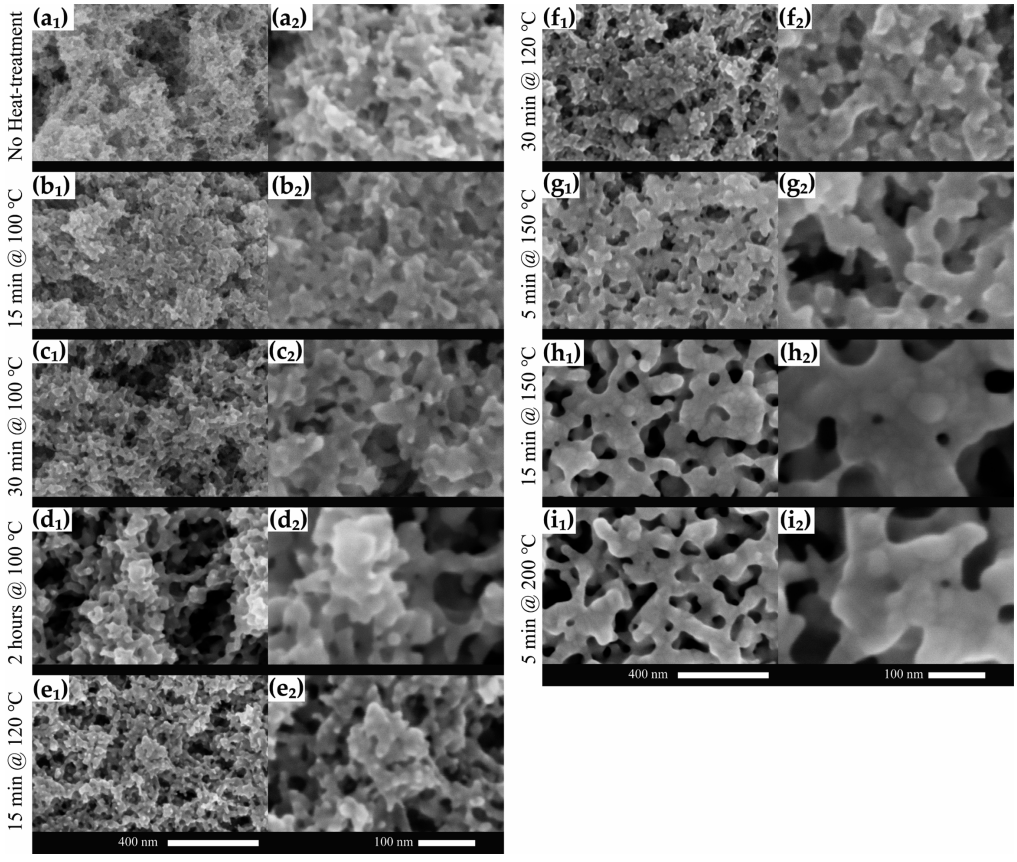

Figure 5.2: (a1, a2) SEM images of the morphology of AuNPs deposited on a silicon substrate and transformation of the morphology (b-i) after thermal post-treatment in a vacuum environment. All AuNPs deposited with SAM voltage/current setting of V = 0.9 kV and I = 5 mA.

Concerning particles far from the centric region of the flow, the majority of them follow the flow and do not deposit, while a minority of them deposit on the substrate but in a broader region (a white-bluish region in Figure 5.1.a). Therefore, the centric region of the line has a higher density of particles than the boundary of the deposited line and causes a Gaussian-like height distribution in the cross-sectional profile, as shown in Figure 5.1-c1 to c5. See Figures C.2.a1 and a2 for comparison between centric region and boundaries.

Figure 5.2.a1 shows a deposited film of AuNPs on a silicon substrate and the film's characteristic morphology in a high-magnification SEM image. The film consists of dense and randomly shaped microstructures formed by aggregation of primary NPs with various sizes and agglomerates, resulting in a high-porosity three-dimensional (3D) structure with nanometric features.

These microstructures have valleys and peaks with hundreds of nanometers difference in height, as indicated in AFM Figure 5.3.a and Figure C.3.a.

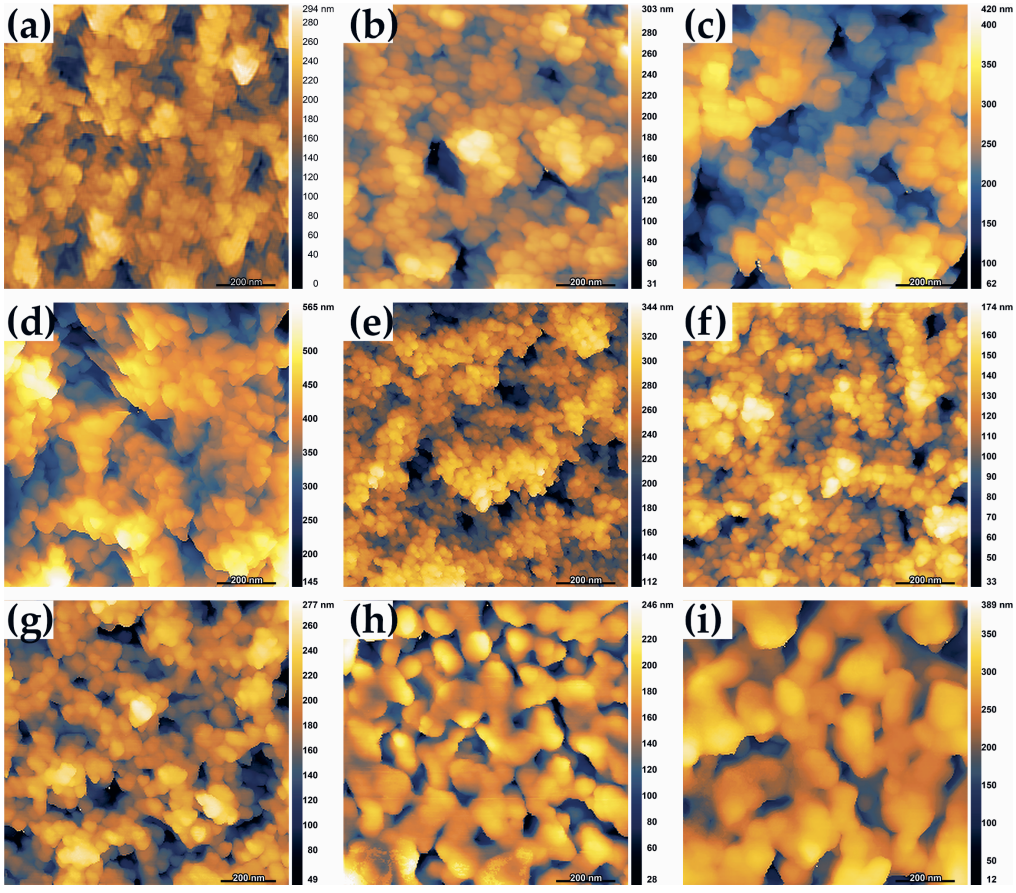

Figure 5.3: AFM morphology of 1.0×1.0 (μm^2) areas of a) non-heat treated samples (b) 15 minutes at 100 ℃, (c) 30 minutes at 100 ℃, (d) 120 minutes at 100 ℃, (e) 15 minutes at 120 ℃, (f) 30 minutes at 120 ℃, (g) 5 minutes at 150 ℃, (h) 15 minutes at 150 ℃, (i) 5 minutes at 200 ℃.

The transformation of the deposited film's surface morphology by different thermal post-treatment is summarised in SEM images in Figure 5.2.b-i, AFM images in Figure 5.3.b-i and Figure C.3.b-i. Comparing SEM images in Figure 5.2.a2-f2 and AFM images in Figure 5.3.a-f, it is possible to see that temperature as high as 120 ℃ is not enough for inducing the coalescence of AuNPs and a significant change in the morphology of the AuNPs film, even by increasing the time of thermal treatment. Increasing the temperature to 150 ℃, AuNPs start to merge, and larger structures are formed as depicted by SEM (Figure 5.2.g1- g2) and AFM (Figure 5.3.g and Figure C.3.g). The further increase of thermal treatment time at 150 ℃ from 5 to 15 minutes promotes the coalescence of AuNPs and the formation of a morphology containing larger nanostructures and voids (Figure 5.2. h1- h2, Figure 5.3. h and Figure C.3.h). A similar microstructure is formed

in the samples thermally treated at 200 ℃ for 5 minutes, as shown in Figure 5.2.i1- i2 and Figure 5.3.i. Looking at the high-magnification SEM images of Figure 5.2. h2 and i2, it is observable that small particles merged to form larger structures, but their boundary is still visible and not entirely reshaped.

The temperatures used for the thermal post-treatment are much lower than the bulk melting temperature of gold (1064℃) but high enough to trigger the coalescence of AuNPs, and the consequent evolution of the film's morphology. Nanoparticles have lower melting temperatures than their bulk counterpart, primarily due to a higher surface-to-volume ratio [35, 36]. This effect becomes more evident when particles' size becomes smaller than 20 nm [35]. Moreover, the impaction deposition on a substrate as a result of dADW forms a dense, highly compacted AuNP film, which can play a positive role in the coalescence of neighbouring particles in the early stage of sintering [37].

5.3.2 Photoluminescence experiment of the deposited film

To study the effect of thermal post-treatment on the optical behaviour of AuNPs film, Photoluminescence (PL) spectroscopy with three laser excitations was employed. 30 PL spectrums were randomly measured in the cross-section of the line for each non-treated and heat-treated samples, along with the PL spectrum of bulk gold in response to laser excitations of 488 nm, 514 nm, and 633 nm (Figure C.4,C.6, and C.8). The PL spectrum of each sample under different laser excitations shows that there are variations in the intensities. To compare the shape of the PL spectrums and their peak position, each spectrum was normalised with its peak intensity; therefore, all spectrums have a maximum unity (Figure C.5, C.7, and C.9). Figure C.5, Figure C.7, and Figure C.9 show the normalised PL spectrums for all samples under different laser excitation, and it can be seen that the normalised PL spectrums of all 30 points for each sample are approximately similar. This similarity in each sample's shape and peak position indicates that the optical property in the line's cross-section is consistent; however, the AuNPs density and particle distribution are different in the line's cross-section. Therefore variation in the intensity of the non-normalised PL spectrum can be regarded as the difference in the density of AuNPs in the centric region of the line compared to the boundary region as depicted in Figure C.2.

Figure 5.4 shows the averaged PL spectrum for each sample, using 30 normalised PL spectrums, along with one for bulk gold under different laser excitations. As shown in Figure 5.4.a and Figure C.5.a-i for laser excitation of 488 nm, spectrums of AuNPs deposited samples have similar shapes, consisting of a broad peak centred around 600-605 nm (2.049-2.066 eV) (Table 5.2). Comparing these results with the PL spectrum of bulk gold (Figure C.5.j), the spectral distribution broadened, and the intensity red-shifted about 110 nm (455 meV), as recorded in Table 5.2. This red-shift in the PL spectrum of AuNPs compared to bulk gold can be attributed to the localised surface plasmon resonance in the AuNPs film's nanostructure. Additionally, the similarity in the shape and peak position of PL spectrums of thermally treated samples compares to non-thermally treated samples indicates that the AuNPs have a weak plasmonic response under 488 nm laser excitation. This weak plasmonic response is also consistent with extinction spectrums of gold nanoparticles with different sizes calculated based on the Mie theorem [38, 39].

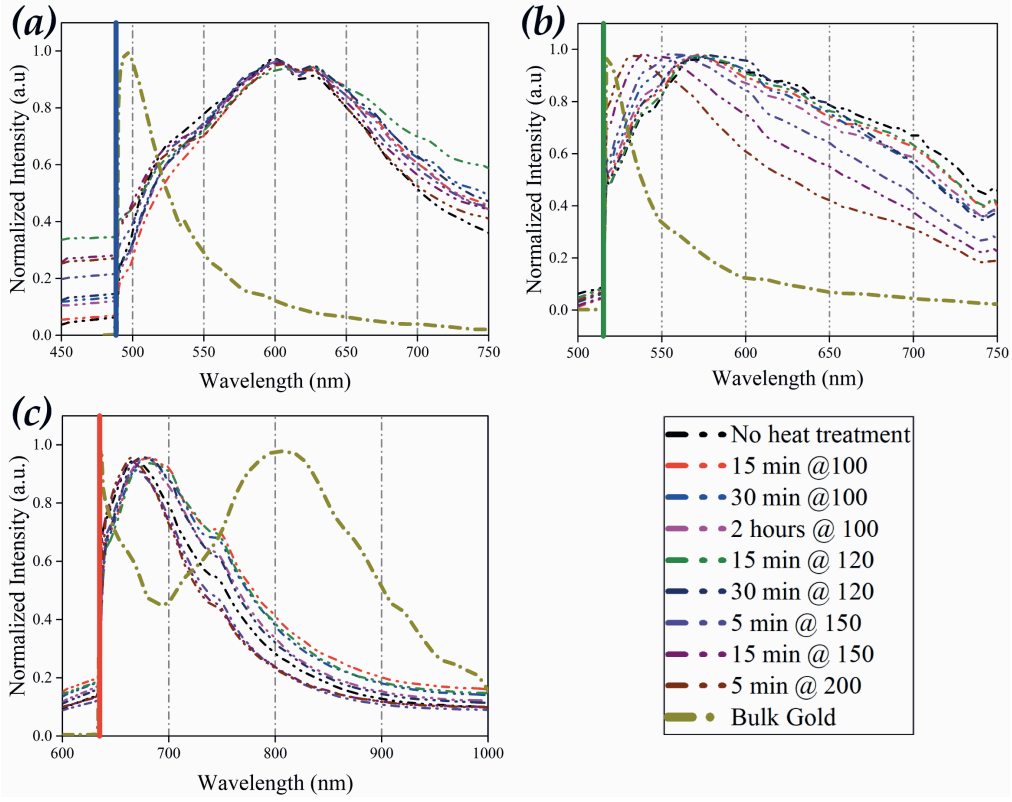

Figure 5.4: The average and normalized photoluminescence response spectrums of non-thermally treated and heat-treated samples compare to bulk gold at excitation laser of a) 488 nm b) 514 nm c) 633 nm. PL measurement conditions: grating of 600 gr $cm^{-}1$, objective lens = 10× (NA = 0.25); for 488 nm laser: acquisition time = 20 s, integration time = 1; for 514 nm laser: acquisition time = 10 s, integration time = 2; 633 nm laser: acquisition time = 10 s, integration time = 1. For all lasers, 30 measurements (3 in length × 10 in cross-section) were performed, and the spectrums were normalized by the highest peak. All AuNPs deposited with SAM voltage/current setting of V = 0.9 kV and I = 5 mA.

Figure 5.4.b shows that the thermal post-treatment significantly affects the PL responses of AuNPs deposited film under 514 nm laser excitation. The PL spectrum of the sample without heat-treatment (Figure C.7.a) has a broad spectrum with maximum luminescence intensity around 577 nm (2.148 eV), which red-shifted about 60 nm (250 meV) compared to bulk gold (Figure C.7.j and Table 5.2). Thermal-treatments of 100 ℃ with a duration of up to 2 hours and 120 ℃ for 30 minutes (Figure C.7.b-f) have no significant effect on the PL spectrum's shape and peak position. However, a further increase in the thermal treatment's temperature or time leads to a significant blue-shift in the luminescence's peak and narrowing the PL spectrum compared to the non-treated AuNPs sample. The PL peaks' position of samples with heat treatment of 5 minutes and 15 minutes at 150 ℃ and 5 minutes at 200 ℃ are 555 nm (2.23 eV), 539 nm (2.3 eV),

and 535 nm (2.317 eV), respectively (Figure C.7.g-i and Table 5.2). Considering the PL spectrums of heat-treated samples, it is observable that heat-treatment causes optical behaviour to move towards the bulk behaviour.

Table 5.2: Position of PL spectrum's peak under laser excitation of 488 nm, 514 nm, and 633 nm for bulk gold, heat-treated samples, and non-thermally treated sample

Sample	Peak position under laser excitation of 488 nm (nm) - (eV)	Peak position under laser excitation of 514 nm (nm) - (eV)	Peak position under laser excitation of 633 nm (nm) - (eV)
No heat treatment	600 - 2.066	577 - 2.148	668 - 1.856
15 minutes at 100 ℃	601 - 2.063	571 - 2.171	683 - 1.815
30 minutes at 100 ℃	601 - 2.063	569 - 2.179	679 - 1.825
2 hours at 100 ℃	602 - 2.059	571 - 2.171	677 - 1.831
15 minutes at 120 ℃	603 - 2.056	573 - 2.163	680 - 1.823
30 minutes at 120 ℃	601 - 2.063	573 - 2.163	677 - 1.831
5 minutes at 150 ℃	601 - 2.063	555 - 2.234	666 - 1.861
15 minutes at 150 ℃	603 - 2.056	539 - 2.300	665 - 1.864

As shown in Figure 5.4.c and recorded in Table 5.2, the luminescence spectrum of bulk gold under 633 nm laser excitation has a broad peak at about 800 nm (1.549 eV). Figure 5.4.c and Figure C.9.a-i show a significant blue-shift of an average 130 nm (300 meV) and narrowing in the PL spectrum distribution of the AuNPs deposited film, with or without heat-treatment, compared to bulk gold. Additionally, heat-treatment of over 150 ℃ leads to PL spectrums with a peak centred around 666 nm (1.861 eV) and a narrower spectrum compared to other heat-treated and non-thermally treated samples. In contrast to the heat-treatment effect on the PL spectrum of AuNPs under 514 nm laser excitation, in 633 nm, heat-treatment causes a more pronounced peak in the PL spectrum far from the bulk spectrum.

5.3.3 SERS experiments on Rhodamine B

To evaluate the AuNPs film's efficiency as a SERS-active substrate, a series of Raman measurements were performed on different Rhodamine B (RhB) concentrations as a probe molecule. Rhodamine B's characteristic Raman peaks lie in the range of 550-1700 cm^{-1}, namely 621 cm^{-1} (for xanthene ring deformation), 1199 cm^{-1} and 1279 cm^{-1} (for C–C bridge band stretching and aromatic C–H bending), 1358 cm^{-1} (for aromatic C–C bending) and 1648 cm^{-1} (for aromatic C–C bending and C=C stretching), which were considered in this study for SERS characterisation. The Raman spectral range can be converted from wavenumber into an absolute wavelength using equation 1 as a laser excitation wavelength function. For 488 nm laser excitation, the RhB spectral range lies in the range of 501.5-532.5 nm; for 514 nm laser excitation, the RhB spectral range is 529.5-564 nm, and for 633 laser excitation, the RhB spectral range is 655.8-709.5 nm. Regarding the relative position of PL peak of AuNPs film and Raman spectral range of RhB, 514 nm and 633 nm laser excitations were chosen for the Raman experiment. A total of 160 Raman measurements (20 points in the cross-section of line and eight different cross-sections) were performed on AuNPs film for different concentrations of RhB.

$$\lambda[nm] = \frac{10^7}{\frac{10^7}{\lambda_{excitation}[nm]} - RamanShift[cm^{-1}]} \tag{5.1}$$

The first sets of experiments are related to RhB detectability, the limit-of-detection (LOD), and the SERS signal's reproducibility on the AuNPs patterns deposited on a silicon substrate. Figure 5.5.a and b reports the Raman spectrum of RhB with concentrations of 1.0×10^{-3}, 1.0×10^{-5}, 1.0×10^{-6}, 1.0×10^{-7}, and 1.0×10^{-8} M, averaged over 160 measured spots under laser excitation of 514 nm and 633 nm, respectively. Comparing the SERS signal of RhB under different laser excitations shows that different characteristic peaks of RhB have different enhancement. This selective enhancement may be related to the relative position of LSPRs in the AuNPs films to the Raman spectral range of RhB.

Considering the 621 cm^{-1}, as the weakest characteristic peaks of RhB under excitation of 514 nm, appeared evidently from 1.0×10^{-3} to 1.0×10^{-7} M of RhB. At the concentration of 1.0×10^{-8} M, the 621 cm^{-1} peak is not observable, but the peak of 1648 cm^{-1} as the strongest peak is present; hence the LOD can be considered as 1.0×10^{-8} M. Using 633 nm laser excitation, all characteristic peaks are distinctively present in concentration as low as 1.0×10^{-7} M. But reducing the concentration to 1.0×10^{-8} M, the background data make the characteristic peaks of RhB less evident.

Figure 5.5.c, d shows the correlation of the main characteristic peaks of RhB with the concentration of the RhB. Comparing the main characteristic peaks of RhB under the laser excitation wavelength of 514 nm and 633 nm, all characteristic peaks decreased about 2 cm^{-1} in the presence of the 633 nm laser, as depicted in Figure 5.5.c and d. This might be related to the shift in the peaks due to the enhanced resonance Raman scattering [40, 41] effect for 514 nm laser excitation as RhB has a sharp peak at 552 nm in UV-Vis absorption [42, 43], which is close to the 514 nm excitation laser. It can be seen from Figure 5.5.c, d that for each characteristic peak and concentration, there is a distribution of intensities, which shows the level of reproducibility of the SERS signal for RhB. The SERS signal distribution for similar concentration and corresponding characteristic peak shows that the 633 nm laser excitation leads to a broader intensity than 514nm, yet both lasers have a good reproducibility level. Moreover, the results indicate that the Raman intensity of each characteristic peak increases with the concentration of RhB. A relatively good linear relationship was obtained between intensity and log[concentration] in the range of 10^{-3} M to 10^{-7} M for all characteristic peaks, with R^2 in the range of 0.95-0.98.

Interestingly, the slopes of the lines at Figure 5.5.c, d under the same wavelength are different for different characteristic peaks, indicating that the SERS enhancement has a different effect on different vibrational modes. Under the wavelength of 514 nm, the Raman characteristic peaks of RhB have higher enhancement by increasing their wavenumber, i.e., 621 cm^{-1} has the lowest enhancement and 1648 cm^{-1} has the highest enhancement. Additionally, the slope of 1648 cm^{-1} is 1354 and 6 times higher than the slope of 621 cm^{-1}, which shows that the 1648 cm^{-1} vibrational mode has a higher enhancement at a lower concentration than 621 cm^{-1}. However, under excitation of 633 nm, the slope of the line has a narrower range between 320 at 1197 cm^{-1} 646 for 619 cm^{-1} and 691 for 1646 cm^{-1}.

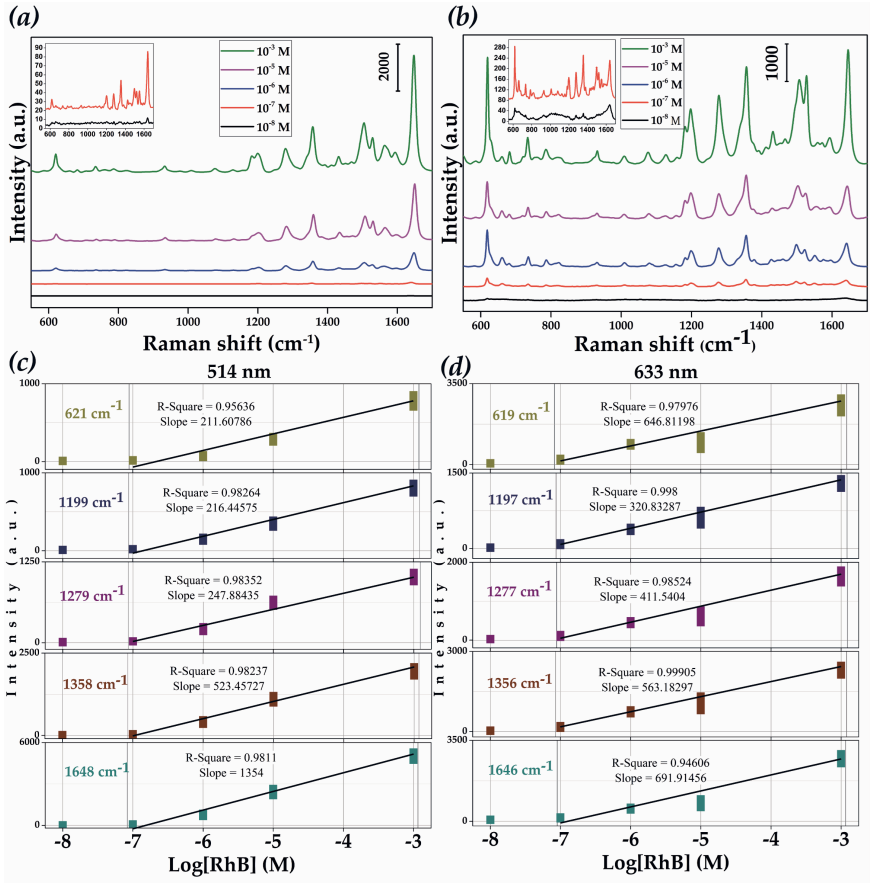

Figure 5.5: Averaged Raman spectrums of 160 measurements on the RhB with concentrations of 1.0×10^{-3}, 1.0×10^{-5}, 1.0×10^{-6}, 1.0×10^{-7}, and 1.0×10^{-8} M RhB adsorbed on AuNPs patterns (a) under laser excitation of 514 nm and, (b) under laser excitation of 633 nm, (the inset in a and b is related to the concentration of 1.0×10^{-7} and 1.0×10^{-8} M RhB). Raman intensities and distribution of 160 main characteristic peaks of RhB at different concentrations under laser excitation of c) of 514 nm and d) 633 nm. Raman measurement conditions for 514 nm argon-ion laser and 633 nm He-Ne laser; acquisition time = 10 s, integration = 2; objective lens = 50× (NA = 0.5).

The second set of experiments is related to the effect of different thermal post-treatments on the SERS performance and enhancement of AuNP films using 1.0×10^{-6} M RhB under laser excitation of 514 and 633 nm. Figure 5.6. a and b show that all characteristic peaks of RhB are distinguishably present for both laser excitations and all heat-treatments. The distributions of 160 intensities for each characteristic peak and laser excitations of 514 nm and 633 nm depicted in Figure 5.6. c and d show that all characteristic peaks of thermally treated samples follow approximately the same trends. For example, all characteristic peaks of samples heat-treated at 150 ℃ for 15 minutes have almost the same distribution level and compared to corresponding

peaks in other samples have the same relations. Considering the results in Figure 5.6, it can be seen that samples with no heat-treatment and heat-treatment of 2 hours at 100 ℃ have better performance than other heat-treatments for the detection of low-concentrated RhB under both laser excitations, with slightly a narrower distribution of 2 hours at 100℃.

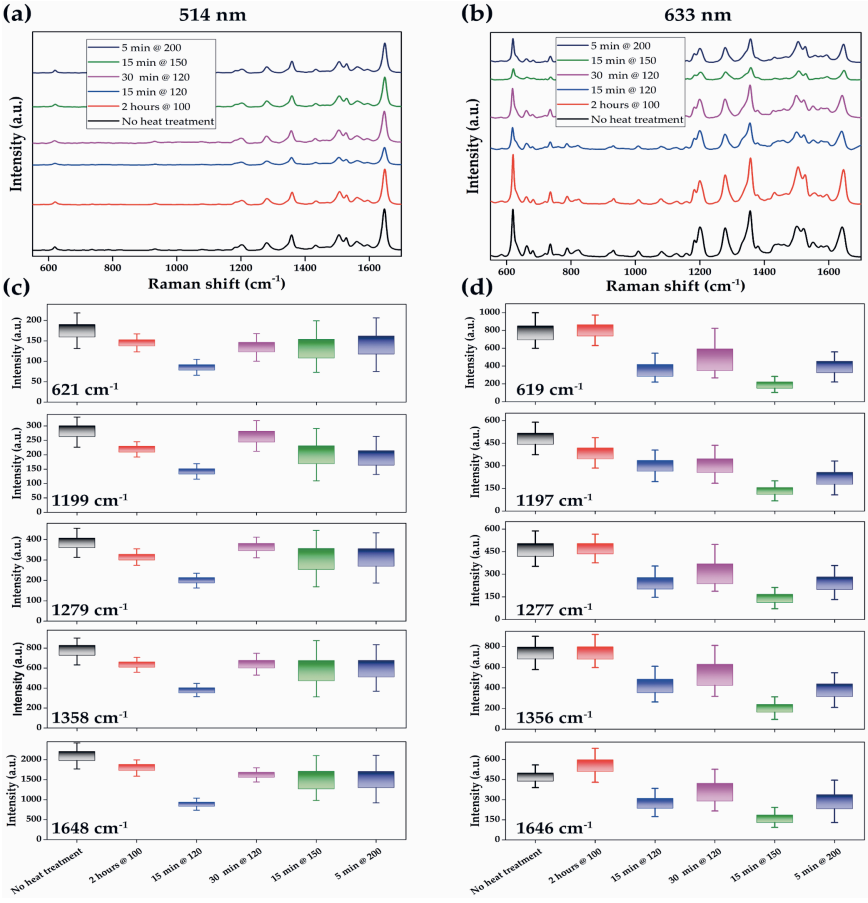

Figure 5.6: Averaged Raman spectrums of 160 measurements on the RhB with concentrations of 1.0×10^{-6}, RhB adsorbed on AuNPs samples without heat-treatment and heat-treatment of 2 hours at 100 ℃, 15 minutes at 120 ℃, 30 minutes at 120 ℃, 15 minutes at 150 ℃, 5 minutes at 200 ℃ (a) under laser excitation of 514 nm and, (b) under laser excitation of 633 nm. Raman intensities and distribution of 160 main characteristic peaks of RhB on different samples c) under laser excitation of 514 nm and d) under laser excitation of 633 nm. Raman measurement conditions for 514 nm argon-ion laser and 633 nm He-Ne laser; acquisition time = 10 s, integration = 2; objective lens = 50× (NA = 0.5).

Increasing the thermal treatment temperature to 120 ℃ leads to more uniform intensity distributions for the 514 nm laser, and for the 633 nm laser, this happens at the thermal treatment of

150 ℃ and 15 min. At the same time, both heat-treatments have the lowest intensities in their corresponding laser excitation. The SERS performance results indicate that heat-treatment leads to a different effect on AuNP films than copper nanoparticles film and does not enhance the SERS signal of RhB [20] as it did for copper SERS substrate.

Comparing the SERS results of different samples in Figure 5.6.c, d indicates that, surprisingly, samples have different intensity distributions for each laser. In Figure 5.6.c, samples with heat treatments of 2 hours at 100 ℃ and 15 minutes at 120 ℃ have the lowest distributions and samples of 15 minutes at 150 ℃ and 5 minutes at 200 ℃ have the highest distribution in the intensities of the characteristic peaks. However, an opposite trend is observable for laser excitation of 633 nm in Figure 5.6.d, which may be related to the relative position of AuNPs' LSPR to the laser excitation wavelength. Therefore, using the same sample may result in different distribution under 514 nm or 633 nm laser excitations.

5.4 Conclusions

The results of this work demonstrate: 1) the potential of the dry aerosol direct writing (dADW) method to deposit very fine gold nanoparticles with a size distribution of 0-20 nm on selected regions on a substrate; 2) the ability to tune the optical behaviour of the deposited film through low-temperature thermal treatment; 3) the suitability of the deposited metal nanoparticles (MNPs) patterns as SERS sensors. The advantage of directly coupling the nanoparticle generator unit with the deposition chamber enables solvent-free additive manufacturing of selectively deposited metal nanoparticles and alloys on wide ranges of substrates, without any need for surface functionalisation or conditioning chemicals in usual wet nanoparticle suspensions.

We demonstrated that AuNPs patterns created by ADW on a silicon substrate have a Gaussian-shaped height distribution containing randomly formed microstructures of hundreds of nanometres' heights. These microstructures are formed by impaction of primary AuNPs or agglomerates of AuNPs on the substrate, caused by the kinetic energy they gained in the converging nozzle, and formed a high-porosity three-dimensional (3D) structure with nanometric features.

We also reported that a low-temperature thermal post-treatment affects the AuNPs patterns' morphology and their optical properties. SEM and AFM imaging revealed that temperatures much lower than the bulk melting point of gold are high enough to alter the microstructure of AuNPs, due to the extremely fine sizes of AuNPs and densely packed nanostructure. The results indicated that at temperatures as low as 150 ℃ and up to 200 ℃, AuNP films' microstructure significantly evolves to form a nanostructure containing voids and networks of bridges. Concerning the optical properties of the manufactured films, photoluminescence (PL) measurement under three laser excitations of 488 nm, 514 nm, and 633 nm shows that the AuNPs patterns have significantly different optical behaviour than bulk gold. Moreover, thermally treated samples' optical behaviour alters with changing the time or temperature of thermal treatment, especially for temperatures higher than 150 ℃ and under laser excitation of 514 nm and 633 nm.

Finally, we explored AuNPs patterns' efficiency as a SERS-active substrate to detect low-concentrated Rhodamine B (RhB) as a probe molecule. We demonstrated that limit-of-detection (LOD) as low as 1.0×10^{-8} M could be achieved using a 514 nm laser excitation and 1.0×10^{-7} with a 633 nm laser. The stronger enhancement of RhB under laser excitation of 514 nm indicates that surface-enhanced resonance Raman scattering is involved in this process. We observed linear relation between the logarithmic concentration of RhB and the intensity of dif-

ferent characteristic peaks of RhB in the range of 1.0×10^{-7} to 1.0×10^{-3} with high coefficients of determination for all characteristic peaks. Moreover, we demonstrated the uniformity of the Raman signal of RhB in 160 random positions on the AuNPs patterns. Although a high level of uniformity of SERS signal is achieved in this study, it should be mentioned that this distribution in SERS signals is related to the distribution of hot-spots on the substrate and the defocusing of the laser beam on the substrate.

Although the heat-treatment of AuNPs did not lead to a significant enhancement of the Raman signal as happened in our previous copper nanopatterns 20, the ability to control the optical behaviour of AuNPs with a simple heat-treatment leads to the fabrication of SERS-active substrates enabling the resonance Raman scattering of analytes with different UV-Vis peaks. This simple tunability of the morphology and, consequently, the metallic nanostructure's optical behaviour through a low-temperature thermal treatment could allow in the future to fabricate patterns with desired optical behaviour. Furthermore, the ability of dADW to selectively deposit nanoparticles of different metals and alloys on wide ranges of substrates (Si, glass, paper, and polymer) and integrability with other manufacturing techniques facilitate the fabrication of new on-chip SERS sensors.

References

[1] M. Liebel, N. Pazos-Perez, N. F. van Hulst, and R. A. Alvarez-Puebla, "Surface-enhanced raman scattering holography," *Nature Nanotechnology*, vol. 15, pp. 1005–1011, 12 2020.

[2] C. Fang, A. Agarwal, K. D. Buddharaju, N. M. Khalid, S. M. Salim, E. Widjaja, M. V. Garland, N. Balasubramanian, and D. L. Kwong, "Dna detection using nanostructured sers substrates with rhodamine b as raman label," *Biosensors and Bioelectronics*, vol. 24, pp. 216–221, 2008.

[3] H.-N. Wang, A. Dhawan, Y. Du, D. Batchelor, D. N. Leonard, V. Misra, and T. Vo-Dinh, "Molecular sentinel-on-chip for sers-based biosensing," *Physical Chemistry Chemical Physics*, vol. 15, p. 6008, 2013.

[4] E.-M. Höhn, R. Panneerselvam, A. Das, and D. Belder, "Raman spectroscopic detection in continuous microflow using a chip-integrated silver electrode as an electrically regenerable surface-enhanced raman spectroscopy substrate," *Analytical Chemistry*, vol. 91, pp. 9844–9851, 2019.

[5] K. H. Chen, M. J. Pan, Z. Jargalsaikhan, T. O. Ishdorj, and F. G. Tseng, "Development of surface-enhanced raman scattering (sers)-based surface-corrugated nanopillars for biomolecular detection of colorectal cancer," *Biosensors*, vol. 10, 2020.

[6] L. Zhang, J. Liu, G. Zhou, and Z. Zhang, "Controllable in-situ growth of silver nanoparticles on filter paper for flexible and highly sensitive sers sensors for malachite green residue detection," *Nanomaterials*, vol. 10, p. 826, 4 2020.

[7] K.-Q. Lin, J. Yi, J.-H. Zhong, S. Hu, B.-J. Liu, J.-Y. Liu, C. Zong, Z.-C. Lei, X. Wang, J. Aizpurua, R. Esteban, and B. Ren, "Plasmonic photoluminescence for recovering native chemical information from surface-enhanced raman scattering," *Nature Communications*, vol. 8, p. 14891, 4 2017.

[8] S.-Y. Ding, J. Yi, J.-F. Li, B. Ren, D.-Y. Wu, R. Panneerselvam, and Z.-Q. Tian, "Nanostructure-based plasmon-enhanced raman spectroscopy for surface analysis of materials," *Nature Reviews Materials*, vol. 1, p. 16021, 6 2016.

[9] A. Y. F. Mahmoud, C. J. Rusin, and M. T. McDermott, "Gold nanostars as a colloidal substrate for in-solution sers measurements using a handheld raman spectrometer," *The Analyst*, vol. 145, pp. 1396–1407, 2020.

[10] B. Sharma, R. R. Frontiera, A. I. Henry, E. Ringe, and R. P. V. Duyne, "Sers: Materials, applications, and the future," *Materials Today*, vol. 15, pp. 16–25, 2012.

[11] B. Doiron, M. Mota, M. P. Wells, R. Bower, A. Mihai, Y. Li, L. F. Cohen, N. M. N. Alford, P. K. Petrov, R. F. Oulton, and S. A. Maier, "Quantifying figures of merit for localized surface plasmon resonance applications: A materials survey," *ACS Photonics*, vol. 6, pp. 240–259, 2019.

[12] K. A. Willets and R. P. V. Duyne, "Localized surface plasmon resonance spectroscopy and sensing," *Annual Review of Physical Chemistry*, vol. 58, pp. 267–297, 5 2007.

[13] K. Ataka, S. T. Stripp, and J. Heberle, "Surface-enhanced infrared absorption spectroscopy (seiras) to probe monolayers of membrane proteins," *Biochimica et Biophysica Acta (BBA) - Biomembranes*, vol. 1828, pp. 2283–2293, 10 2013.

[14] J. F. Li, C. Y. Li, and R. F. Aroca, "Plasmon-enhanced fluorescence spectroscopy," 2017.

[15] M. Bauch, K. Toma, M. Toma, Q. Zhang, and J. Dostalek, "Plasmon-enhanced fluorescence biosensors: a review," *Plasmonics*, vol. 9, pp. 781–799, 8 2014.

[16] E. Kohr, B. I. Karawdeniya, J. R. Dwyer, A. Gupta, and W. B. Euler, "A comparison of sers and mef of rhodamine 6g on a gold substrate," *Phys. Chem. Chem. Phys.*, vol. 19, pp. 27074–27080, 2017.

[17] J. K. Majhi and P. K. Kuiri, "Enhancement of spectral shift of plasmon resonances in bimetallic noble metal nanoparticles in core–shell structure," *Journal of Nanoparticle Research*, vol. 22, p. 86, 4 2020.

[18] G. Neri, E. Fazio, P. G. Mineo, A. Scala, and A. Piperno, "Sers sensing properties of new graphene/gold nanocomposite," *Nanomaterials*, vol. 9, pp. 1–13, 2019.

[19] Q. LI, Y. LYU, T. PAN, D. LI, H. LU, and Y. GONG, "Development of a coupled supersonic inlet-fan navier–stokes simulation method," *Chinese Journal of Aeronautics*, vol. 31, pp. 237–246, 2018.

[20] S. Aghajani, A. Accardo, and M. Tichem, "Aerosol direct writing and thermal tuning of copper nanoparticle patterns as surface-enhanced raman scattering sensors," *ACS Applied Nano Materials*, vol. 3, pp. 5665–5675, 6 2020.

[21] S. Harmsen, M. A. Wall, R. Huang, and M. F. Kircher, "Cancer imaging using surface-enhanced resonance raman scattering nanoparticles," *Nature Protocols*, vol. 12, pp. 1400–1414, 7 2017.

[22] S. Harmsen, S. Rogalla, R. Huang, M. Spaliviero, V. Neuschmelting, Y. Hayakawa, Y. Lee, Y. Tailor, R. Toledo-Crow, J. W. Kang, J. M. Samii, H. Karabeber, R. M. Davis, J. R. White, M. van de Rijn, S. S. Gambhir, C. H. Contag, T. C. Wang, and M. F. Kircher, "Detection of premalignant gastrointestinal lesions using surface-enhanced resonance raman scattering-nanoparticle endoscopy.," *ACS nano*, vol. 13, pp. 1354–1364, 2 2019.

[23] Y. Liu, Y. Chen, Y. Zhang, Q. Kou, Y. Zhang, Y. Wang, L. Chen, Y. Sun, H. Zhang, and Y. MeeJung, "Detection and identification of estrogen based on surface-enhanced resonance raman scattering (serrs).," *Molecules (Basel, Switzerland)*, vol. 23, p. 1330, 6 2018.

[24] F. Nicolson, L. E. Jamieson, S. Mabbott, K. Plakas, N. C. Shand, M. R. Detty, D. Graham, and K. Faulds, "Surface enhanced resonance raman spectroscopy (serrs) for probing through plastic and tissue barriers using a handheld spectrometer.," *The Analyst*, vol. 143, pp. 5965–5973, 12 2018.

[25] L. Petti, R. Capasso, M. Rippa, M. Pannico, P. L. Manna, G. Peluso, A. Calarco, E. Bobeico, and P. Musto, "A plasmonic nanostructure fabricated by electron beam lithography as a sensitive and highly homogeneous sers substrate for bio-sensing applications," *Vibrational Spectroscopy*, vol. 82, pp. 22–30, 1 2016.

[26] T.-J. Wang, K.-C. Hsu, Y.-C. Liu, C.-H. Lai, and H.-P. Chiang, "Nanostructured sers substrates produced by nanosphere lithography and plastic deformation through direct peel-off on soft matter," *Journal of Optics*, vol. 18, p. 055006, 5 2016.

[27] P. C. Wuytens, A. G. Skirtach, and R. Baets, "On-chip surface-enhanced raman spectroscopy using nanosphere-lithography patterned antennas on silicon nitride waveguides," *Optics Express*, vol. 25, p. 12926, 5 2017.

[28] C.-C. Ho, K. Zhao, and T.-Y. Lee, "Quasi-3d gold nanoring cavity arrays with high-density hot-spots for sers applications via nanosphere lithography," *Nanoscale*, vol. 6, pp. 8606–8611, 2014.

[29] M. Tahghighi, D. Janner, and J. Ignés-Mullol, "Optimizing gold nanoparticle size and shape for the fabrication of sers substrates by means of the langmuir–blodgett technique," *Nanomaterials*, vol. 10, p. 2264, 11 2020.

[30] N. Schwenk, B. Mizaikoff, S. Cárdenas, and Ángela I. López-Lorente, "Gold-nanostar-based sers substrates for studying protein aggregation processes.," *The Analyst*, vol. 143, pp. 5103–5111, 10 2018.

[31] Z. Fusco, R. Bo, Y. Wang, N. Motta, H. Chen, and A. Tricoli, "Self-assembly of au nanoislands with tuneable organized disorder for highly sensitive sers," *Journal of Materials Chemistry C*, vol. 7, pp. 6308–6316, 2019.

[32] Y. Song, T. Xu, L.-P. Xu, and X. Zhang, "Superwettable nanodendritic gold substrates for direct mirna sers detection.," *Nanoscale*, vol. 10, pp. 20990–20994, 12 2018.

[33] N. S. Tabrizi, M. Ullmann, V. A. Vons, U. Lafont, and A. Schmidt-Ott, "Generation of nanoparticles by spark discharge," *Journal of Nanoparticle Research*, vol. 11, pp. 315–332, 2 2009.

[34] N. S. Tabrizi, Q. Xu, N. M. van der Pers, and A. Schmidt-Ott, "Generation of mixed metallic nanoparticles from immiscible metals by spark discharge," *Journal of Nanoparticle Research*, vol. 12, pp. 247–259, 1 2010.

[35] G. Guenther and O. Guillon, "Models of size-dependent nanoparticle melting tested on gold," *Journal of Materials Science*, vol. 49, pp. 7915–7932, 2014.

[36] P. Buffat and J.-P. P. Borel, "Size effect on the melting temperature of gold particles," *Physical Review A*, vol. 13, pp. 2287–2298, 6 1976.

[37] E. Goudeli and S. E. Pratsinis, "Crystallinity dynamics of gold nanoparticles during sintering or coalescence," *AIChE Journal*, vol. 62, pp. 589–598, 2 2016.

[38] P. K. Jain, K. S. Lee, I. H. El-Sayed, and M. A. El-Sayed, "Calculated absorption and scattering properties of gold nanoparticles of different size, shape, and composition: Applications in biological imaging and biomedicine," *Journal of Physical Chemistry B*, vol. 110, pp. 7238–7248, 2006.

[39] G. V. Hartland, "Optical studies of dynamics in noble metal nanostructures," *Chemical Reviews*, vol. 111, pp. 3858–3887, 2011.

[40] R. A. Álvarez Puebla, "Effects of the excitation wavelength on the sers spectrum," *The Journal of Physical Chemistry Letters*, vol. 3, pp. 857–866, 4 2012.

[41] G. McNay, D. Eustace, W. E. Smith, K. Faulds, and D. Graham, "Surface-enhanced raman scattering (sers) and surface-enhanced resonance raman scattering (serrs): A review of applications," *Applied Spectroscopy*, vol. 65, pp. 825–837, 2011.

[42] AL-Jobouri, "Adsorption study of rhodamin b dye on iraqi bentonite and modified bentonite by nanocompounds tio₂, zno, al₂o₃ and sodium dodecyl sulfate," *American Journal of Environmental Sciences*, vol. 9, pp. 269–279, 3 2013.

[43] L. Zhang, P. Li, L. Luo, X. Bu, X. Wang, B. Zhao, and Y. Tian, "Sensitive detection of rhodamine b in condiments using surface-enhanced resonance raman scattering (serrs) silver nanowires as substrate," *Applied Spectroscopy*, vol. 71, pp. 2395–2403, 2017.

6

Conclusions & Recommendations

6.1 Conclusions

This dissertation proposes a novel, simple, solvent-free direct writing method for the selective deposition of nanoparticles within micrometric patterns. Furthermore, it evaluates the morphological and optical properties of the deposited patterns, as well as the degree of control of these properties via post-deposition thermal treatment. Additionally, it investigates the performance of the proposed manufacturing method for the development of surface-enhanced Raman scattering (SERS) devices. This chapter summarizes the achieved findings addressing the primary research objectives, which were defined in **Chapter 1**.

1. Evaluating the effect of process and nozzle design parameters on the resolution of patterns consisting of <100nm diameter nanoparticles

In the context of particles in a flow and using aerosol physics, it is proved that the most important force for < 100 nm nanoparticles is the steady flow Stokes drag force, while other forces are negligible in comparison. The performance of two aerodynamic focusing strategies, converging nozzle (CN) and sheath-gas nozzle (SGN), for writing high-resolution and sharp patterns is investigated. The effect of various design and process parameters on the performance of each nozzle is evaluated numerically. The computational cost of nozzle evaluation and optimization is greatly reduced by not taking into account minor forces in the particle trajectory calculation. Numerical analysis revealed that, unlike the CN, the SGN can collimate particles within the nozzle while being less sensitive to design parameters. Moreover, it is found that the collection efficiency (CE) and focusing ratio (FR) both improved in presence of the SGN and smaller particles (< 10 nm) are collected on the substrate. The results showed that SGN could write narrower lines than CN with equal nozzle diameters, and even with larger working distances, down to 27% of nozzle diameter due to the confinement of the main flow in the centric region caused by a secondary flow. Combining these parameters simplifies the manufacturing of nozzles capable of printing patterns with feature sizes smaller than 100 μm. Furthermore, experimental results revealed that lines printed with CN have a large splash zone, compromising the sharpness of the lines, whereas SGN printed lines have a clear boundary and high sharpness. In light of these investigations, it is, therefore, possible to conclude that dADW using SGN for aerosol flow focusing is capable of fabricating patterns with a wide range of line widths and high sharpness. Moreover, the use of modular SGN with commercial dispensing tips, as introduced in Section 3.4, enables the dADW of fabricating high-resolution patterns with a wide range of widths (20-1000 μm). In conclusion, this study shows that dADW can compete with commercial solution-based nanoparticle deposition methods such as AerosolJet printing and Inkjet printing in printing high-resolution narrow lines while avoiding the disadvantages of wet methods such as the presence of chemical agents.

2. Investigating the effect and level of control over the morphology and optical properties of nanoparticle film using post-deposition thermal treatment

As-deposited Cu and Au NP films have similar morphology, microstructure, and nanostructure, with dense and randomly shaped microstructures formed by primary NPs and agglomerates. These structures feature various sizes, resulting in a high-porosity three-dimensional (3D) architecture composed by nanometric features. The morphology similarities are due to the

deposition mechanism, which is a kinetic deposition and is not material dependent. These microstructures display valleys and peaks with height differences of hundreds of nanometres. To address the second goal of this dissertation, the level of control and evolution of NP morphology through post-deposition low-temperature thermal treatment is investigated. The nature of the obtained morphology was discovered to be dependent on the material, oxidation level, time, and temperature of the thermal treatment. It is also shown that heat treatment of copper causes first the reduction of cupric oxide (CuO) to cuprous oxide (Cu_2O), followed by the coalescence of nanoparticles to form larger structures. This reduction of CuNPs prior to coalescence requires more time for micro and nanostructural alteration compared AuNPs, and the resulting structure has a fundamentally different form where the treatment of copper nanoparticles results in the formation of multi-facet, crystalline-like microstructures with sharp edges and corners.

Unlike Cu, Au nanoparticles are chemically stable and do not oxidize during or after deposition; thus, during post-deposition thermal treatment, they only go through a coalescence process, which takes up to 5 min compared to 120 min for copper. It is also found that the thermal treatment of AuNPs leads to significantly different microstructures compared to CuNPs. The resulting AuNPs microstructure is composed of larger structures, voids and networks of bridges, similar to the morphology of gold nanofoam achieved through wet methods such as solution-based reduction synthesis [1] or selective etching of Ag in Ag-Au alloys [2]. Furthermore, it is demonstrated that the evolution of the AuNPs film morphology directly affects the optical properties of the patterns. It has been discovered that the optical behaviour of AuNPs patterns differs significantly from that of bulk gold and that this property can be controlled and tuned using post-deposition thermal treatment. The optical behaviour of thermally treated samples changes as the time or temperature of thermal treatment is changed, especially at temperatures above 150 ℃. Because of the ease with which the morphology and optical properties can be controlled and tuned via simple and low-temperature thermal treatment, the dADW method can be used to enable a wide range of functionalities such as surface-enhanced Raman scattering.

3. Exploring the performance of nanoparticle patterns as SERS-active substrates

The performance of Cu and Au NPs patterns as a SERS-active substrate is investigated to address the dADW's ability to fabricate patterns enabling specific functionality. It has been discovered that as-deposited CuNPs patterns are able to detect a reference dye (Rhodamine B (RhB)) at concentrations as low as 1 μM, whereas AuNPs can detect RhB at concentrations as low as 10 nM. This difference is attributed to the intrinsic gold's plasmonic enhancement higher than the enhancement of copper and to gold's chemical stability, as copper oxidizes and compromises plasmonic enhancement. Furthermore, it has been discovered that the SERS enhancement of CuNPs patterns is strongly dependent on thermal treatment and improves by a factor of ten due to structural enlargement and the formation of sharp corners and edges, which significantly impact local electromagnetic enhancement. However, unlike CuNPs patterns, heat-treated AuNPs did not significantly enhance the Raman signal but improved the uniformity of the Raman signal across the pattern. The ability to control the optical behaviour of AuNPs led to the development of SERS substrates, which enabled the resonance Raman scattering of analytes with different UV-Vis peaks. The selective deposition of metal NPs on various substrates, the ease with which the morphology and optical properties can be controlled, and the compatibility with other fabrication methods can pave the way for the realization of SERS sensors integrated into a microfluidic device.

6.2 Recommendations

This dissertation presents a novel and simple method for selective deposition of very fine nanoparticles in a dry regime on a wide range of substrates. Furthermore, it demonstrated the effect of post-processing on material and optical properties, as well as the fabrication of applications such as SERS. This work lays the basis for dADW nanoparticle deposition and application development, but there is still room for advancement in dADW and related applications:

- As explained in **Chapter 3**, the number of particles that reach the nozzle is determined by the volumetric flow rate that can pass through the nozzle, which is a function of the nozzle diameter and the ratio of upstream to downstream pressure. The average flow velocity and particle velocity depend on the volumetric flow rate, which defines the time particles need to travel from the generation site to the deposition site. Moreover, as discussed in **Chapter 3**, the agglomeration of particles varies when the travel time changes. Changing the ratio of aerosol to the total flow rate in an existing dADW system using SGN causes changes in the number of particles reaching the nozzle and the particle agglomeration state, resulting in changes in pattern porosity and density, and resolution. More research is needed to decouple particle numbers from volumetric flow rate and to have a constant or tuneable particle density featuring the same agglomeration state regardless of volumetric flow rate.

- The particle size delivered by SAM ranges from 0 to 20 nm for primary particles. However, due to their stronger plasmonic behaviour, larger particle sizes are required for many applications, such as those related to plasmonics in the visible range (e.g. SERS). Because of the energy and temperature of the system, nucleation and coalescence are isotropic in the early phase of particle formation, but as temperature decreases, isotropic growth ceases, and the particles grow by agglomeration and form arbitrary sizes and shapes. Previous research in the aerosol field has shown that a tube furnace with a temperature as high as 1000 ℃ in part of the particle trajectory can extend the particle distribution over 20 nm. This element can extend the isotropic growth of particles or provide enough energy for agglomerates to evolve to spherical shapes by sintering [3, 4]. Adding a tube furnace or other instrumentation that allows for the extension of isotropic growth and sintering will extend this approach to the creation and deposition of bigger particles.

- In this dissertation, we focused on post-deposition low-temperature thermal treatment for controlling and tuning the morphology and optical properties of the NPs patterns. Although the effectiveness of thermal treatment aided in the manufacture of functional patterns with dADW, vacuum ovens use a significant amount of energy and heat a vast area. In comparison to vacuum ovens, a laser sintering technology that can be integrated within the deposition chamber and impose local sintering during deposition requires less energy since it does not need to heat up the whole system. The localizability of laser sintering allows for sintering to be imposed in the desired location rather than over the entire area. This is significant in light of the results of **Chapter 5**, which demonstrated that different sintering times and temperatures have different optical properties, which can all be generated in one pattern using local sintering.

- This dissertation focused on mono-metal nanoparticles such as copper and gold for micropatterning purposes and further applications such as surface-enhanced Raman scat-

tering. SAM is able to generates other mono-metal materials such as nickel, aluminium, and platinum and bi-metal or alloy nanoparticles. Therefore, it is suggested to explore further the creation of bi-metal or alloy nanoparticle patterns using dADW, which can have novel features and applications, such as gas sensing, bio-sensing and catalysis.

References

[1] F. J. Burpo, E. A. Nagelli, L. A. Morris, J. P. McClure, M. Y. Ryu, and J. L. Palmer, "Direct solution-based reduction synthesis of au, pd, and pt aerogels," *Journal of Materials Research*, vol. 32, pp. 4153–4165, 11 2017.

[2] A. J. Welch, J. S. Duchene, G. Tagliabue, A. Davoyan, W. H. Cheng, and H. A. Atwater, "Nanoporous gold as a highly selective and active carbon dioxide reduction catalyst," *ACS Applied Energy Materials*, vol. 2, pp. 164–170, 1 2019.

[3] A. A. Lizunova, A. A. Efimov, P. V. Arsenov, and V. V. Ivanov, "Influence of the sintering temperature on morphology and particle size of silver synthesized by spark discharge," *IOP Conference Series: Materials Science and Engineering*, vol. 307, p. 012081, 2 2018.

[4] J. Harra, J. Mäkitalo, R. Siikanen, M. Virkki, G. Genty, T. Kobayashi, M. Kauranen, and J. M. Mäkelä, "Size-controlled aerosol synthesis of silver nanoparticles for plasmonic materials," *Journal of Nanoparticle Research*, vol. 14, pp. 1–10, 6 2012.

A

Appendix A

This chapter provides supplementary information for chapter 3, including experimental measurements such as white light interferometry, scanning electron microscopy, optical microscopy, and numerical results.

The contents of this chapter have been published as supplementary information in:

- Aghajani, S., Accardo, A., & Tichem, M. (2022). Process and nozzle design for high-resolution dry aerosol direct writing (dADW) of sub-100 nm nanoparticles. Additive Manufacturing, 54, 102729. DOI:10.1016/J.ADDMA.2022.102729

A.1 Modelling

The governing equation for flow profile calculations are as follows:

$$\begin{aligned}
&\nabla.\left(\rho_f V_f\right) = 0 \\
&\rho_f\left(V_f \cdot \nabla\right) V_f = \nabla \cdot \left[-pI + \left(\mu_f + \mu_T\right)\left(\nabla V_f + \left(\nabla V_f\right)^T\right) - (\tfrac{2}{3})\left(\mu_f + \mu_T\right)\left(\nabla \cdot V_f\right) I - (\tfrac{2}{3})\rho_f k I\right] \\
&\rho_f C_p V_f \cdot \nabla T - k_t \nabla^2 T = Q
\end{aligned} \tag{A.1}$$

Where ρ_f, V_f, p, μ_f, μ_T, C_P, k_t, T, and Q are the gas density, gas velocity, pressure, dynamic viscosity, turbulent dynamic viscosity, heat capacity at constant pressure, thermal conductivity, gas temperature, and heat source, respectively. The turbulent model is simulated using the Reynolds-averaged Navier–Stokes (RANS) model, including the k–ε model. The following are the k–equations for turbulent kinetic energy (k) and the ε-equations for turbulent dissipation rate (ε):

$$\begin{aligned}
&\rho_f\left(V_f \cdot \nabla\right) k = \nabla \cdot \left[\left(\mu_f + \frac{\mu_T}{\sigma_\varepsilon}\right)\nabla k\right] + p_k - \rho_f \varepsilon \\
&\rho_f\left(V_f \cdot \nabla\right) \varepsilon = \nabla \cdot \left[\left(\mu_f + \frac{\mu_T}{\sigma_\varepsilon}\right)\nabla \varepsilon\right] + C_{\varepsilon 1}\varepsilon\left(\frac{\varepsilon}{k}\right) p_k - C_{\varepsilon 2}\rho_f\left(\frac{\varepsilon^2}{k}\right) \\
&\mu_T = \rho C_\mu\left(\frac{k^2}{\varepsilon}\right) \\
&p_k = \mu_T\left[\nabla V_f + \left(\nabla V_f\right)^T - \left(\frac{2}{3}\right)\left(\nabla \cdot V_f\right)^2\right] - \left(\frac{2}{3}\right)\rho_f k \nabla \cdot V_f
\end{aligned} \tag{A.2}$$

Sutherland's law, which relates the dynamic viscosity (μ_f) and conductivity (k_t) to the gas temperature and constants dependent on the gas species as follows:

$$\begin{aligned}
&\frac{\mu_f}{\mu_{ref}} = \left(\frac{T}{T_{\mu,ref}}\right)^{\frac{3}{2}}\left(\frac{T_{\mu,ref} + S_{\mu_f}}{T + S_{\mu_f}}\right) \\
&\frac{k_t}{k_{t,ref}} = \left(\frac{T}{T_{t,ref}}\right)^{\frac{3}{2}}\left[\frac{T_{t,ref} + S_{k_t}}{T + S_{k_t}}\right]
\end{aligned} \tag{A.3}$$

Where μ_{ref}= 2.23 × 10^{-5} [Pa.s], $T_{\mu,ref}$=293 [k], S_{μ_f}=152 [K], $k_{t,ref}$=0.0179 [W/(m.K)], $T_{t,ref}$=300 [K], and S_{k_t}=166.7 [K].

A

A.2 White light interferometry (WLI)

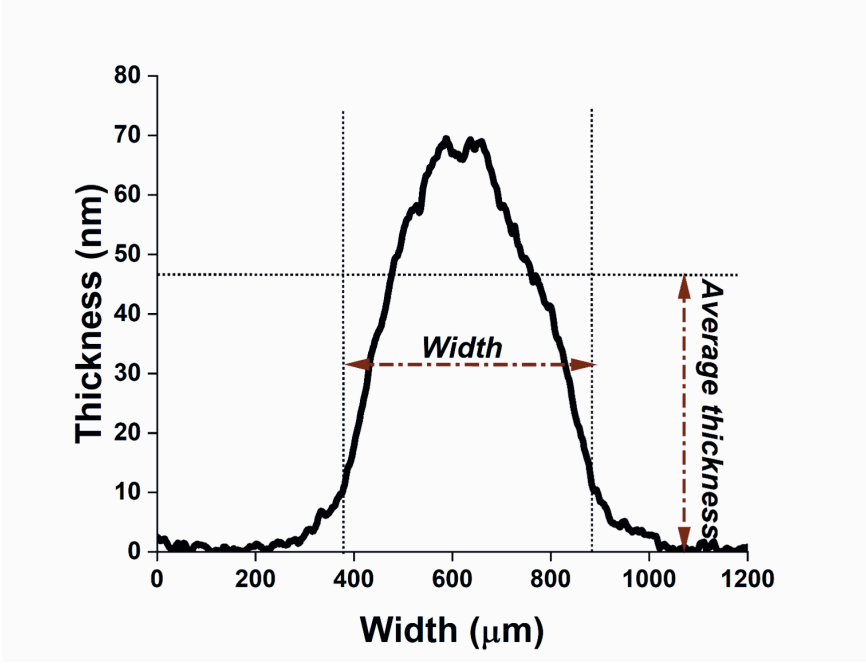

Figure A.1: A typical white light interferometry result of the cross-section of a line and the average thickness and width of a line.

A.3 Simulation results

A.3.1 Gold nanoparticles

Table A.1: Specific design and operating configuration used for each simulation of the converging nozzle

Studying Parameter	Nozzle throat diameter (D-μm)	Angle (θ)	Working distance (μm)	Downstream pressure (Pa)
Angle	400	-	1000	100
Nozzle throat	-	10	$1 \times D$	100
Working distance	400	10	-	100
Downstream pressure	400	10	1000	-

A.3.1.1 Converging nozzle

The contraction factor CF distribution of each particle size in Figure A.2 indicates that this parameter is sensitive to the radial position as is illustrated concerning radial position for gold nanoparticles of various sizes and two angles of 1° and 30° in Figure A.3. a. This distribution of CF is because of variation in the axial and radial velocity of particles due to their radial

position, as shown in Figure A.4 a-h. Figure A.2. a, shows the effect of angle on CF for gold nanoparticles, and it can be seen that CF is highly size-dependent for higher angles (15° and 30°); however, for the lower angle, the difference for CF of the smallest and largest particle is less than 1%. Although in higher angles, particles gain higher inward radial velocities (Figure A.2. e and f), which is beneficial for increasing the CF by pushing particles to the centreline; but increasing the angle lead to decreasing the length of the converging section; therefore, particles have lower time to move toward the centre. Moreover, due to the higher length of the converging section in lower angles, particles have enough time to adapt their axial velocity to the flow's velocity, thus reaching higher velocities as shown in Figure A.4. a.

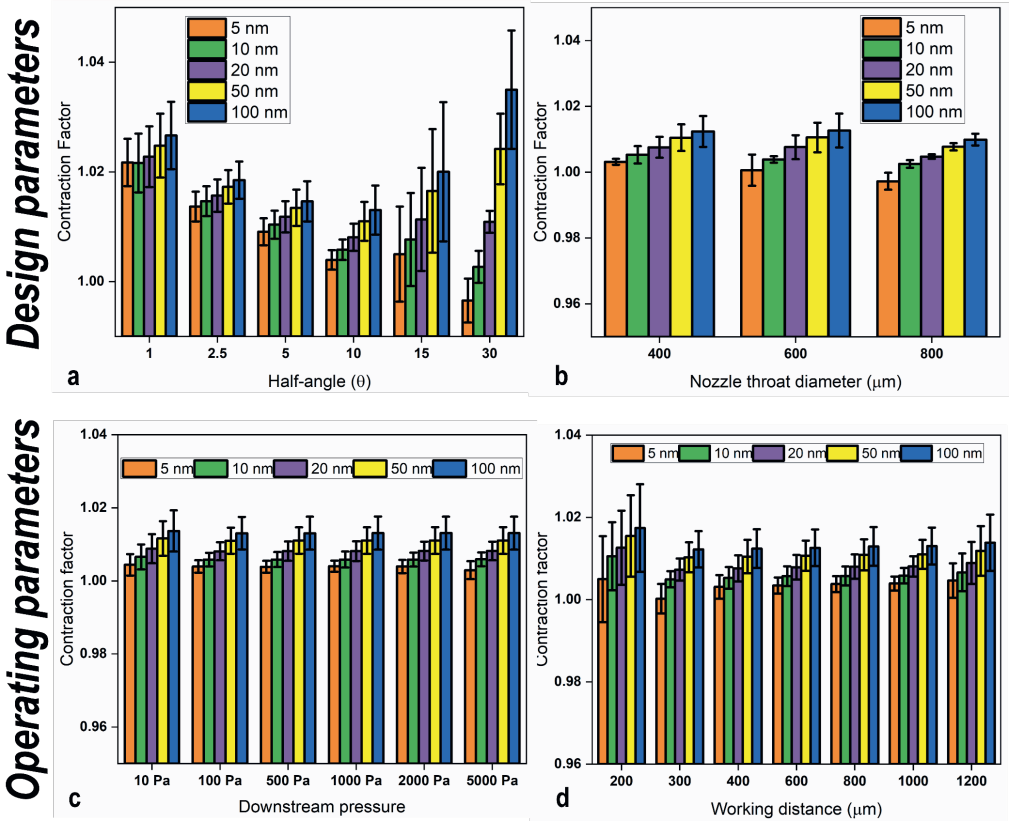

Figure A.2: Contraction factor for gold nanoparticles with sizes indicated in the figure for CN considering design parameters of a) angle of converging nozzle, b) throat diameter, and operating parameters of c) downstream pressure and d) distance between nozzle and the impaction plate.

Considering Figure A.2. b for the effect of nozzle throat diameter on contraction factor, it can be seen that CF is equal unity, which means that the only effect of this nozzle is decreasing the width of the beam due to a decrease in the nozzle diameter. As shown in Figure A.2. c and d, the operating parameters have no significant importance, as it is trivial due to the definition of

A

CF in the nozzle throat, in which flow velocity reaches sonic (Ma=1), and downstream changes have no effect of the upstream.

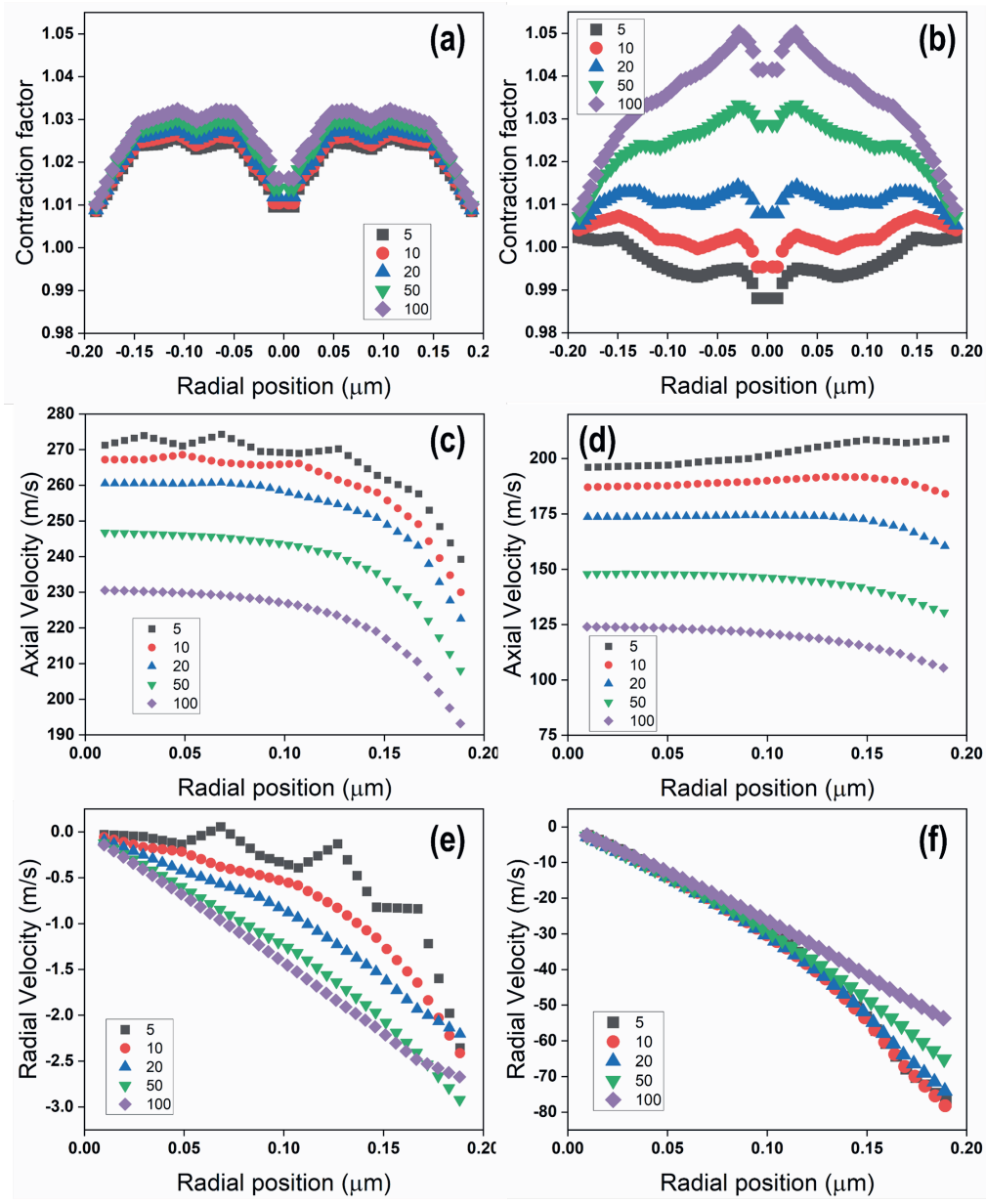

Figure A.3: The CF with respect to the radial position and axial and radial velocity in the radius of nozzle for AuNPs of different sizes as indicated in the figure for converging angles of a), c) and e) 1° and b), d) and e) 30°, respectively.

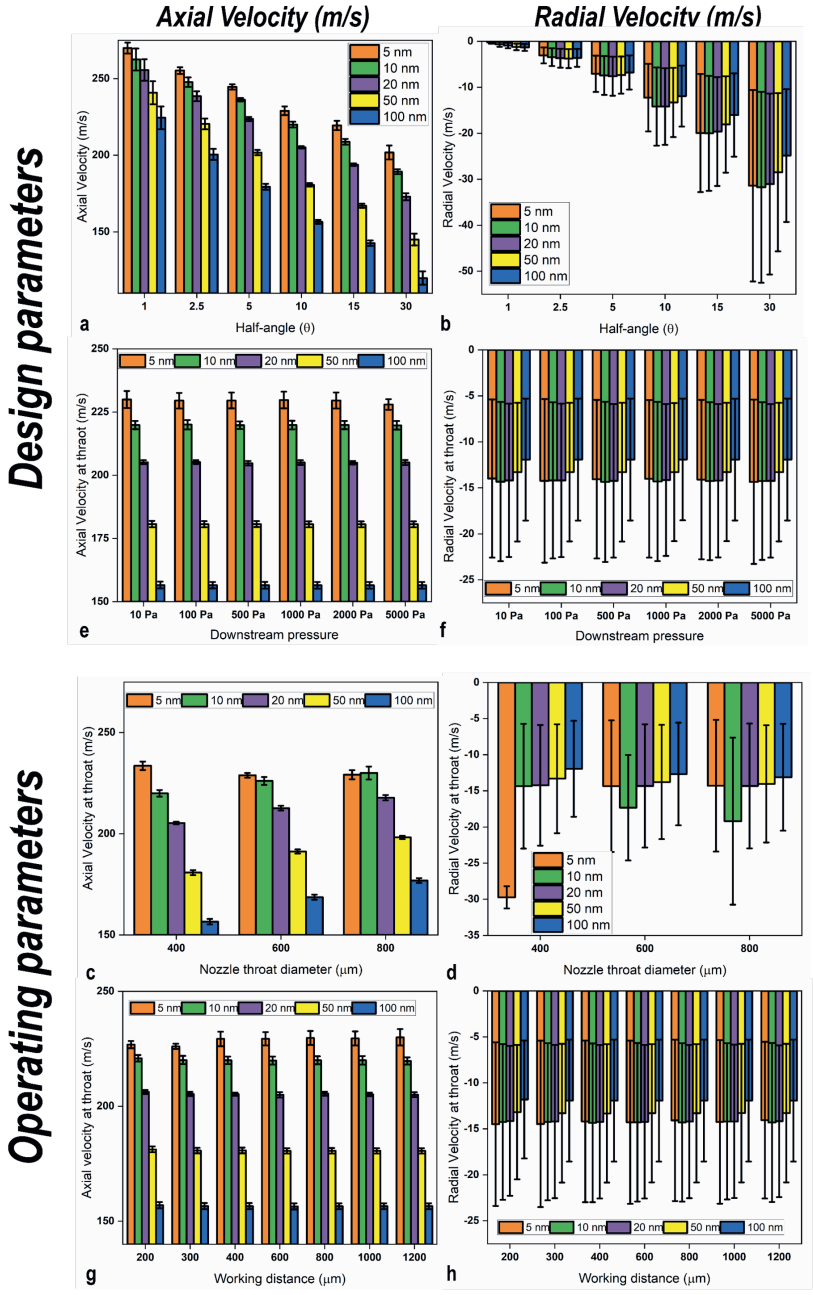

Figure A.4: The axial and radial velocity with sizes indicated in the figure for CN at the throat of the nozzle a) and b) the angle of converging nozzle, c) and d) the throat diameter, e) and f) the downstream pressure and g) and h) the distance between nozzle and the impaction plate (working distance).

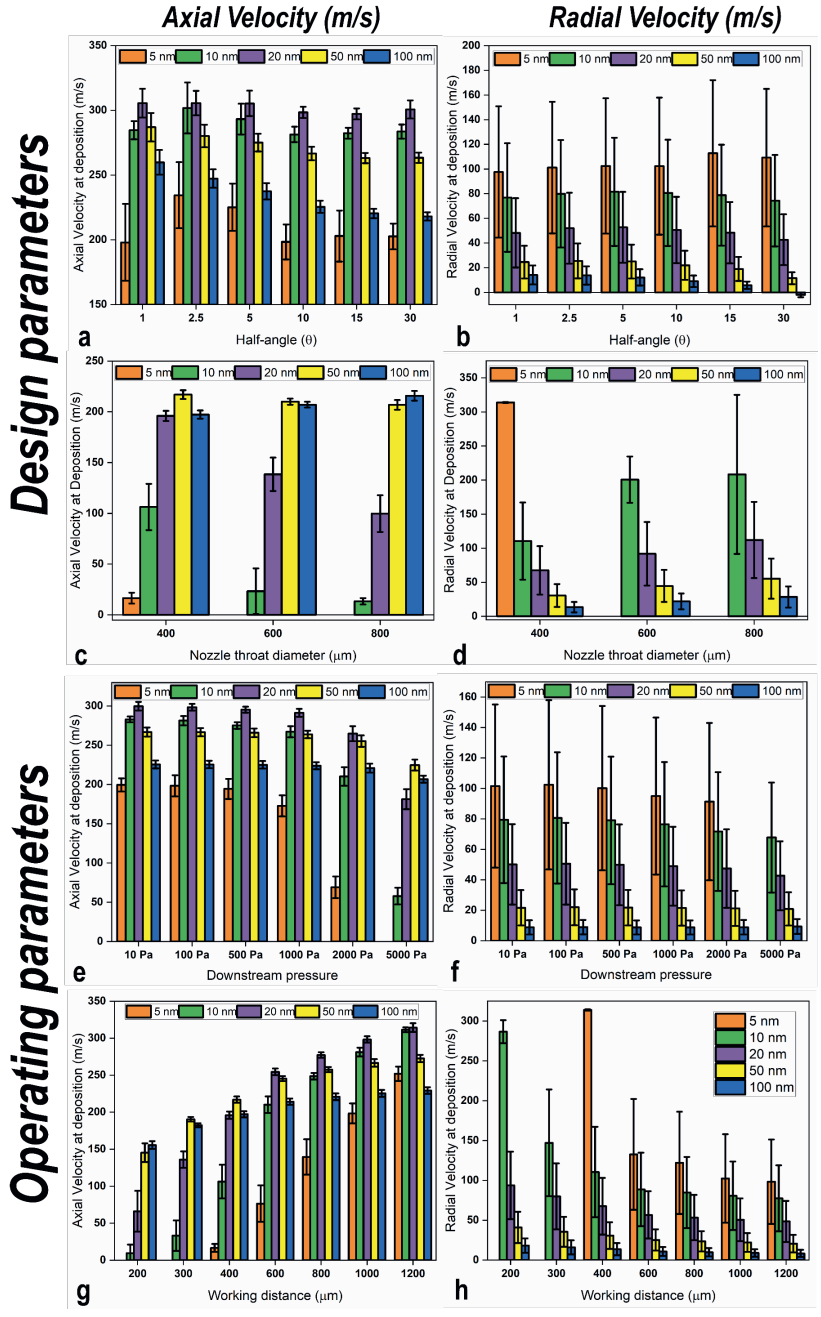

Figure A.5: The axial and radial velocity with sizes indicated in the figure for the CN, when impacting on the impaction plate; a) and b) for the angle of converging nozzle, c) and d) for throat diameter, e) and f) for downstream pressure and g) and h) for WD.

In terms of axial velocity of different particles when they hit the substrate, as shown in Figure A.5.a for different angles, it can be seen that increasing the particle size leads to an increase in the axial velocity until specific sizes, and then decreases. This is due to particle relaxation time and the presence of both an expansion zone and a stagnation zone in the particle path to the impaction plate. Lower relaxation numbers cause particles to adapt faster and gain more velocity in the expansion zone, resulting in a faster drop in velocity in the bow shock, and vice versa. The highest axial velocity on the deposition of gold is for particles with a diameter of 20 nm, and after these sizes, the axial velocity decreases.

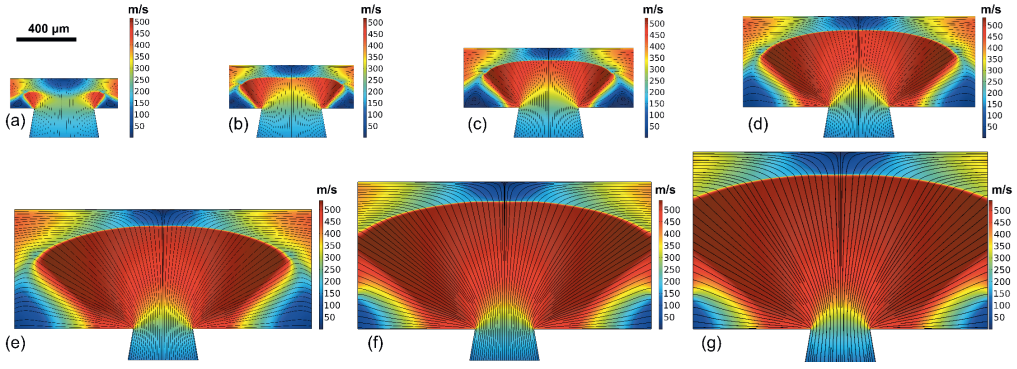

Figure A.6: Velocity field and streamline of the flow after leaving the nozzle and in front of impaction plate for the nozzle to substrate distance of a) 200 µm, WD/D=0.5, b) 300 µm, WD/D=0.75, c) 400 µm, WD/D=1.0, d) 600 µm, WD/D=1.5, e) 800 µm, WD/D=2.0, f) 1000 µm, WD/D=2.5 and g) 1200 µm, WD/D=3.0. For all the simulations, the downstream pressure is set to 100 Pa and the nozzle throat diameter of 400 µm.

A.3.1.2 Sheath gas nozzle

Table A.2: Specific design and operating configuration used for each simulation for sheath gas nozzle

Studying Parameter	Nozzle throat diameter (D-µm)	Angle (θ)	Working distance (µm)	Downstream pressure (Pa)	Aerosol to the total flow
Angle	400	-	400	100	2/8
Inlet nozzle throat	400	10	400	100	2/8
Working distance	400	10	-	100	2/8
Downstream pressure	400	10	400	-	2/8
Aerosol to total flow	400	10	400	100	-

Figure A.7. a shows that the CF is 2.12±2.5% for all particle sizes and aerosol nozzle radius, with slightly better performance for a 1 mm radius. It is also observable in Figure A.8. a and b that this parameter has a negligible effect on the axial and radial velocity of particles, as they gain a majority of their velocity in the converging nozzle. Figure A.7. b present the result for the effect of the converging angle on the contraction factor. The most interesting aspect of this graph is that the angle of the converging nozzle has minimal effect on the CF up to 15° and even has negligible effect considering the size and density of particles, which is entirely different from the converging nozzle. Moreover, even at an angle as high as 30° , the difference between CF for

different particles sizes is less than 2%. Considering the axial and radial velocity at the throat for different angles as shown in Figure A.8. c and d, it is evident that similar to the converging nozzle, increasing the angle leads to a decrease in the axial velocity and an increase in the radial velocity but has not a significant effect on the CF. As mentioned for converging nozzles and considering Figure A.7. c and d, the operating parameter of downstream pressure and working distance have a negligible impact (< 2%) on the CF since they influence the flow field when the gas leaves the nozzle. These parameters do not affect particles' axial and radial velocity at the throat, as depicted in Figure A.8. e-h.

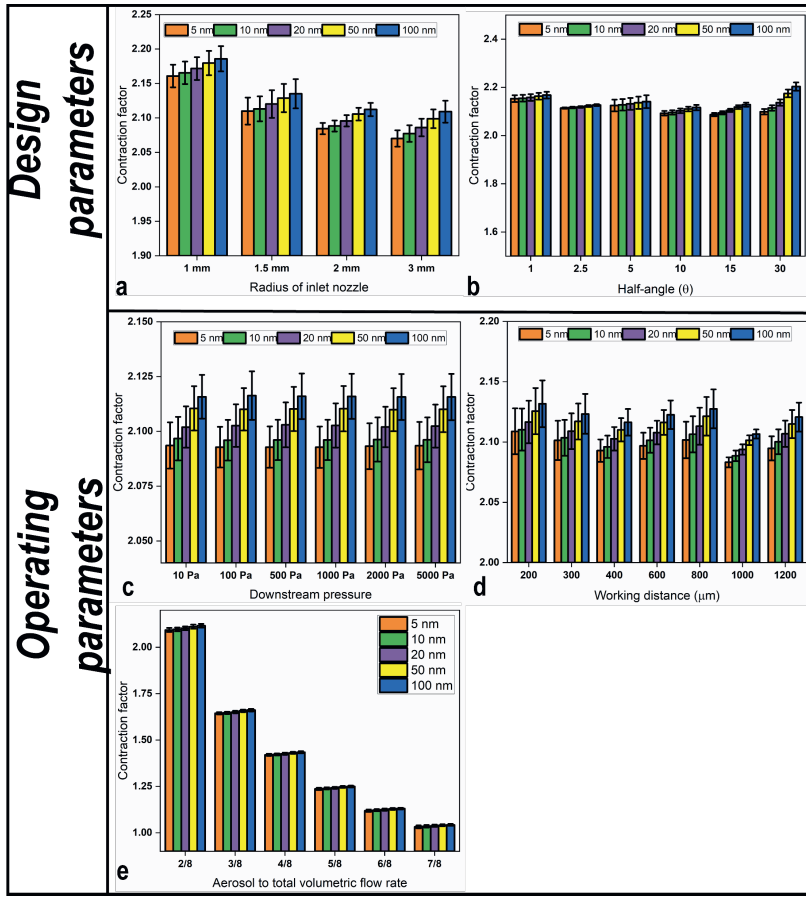

Figure A.7: Contraction factor for AuNPs with sizes indicated in the figure for SGN considering design parameters of, a) Aerosol throat diameter, b), angle of the converging nozzle and operating parameters of c) downstream pressure, d) WD, and e) the ratio of aerosol flow rate to the total flow rate.

Considering Figure A.7, it is evident that the ratio of aerosol flow rate to the total flow rate has the most crucial effect on CF. Increasing this ratio of aerosol means decreasing the sheath

gas and moving toward the converging nozzle with CF equals unity. It is possible to formulate the ratio of flow rates by the assumption of no pressure and temperature gradient in the cross-section of the nozzle as follow:

$$\frac{\dot{Q}_{Aerosol}}{\dot{Q}_{Total}} \approx \frac{\bar{V}_{z,Aerosol}}{\bar{V}_{z,Total}} \times \left(\frac{A_1}{A_{Total}}\right) \xrightarrow{A=\pi r^2} \frac{\dot{Q}_{Aerosol}}{\dot{Q}_{Total}} \approx \frac{\bar{V}_{z,Aerosol}}{\bar{V}_{z,Total}} \times \left(\frac{r_1}{r_N}\right)^2 \tag{A.4}$$

Where $\bar{V}_{z,Aerosol}$ and $\bar{V}_{z,Total}$ is the average axial velocity of aerosol and total flow in the nozzle throat, respectively, r_1 and $r_N$are the radius of aerosol flow and the nozzle radius, respectively. According to equation A.4, the flow rates ratio depends on the average axial velocity of aerosol flow to the total flow ($\bar{V}_{z,Aerosol}/\bar{V}_{z,Total}$) and power of two of aerosol flow's radius to the nozzle radius (r_1/r_N). Figure A.9 presented the axial flow velocity in different sections of the converging nozzle from 2250 μm far from the throat up to the nozzle throat, and it can be seen that the axial flow velocity is completely developed across the section and increases when it reaches the throat. The only difference in the axial velocity profile happens strictly at the throat, in which a region far from the centre reaches a higher velocity than centric regions due to sudden contraction in the throat [1]. Moreover, closer to the throat, the boundary layer decreases due to a decrease in the radius, and axial velocity has a sharper decline in the boundary.

The axial flow velocities at various sections depicted in Figure A.9 are valid for all flow ratios independent of the flow rate ratios as the total flow remains constant. Therefore, the value of $\bar{V}_{z,Aerosol}$ consequently $\bar{V}_{z,Aerosol}/\bar{V}_{z,Total}$ in the throat can be calculated for different flow rate ratios. Table A.3 shows the value of $\bar{V}_{z,Aerosol}/\bar{V}_{z,Total}$ for different flow rate ratios, and it is evident that $\bar{V}_{z,Aerosol}/\bar{V}_{z,Total}$ is very close to unity due to the complete development of axial flow in the converging section. Applying this assumption into equation A.4 turns the flow rate ratio independent of the axial flow velocity ratio and makes it the only function of radiuses (r_1/r_N). According to Figure A.8. e and Figure A.16. e, the CF has minimal dependence on the size of particles; therefore, averaging over all CF for all particles sizes and plotting to the inverse of flow rate ratios in Figure A.10 shows that CF follows the square root of total flow rate to the aerosol flow rate ($CF \simeq \sqrt{\dot{Q}_{Total}/\dot{Q}_{Aerosol}}$). Using mentioned assumptions about independency of flow rate ratios to the velocities it can be seen that CF is approximately is equal r_N/r_1. Moreover, Figure A.10 depicted that CF is not dependent on the density of the particles as gold and copper nanoparticles have similar values.

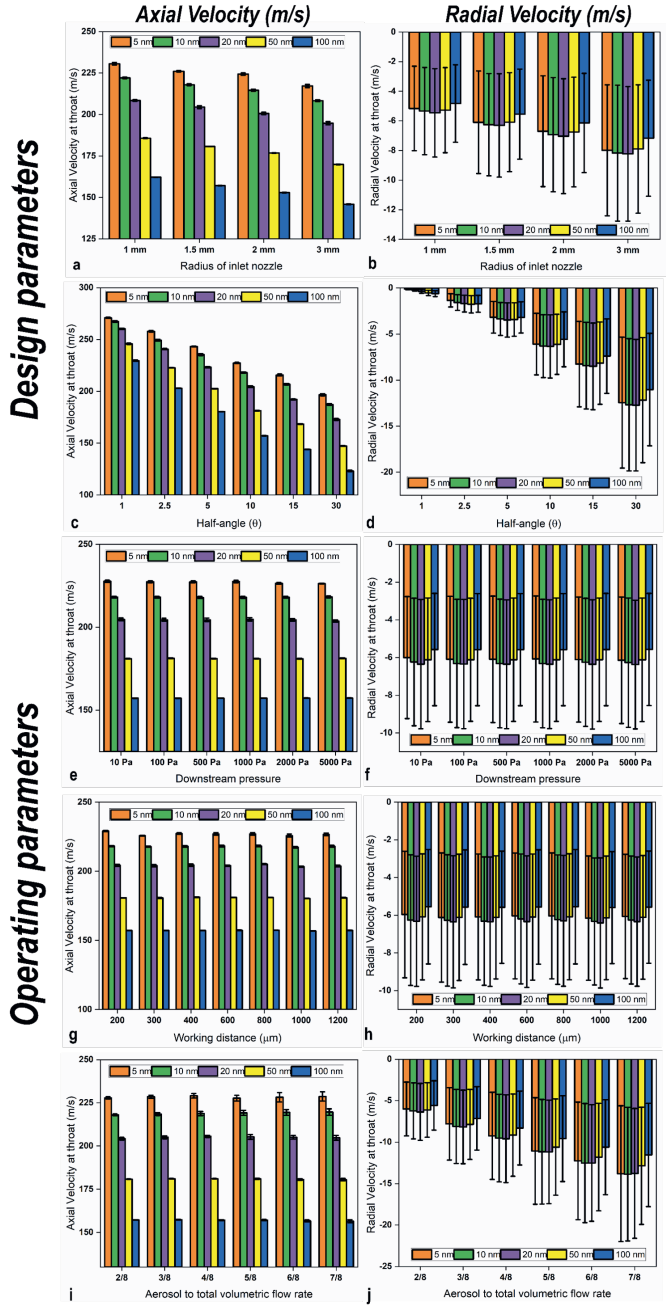

Figure A.8: Axial and radial velocity for AuNPs with sizes indicated in the figure at the throat for the SGN a) and b) aerosol throat diameter, c) and d), angle of converging nozzle, e) and f) downstream pressure, g) and h) WD, and i) and j) aerosol flow rate to the total flow rate.

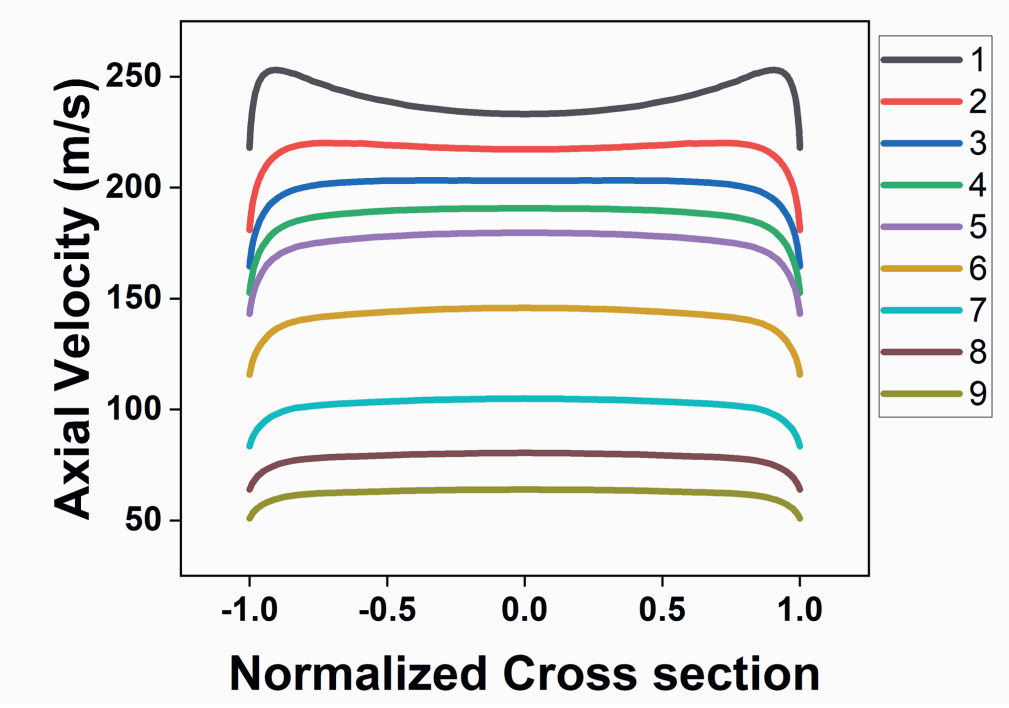

Figure A.9: Axial velocity in the different section of the nozzle up to the throat, (the cross-section normalised with the radius of the nozzle at that section), 1) at the throat, and other with a distance of 2) 25 µm, 3) 75 µm, 4) 150 µm, 5) 250 µm, 6) 450 µm, 7) 850 µm, 8) 1450 µm, 9) 2250 µm form the nozzle throat.

Table A.3: The ratio of average flow velocities for different flow rate ratios

Flow rate ratio aerosol to the total	$\frac{\bar{V}_{z,Aerosol}}{\bar{V}_{z,Total}}$
2/8	0.97
3/8	0.97
4/8	0.98
5/8	0.98
6/8	0.99
7/8	1.00

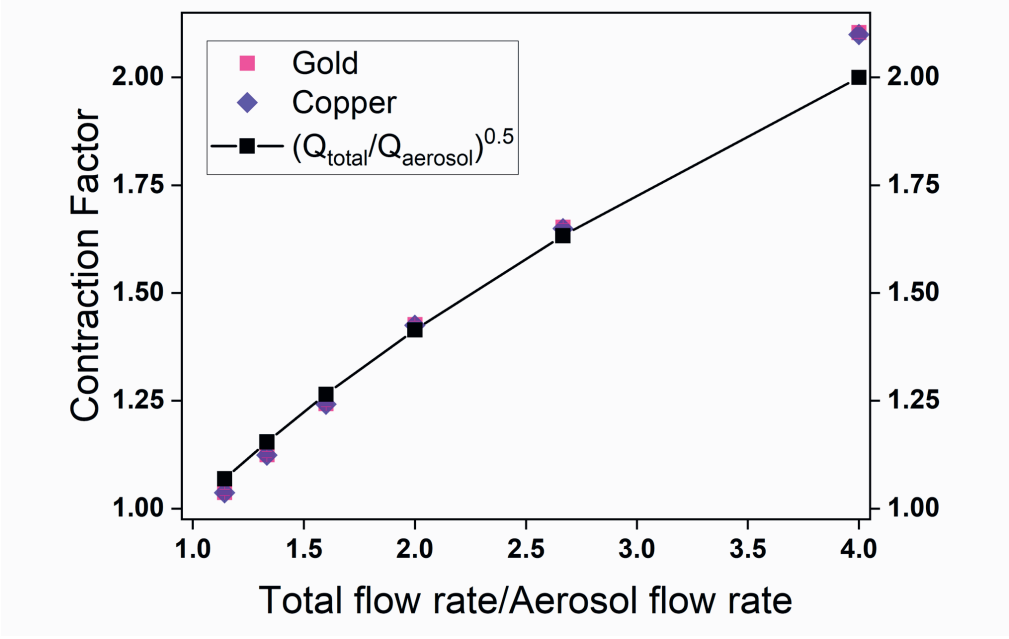

Figure A.10: Averaged contraction factor for copper and gold nanoparticles with various sizes plot regarding the total flow rate per aerosol flow rate

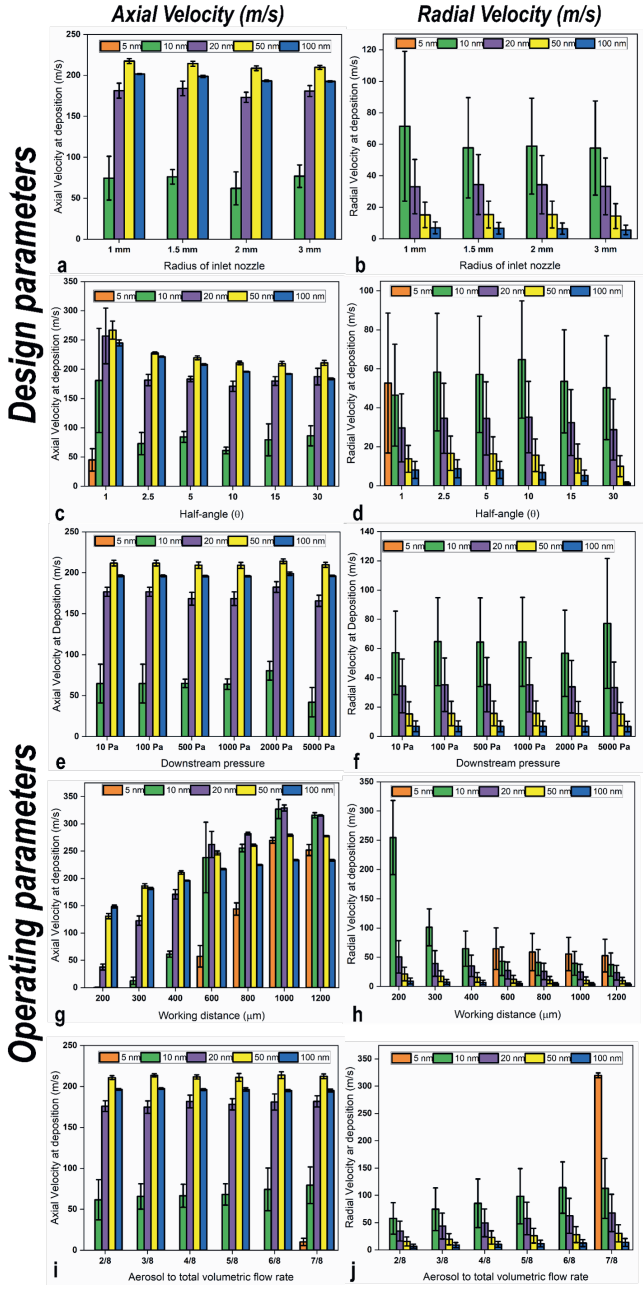

Figure A.11: Axial and radial velocity upon hitting the impaction plate for AuNPs with sizes indicated in the figure for SGN; a) and b) for aerosol throat diameter, c) and d), for the angle of the converging nozzle and operating parameters of e) and f) for downstream pressure and g) and h) WD, and i) and j) for aerosol flow rate to the total flow rate.

A

A.3.2 Copper nanoparticles
A.3.2.1 Converging nozzle

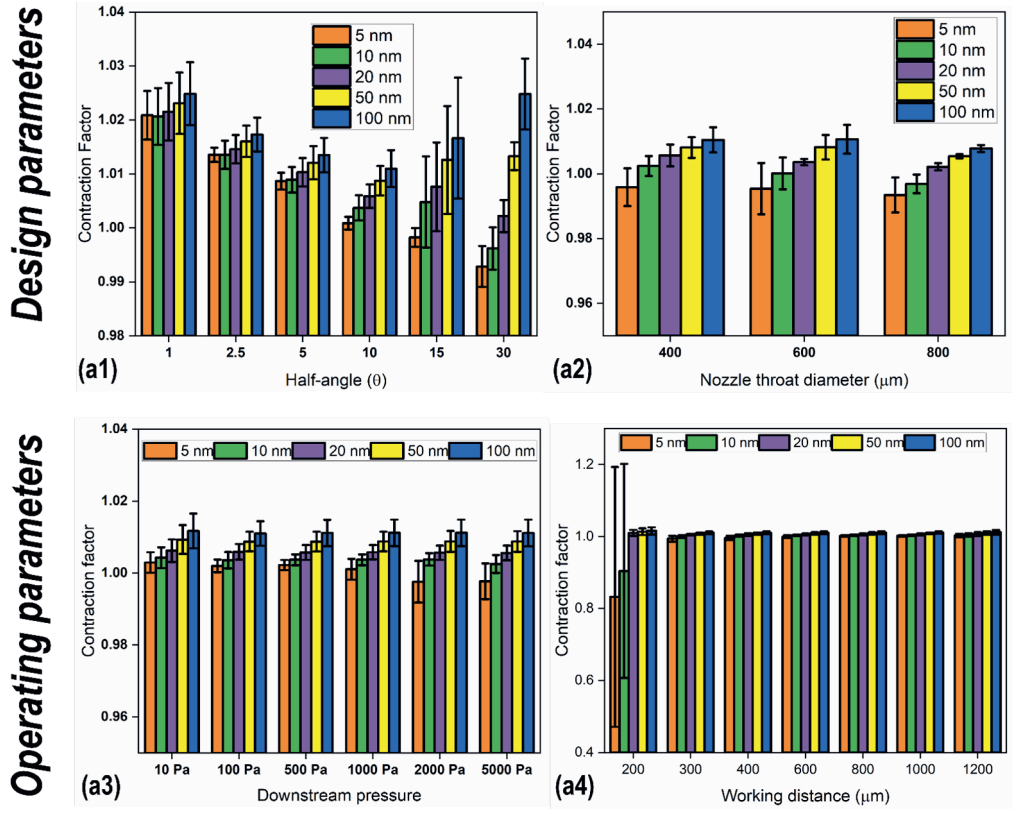

Figure A.12: Contraction factor for copper nanoparticles with sizes indicated in the figure for CN considering design parameters of a) angle of converging nozzle, b) throat diameter, and operating parameters of c) downstream pressure and d) WD.

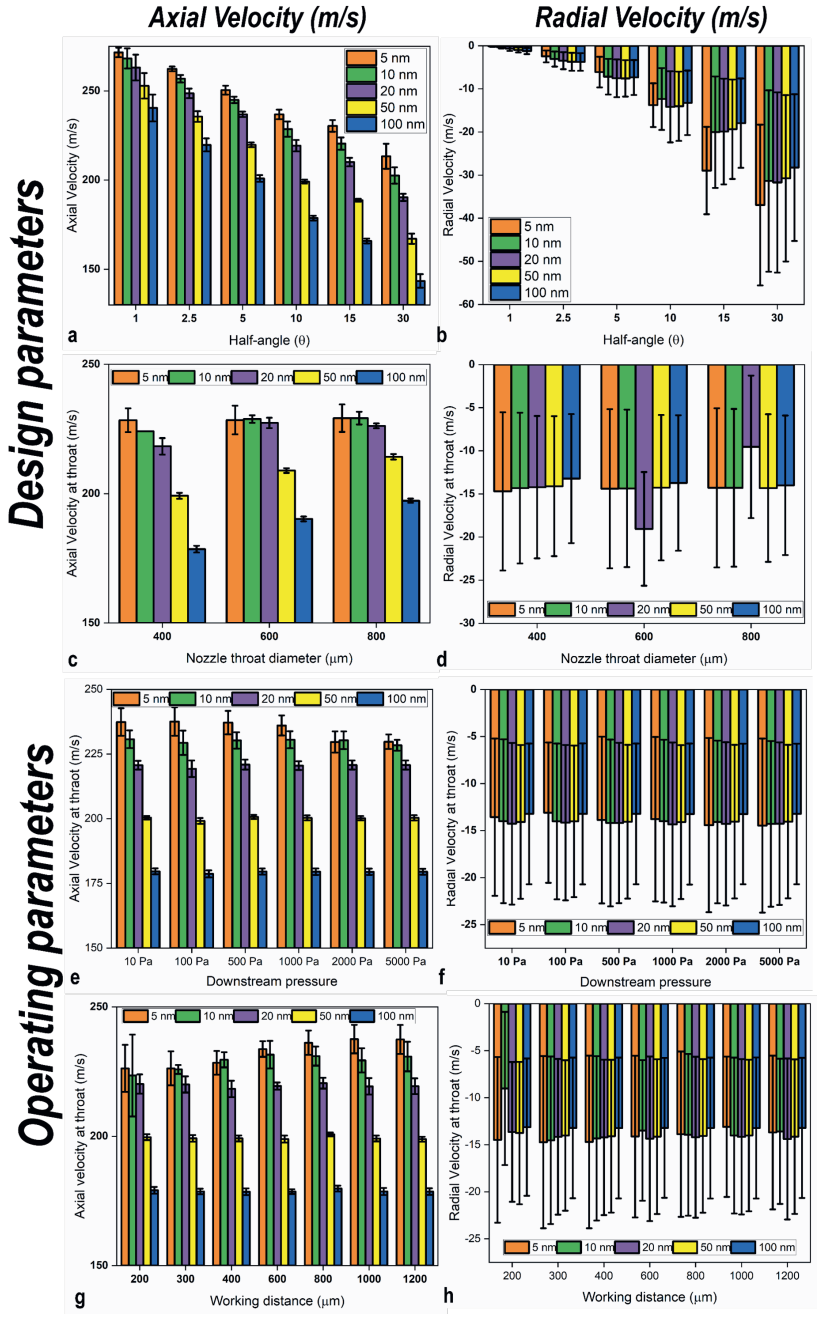

Figure A.13: Axial and radial velocity for copper nanoparticles with sizes indicated in the figure for CN at the throat of the nozzle; a) and b) for the angle of converging nozzle, c) and d) for throat diameter, e) and f) for downstream pressure and g) and h) WD

Considering Figure A.14 and compare to gold nanoparticles in Figure A.2 for the collection efficiency, the copper nanoparticles have partial or no deposition on larger particles up to 10 nm due to their lower densities than gold nanoparticles. Moreover, the FR shows that copper has lower FR than gold nanoparticles for identical size particles, implying that FR depends on the inertia of particles either through size or density. The effects of the other parameters are similar to those of gold in terms of focusing ratio (both of which the collection efficiency are 100%). Furthermore, due to copper nanoparticles' lower density and inertia than gold nanoparticles, downstream pressure has a more pronounced effect on copper nanoparticles.

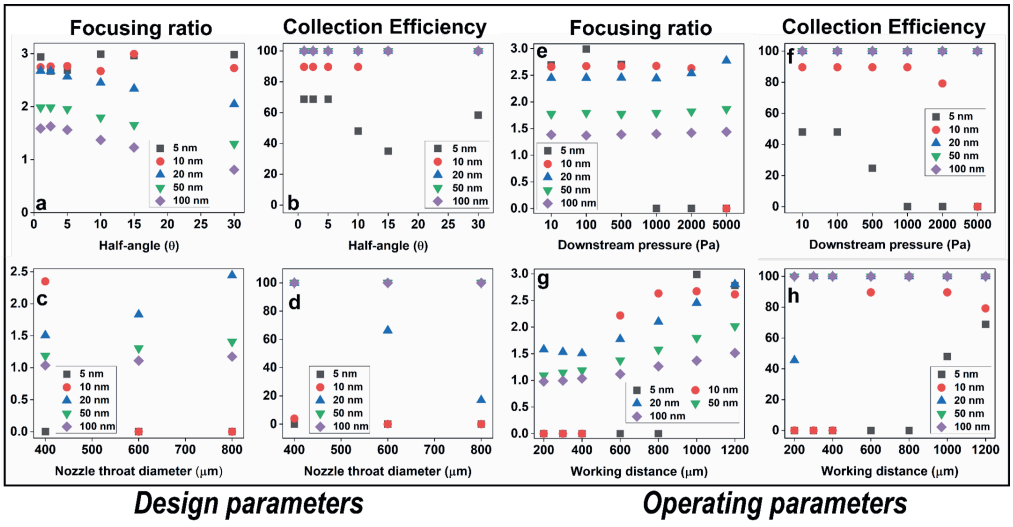

Figure A.14: FR and CE for copper nanoparticles with sizes indicated in the figure for CN considering design parameters of a) and b) for the angle of converging nozzle, c) and d) for throat diameter and operating parameters of e) and f) for downstream pressure and g) and h) WD.

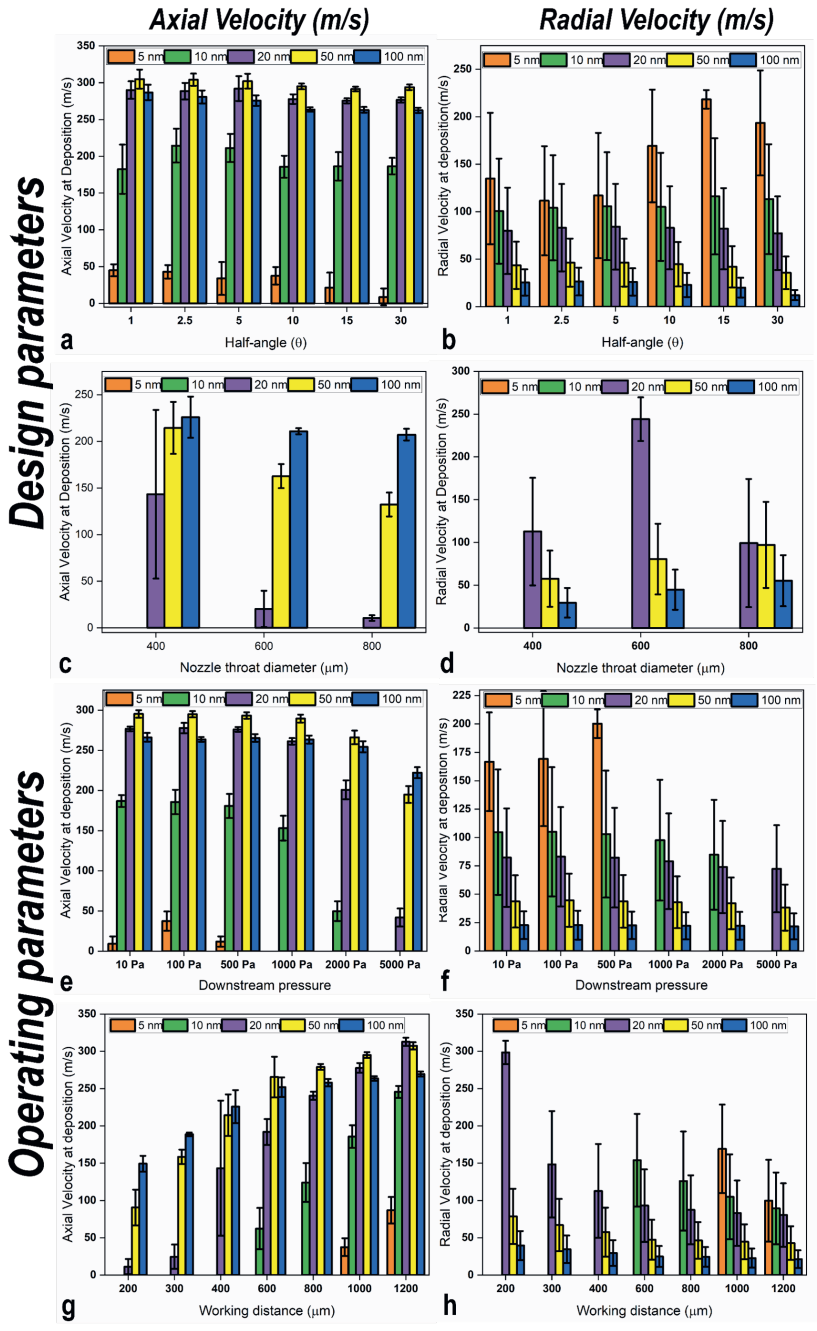

Figure A.15: Axial and radial velocity for copper nanoparticles when impacting on the impaction plate with sizes indicated in the figure for CN, a) and b) for the angle of converging nozzle, c) and d) for throat diameter, e) and f) for downstream pressure and g) and h) WD.

A

A.3.2.2 Sheath gas Nozzle

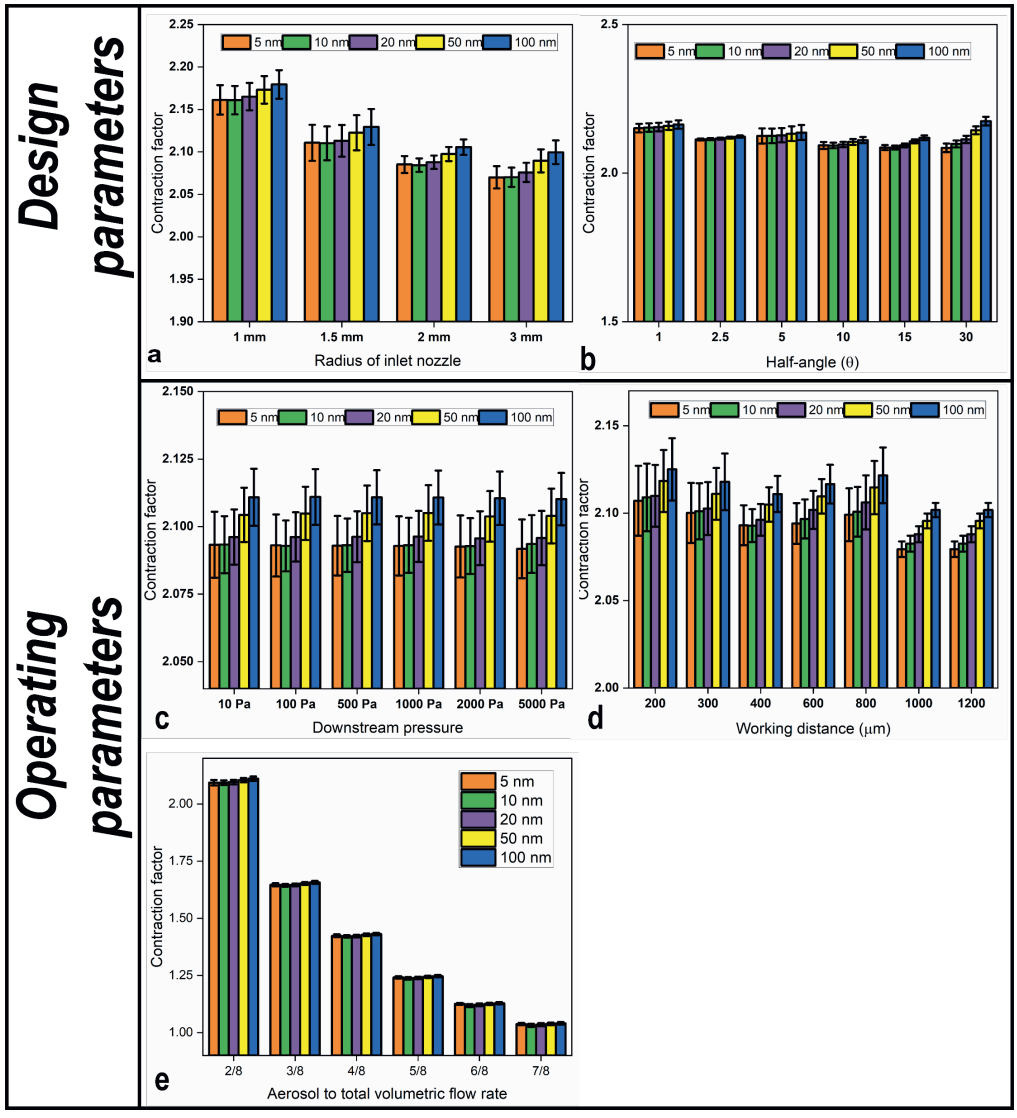

Figure A.16: CF for copper nanoparticles with sizes indicated in the figure for SGN considering design parameters of a) Aerosol throat diameter, b), angle of the converging nozzle and operating parameters of c) downstream pressure, d) WD, and e) the ratio of aerosol flow rate to the total flow rate.

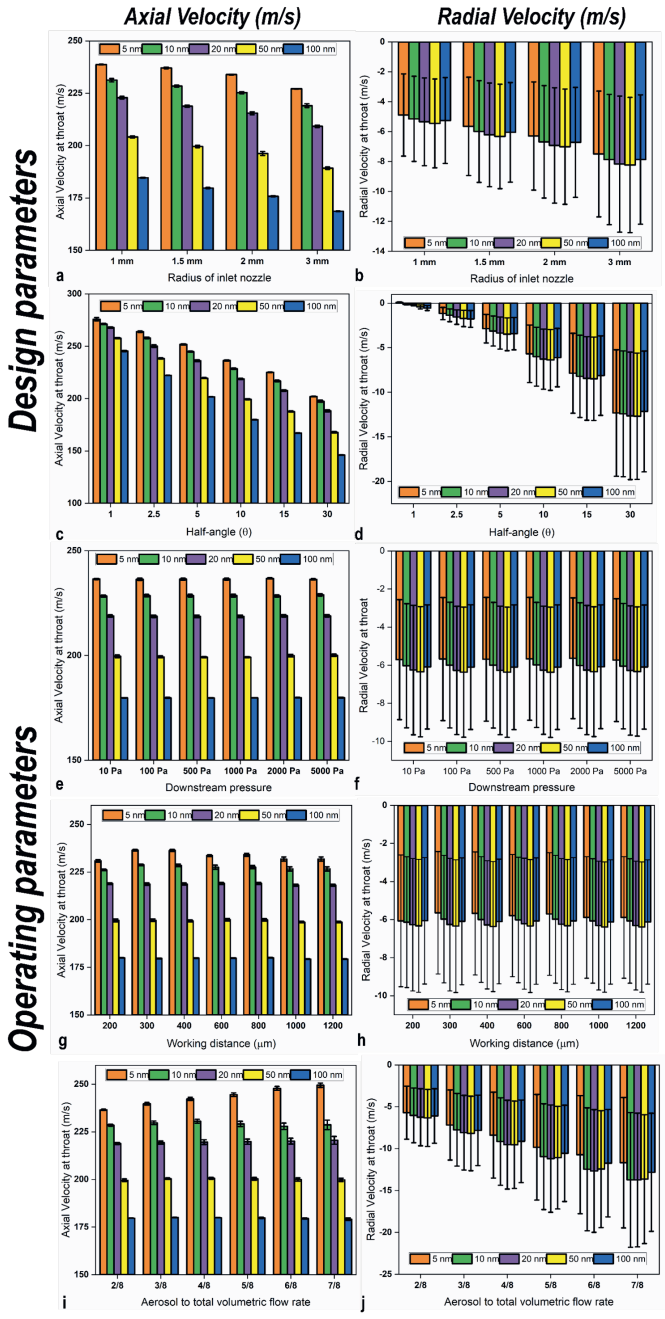

Figure A.17: Axial and radial velocity for copper nanoparticles with sizes indicated in the figure at the throat for the SGN; a) and b) for aerosol throat diameter, c) and d), for the angle of converging nozzle and operating parameters of e) and f) for downstream pressure and g) and h) WD, and i) and j) for aerosol flow rate to the total flow rate.

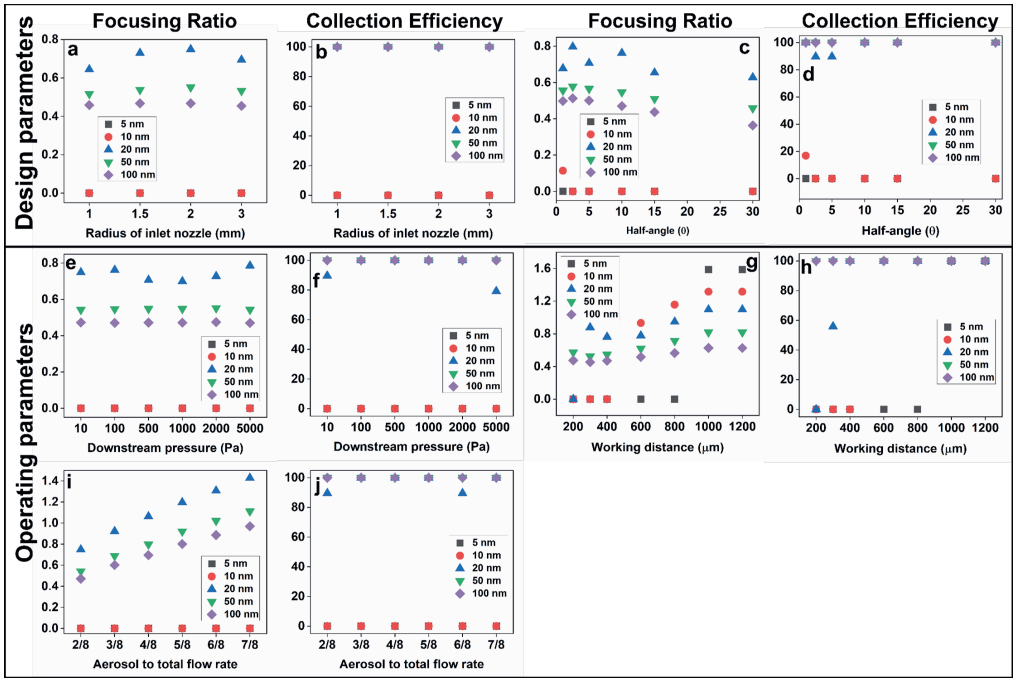

Figure A.18: FR and CE for copper nanoparticles with sizes indicated in the figure for SGN considering design parameters of, a) and b) for Aerosol throat diameter, c) and d) for the angle of converging nozzle, and operating parameters of e) and f) for downstream pressure and g) and h) WD, and i) and j) for the ratio of aerosol flow rate to the total flow rate.

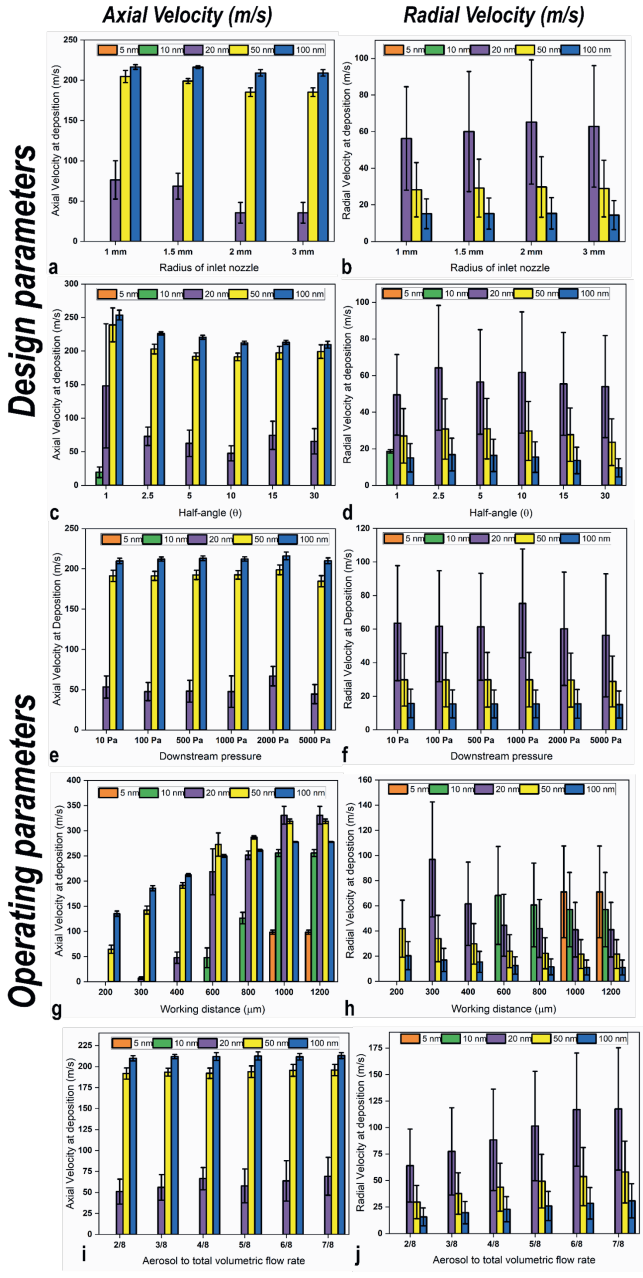

Figure A.19: Axial and radial velocity for copper nanoparticles upon hitting the impaction plate with sizes indicated in the figure for SGN; a) and b) for intel aerosol throat diameter, c) and d), for the angle of the converging nozzle and operating parameters of e) and f) for downstream pressure and g) and h)WD, and i) and j) for the aerosol flow rate to the total flow rate.

A

A.4 Experimental results

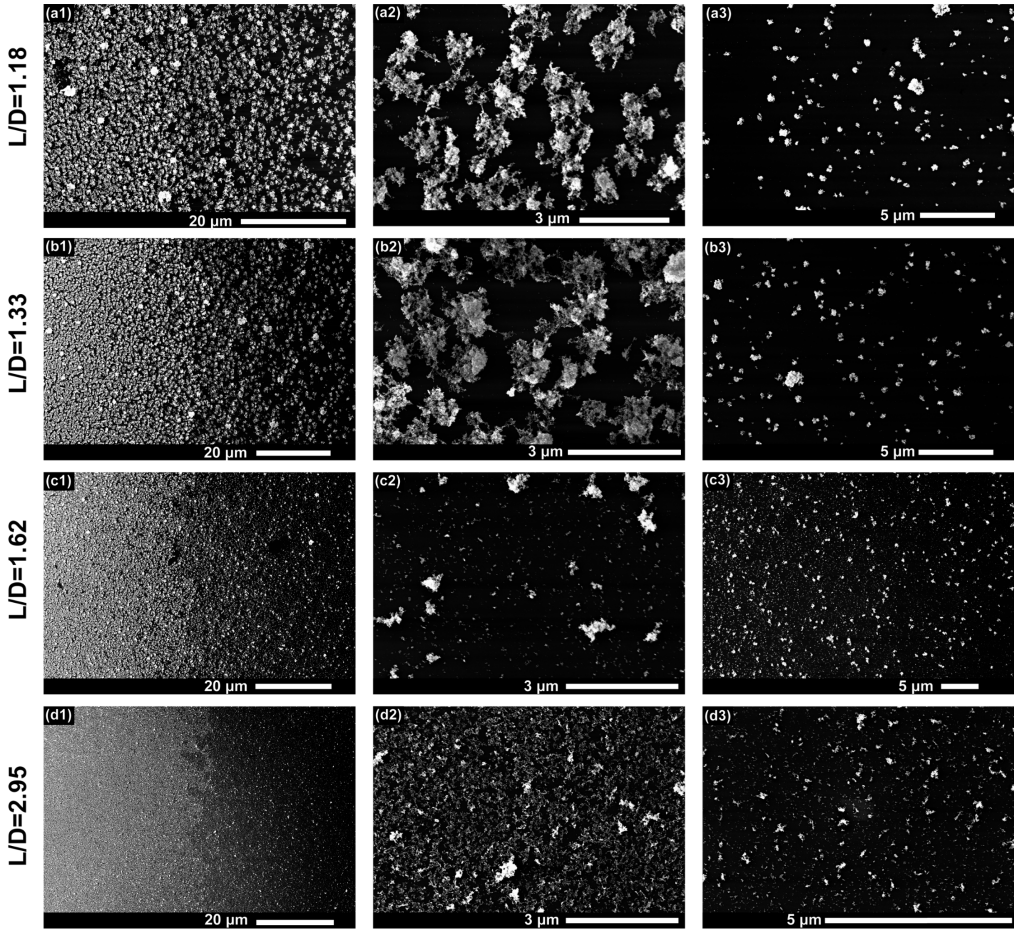

Figure A.20: (a1-d1) SEM images of the border between boundary and splash zones for lines printed with 339 µm nozzle and WDs as indicated in the figure and (a2-d2) focusing in splash zones closer to the boundary, and (a3-d3) further away from the line in the splash zone.

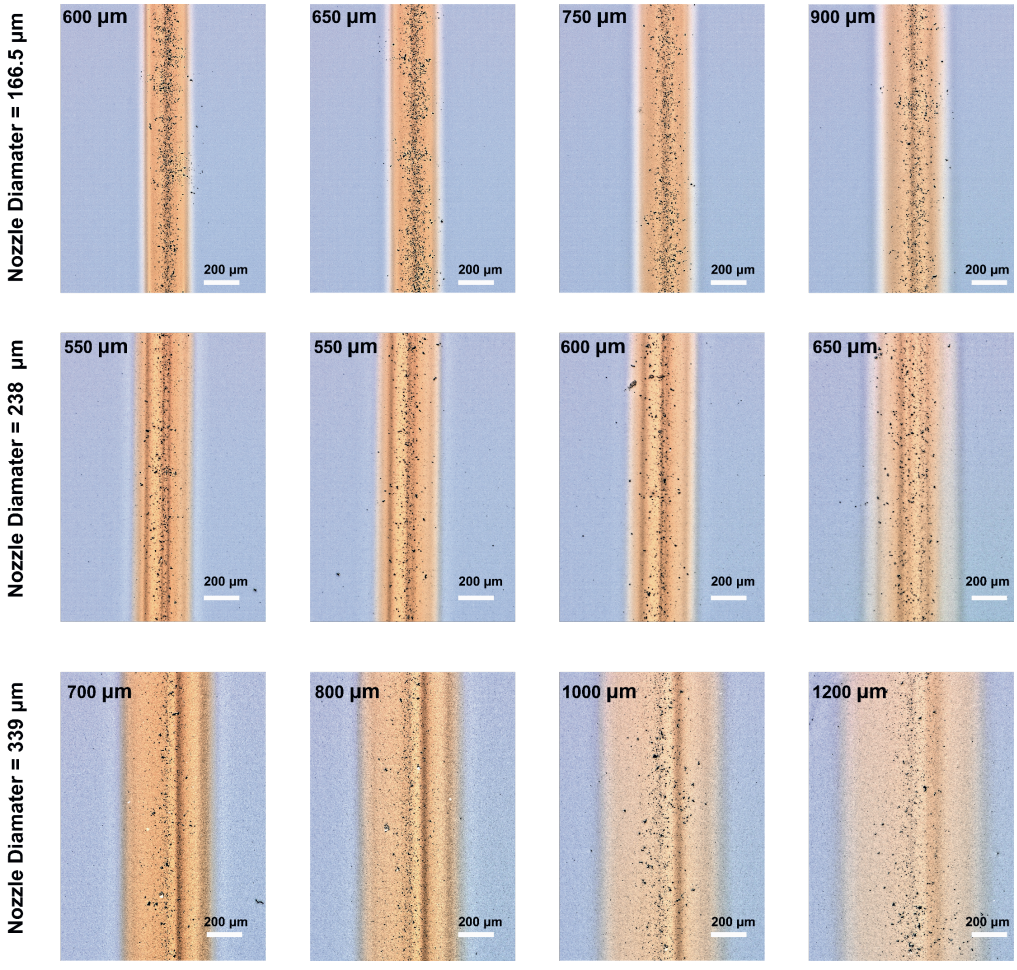

Figure A.21: The optical microscopy images of lines printed by converging nozzles with diameters as stated in the image at different WDs.

References

[1] S. F. C. Stewart, P. Hariharan, E. G. Paterson, G. W. Burgreen, V. Reddy, S. W. Day, M. Giarra, K. B. Manning, S. Deutsch, M. R. Berman, M. R. Myers, and R. A. Malinauskas, "Results of fda's first interlaboratory computational study of a nozzle with a sudden contraction and conical diffuser," *Cardiovascular Engineering and Technology*, vol. 4, pp. 374–391, 12 2013.

B

Appendix B

This chapter provides supplementary information for chapter 4, including Optical micrographs of possible patterning on different substrates; SEM and HR-SEM images of the samples with and without heat treatment; EDS spectra of different samples; extinction cross-section calculation for nanoparticles; Raman spectra of RhB on samples with and without heat treatment under excitation laser of 488, 514, and 633 nm; Raman spectra of RhB on samples patterned with higher deposition velocity and Raman spectra of RhB with a concentration of 1 mM on bare silicon as a reference sample.

The contents of this chapter have been published as supplementary information in:

- Aghajani, S., Accardo, A., & Tichem, M. (2020). Aerosol Direct Writing and Thermal Tuning of Copper Nanoparticle Patterns as Surface-Enhanced Raman Scattering Sensors. ACS Applied Nano Materials, 3(6), 5665–5675. DOI:10.1021/acsanm.0c00887

B.1 Printability of dry aerosol direct writing

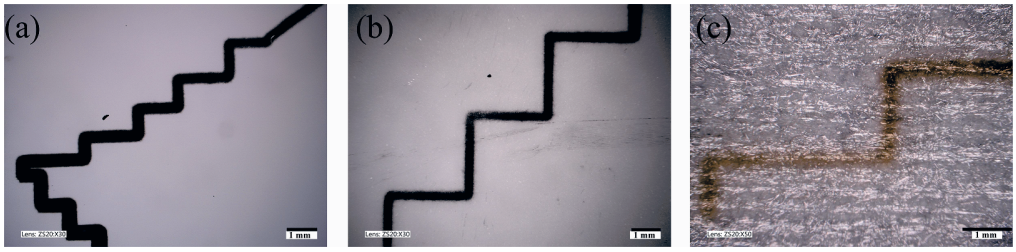

Figure B.1: Optical image of possible patterning on different substrates: a) Silicon, b) glass, c) dust-free napkin.

B.2 SEM analyses

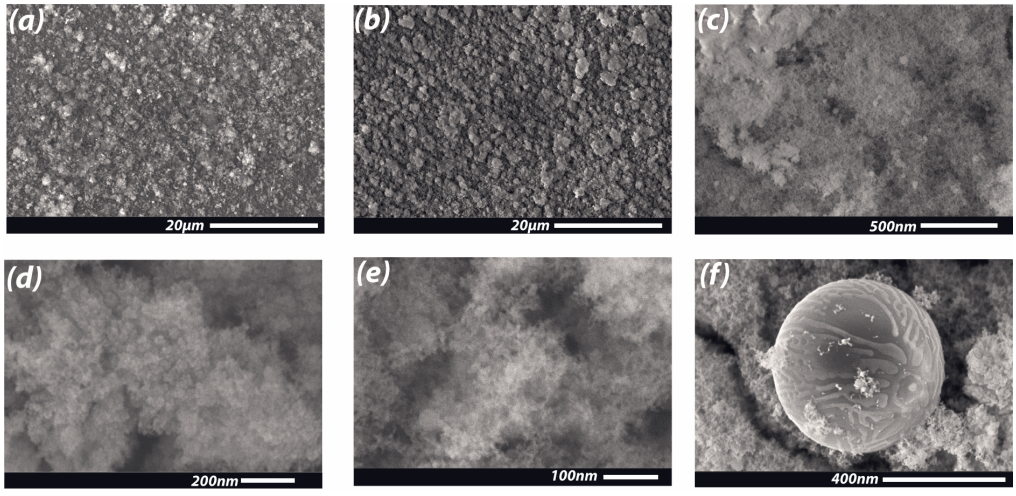

Figure B.2: SEM images of the CuNPs deposited on a silicon substrate with SAM voltage/current setting of V=1.2 kV, I=8 mA a) Centric region and b) boundary of the line, c) presence of microparticles in the film of CuNPs, d) and e) Morphology of film at high-resolution image f) a typical microparticle

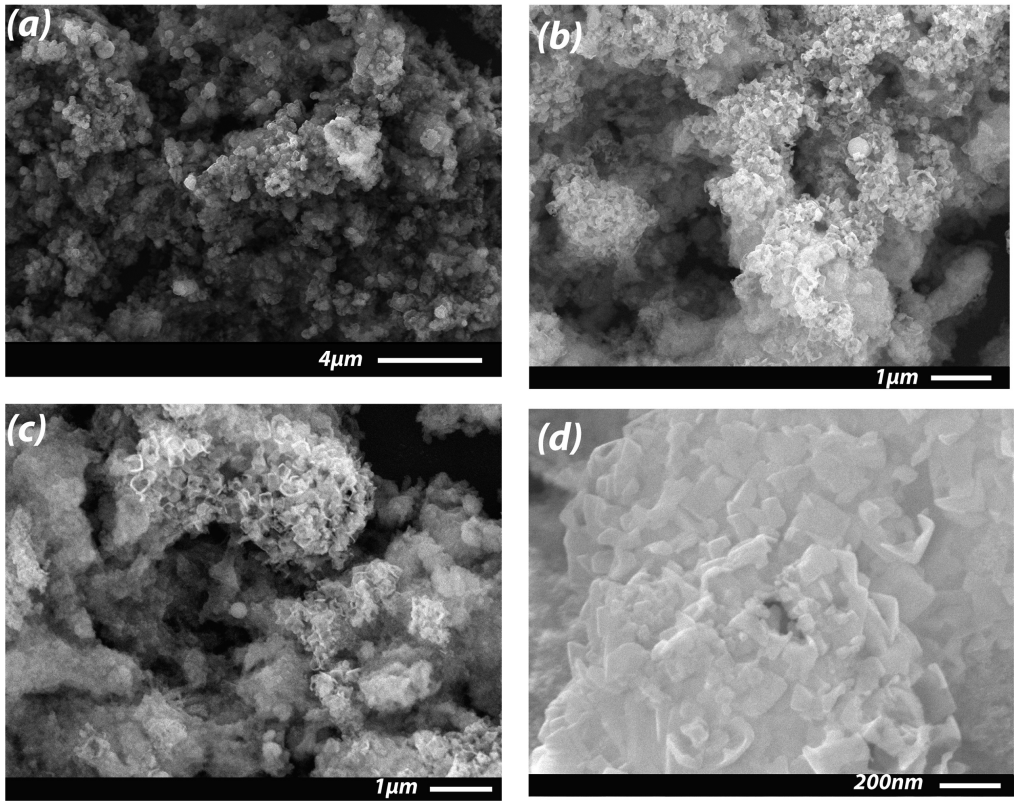

Figure B.3: SEM images of the transformation of the CuNPs deposited on a silicon substrate to crystalline form after thermal treatment in vacuum oven for 1 hour at 200℃ and SAM voltage/current setting of V=1.2 kV, I=8 mA

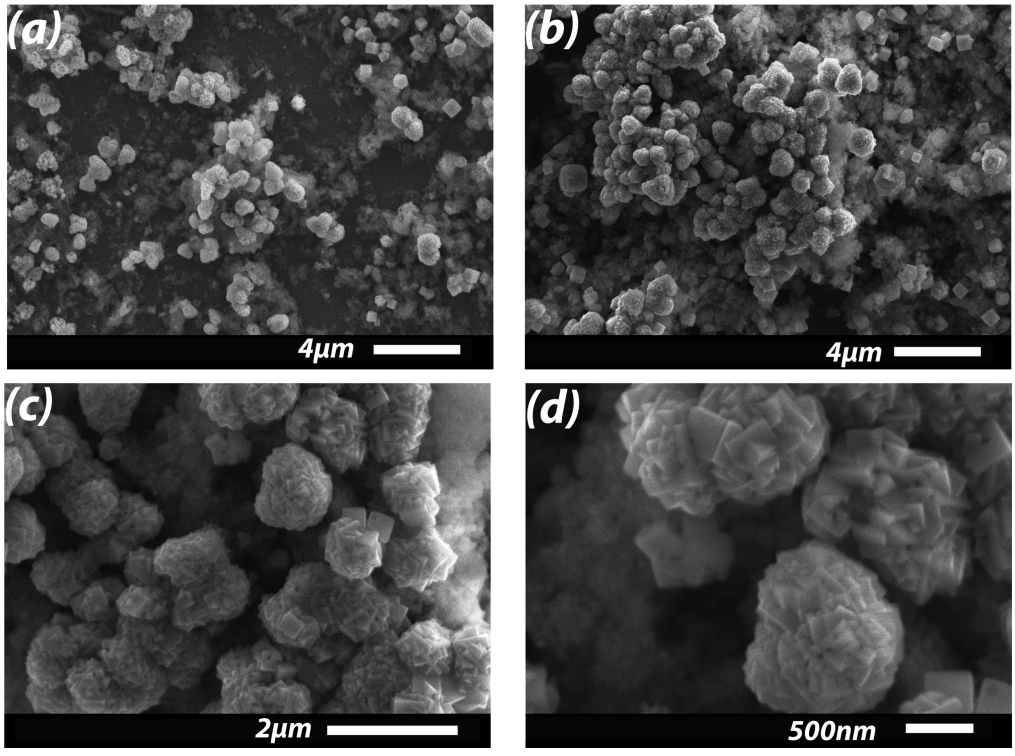

Figure B.4: SEM images of CuNPs deposited on a silicon substrate after thermal treatment in a vacuum oven for 2 hours at 200℃ and SAM voltage/current setting of V=1.2 kV, I=8 mA. a) evolution of morphology from cubic aggregates to bulk aggregates moving from center to the boundary b),c),d) high magnification of bulk aggregates

B.3 EDS analyses

The elemental analysis of samples with heat-treatment at 200 ℃ for 1 and 2 hours (Table B.1), shows the presence of chlorine in the CuNPs film. The EDS result of a silicon substrate underwent same thermal treatment as the last sample (2 hours at 200 ℃) showed in 4.4.b, which contains no trace of chlorine in the spectra. Therefore, presence of chlorine in the EDS analysis of samples heat-treated at 200 ℃ is related to reaction of copper or copper oxide with chlorine existed in air.

Table B.1: The EDS report of CuNP deposited on the silicon substrate in two regions: inside the line and at boundary of the line

	Centric region					Boundary region				
	%Cu	%O	%Si	%C	%Cl	%Cu	%O	%Si	%C	%Cl
No heat-treatment	33	33	11	21	-	8	19	45	26	-
	39	38	-	21	-					
	33	33	10	22	-	20	32	25	21	-
	39	38	1	21	-					
Heat treated for 1 hour at 100 ℃	22	24	24	28	-	5	13	50	30	-
	33	32	6	27	-					
	31	26	16	26	-	7	15	45	32	-
	33	30	8	26	-					
Heat treated for 1 hour at 200 ℃	34	26	5	26	6	28	15	9	11	4
	34	28	3	27	6					
	32	28	2	30	6	10	18	39	29	1
	36	25	3	27	6					
Heat treated for 2 hours at 200 ℃	25	16	12	33	12	16	21	17	37	6
	31	15	1	35	16					
	30	17	4	33	14	12	16	31	34	5
	29	17	2	36	14					

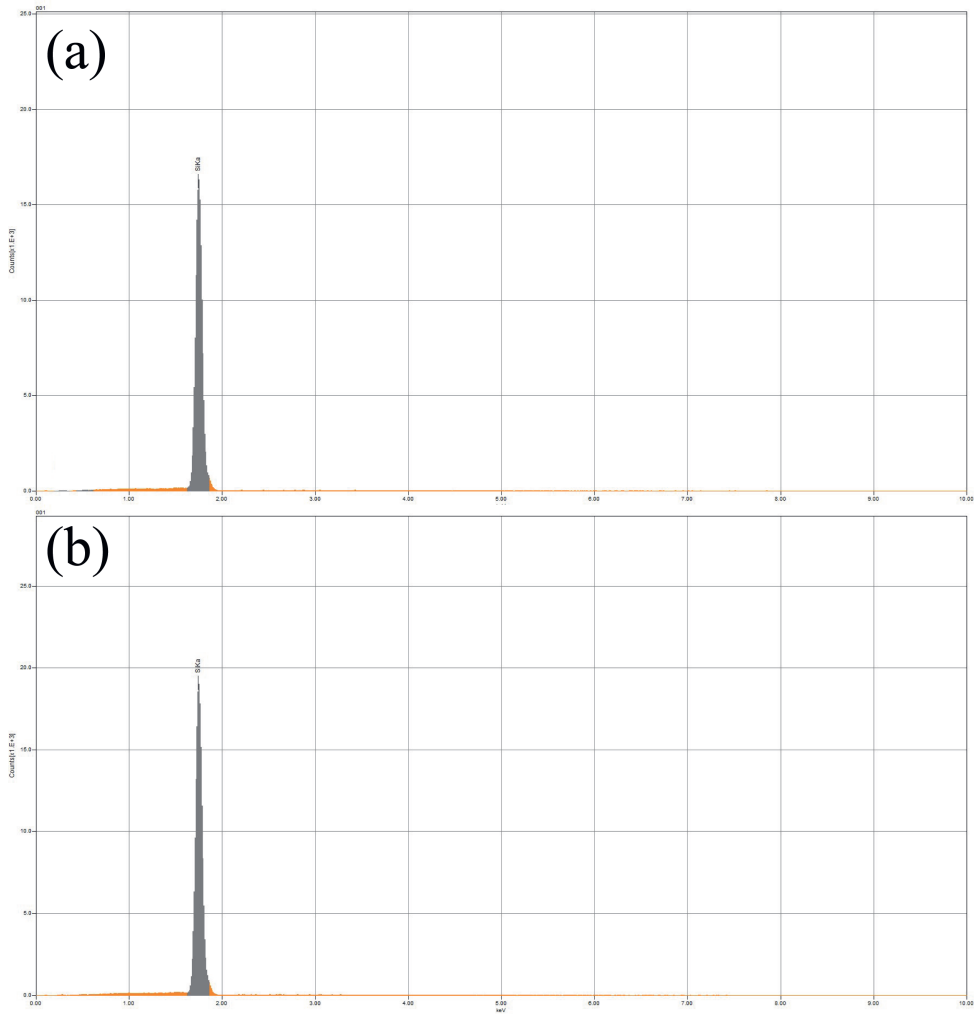

Figure B.5: EDX spectra of a Silicon substrate a) Sample without heat treatment b) Samples heated for 2 hours at 200 ℃

B.4 Laser selection for Raman measurements

The Raman spectroscopy setup used in this study is equipped with three wavelength lasers, 488 nm, 514 nm and 633 nm. To choose the best wavelength for laser we used a theoretical estimation for deposited CuNPs surrounded by air with relative permittivity of 1 (ε_s = 1). The Mie theorem is used to calculate the extinction cross section (σ_{ext}) of the spherical nanoparticles as below [1]:

$$\sigma_{ext} = \frac{24\pi^2 R^3 \varepsilon_s^{3/2} \varepsilon_2}{\lambda\left(\left(\varepsilon_1 + 2\varepsilon_s\right)^2 + \varepsilon_2^2\right)} \tag{B.1}$$

B

Where (R) is the radius of the nanoparticle, (λ) is wavelength, (ε_1) and (ε_2) are the real and imaginary parts of the relative permittivity of the metal which is equal to:

$$\varepsilon_{Bulk}(\omega) = \varepsilon_1(\omega) + i\varepsilon_2(\omega) \tag{B.2}$$

For nanoparticles with characteristic length ($2 \times R$) smaller than the electron mean free path (λ_0), their relative permittivity (ε_{bulk}) is no longer just function of the wavelength but function of the size of the particles and can be written as [2]:

$$\varepsilon(\omega, R) = \varepsilon_{Bulk} + \omega_p^2 \left(\frac{1}{\omega^2 + \left(\frac{v_f}{\lambda_0}\right)^2} - \frac{1}{\omega^2 + \left(\frac{v_f}{\lambda_0} + A\frac{v_f}{R}\right)^2} \right) + i\frac{\omega_p^2}{\omega} \left(\frac{\frac{v_f}{\lambda_0} + A\frac{v_f}{R}}{\omega^2 + \left(\gamma_0 + A\frac{v_f}{R}\right)^2} - \frac{\frac{v_f}{\lambda_0}}{\omega^2 + \left(\frac{v_f}{\lambda_0}\right)^2} \right) \tag{B.3}$$

Where (ω_p) is the bulk plasmonic frequency, (v_f) is the Fermi velocity and (A) is a constant usually taken as unity (1). For copper the electron mean free path (λ_0) is equal to 39.9 nm [3], therefore for particles with diameter less than 40 nm, the previous correction applies. This correction is important since the nanoparticles generated in the spark ablation method have a size distribution of the radius smaller than 20 nm. The calculated extinction spectra for different particles' size are shown in Figure B.6. In this figure the wavelength of the available lasers are shown and it is possible to identify the most suitable laser. It is clear how a 633 nm laser is located after the resonance peak of the copper nanoparticles and cannot excite them. Two other laser wavelengths of 488 nm and 514 nm are located before the peak and they can both activate the LSPR, although 514 nm is closer to the peak. Figure B.7.a shows the Raman measurements of 1 μM RhB on the deposited CuNPs for two excitation wavelengths of 488 nm and 514 nm. As it can be observed, the 514 nm provides better enhancement of the Raman signal. For samples with thermal treatment and fusion of particles, the Mie theorem cannot be used since the nanoparticles fused together form bigger structures. To evaluate the performance of different excitation wavelengths on the heat-treated samples, a thermal treated sample at 200 ℃ for 1 hour was measured with the 3 mentioned wavelengths. As shown in Figure B.7. b, the 514 nm laser provides the highest enhancement of the SERS signal.

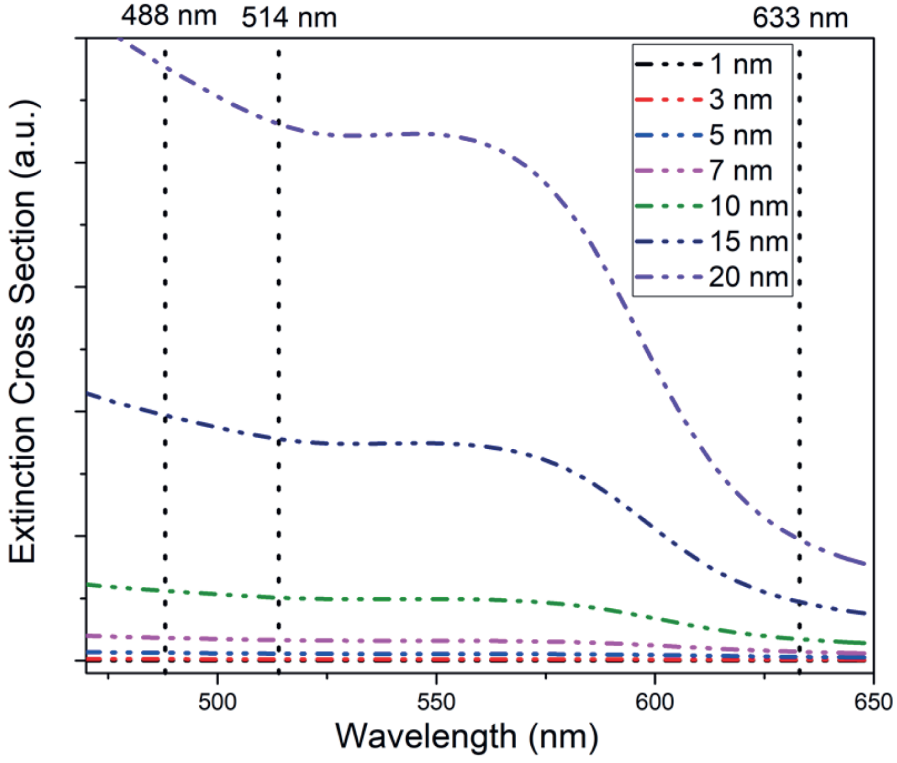

Figure B.6: Extinction cross section calculated for copper nanoparticles with different radius based on Mie theorem and surrounding medium of air with relative permittivity of 1 (ε_s= 1)

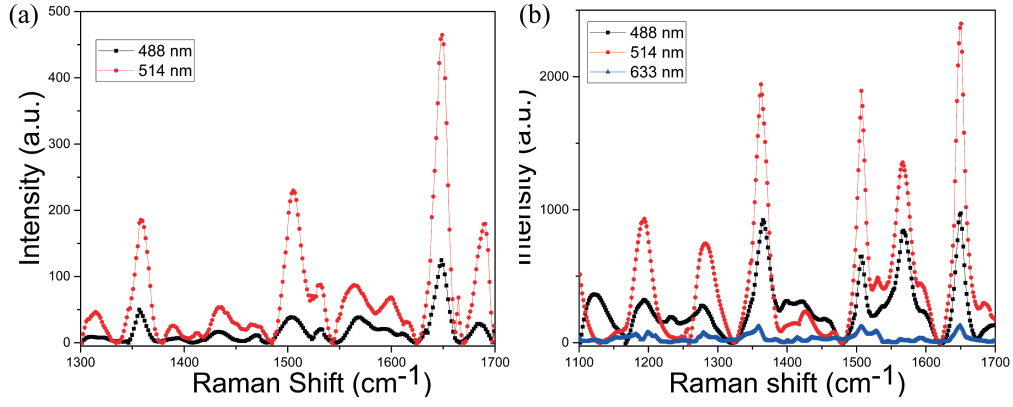

Figure B.7: Raman spectra of 1.0×10-6 M RhB on CuNPs patterns with different excitation laser wavelengths of 488 nm, 514 nm and 633 nm a) Samples without heat treatment b) Samples with heat treatment for 1 hour at 200 ℃. Raman measurement conditions: Acquisition time = 50 s; objective lens = 50X (NA=0.5)

B.5 Effect of deposition speed on the Raman intensity of RhB

Same results observed for heat-treated sample at 200 ℃ and 1 hour, with higher Intensity at boundary and less uniform Raman result with higher deposition speed.

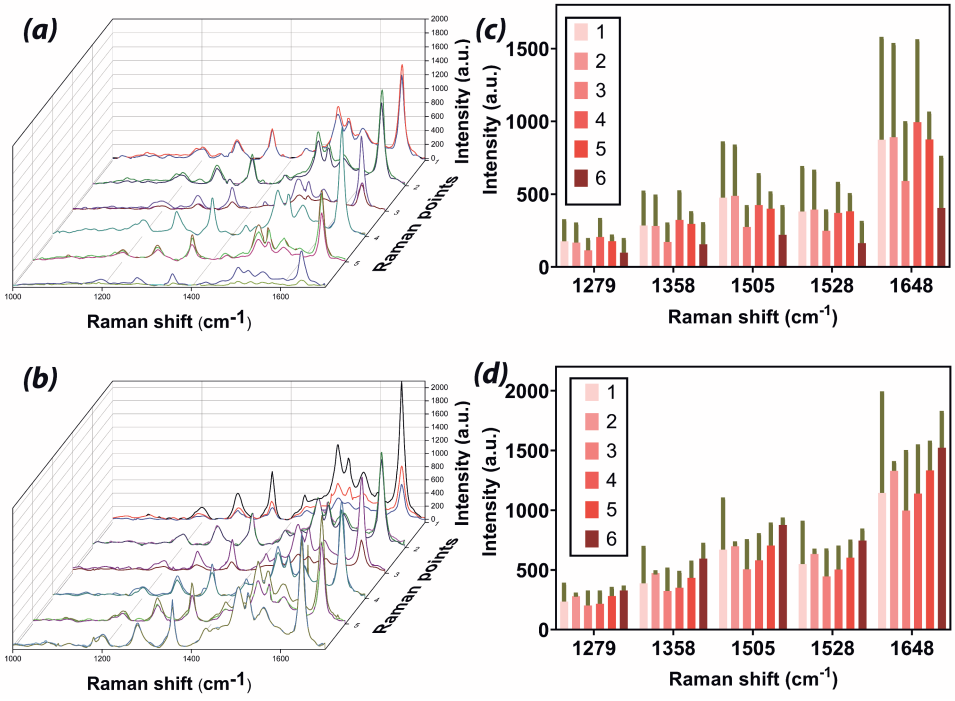

Figure B.8: a, b: Raman spectra of 1.0×10^{-6} M RhB on CuNPs patterns obtained at writing speed of 20 μm s^{-1} and 10 μm s^{-1} respectively and 1-hour thermal treatment of 200℃ for 18 points in 6 regions. b, d) main peaks of RhB for each of the 6 Raman regions. Raman measurement conditions: Argon ion laser operating at 514 nm and power of 20 μW; acquisition time = 30 s; objective lens = 50X (NA=0.5).

B.6 Reference sample for calculation of enhancement factor

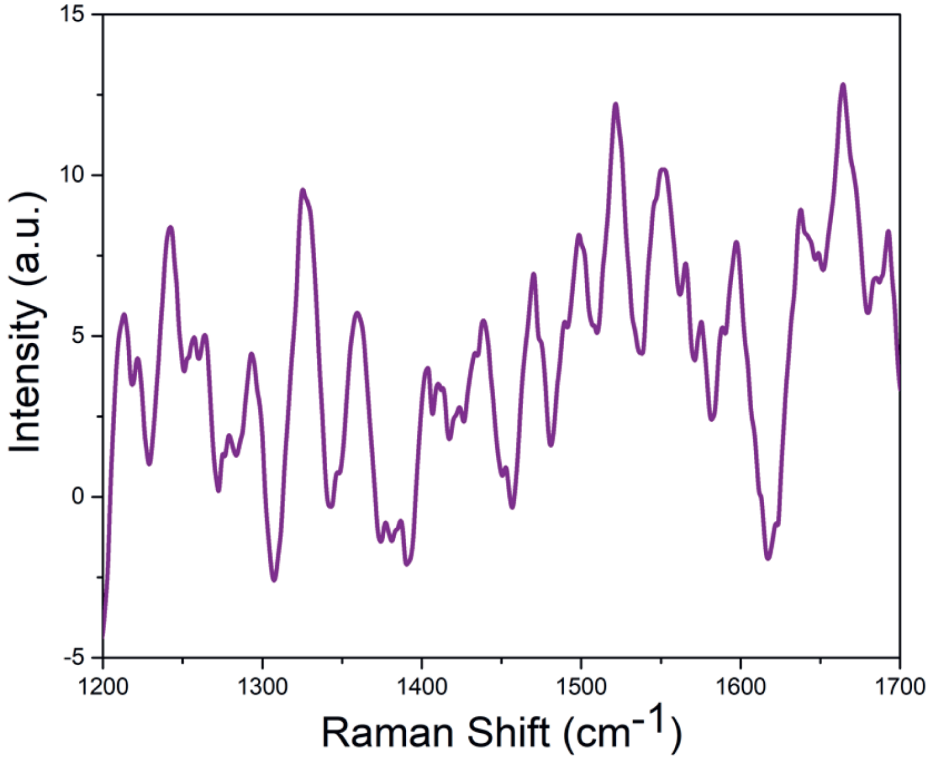

Figure B.9: Raman spectra of a 1.0×10^{-3} M (1mM) RhB on bare silicon. Raman measurement conditions: Argon ion laser operating at 514 nm and power of 20 μW; acquisition time = 30 s; objective lens = 50X (NA=0.5).

References

[1] G. V. Hartland, "Optical studies of dynamics in noble metal nanostructures," *Chemical Reviews*, vol. 111, pp. 3858–3887, 2011.

[2] H. Müller, "Optical properties of metal clusters," *Zeitschrift für Physikalische Chemie*, 1996.

[3] D. Gall, "Electron mean free path in elemental metals," *Journal of Applied Physics*, vol. 119, p. 085101, 2 2016.

C

Appendix C

This chapter provides supplementary information for chapter 5, including SEM and HR-SEM images of the samples with and without heat treatment, AFM images of different samples, photoluminescence spectra of samples with and without heat treatment under excitation laser of 514 and 633 nm.

The contents of this chapter have been published as supplementary information in:

- Aghajani, S., Accardo, A., & Tichem, M. (2021). Tunable photoluminescence and SERS behaviour of additively manufactured Au nanoparticle patterns. RSC Advances, 11(28), 16849–16859. DOI:10.1039/D1RA02266K

C.1 SEM analyses

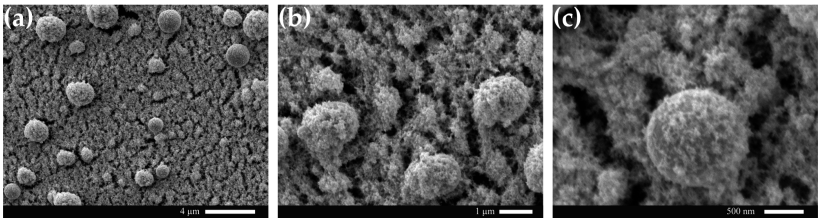

Figure C.1: SEM images of the AuNPs deposited on a silicon substrate with SAM voltage/current setting of V=0.9 kV, I=5 mA a) Low magnification of Microparticles together with agglomeration of primary nanoparticles , and high magnification of b) agglomeration of primary nanoparticles on the microparticles and , c) microparticles in the film of AuNPs.

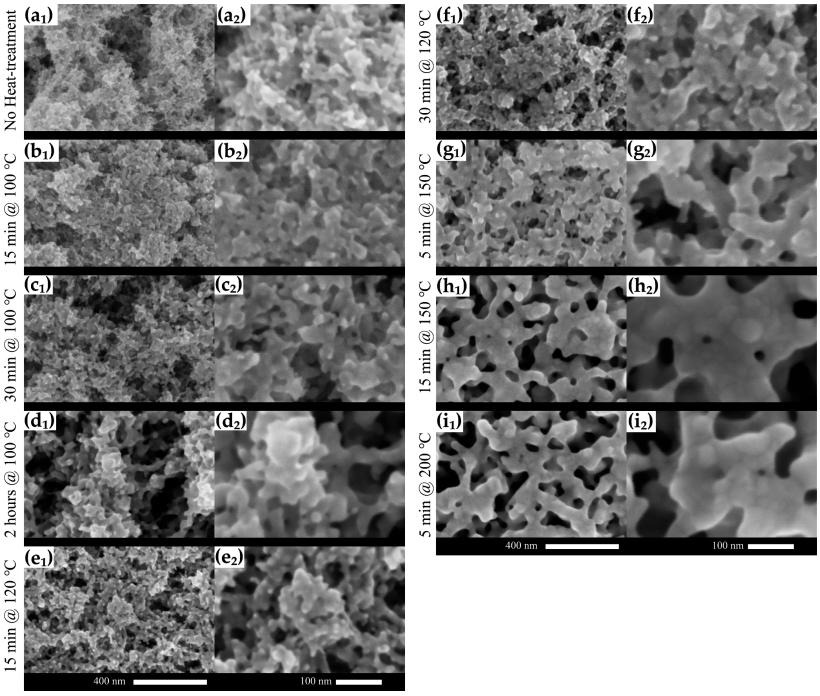

Figure C.2: (a1, a2) SEM images of the morphology of AuNPs deposited on centric region of the line and the boundary (Sample 1), and the same comparison for thermal treated samples as (b1, b2) 15 minutes at 100 ℃ (Sample 2), (c1, c2) 30 minutes at 100 ℃ (Sample 3), (d1, d2) 120 minutes at 100 ℃ (Sample 4), (e1,e2) 15 minutes at 120 ℃ (Sample 5), (f1, f2) 30 minutes at 120 ℃ (Sample 6), (g1, g2) 5 minutes at 150 ℃ (Sample 7), (h1, h2) 15 minutes at 150 ℃ (Sample 8), (i1, i2) 5 minutes at 200 ℃ (Sample 9). All AuNPs deposited with SAM voltage/current setting of V = 0.9 kV and I = 5 mA.

C

C.2 AFM analyses

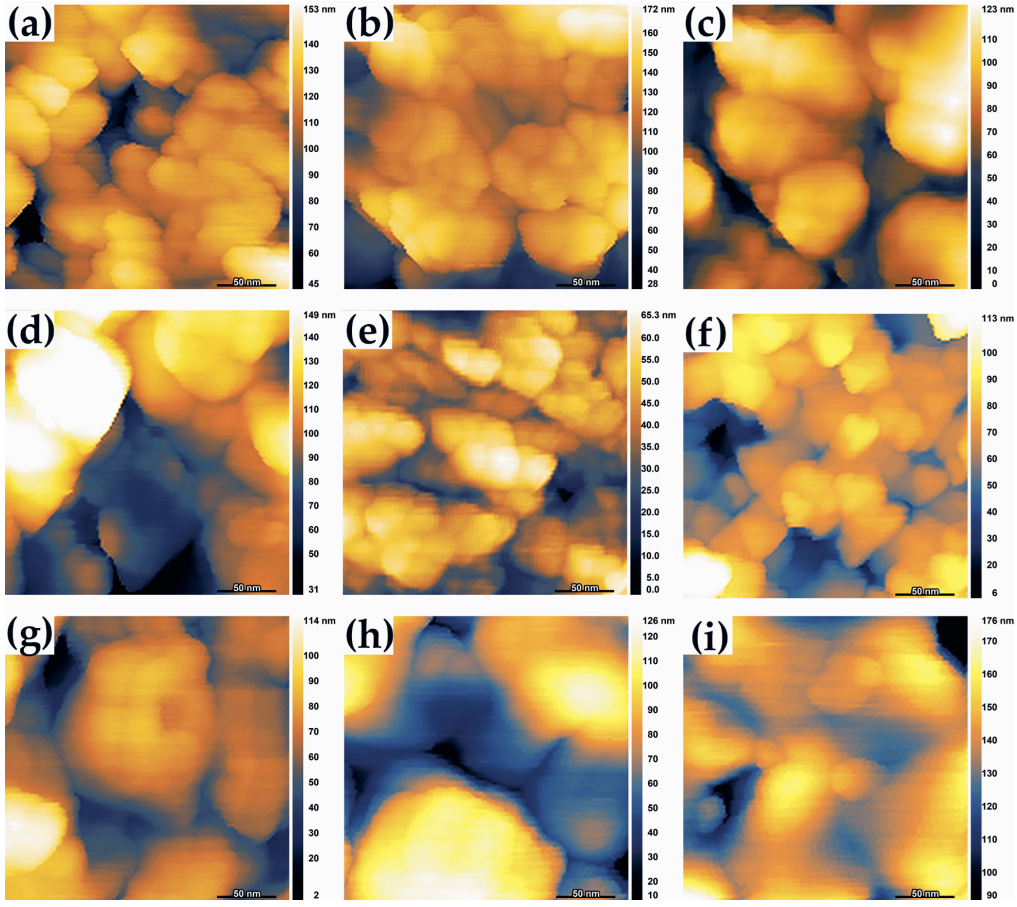

Figure C.3: AFM morphology of 250 × 250 nm2 areas of a) non-heat treated samples (b) 15 minutes at 100 ℃, (c) 30 minutes at 100 ℃, (d) 120 minutes at 100 ℃, (e) 15 minutes at 120 ℃, (f) 30 minutes at 120 ℃, (g) 5 minutes at 150 ℃, (h) 15 minutes at 150 ℃, (i) 5 minutes at 200 ℃.

C.3 Photoluminescence analyses

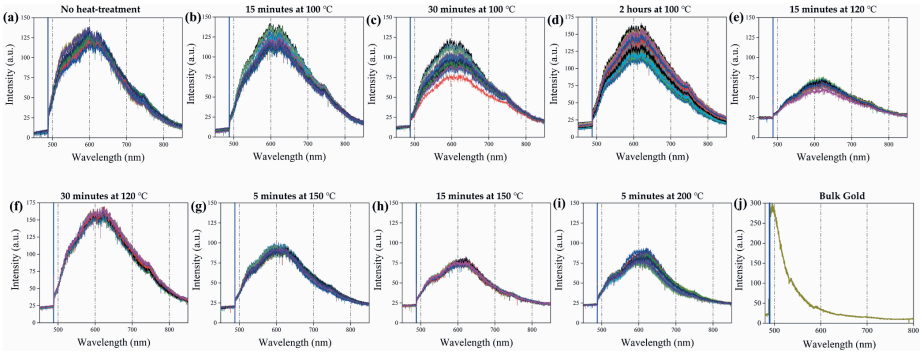

Figure C.4: The photoluminescence response spectra of a) non-thermally treated sample, b) 15 minutes at 100 ℃, c) 30 minutes at 100 ℃, d) 120 minutes at 100 ℃, e) 15 minutes at 120 ℃, f) 30 minutes at 120 ℃, g) 5 minutes at 150 ℃, h) 15 minutes at 150 ℃, i) 5 minutes at 200 ℃, and j) Bulk gold, under laser excitation 488 nm. PL measurement conditions: grating of 600 gr cm-3, objective lens = 10× (NA = 0.25); acquisition time = 20 s, integration time = 1. For all lasers, 30 measurements (3 in length × 10 in cross-section) were performed. All AuNPs deposited with SAM voltage/current setting of V=0.9 kV and I=5mA.

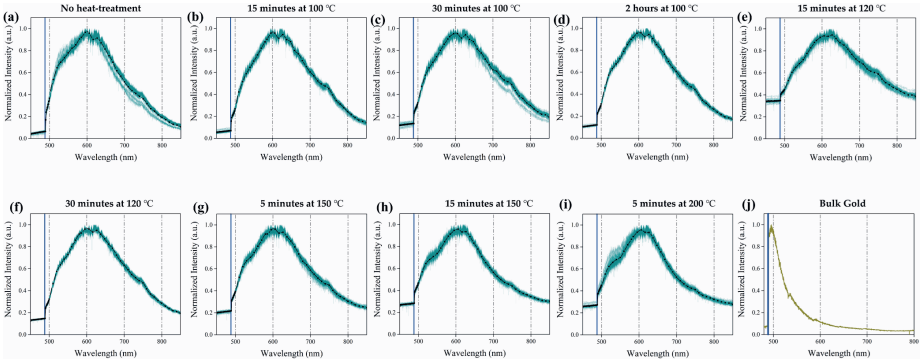

Figure C.5: The normalized photoluminescence response spectra with peak of a) non-thermally treated sample, b) 15 minutes at 100 ℃, c) 30 minutes at 100 ℃, d) 120 minutes at 100 ℃, e) 15 minutes at 120 ℃, f) 30 minutes at 120 ℃, g) 5 minutes at 150 ℃, h) 15 minutes at 150 ℃, i) 5 minutes at 200 ℃, and j) Bulk gold, under laser excitation 488 nm. PL measurement conditions: grating of 600 gr cm-3, objective lens = 10× (NA = 0.25); acquisition time = 20 s, integration time = 1. For all lasers, 30 measurements (3 in length × 10 in cross-section) were performed. All AuNPs deposited with SAM voltage/current setting of V=0.9 kV and I=5mA.

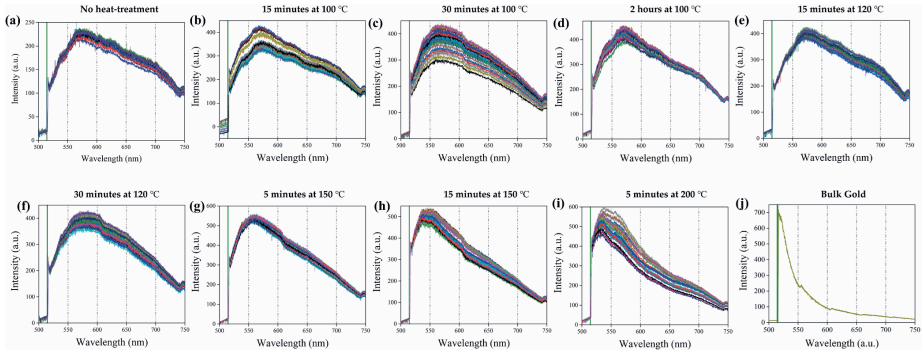

Figure C.6: The photoluminescence response spectra of a) non-thermally treated sample, b) 15 minutes at 100 ℃, c) 30 minutes at 100 ℃, d) 120 minutes at 100 ℃, e) 15 minutes at 120 ℃, f) 30 minutes at 120 ℃, g) 5 minutes at 150 ℃, h) 15 minutes at 150 ℃, i) 5 minutes at 200 ℃, and j) Bulk gold, under laser excitation 514 nm. PL measurement conditions: grating of 600 gr cm-3, objective lens = 10× (NA = 0.25); acquisition time = 10 s, integration time = 2. For all lasers, 30 measurements (3 in length × 10 in cross-section) were performed. All AuNPs deposited with SAM voltage/current setting of V=0.9 kV and I=5mA.

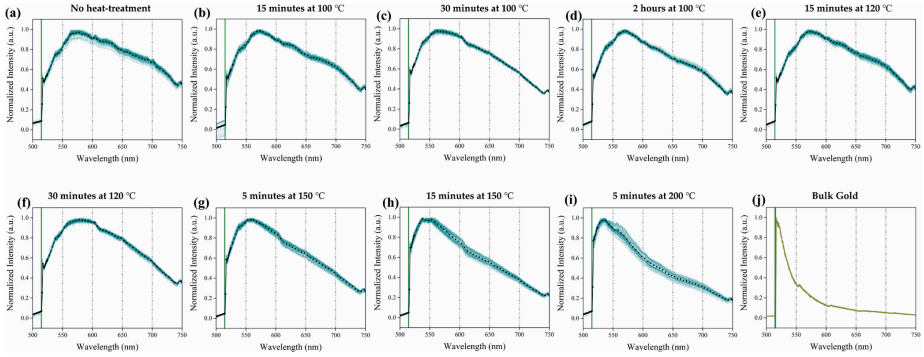

Figure C.7: The normalized photoluminescence response spectra with peak of a) non-thermally treated sample, b) 15 minutes at 100 ℃, c) 30 minutes at 100 ℃, d) 120 minutes at 100 ℃, e) 15 minutes at 120 ℃, f) 30 minutes at 120 ℃, g) 5 minutes at 150 ℃, h) 15 minutes at 150 ℃, i) 5 minutes at 200 ℃, and j) Bulk gold, under laser excitation 514 nm. PL measurement conditions: grating of 600 gr cm-3, objective lens = 10× (NA = 0.25); acquisition time = 10 s, integration time = 2. For all lasers, 30 measurements (3 in length × 10 in cross-section) were performed. All AuNPs deposited with SAM voltage/current setting of V=0.9 kV and I=5mA.

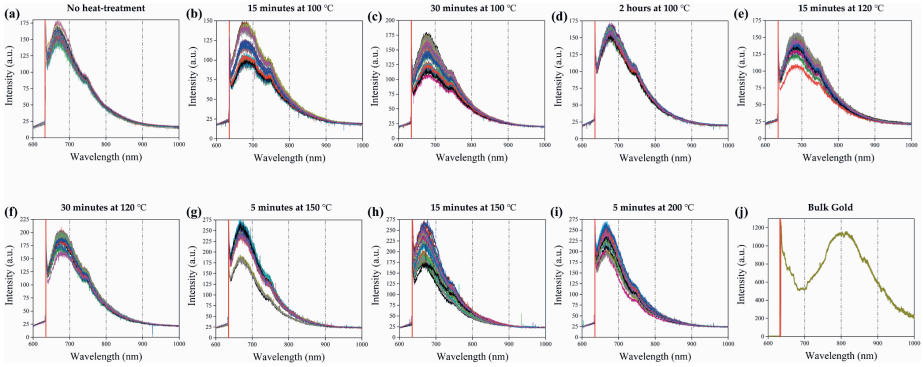

Figure C.8: The photoluminescence response spectra of a) non-thermally treated sample, b) 15 minutes at 100 ℃, c) 30 minutes at 100 ℃, d) 120 minutes at 100 ℃, e) 15 minutes at 120 ℃, f) 30 minutes at 120 ℃, g) 5 minutes at 150 ℃, h) 15 minutes at 150 ℃, i) 5 minutes at 200 ℃, and j) Bulk gold, under laser excitation 633 nm. PL measurement conditions: grating of 600 gr cm-3, objective lens = 10× (NA = 0.25); acquisition time = 10 s, integration time = 1. For all lasers, 30 measurements (3 in length × 10 in cross-section) were performed. All AuNPs deposited with SAM voltage/current setting of V=0.9 kV and I=5mA.

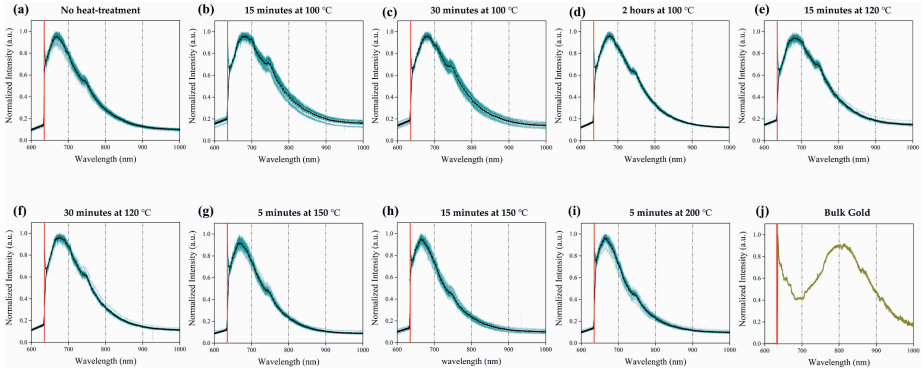

Figure C.9: The normalized photoluminescence response spectra with peak of a) non-thermally treated sample, b) 15 minutes at 100 ℃, c) 30 minutes at 100 ℃, d) 120 minutes at 100 ℃, e) 15 minutes at 120 ℃, f) 30 minutes at 120 ℃, g) 5 minutes at 150 ℃, h) 15 minutes at 150 ℃, i) 5 minutes at 200 ℃, and j) Bulk gold, under laser excitation 633 nm. PL measurement conditions: grating of 600 gr cm-3, objective lens = 10× (NA = 0.25); acquisition time = 10 s, integration time = 1. For all lasers, 30 measurements (3 in length × 10 in cross-section) were performed. All AuNPs deposited with SAM voltage/current setting of V=0.9 kV and I=5mA.

Curriculum Vitæ

Saleh Aghajani

1990/03/10 Born in Tehran, Iran

Education

2018-2022 **Ph.D** in Micro and Nano Engineering
Department of Precision and Microsystems Engineering
Delft University of Technology, Delft, The Netherlands
Thesis:
Dry Aerosol Direct Writing for Selective Nanoparticle Deposition
Promotor: Dr. Ir. Marcel Tichem
Co-Promotor: Dr. Angelo Accardo

2014-2017 **M.Sc** in Material Science and Nanotechnology
Politecnico Di Milano, Milan, Italy
Thesis:
Template guided deposition of nanoparticles inks on structured surfaces
Academic Supervisor: Dr. Carlo Spartaco Casari
Industrial Supervisor: Dr. Rolando Ferrini

2008-2013 **B.Sc** in Mechanical Engineering
Amirkabir University of Technology (Tehran Polytechnic), Tehran, Iran
Thesis:
A semi-analytical solution for stress analysis of moderately thick functionally-graded material (FGM) rectangular panels with various boundary conditions under concentrated loading-EKM method
Supervisor: Dr. M. M. Aghdam

Experience

Jul. 2022-Present	**Application Engineer** *Mesoline, Rotterdam, The Netherlands*
Jan. 2017-Oct.2017	**Internship** *Swiss Centre for Electronics and Microtechnology (CSEM), Basel, Switzerland*
Sep. 2013-Aug. 2014	**Mechanical Design Engineer** Imaco Fire Company, Tehran, Iran

List of Publications

Journal papers:

1. **Aghajani, S.**, Accardo, A., & Tichem, M. (2020). Aerosol Direct Writing and Thermal Tuning of Copper Nanoparticle Patterns as Surface-Enhanced Raman Scattering Sensors. ACS Applied Nano Materials, 3(6), 5665–5675. DOI:10.1021/acsanm.0c00887

2. **Aghajani, S.**, Accardo, A., & Tichem, M. (2021). Tunable photoluminescence and SERS behaviour of additively manufactured Au nanoparticle patterns. RSC Advances, 11(28), 16849–16859. DOI:10.1039/D1RA02266K

3. **Aghajani, S.**, Accardo, A., & Tichem, M. (2022). Process and nozzle design for high-resolution dry aerosol direct writing (dADW) of sub-100 nm nanoparticles. Additive Manufacturing, 54, 102729. DOI:10.1016/J.ADDMA.2022.102729

Conference papers:

1. **Aghajani, S.**, Accardo, A., & Tichem, M. Dry Aerosol Direct Writing (dADW) of metallic nanoparticle micro-patterns.
   48th International conference on Micro and Nano Engineering - Eurosensors (MNE-ES), Leuven, Belgium, September 2022.

2. **Aghajani, S.**, Accardo, A., & Tichem, M. Aerosol Direct Writing of Cu and Au Nanoparticle Patterns for SERS-active Substrates.
   47th Micro and Nano Engineering (MNE) Conference, Turin, Italy, September 2021.

3. **Aghajani, S.**, Accardo, A., & Tichem, M. Aerosol Direct Writing of 3D Copper Nanopatterns as SERS-active Substrate.
   International MicroNanoConference 2020 (iMNC 2020), December 2020.

4. **Aghajani, S.**, Entink, B., Sasso, L., & Tichem, M. Sonic and sub-sonic gas-phase printing of nanoparticle patterns.
   International MicroNanoConference 2018 (iMNC 2018), Amsterdam, The Netherlands, December 2018.

Acknowledgments

Looking for a new intellectual challenge led me to the technical university of Delft. Starting my PhD study was beginning a new chapter in my life that would help me achieve my long-term goals. Despite many ups and downs, joys and sorrows, I learned and grew beyond my expectations in various aspects through this journey. I owe it all to the many people who have offered me their genuine support and encouragement. I want to take this opportunity to thank them all.

First, I would like to thank my promoter and supervisor, **Dr Ir. Marcel Tichem**, for allowing me to work on this exciting, novel and multidisciplinary project in the Micro and Nano engineering (MNE) group. Your expert supervision and ability to foster a friendly and dynamic work environment enabled me to grow personally and professionally. When **Dr Angelo Accardo** joined PME and became my co-promoter, my supervision team grew even stronger. Marcel and Angelo, you taught me how to approach difficult and complex problems and solve them effectively and independently. Your encouragement and guidance allowed me to confidently and independently pursue my research interests. I am forever grateful for your support. Also, I'd like to thank **Dr Luigi Sasso**, who was in my supervision team. Even though we only had a little time together, it was fascinating and fruitful.

To complete this project, I used a wide range of experimentation, primarily found in the PME department, all of which is dependent on our technical team, **Patrick**, **Spiridon**, **Bradley**, **Gideon**, **Alex** and **Rob**, who not only provide training and lab support but also actively volunteer for any assistance in experimental works. I want to specially thank **Patrick Van Holst**, **Harry Jansen** and **Gideon Emmaneel** for their endless support on my setup for building, maintenance and optimization, which I couldn't do without their help. In addition, I want to thank **Spiridon van Veldhoven**, **Bradley But** and **Alex van den Bogaard** for lots of assistance, including training, 3D printing, and all the support. Also, I like to thank **Cees Kwakernaak** in the department of Material Science and Engineering (MSE) for SEM training. It is also helpful to have the support of PME secretaries. I want to thank **Birgit**, **Corinne**, **Eveline**, **Annemieke**, **Marli**, and **Marianne** for making my work easier. Moreover I would like to thanks our department manager **Lisette**, for all the efforts to make our life in PME better.

I had the privilege to be part of the Micro and Nano Engineering group (MNE) during my doctoral studies and was surrounded by many wonderful people. **Ivan Buijsters**, **Murali Ghatkesar**, **Guido Janssen**, **Andres Hunt**, **Urs Staufer**, **Daniel Fan**, **Thomas Manzaneque Garcia**, **Andre Sartori**, **Livia Angeloni**, **Cristina Varone**, **Kai Wu**, **Alkisti Gkouzou**, **Ahmed Sharaf**, **Pieter van Altena**, **Qais Akolawala**, **Abilash Chandrashekar**, **Zichao Liu**, **Gürhan Özkayar**, **Eleonoor Verlinden** and many more I might forget to mention, thank you for the lovely time, discussions, brainstorming and occasional outings.

I would also like to thank all the friends I found in PME: **Yong Zhang**, **Malte ten Wolde**, **Sabiju Valiya Valappil**, **Dave Sonneveld**, **Irek Roslon**, **Rajit Ranjan**, **Vibhas Mishra**, **Gerben van der Meer**, **Hanqing Liu**, **Stijn Koppen**, **Inge van der Knijff**, **Ata Keşkekler**, **Nils Hermann**, **Andrea Cupertino**, **Arnoud Delissen**, **Xianfeng Chen**, and **Satadal Dutta**.

In July 2022, I became a part of a new family by joining Mesoline B.V. as an application engineer in the field of micro and nanomanufacturing. This was a new story which I chose with lots of enthusiasm and I have to confess it increases over time. I would like to thanks **Thomas** our CEO for founding me and giving me the job. Also, I would like to thank **Marnix** our CTO and **Serhii**, the head of research in Mesoline, who helped me to learn and engage in lots of complex and intellectual challenges. Moreover, I like to thank the rest of the group, **Victoria**, **Marienne**, **Marina**, **Vivek**, **Pieter**, **Niels**, **Christian**, **Akshay** and **Amir**.

Living in Delft for the past four years has been a wonderful experience, made even better by the abundance of supportive friends. **Ali & Azar**, **Nima & Delaram**, **Amin & Maryam**, **Siamak & Sanaz**, **Gurhan & Parinaz**, **Hadi**, **Banfasheh & Mohammad**, **Hassan & Elaheh**, **Farbod**, you always make life more fun. I would like to thank you for being a part of my life.

As a bonus, I'd like to thank specifically **Ali & Shaghayegh**, **Ali & Shahrzad**, **Davood & Afagh**, **Sonia** and **Zahra** for wonderful nights of board games and gatherings that made my life in the Netherlands even more enjoyable. I hope these gatherings continue, as I have thoroughly enjoyed previous ones.

I'd like to thank my old friends **Amir Abbas**, **Ghobad**, **Mina**, **Sina**, and **Bahram** for being in my life for more than 6 years from good old times in Milano (**Amir Abbas** for more than 15 years and from Iran, it's hard to believe but still we are in the same country). Despite our many differences and disagreements, we remain friends, which is incredible, and you were my family when I was far from mine. I would love to have you in my life for many years ahead.

One of the reasons I chose to come to the Netherlands was and is my beloved aunt and uncle, **Zohreh** and **Sirus**. I've moved a lot in the last ten years for school and internships, but coming to the Netherlands was the easiest because of my aunt and uncle's help and kindness. Also, I had the chance to have amazing cousins **Saman**, **Sabrina**, **Yasaman** and her husband **Amir Houshang** in the Netherlands. Thanks for lots of great times.

I want to express my gratitude in particular to my Father-in-law (**Mohammadreza**) and kind mother-in-law **Fatemeh** and my generous sisters-in-law **Mahdieh** and **Mahdis**, who never ceased to amaze me with their wonderful and delectable gifts. For all their assistance and support during my wedding, I would also like to thank my brother-in-laws, **Amirhossein** and particularly **Mahmoud**.

A special thanks go out to my parents, **Fatemeh** and **Yosef**, for their constant support, encouragement and sacrifices, as well as the valuable lessons they taught me, which helped shape my character. I'd like to express my gratitude to my four brothers, **Saber**, **Sadegh**, **Saeb** (**Hassan**), and **Saed** (**Hosein**), for their unwavering support throughout my life. Knowing that you're behind me gives me the confidence to keep going no matter what happens. I can't tell you how grateful I am for all of your help, advice, and encouragement. My life wouldn't be the same without you by my side, and you've been there for me through thick and thin.

This is where I run out of words to express my gratitude, and it's all because of my friend, wife, and soulmate, **Mahnaz**. In my opinion, you're one of the most powerful and intelligent people I've ever met, and I'm thrilled to have you on my side. As a team, we've overcome a lot of challenges and shown that no matter how difficult things get, we can always count on each other. Love for you is indescribably strong and bursts forth whenever I think of you.

Saleh Aghajani
Delft, June 2022

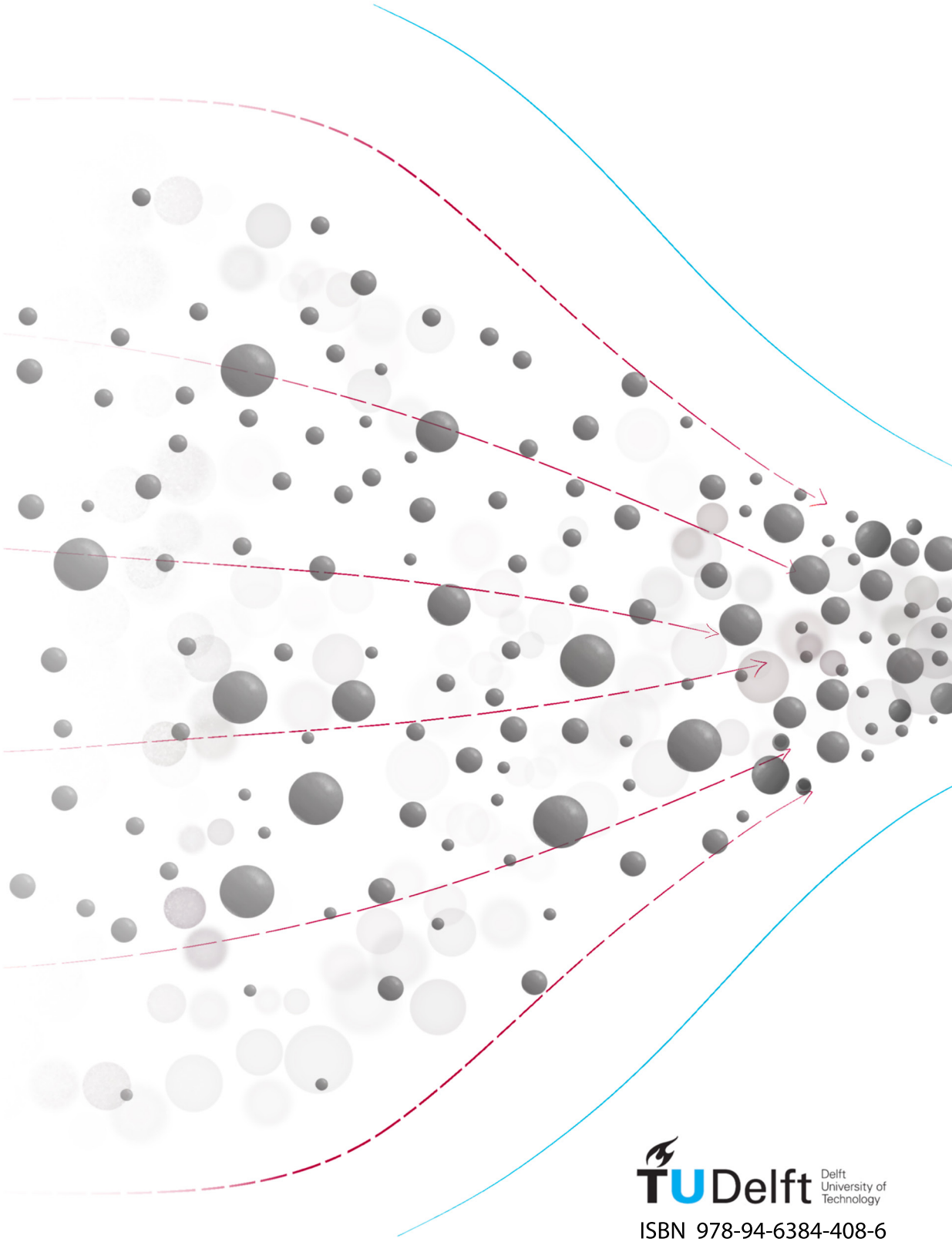

TU Delft Delft University of Technology
ISBN 978-94-6384-408-6